UNIVERSITY OF CALIFORNIA
SANTA CRUZ

INTERACTIONS BETWEEN BLACK HOLES, STARS, AND GALAXIES (AND SOME STRING THEORY)

A dissertation submitted in partial satisfaction of the
requirements for the degree of

DOCTOR OF PHILOSOPHY

in

ASTRONOMY AND ASTROPHYSICS

by

Jamie A.P. Law-Smith

June 2021

The Dissertation of Jamie A.P. Law-Smith is approved:

Enrico Ramirez-Ruiz, Chair

Michael Dine

Ryan J. Foley

Quentin Williams
Interim Vice Provost and Dean of Graduate Studies

Table of Contents

List of Figures

List of Tables

Abstract

Interactions between black holes, stars, and galaxies (and some string theory)

by

Jamie A.P. Law-Smith

A physical understanding of the high energy interactions between black holes and stars, coupled with the context of their galactic birthplaces, will allow us to use these systems as tools to better understand black holes at all masses, the lives and deaths of stars, and the dynamics in galactic centers. This dissertation is concerned with interactions at different physical scales: At the solar radius scale, we present the first simulations of successful common envelope ejection leading to binary neutron star formation in 3D hydrodynamics. At the AU scale, we discuss the tidal disruption of a star by a supermassive black hole. We construct the "tidal disruption menu" of objects and black holes that lead to observable tidal disruption flares. We use an analytic framework to calculate the composition of the fallback material onto the supermassive black hole as a function of time. We present the first simulations of tidal disruptions of stars with realistic structures and compositions, which predict abundance anomalies at the peak timescale. We present the STARS library, a grid of simulations interpolated to provide the mass fallback rate to the black hole for a main-sequence star of any mass, age, and impact parameter. We show that all of our simulations can be reduced to a single relationship. Connecting these phenomena to kpc-scale galaxy physics, we present a systematic study of tidal disruption event host galaxies in the context of the local galaxy population, and in particular our finding that they are highly centrally

concentrated. Finally, at cosmological scales, we present a study on the obstacles to constructing de Sitter space in theories of quantum gravity. We find that, within controlled approximations, one lacks the tools to construct de Sitter space in string theory.

Acknowledgments

Thank you Enrico Ramirez-Ruiz, Michael Dine, Douglas N.C. Lin, Selma E. de Mink, and Ryan J. Foley for your incredible support, your patience, your guidance, and your time and energy.

Thank you Ruth Murray-Clay, Daniel Kasen, Kevin Bundy, Xavier Prochaska, Michael Bolte, Andrew Skemer, Robert Fisher, Anthony Aguirre, and Stefano Profumo for your advice and scientific input over the years.

Thank you Rosa Wallace Everson, Lieke van Son, Ylva Gtberg, Alejandro Vigna-Gmez, Zhuoxiao Wang, Xiaojia Zhang, Sara Ellison, Katie Auchettl, Tiara Hung, Jane Dai, Monica Gallegos-Garcia, David Coulter, Morgan MacLeod, James Guillochon, Phillip Macias, Brenna Mockler, Tenley Hutchinson-Smith, Yan Yu, Shijun Sun, Duncan Wood, Decker French, Elena Rossi, Nicholas Stone, Nick Leaf, Sierra Dodd, Ricardo Yarza, Nathaniel Roth, Josiah Schwab, and Dongwook Lee for being wonderful collaborators and many of you good friends. Thank you Lindsay Lauver and Jenna Scarpelli for your administrative wizardry and support.

Thank you Ariadna Murguia-Berthier, Alexa Villaume, Maggie Thompson, Emily Martin, Maria Hamilton, Monine Rodriguez, Mickey Rosenthal, Tyler Takaro, Kevin McKinnon, Bruno Villasenor Alvarez, Ian Boothby, Lakshmi Subbaraj, Faith Deis, Jeffrey Herr, Daniel Broudy, Raina Gandhi, Olu Animashaun, Andrew Holmes, Elizabeth Lenczowski Holmes, Ashley Covington, Nick Delisi, Max Huseby, Steph Sallum, Jim Hollenbach, Chris Mankovich, and Jieun Choi for so many great times and special memories.

Thank you Diana, Mom, Dad, Jennifer, Michael, Steph, Sharon, Phil, Adam, Mackenzie, and all of my extended family for your love and support. Thank you Diana for going through this journey with me side by side.

Published Material

The text of this dissertation includes reprints of the following previously published material.

Chapter 2 was published in the literature as Law-Smith et al. (2017a). Chapter 3 was published in the literature as Law-Smith et al. (2017c). Chapter 4 was published in the literature as Gallegos-Garcia et al. (2018) (led by Monica Gallegos-Garcia and co-advised by myself). Chapter 5 was published in the literature as Law-Smith et al. (2019). Chapter 6 was published in the literature as Law-Smith et al. (2020a). Chapter 7 was published in the literature as Law-Smith et al. (2020b). Chapter 8 was published in the literature as Dine et al. (2021) (alphabetical author order).

Scientific Acknowledgments

This dissertation is based on work supported by NASA grant NNG17PX03C, NASA ATP grant NNX14AH37G, NSF grant AST-1615881, NSF grant AST-1911206, NSF grant AST-1852393, the Danish National Research Foundation (DNRF132), the Packard Foundation, the Heising-Simons Foundation, and the Gordon & Betty Moore Foundation. We acknowledge use of the *Hyades* supercomputer at UCSC, funded by NSF grant AST-1229745 and UCSC, the *lux* supercomputer at UCSC, funded by NSF MRI grant AST-1828315, and the HPC facility at the University of Copenhagen, funded by a grant from VILLUM FONDEN (project number 16599).

To my family

Chapter 1

Introduction

A physical understanding of the high energy interactions between black holes and stars, coupled with the context of their galactic birthplaces, will allow us to use these systems as tools to better understand black holes at all masses, the lives and deaths of stars, and the dynamics in galactic centers. This dissertation is concerned with interactions at different physical scales: at the solar radius scale, the formation of a binary neutron star; at the AU scale, the tidal disruption of a star by a supermassive black hole; at the kpc scale, connecting these phenomena to their galactic birthplaces; and finally, at cosmological scales, de Sitter space in theories of quantum gravity.

1.1 Stellar interactions in a galaxy

Before discussing the particular stellar interactions studied in this dissertation, we make a brief overview of the possible stellar interactions in a galaxy. There are broadly three different sites. In the center of most galaxies is a nuclear star cluster

(with stellar densities of $\sim 10^6$ stars/pc^3) hosting a supermassive black hole. Here, for example, a star can be tidally disrupted by the supermassive black hole. Or, as another example, binary star encounters with the supermassive black hole can lead to hypervelocity stars. There is also occasionally an actively accreting disk around the supermassive black hole, or the remnants of a disk, and stars may interact with this disk. A globular cluster ($\sim 10^3$ stars/pc^3), perhaps on the outskirts of the galaxy, can host, for example, stellar mergers, which are thought to produce the "blue stragglers" on the HR diagram. Or, as another example, two stellar mass black holes can be dynamically assembled into a tight binary and emit gravitational waves. Some globular clusters may also host intermediate mass black holes, a key missing link between stellar mass black holes and supermassive black holes. In addition to in each of these sites, the "field" of a galaxy (~ 1 star/pc^3) can also host binary star systems. Binary star systems can interact via a common envelope episode, which can lead to, for example, compact object binaries that produce gravitational waves, X-ray binaries, supernovae, and gamma-ray bursts.

1.2 Tidal disruptions of stars by supermassive black holes

In the center of most galaxies is a supermassive black hole. Surrounding the black hole is a dense system of stars. The stars undergo a random walk in angular momentum space through scatterings with other stars. An encounter with another star can send a star onto a nearly radial "loss cone" orbit that brings it close enough to the supermassive black hole that it is ripped apart by the black hole's tidal field. This is a

tidal disruption event (e.g., Hills 1975a; Carter & Luminet 1982a; Rees 1988a; Evans & Kochanek 1989a).

Through a detailed theoretical understanding of disruption itself, coupled with comparison to well-sampled observations, we can determine the black hole's and star's properties and probe accretion/AGN physics on the timescale of weeks. Through the relative rates and demographics of tidal disruptions, we can learn about galaxy properties, such as nuclear stellar populations and the dynamical mechanisms operating in galactic centers. Most supermassive black holes in the local Universe are quiescent—for every active black hole there are approximately 170 quiescent black holes (Gair et al. 2010). Tidal disruption events are a direct probe of these objects, and thus of the supermassive black hole mass function.

In Chapter 2, we construct the "tidal disruption menu" of objects and black holes that lead to observable tidal disruption flares. Typical white dwarfs can effectively probe black holes with masses $\lesssim 10^5 M_\odot$, main sequence stars can effectively probe black holes with masses $10^6 M_\odot \lesssim M_{\rm BH} \lesssim 10^8 M_\odot$, and only evolved stars can probe black holes with masses $\gtrsim 10^8 M_\odot$. Low-mass white dwarfs with extended hydrogen envelopes can effectively probe black holes with masses $10^5 M_\odot \lesssim M_{\rm BH} \lesssim 10^7 M_\odot$, thus filling a gap in the menu. We calculate the unique disruption properties of these objects.

In Chapter 4, we use an analytic framework to calculate the composition of the fallback material onto the supermassive black hole as a function of time. This allows for a large, inexpensive parameter space study. We predict abundance anomalies in nitrogen, carbon, and oxygen in the fallback material that will help to constrain the

nature of the disrupted star.

In Chapter 5, we present the first simulations of tidal disruptions of stars with realistic structures and compositions. We construct stars in a 1D stellar evolution code and calculate their disruption in a 3D hydrodynamics code. We find significant differences in the shape of the mass fallback rate curves from earlier results using polytropic stellar structures. We find that strong abundance anomalies can appear before the peak timescale, in contrast to predictions from the "frozen-in" model.

In Chapter 6, we present the STARS (Stellar TDEs with Abundances and Realistic Structures) library, a grid of simulations interpolated to provide the mass fallback rate to the black hole for a main-sequence star of any mass, age, and impact parameter. In each of the key tidal disruption quantities, we are able to reduce all of our simulations to a single relationship that depends only on stellar structure, characterized by a single parameter $\rho_c/\bar{\rho}$.

1.3 The common envelope phase and binary neutron star formation

In a landmark discovery, both gravitational waves and electromagnetic radiation have been observed from the same astrophysical event, a binary neutron star merger (Abbott et al. 2017a,b; Coulter et al. 2017; Goldstein et al. 2017). However, we do not understand how systems such as this one are formed.

Dynamical assembly is not an effective pathway for binary neutron star mergers (e.g., Ye et al. 2020); they are instead thought to originate almost exclusively from

interacting binaries (Tutukov & Yungelson 1973, 1993; Belczynski et al. 2016). Massive stars are the progenitors of neutron stars and stellar mass black holes, and the majority of massive stars are in interacting binaries (Sana et al. 2012). Binary stars must undergo common envelope evolution (e.g., Paczynski 1976; Iben & Livio 1993), during which two stars share an envelope, for the resulting black holes and/or neutron stars to merge via emission of gravitational radiation within a Hubble time.

Understanding the common envelope phase has resisted five decades of research, both because of theoretical challenges (e.g., the relevant physical and temporal scales span over six orders of magnitude) and, until recently, the lack of observational data. Besides helping to understand the origin of binary neutron star mergers, more broadly, understanding the common envelope phase will lead to a better understanding of the lives and deaths of massive stars and nucleosynthesis in the Universe (most of the elements on the periodic table are produced in systems that go through a common envelope phase).

In Chapter 7, we present the first simulations of common envelope ejection leading to binary neutron star formation in 3D hydrodynamics. We overcome the prohibitive computational cost of simulating this system by using a 1D energy formalism, a 3D "wind tunnel" study, and a 2D integrator to inform our 3D hydrodynamics simulations. The theoretical framework developed with this work will allow for the modeling of virtually any binary star system.

1.4 Galactic birthplaces

Analysis of the host galaxies of high energy astrophysical phenomena can provide insight into the environments in which they are created and thus their physical nature. As an example, understanding galactic birthplaces is how we first understood the two mechanisms of supernovae, core-collapse vs. thermonuclear.

The work in this dissertation focuses on the host galaxies of tidal disruption events—on connecting the AU-scale processes that lead to these events to global galaxy properties and galaxy evolution. The relative rates of tidal disruption events in different galaxy hosts can help determine the dynamical mechanisms operating in galactic nuclei. Tidal disruption event rates are typically calculated from two-body relaxation in a spherical star cluster (Magorrian & Tremaine 1999a; Wang & Merritt 2004a). However, this simple picture is likely incorrect. Stars can interact with one another coherently, leading to rapid angular momentum evolution (Rauch & Tremaine 1996); for example, this occurs for eccentric nuclear disks (Madigan et al. 2018). A second massive body, such as an inspiraling moderately massive black hole, could also induce large-angle scatterings of stars (Ivanov et al. 2005; Chen et al. 2009). These processes and others could result in enhanced rates within particular galaxy hosts (for a review, see Alexander 2017). Moreover, tidal disruption events have been preferentially observed in rare quiescent Balmer-strong galaxies (also known as post-starburst galaxies, or more restrictively as E+A galaxies; Arcavi et al. 2014a; French et al. 2016a), implying a rate enhancement in these galaxies.

In Chapter 3, we study tidal disruption event host galaxies in the context

of the local galaxy population. By creating matched galaxy samples, we determine that selection effects can account for some, but not all, of the E+A overrepresentation. We find that tidal disruption event host galaxies have atypical photometric properties compared to similar, "typical" galaxies. In particular, we tidal disruption event host galaxies are highly centrally concentrated, suggesting higher nuclear stellar densities and a physical explanation for an enhanced rate. We also find that tidal disruption event host galaxies live in the "green valley" between blue star-forming spiral galaxies and red elliptical galaxies. The galaxy-matching framework developed with this work is general and has recently been applied to study the host galaxies of changing-look quasars (Dodd et al. 2021).

1.5 de Sitter space in theories of quantum gravity

The presently observed dark energy (Perlmutter et al. 1999; Percival et al. 2010; Aghanim et al. 2018) is consistent with a de Sitter solution of Einsteins equations. Shortly after the Big Bang, the universe also likely went through a period of exponential expansion (Guth 1987; Starobinsky 1987; Linde 1982; Albrecht & Steinhardt 1987). So de Sitter space plays an important role in understanding our present and past universe. However, it is difficult, and perhaps even impossible, to construct stable or metastable de Sitter space in our current understanding of theories of quantum gravity. This fact has implications for inflation, the nature of the presently observed dark energy, and whether string theory is the correct theory of quantum gravity.

In Chapter 8, we study the obstacles to constructing de Sitter space in string

theory. We find that, within controlled approximations, one lacks the tools to construct de Sitter space in string theory. Such approximations would require the existence of a set of (arbitrarily) small parameters, subject to severe constraints. But beyond this one also needs an understanding of big-bang and big-crunch singularities that is not currently accessible to standard approximations in string theory.

Chapter 2

Low-mass White Dwarfs with Hydrogen Envelopes as a Missing Link in the Tidal Disruption Menu

Abstract

We construct a menu of objects that can give rise to bright flares when disrupted by massive black holes (BHs), ranging from planets to evolved stars. Through their tidal disruption, main sequence and evolved stars can effectively probe the existence of otherwise quiescent supermassive BHs and white dwarfs can probe intermediate mass BHs. Many low-mass white dwarfs possess extended hydrogen envelopes, which

allow for the production of prompt flares in disruptive encounters with moderately massive BHs of 10^5–10^7 $M_\odot$—masses that may constitute the majority of massive BHs by number. These objects are a missing link in two ways: (1) for probing moderately massive BHs and (2) for understanding the hydrodynamics of the disruption of objects with tenuous envelopes. A flare arising from the tidal disruption of a 0.17 $M_\odot$ white dwarf by a 10^5 $M_\odot$ BH reaches a maximum between 0.6 and 11 days, with a peak fallback rate that is usually super-Eddington and results in a flare that is likely brighter than a typical tidal disruption event. Encounters stripping only the envelope can provide hydrogen-only fallback, while encounters disrupting the core evolve from H- to He-rich fallback. While most tidal disruption candidates observed thus far are consistent with the disruptions of main sequence stars, the rapid timescales of nuclear transients such as Dougie and PTF10iya are naturally explained by the disruption of low-mass white dwarfs. As the number of observed flares continues to increase, the menu presented here will be essential for characterizing nuclear BHs and their environments through tidal disruptions.

2.1 Introduction

When a star wanders too close to a massive black hole (MBH), it can be ripped apart by the hole's tidal field (Hills 1975a; Frank 1978; Gurzadian & Ozernoi 1979; Carter & Luminet 1982a; Rees 1988a). In a typical disruption, half of the material will be ejected on hyperbolic trajectories and half of the material will remain bound to the MBH; the accretion of this material gives rise to a transient usually referred to

as a tidal disruption event (TDE). With accurate theoretical modeling, TDEs allow us to uncover the mass of the black hole, the characteristics of the surrounding stellar population, the dynamics of the galactic nucleus, and the physics of black hole accretion under well-defined conditions (Guillochon et al. 2014a). TDEs can also provide a direct and unambiguous probe of the MBH occupation fraction of low-mass galaxies, which is crucial for constraining MBH seed formation efficiency at high redshifts—a dominant mechanism of initial galaxy formation (De Colle et al. 2012; Guillochon & Ramirez-Ruiz 2015a; Stone & Metzger 2016a; Kochanek 2016b). The opportunity to study BHs in the local universe through TDEs is important, because for every actively accreting BH, there are ~ 170 quiescent BHs (Greene & Ho 2007a; Gair et al. 2010).

TDEs are observationally identified by a combination of a dramatic increase in brightness, proximity to a non-active host galaxy's center, and weak or no color evolution at optical/UV wavelengths, with a decay in luminosity that is theoretically predicted to follow a $t^{-5/3}$ law (for reviews of the observations, see e.g. Komossa 2015a; Auchettl et al. 2017a). The most compelling events are those in which the rise, peak, and decay of the optical/UV transient are observed with frequent cadence, as each of these phases of a TDE contain vital information about the disruption, and can be used to constrain the properties of the host black hole and the object that was disrupted (e.g., Gezari et al. 2012a; Guillochon et al. 2014a). Taken in a statistical sense, the observed rates of tidal disruption and, in particular, the relative rates of disruptions of different stellar objects, will hold tremendous distinguishing power in terms of both the dynamical mechanisms operating in galactic centers and the properties of the populations of stars themselves

(MacLeod et al. 2012a, 2014, 2016a).

A central objective of this work is to understand the menu of all possible TDEs about massive BHs—i.e., which objects produce tidal disruption flares for which BH masses, and how they dictate the properties of the fallback accretion rate onto the BH. An object of mass M and radius R can be torn apart if it crosses the tidal radius, $r_{\rm t} = (M_{\rm bh}/M)^{1/3}\ R$, of a BH with mass $M_{\rm bh}$. Therefore, the characteristics of a particular stellar object hold information about the nature of its disruption—whether it occurs near the BH's innermost bound circular orbit, and, if so, how relativistic the encounter is. BHs with masses $\gtrsim 10^7\ M_\odot$ are well probed by MS stars, evolved stars, and planets, but the debris could be ineffective at circularizing for BHs with masses $\lesssim 10^6\ M_\odot$, as shown by semi-analytic results in Guillochon & Ramirez-Ruiz (2015a), as well as the Newtonian and relativistic hydrodynamic simulations of Guillochon et al. (2014a) and Shiokawa et al. (2015). BHs with masses $\lesssim 10^5\ M_\odot$ could be probed by typical white dwarfs (although BH spin could raise this limit to $10^6\ M_\odot$; Tejeda et al. 2017a).

Thus far, most observed TDE candidates come from host galaxies with inferred BH masses of $\gtrsim 10^6\ M_\odot$. Even though survey selection effects make seeing TDEs from lower-mass BHs less likely (see e.g., Kochanek 2016b), we should expect to observe them with future surveys if the BH mass function is not truncated below $10^6\ M_\odot$. Tidal disruption flares are potentially a powerful probe of the galaxy occupation fraction of these BHs, and could help discriminate between BH mass functions that are flat, rising (as extrapolated from the M–σ relation), and/or truncated at low masses. Our ability

to use TDEs as direct probes of black hole demographics necessitates a detailed understanding of how the observability of TDEs depends on the properties of the disrupted star. Constructing a complete menu of stellar tidal disruption simulations—as we do in this work—is an important step in addressing these questions.

Theoretical studies of stellar structure and fallback rate began with Lagrangian (Evans & Kochanek 1989a) and Eulerian (Khokhlov et al. 1993b) calculations, and have evolved to include detailed studies of MS stars (Lodato et al. 2009a; Ramirez-Ruiz & Rosswog 2009; Guillochon & Ramirez-Ruiz 2013a), giant planets (Guillochon et al. 2011; Liu et al. 2013), white dwarfs (Luminet & Pichon 1989; Kobayashi et al. 2004; Rosswog et al. 2008a,b, 2009; Zalamea et al. 2010; Clausen & Eracleous 2011; Krolik & Piran 2011; Haas et al. 2012; Cheng & Bogdanović 2014a; MacLeod et al. 2014, 2016a; Vick et al. 2016), and giant stars (MacLeod et al. 2012a, 2013).

A finding common to all calculations is that a more centrally concentrated object has a quicker-peaking fallback rate and requires a deeper encounter for full disruption than a less centrally concentrated object. Here, "deeper" is in relation to the tidal radius definition, which relates to the average density. The presence of a core is also important in determining the fallback rate; in giant stars, the massive core plays a key role yet typically remains intact, while in giant planets, the lighter core is much more vulnerable. These considerations are crucial, as we expect the stellar structure to be imprinted on the luminosity evolution of the flare. In many of the observed events, the luminosity evolution closely follows the predicted mass fallback onto the BH (a classic example is PS1-10jh; Gezari et al. 2012a; Guillochon et al. 2014a). This preservation of

the fallback rate implies that circularization of the debris is prompt in these cases; the mass feeding rate is primarily determined by fallback and is not significantly delayed by viscous effects.

Flares can be delayed if the amount of energy dissipated per orbit—or "viscosity"—is small. When the stream's self-intersection point is relatively close to the BH, energy dissipation is large, allowing the debris to circularize quickly (Bonnerot et al. 2016a). Once the disk is formed, the viscous transport timescale (i.e., the time it takes material to accrete) at the circularization radius is much shorter than the peak fallback timescale. When the stream's self-intersection point is much farther from the BH than the peri-apse distance, however, circularization is not effective, and a highly elliptical disk is formed (Ramirez-Ruiz & Rosswog 2009; Shiokawa et al. 2015). In this case, the viscous timescale can be significantly longer than the peak fallback timescale (Guillochon & Ramirez-Ruiz 2015a).

Stellar structure in tidal disruption calculations has thus far been implemented using polytropic profiles, with the simplest examples being the single-polytrope models of MS stars and WDs. Evolved stars and planets with cores are not well described by a single polytrope; these objects have been studied using a nested polytrope in which the envelope is a significant fraction of the total mass (MacLeod et al. 2012a; Liu et al. 2013).

In this work we perform the first tidal disruption calculations for objects where the atmosphere has a small mass relative to the core, with our primary motivating physical example being a low-mass He WD with a hydrogen envelope—though we note

that this structure could potentially also be used to model hot Jupiters or very evolved stars. Any WD below $\approx 0.46\ M_\odot$ has a helium core, and possesses a hydrogen envelope that, despite its comparatively low mass, can extend to several times the core's radius (e.g., Nelemans et al. 2001). In this work, we calculate the disruption of these objects and predict their observational properties. We argue that these objects are a missing link in two ways: (1) for probing moderately massive BHs, and (2) for understanding the hydrodynamics of the disruption of objects with tenuous envelopes, as such structures have not yet been studied. We find that these low-mass WDs with hydrogen envelopes offer prompt flares at higher-mass BHs than their more typical WD counterparts, and occupy a unique parameter space in time and luminosity at peak.

In Section 2.2, we develop the tidal disruption menu, which is our motivation for the hydrodynamical simulations of this paper. In Section 2.3, we discuss the particulars of He WDs. In Section 2.4, we outline our hydrodynamical setup for disrupting these objects, and in Section 7.3 we present numerical results from these simulations. In Section 2.6, we present an overview of tidal disruption flare demographics in terms of peak timescales and fallback rates. In Section 7.4, we summarize our findings and show that fast-rising events such as Dougie and PTF10iya are naturally explained by the disruption of an He WD.

2.2 Tidal Disruption Menu

To determine whether an object is disrupted or swallowed by a black hole, we need to compare the tidal radius, $r_{\rm t}$, to the innermost bound circular orbit of the black

hole,

$$r_{\rm ibco} = \frac{2GM_{\rm bh}}{c^2}\left(1 - \frac{a_*}{2} + \sqrt{1-a_*}\right), \tag{2.1}$$

where $a_* = a/M$, $a = J_*/M_*c$, $M = GM_*/c^2$, and M_* and J_* are the mass and angular momentum of the BH, respectively (Abramowicz & Fragile 2013). For a non-spinning BH, $r_{\rm ibco} = 4GM_{\rm bh}/c^2$, and for a maximally spinning BH, $r_{\rm ibco} = GM/c^2$. If $r_{\rm t} > r_{\rm ibco}$, disruption is possible. Otherwise, the object is swallowed whole (e.g., East 2014). For simplicity we assume here that disruption is only possible when the impact parameter $\beta = r_{\rm t}/r_{\rm peri} \geq 1$; more accurately, disruption is a smooth function of β. For a non-spinning BH, we therefore require

$$M_{\rm bh} \leq M_{\rm bh,\ lim} = \frac{R_\star^{3/2}}{M_\star^{1/2}}\left(\frac{c^2}{4G}\right)^{3/2} \propto \rho_\star^{-1/2} \tag{2.2}$$

for disruption. The mass-radius relationship, then, determines whether an object will be disrupted at a given BH mass. Denser objects such as WDs can only be disrupted by lower-mass BHs while more tenuous objects such as MS or evolved stars can be disrupted by higher-mass BHs.

We can calculate the upper limit for the disruption of a class of objects by using the above relation. We show this menu of BH-object combinations for a non-spinning BH, along with a prompt circularization condition explained below, in Figure 2.1. We use mass-radius relations for WDs, MS stars, evolved stars, and sub-stellar objects. We find that He WDs with hydrogen envelopes play a special role in this menu, as, similar to evolved stars, they can have a wide range of radii at a given mass, depending on their

age. Compared to the relatively tight mass-radius relation for typical white dwarfs, these objects allow access to a higher range of BH masses. More details on He WDs and our stellar evolution calculations of their structure are given in Section 2.3. Our choice of representative masses and ages is justified there.

Many of the tidal disruption candidates observed thus far show a luminosity time evolution that closely follows the mass fallback rate from the star to the BH (see e.g., Guillochon et al. 2014a). This suggests that current observations may select for events in which debris circularization is prompt. Recent work suggests that prompt circularization occurs predominantly for encounters where general relativistic effects are important (Hayasaki et al. 2013a; Dai et al. 2015; Guillochon & Ramirez-Ruiz 2015a). We take a "circularization condition" of $r_{\rm t} < 10GM_{\rm bh}/c^2$ in order to select encounters in this regime. Following Dai et al. (2015) and Guillochon & Ramirez-Ruiz (2015a), this corresponds to a de Sitter apsidal precession of $\Omega \gtrsim 54^\circ$ for non-spinning BHs. Note that more weakly plunging encounters will still circularize some fraction of the time, and that they may also be observable as events where the luminosity evolution is viscously delayed; our condition is meant as a guideline for where we can expect to see predominantly prompt circularization events for a given disruptee. Note also that most events in the X-rays appear to be viscously delayed (Auchettl et al. 2017a).

For a non-spinning BH, our condition for prompt flares is then $4GM_{\rm bh}/c^2 < r_{\rm t} < 10GM_{\rm bh}/c^2$. WDs can only be disrupted by BHs with masses $\lesssim 10^5\ M_\odot$, while MS and evolved stars only obey our prompt flare condition for BHs with masses $\gtrsim 10^6\ M_\odot$. Because of their extended radius, low-mass WDs with hydrogen envelopes can serve

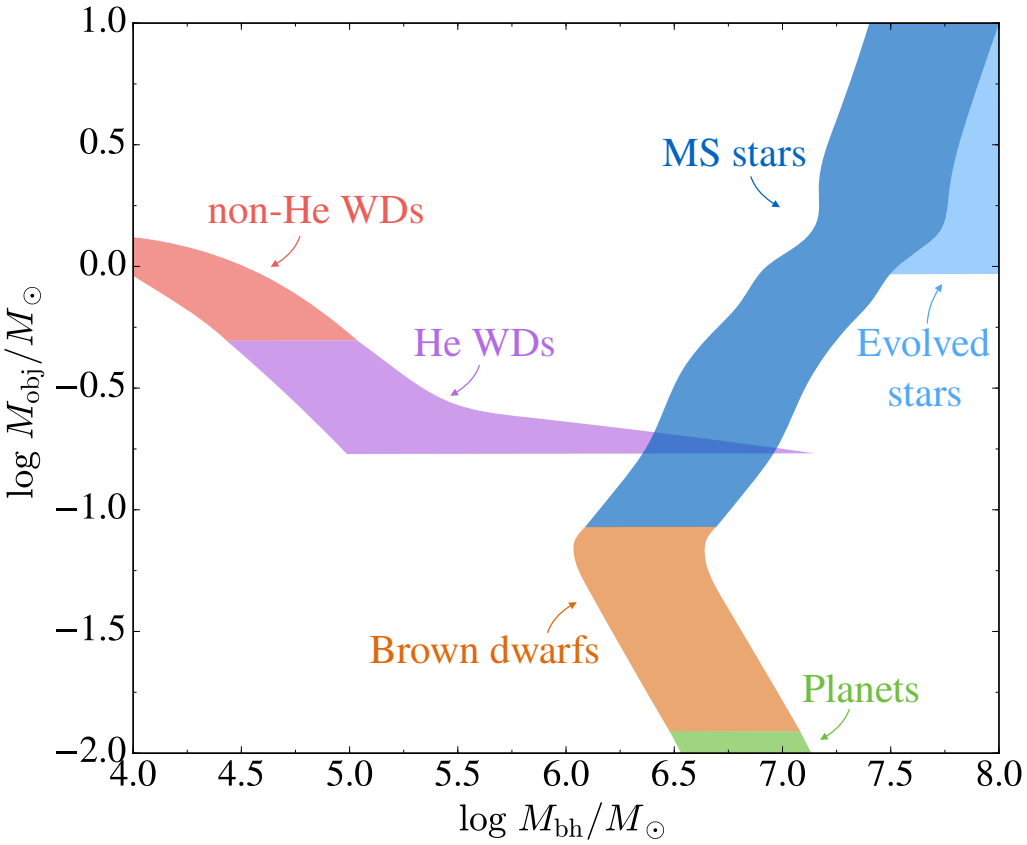

Figure 2.1: Regions where prompt tidal disruption flares are favorable in $M_{\rm obj}$ vs. $M_{\rm bh}$ space for a non-spinning BH. Encounters have $4GM_{\rm bh}/c^2 < r_{\rm t} < 10GM_{\rm bh}/c^2$. Note that disruption is still possible for lower BH masses than shown in each region. We include mass-radius relationships for typical WDs from Zalamea et al. (2010), MS stars from Tout et al. (1996), evolved stars from Bressan et al. (2012, 2013), and sub-stellar objects from the 1 Gyr curve of Chabrier et al. (2009). We define MS stars as $M \geq 0.085\ M_\odot$, brown dwarfs as $0.085\ M_\odot > M \geq 13\ M_{\rm Jup}$, and planets as $M < 13\ M_{\rm Jup}$. For evolved stars, we choose masses above $0.9\ M_\odot$ (here the evolutionary time is approximately equal to the Hubble time) and radii up to the radius at the tip of the red giant branch for this mass star. WDs below $\sim 0.5\ M_\odot$ will be helium-core hydrogen-envelope WDs. We calculate the radii of three He WDs 1 Gyr after formation and interpolate for masses in between. We choose representative masses of $0.17\ M_\odot$, $0.25\ M_\odot$, and $0.38\ M_\odot$, with initial envelope masses of $0.011\ M_\odot$, $0.016\ M_\odot$, and $0.019\ M_\odot$ respectively. This is motivated by the fact that the mass distribution of He WDs is expected to be relatively flat (Maoz et al. 2012).

as a missing link between these two regimes. Their envelope can be disrupted and stripped by higher BH masses than allowed for by typical WDs. These BH masses offer a relatively smaller fraction of prompt flares from MS stars due to their inefficient circularization here. The constraints derived for He WDs, here assumed to be at least 1 Gyr after formation, could be extended to higher-mass BHs for younger He WDs, which have significantly more extended envelopes. For example, a 100 Myr old 0.17 $M_\odot$ He WD can have a radius of 0.5 $R_\odot$, allowing it to be disrupted by a 10^8 $M_\odot$ BH.

Low-mass WDs can thus extend the range of BH masses available to the higher-mass, single-star evolution WDs through tidal disruption.[1] While these objects make up a small fraction of the stellar population, they deserve to be examined in more detail because of their unique location in our prompt circularization menu, which, as we argue, makes their emerging flares more favorable to detection.

2.3 Helium-core Hydrogen-envelope WDs

2.3.1 Properties

Since WDs have an inverse mass-radius relationship, the lowest mass WDs will be able to probe the highest mass BHs. Let us estimate the lowest mass WD available through single-star evolution. Setting the main sequence lifetime equal to the age of the universe ($\approx$ 13.8 Gyr; Hurley et al. 2000) using an analytic formula for the MS lifetime from Hinshaw et al. (2013) gives $M_\mathrm{i} \approx 0.9\ M_\odot$. Using this mass in an empirical

[1] There is some evidence now mounting for observational candidates of WD disruptions by intermediate mass BHs. In particular, an emerging class of ultra-long gamma-ray burst (ULGRB) sources share similar timescales and luminosities to WD disruptions (see Levan et al. 2014; Levan 2015; MacLeod et al. 2014, 2016a).

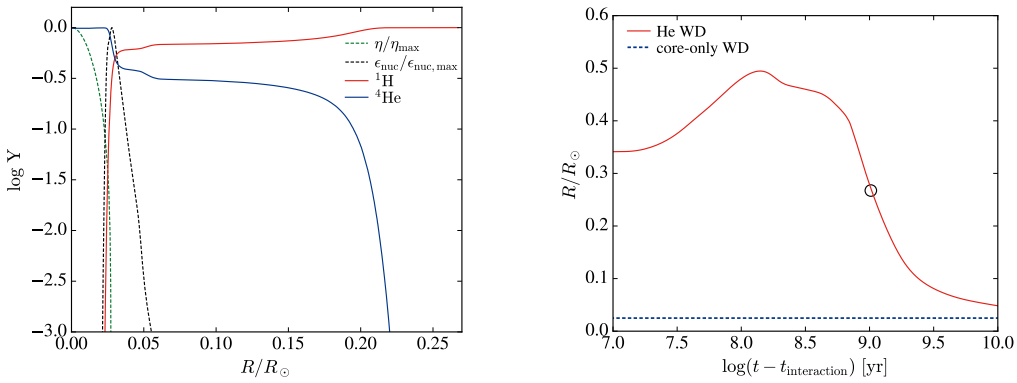

Figure 2.2: Left panel: helium (blue) and hydrogen (red) abundances as a function of radius for a 0.17 $M_\odot$ helium-core hydrogen-envelope WD 1 Gyr after formation. The mass of the hydrogen envelope is only 10^{-2} $M_\odot$, but it extends to roughly 10 times the radius of the core. The green dashed line shows the degeneracy parameter η, indicating the degenerate helium core. The black dashed line shows the nuclear burning fraction $\epsilon_{\rm nuc}$, indicating the thin hydrogen burning region surrounding the core. η and $\epsilon_{\rm nuc}$ are shown normalized to their maximum values. Right panel: radius as a function of time since formation (through a binary interaction) for this WD. Its radius is 10 times larger than that of a WD without an envelope, shown in dashed blue, for more than 1 Gyr. The black circle indicates the age and radius of the object we use in our disruption calculations.

initial–final mass relation for WDs from Catalán et al. (2008) for $M_{\rm i} < 2.7\ M_{\odot}$,

$$M_{\rm f} = (0.096 \pm 0.005) M_{\rm i} + (0.429 \pm 0.015), \tag{2.3}$$

we find that the minimum WD mass possible through single-star evolution is $M_{\rm WD} \approx 0.5\ M_{\odot}$.

WDs less massive than roughly half a solar mass will have formed through binary interactions, barring cases of extreme metallicity (Kilic et al. 2007). Low-mass WDs can be formed either through stable Roche-lobe overflow mass transfer or common-envelope evolution (e.g., Driebe et al. 1998; Sarna et al. 2000; Nelson et al. 2004; Althaus et al. 2013; Nandez et al. 2015). A helium-core WD forms if one component of the binary loses its hydrogen envelope before helium burning. This object has a degenerate helium core and is formed with an extended hydrogen envelope supported by a thin hydrogen burning layer.

The maximum mass of an He WD is approximately $0.46\ M_{\odot}$, and only He WDs are formed below this mass (Sweigart et al. 1990; Nelemans et al. 2001). The final mass of the He WD depends on the mass of the progenitor and the binary orbital properties (e.g., Nelemans et al. 2001). The progenitor star needs a zero-age main sequence mass below $2.3\ M_{\odot}$, as more massive stars do not form helium cores. The strict minimum timescale for formation of an He WD is therefore the MS lifetime of a $2.3\ M_{\odot}$ star, $t_{\rm MS} \approx 1.16$ Gyr (Hurley et al. 2000).

Istrate et al. (2014, 2016) performed calculations of He WD formation via stable mass transfer; we quote some results below. After detachment from Roche-lobe

overflow, the progenitor star enters a "bloated" proto-WD phase where much of the hydrogen in the envelope is burned in stable hydrogen shell burning. The mass of hydrogen left after Roche-lobe detachment is on the order of 10^{-2} $M_\odot$, yet this can fuel a proto-WD phase lasting up to 2.5 Gyr for the lowest mass ($M \lesssim 0.20$ $M_\odot$) WDs.

Istrate et al. (2014) derived a timescale for hydrogen burning,

$$\Delta t_{\rm proto} \simeq 400 \text{ Myr} \left(\frac{0.20 \ M_\odot}{M_{\rm WD}} \right)^7 , \tag{2.4}$$

which describes the star's contraction from Roche-lobe detachment to its maximum effective temperature on the cooling track. Istrate et al. (2016) also defined a cooling timescale, $t_{\rm cool,L_{-2}}$, which is the time from detachment to reaching $\log(L/L_\odot) = -2$ on the cooling track. This timescale is set primarily by the mass of the hydrogen envelope left at the end of the proto-WD phase. Generally, a shorter orbital period at the onset of mass transfer leads to a lower proto-WD mass and a higher final envelope mass.

There is a growing body of observations of these low-mass objects: the targeted survey for extremely low-mass (ELM; $M < 0.3$ $M_\odot$) WDs has found 76 binaries to date, with a median primary mass of ≈ 0.18 $M_\odot$ (Brown et al. 2016b,c). Many of these WDs appear to be bloated, and this bloated state can persist for a long time: Macias et al. (2015) find that roughly half of these systems will still be burning hydrogen when they merge. One object in this sample is the binary system NLTT 11748 (Kaplan et al. 2014), which contains a helium-core hydrogen-envelope WD of mass 0.17 $M_\odot$ and radius 0.043 $R_\odot$, whereas a standard WD mass-radius relation for this mass would give a radius of 0.02 $R_\odot$. This object's bloated size allows it to be disrupted by a

BH of up to 3.8×10^6 $M_\odot$. This WD has a cooling age of 1.6–1.7 Gyr; younger He WDs can have much more extended envelopes, allowing them to be disrupted by even 10^7 $M_\odot$ or 10^8 $M_\odot$ BHs. As an example of this more extreme bloating, observations and astroseismological studies of the eclipsing binary J0247–25 find a He WD with mass 0.186 ± 0.002 $M_\odot$ and radius 0.368 ± 0.005 $R_\odot$ (Maxted et al. 2013). Note that this He WD has a larger radius than a MS star of its mass. In a study of the Galactic WD binary population, Maoz et al. (2012) found that roughly half of WDs in binaries are He WDs, and that the probability density distribution for He WDs is relatively flat below 0.4 $M_\odot$.

It is difficult to estimate the typical age of a He WD upon disruption by a MBH, as these objects are formed from a range of progenitor masses and undergo a binary interaction of uncertain timescale. We do know that nuclear star clusters exhibit a wide range of stellar ages. For example, observations of the nearby S0 galaxy NGC 404 show that half of the mass of the nuclear star cluster is from stars with ages of ≈ 1 Gyr, while the bulge is dominated by much older stars (Seth et al. 2010). In our own Galactic center, roughly 80% of the stars formed over 5 Gyr ago and the remaining 20% formed in the last 0.1 Gyr (Pfuhl et al. 2011). In addition, TDEs have so far been found preferentially in post-starburst galaxies, with significant 1 Gyr old or younger stellar populations (Arcavi et al. 2014b; French et al. 2016b). Another consideration is that in a study of a population of He WDs in the globular cluster NGC 6397, Hansen et al. (2003) found that the progenitor binaries of the He WDs very likely underwent an exchange interaction within the last Gyr. Finally, we note that the two-body relaxation

time is ≈ 0.1 Gyr for a 10^5 $M_\odot$ BH and ≈ 1.8 Gyr for a 10^6 $M_\odot$ BH. Motivated by the above considerations, in our disruption simulations we take the radius of the He WD at 1 Gyr after formation (i.e., since Roche-lobe detachment).

For the tidal disruption calculations in this work, we construct a 0.17 $M_\odot$ He WD consisting of a 0.16 $M_\odot$ degenerate helium core and a 0.01 $M_\odot$ hydrogen envelope using the MESA stellar evolution code (Paxton et al. 2011, 2013, 2015). This envelope mass is consistent with theoretical predictions of hydrogen retention (Althaus et al. 2001; Serenelli et al. 2001; Panei et al. 2007). The left panel in Figure 2.2 shows the relative abundance of helium and hydrogen as a function of radius for this object. The hydrogen envelope extends to roughly 10 times the radius of the core, and is supported by a thin hydrogen burning shell. This snapshot is at 1 Gyr after formation.

We also calculate the radius as a function of time since formation (through a binary interaction) for several He WDs in MESA. This is shown for our 0.17 $M_\odot$ object in the right panel of Figure 2.2. We show the radius of a core-only WD of the same mass for comparison in dashed blue (here we show a fixed radius that does not evolve with time). In a similar calculation for a 0.15 $M_\odot$ WD, we find that a very extended envelope persists for > 10 Gyr.

2.3.2 Disruption and Flaring Rates

The particular tidal disruption rates of different types of objects depend on the detailed dynamics and evolution of the dense stellar system surrounding the central BH. Given these uncertainties, here we make a simple estimate of the relative rate of He WD disruptions. We find that several factors could increase the rate from that suggested by

these objects' low population fraction. We can decompose the observed rate into (1) the fractional disruption rate and (2) the rate of luminous flares.

Disruption

First, the fractional disruption rate. This can be written as $f_{\rm disrupted} = f_{\rm pop} \times f_{\rm rel}$, where $f_{\rm pop}$ is the fraction of the stellar population that are He WDs, and $f_{\rm rel}$ is the specific likelihood of an He WD being disrupted. First we estimate $f_{\rm pop}$. Modeling the Galactic population of double WDs, Nelemans et al. (2001) found a Galactic birth rate of close double white dwarfs of 0.05 $\rm yr^{-1}$ and a formation rate of planetary nebulae of 1 $\rm yr^{-1}$. They found that 63% of the stars in these pairs are He WDs. This implies that the production rate of He WDs is approximately $0.05 \times 0.63 \approx 0.03$ times that of single stellar evolution WDs. Choosing an age of 10 Gyr for the Galactic disk gives a turnoff mass of approximately 1 $M_\odot$ for the stars in our Galaxy. We estimate the WD fraction by dividing the number of stars with masses of 1–8 $M_\odot$ (those that evolve to leave WD remnants) by the number with masses of 0.1–8 $M_\odot$ using a Kroupa (2001) IMF; this gives a WD fraction of approximately 0.16. The population fraction of He WDs is then $f_{\rm pop} \approx 0.16 \times 0.03 \approx 0.005$.

There is a concern that mass segregation might limit $f_{\rm pop}$ in central cluster regions. In clusters, low-mass stars are evaporated from the central regions as above-average mass objects settle deeper in a trend toward energy equipartition on the cluster relaxation time (e.g., Merritt 2013). However, binaries containing an He WD, even though the He WD mass is low, will not be evaporated from the central regions as their total mass is on average higher than the average mass of a typical stellar population.

Indeed, in a study of the central regions of globular cluster NGC 6397, Strickler et al. (2009) found a sample of He WDs with masses of 0.2–0.3 $M_\odot$. These objects show strong Hα absorption lines (indicating that they still retain their hydrogen envelopes), and are significantly more concentrated in the cluster center than either the CO WDs or the turnoff stars. We therefore expect that mass segregation either enhances $f_{\rm pop}$ or, at least, does not reduce it in nuclear star clusters.

This population fraction could also be larger due to the fact that in dense stellar systems, the rate of dynamically assembled compact binaries is observed to be enhanced by a factor of 10–100 when compared to the field (Pooley et al. 2003; Pooley & Hut 2006). We might expect similar enhancements in the dense and dynamical nuclear region surrounding an MBH. Note that the separation of He WDs from their companions is observed to be 10^{10} cm $< a < 3 \times 10^{11}$ cm in the ELM survey, making these binaries stable against ionization for typical nuclear cluster conditions.

For $f_{\rm rel}$, we follow MacLeod et al. (2012a) and scale the specific likelihood of disruption as $f_{\rm rel} \propto r_{\rm t}^{1/4}$. Relative to an MS star, this is $f_{\rm rel} = (R_{\rm He}/R_{\rm MS})^{1/4}(M_{\rm MS}/M_{\rm He})^{1/12}$, which is of order unity for our 0.17 $M_\odot$ He WD and a ~ 0.5 $M_\odot$ MS star. This gives us a conservative total fractional disruption rate of $f_{\rm disrupted} = f_{\rm pop} \times f_{\rm rel} \approx 0.005$. For a hydrogen-depleted He WD, $f_{\rm rel}$ is closer to 1/2. As a potential comparison, simulations of star clusters by Baumgardt et al. (2004) found that the relative fraction of WD disruptions is ≈ 0.15. Multiplying this by the relative production rate of He WDs (roughly 0.03 for every WD in our Galaxy following Nelemans et al. 2001) suggests a fractional disruption rate of $f_{\rm disrupted} \approx 0.005$, consistent with our above estimate.

However, as mentioned, mass segregation and dynamical assembly effects can enhance our above estimate. The estimate using star cluster simulations may also be low, as these simulations include very low-mass BHs and a population of single stars. These calculations therefore model the disruption of only single WDs, which also follow the substantially more compact typical WD mass radius relation. We lack a proper N-body simulation of the relative disruption rates for binary systems such as those that produce He WDs.

Flaring

Second, we consider the relative rate of luminous flares arising from the disruption of He WDs. One consideration is that He WD disruptions will produce a higher peak luminosity relative to MS stars, simply because they are more compact. For 0.5 $M_\odot$ WDs, MacLeod et al. (2014) showed that their disruption rate $\dot{N}$ is lower than that of MS stars, but that, when weighted by their luminosities, the total number of observed transients is higher for these WDs than MS stars for $M_{\rm bh} \lesssim 10^5\ M_\odot$, as the observing volume grows with luminosity. For He WDs, one can similarly expect their luminosity-weighted rates to be higher relative to MS stars than their pure fractional rates estimated above.

The fraction of prompt versus delayed flares is also important here. As suggested earlier, prompt flares occur when general relativistic effects are important. Guillochon & Ramirez-Ruiz (2015a) showed that MS stars are ineffectively circularized for lower BH masses, leading to viscously delayed luminosity evolution. For $10^5 < M_{\rm bh}/M_\odot < 10^6$, the fraction of prompt events from MS stars is $\approx 13\%$ (if we include

events that are viscously slowed only as they rise to peak, this fraction is $\approx 17\%$). Because He WDs are disrupted in the strongly relativistic regime, these objects should be rapidly circularized for these BH masses, as shown in Figure 2.1. As a result, He WD disruptions should make up a higher fraction of prompt flares than their population fraction suggests. This effect becomes especially important at lower BH masses, for which the occupation fraction remains unconstrained (e.g. Gair et al. 2010).

As we will see, even partial disruptions of He WDs with hydrogen envelopes can provide super-Eddington fallback onto the BH. These partial disruptions are also favorably prompt compared to MS disruptions, and could further enhance the relative rate of flares from He WD disruptions.

2.4 Numerical Setup

2.4.1 MESA Calculations

Using the MESA stellar evolution code, we construct a 0.17 $M_\odot$ white dwarf with a 0.16 $M_\odot$ degenerate helium core and a 0.01 $M_\odot$ hydrogen envelope. As noted in the previous section, there is a growing population of observed objects in this mass range. In these low-mass objects, the extended envelope lasts for a long time, as $\Delta t_{\rm proto} \propto M_{\rm WD}^{-7}$ (Equation 2.4). We might therefore be more likely to see flares from the stripped envelopes of objects close to this mass, as they exist in a bloated state for longer than their higher-mass cousins.

We approximate the core and envelope as nested polytropes (e.g., Rappaport et al. 1983; MacLeod et al. 2012a; Liu et al. 2013), using polytropic indices $n_{\rm core} = 1.5$

and $n_{\rm env} = 3.8$. Figure 2.3 shows the density versus radius profile of this object from MESA as well as from the nested polytrope that we matched. We use this nested polytrope as an input to our hydrodynamical simulations as it provides a reasonable description of the object's structure, and makes possible comparisons with non-hydrogen-envelope WD disruption calculations using polytropic equations of state (MacLeod et al. 2014).

A single polytrope is unstable to small variations in pressure p_0 and volume V_0 if $(\partial p/\partial V)_0$ is positive, and this occurs for polytropic indices of $n > 3$. However, it is difficult to derive simple stability criteria for our nested polytrope structure, as it is not differentiable across the core-envelope discontinuity. We instead ensure that two heuristic tests of stability are satisfied: (1) the entropy increases with radius, or $\partial S/\partial r > 0$, and (2) the star does not contract or relax significantly when placed on our hydrodynamical grid structure for 20 dynamical timescales of the full star. The dynamical timescale for the full star is $t_{\rm dyn}^{\rm full} \simeq \sqrt{R^3/GM} = 535$ s. In this work we will often refer to the dynamical timescale of the He core of this WD for comparison; this is $t_{\rm dyn}^{\rm core} = 22.5$ s.

2.4.2 Hydrodynamical Setup

Our simulations of tidal disruption are performed with the basic framework and code described in detail in Guillochon et al. (2009, 2011), MacLeod et al. (2012a), Liu et al. (2013), and Guillochon & Ramirez-Ruiz (2013a). We use FLASH (Fryxell et al. 2000), a 3D adaptive mesh grid-based hydrodynamics code including self-gravity. Hydrodynamics equations are solved using the using the piecewise parabolic method

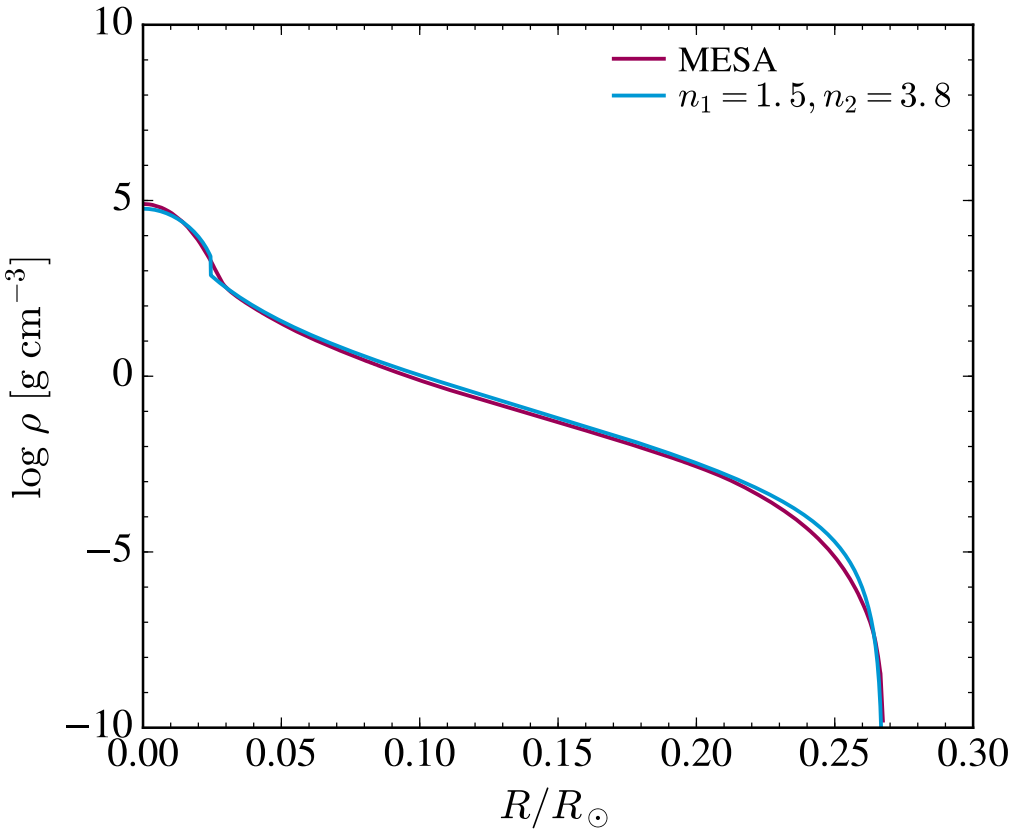

Figure 2.3: Our matching of a nested polytrope with $n_{\rm core} = 1.5$ and $n_{\rm env} = 3.8$ to the MESA density versus radius profile of a 0.17 $M_\odot$ WD with a 0.01 $M_\odot$ hydrogen envelope. We use this nested polytrope in our tidal disruption calculations as our initial condition.

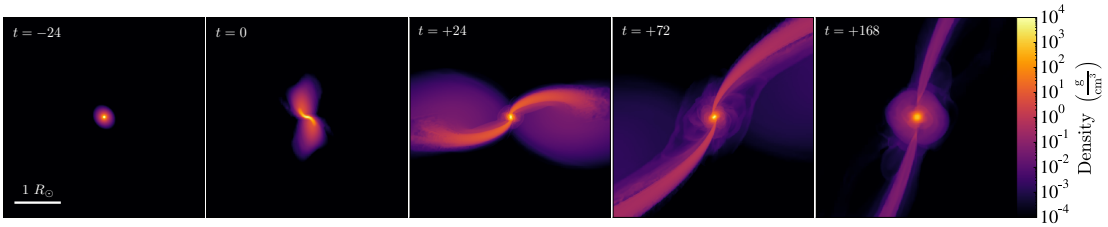

Figure 2.4: 2D slices in density through our 3D simulation box, zoomed in on the star, for a 0.17 $M_\odot$ He WD being disrupted by a 10^5 $M_\odot$ BH. Panels from left to right show the time evolution for a $\beta_{\rm core} = 0.7$ encounter in units of the dynamical time of the core (22.5 s), with $t = 0$ corresponding to pericenter.

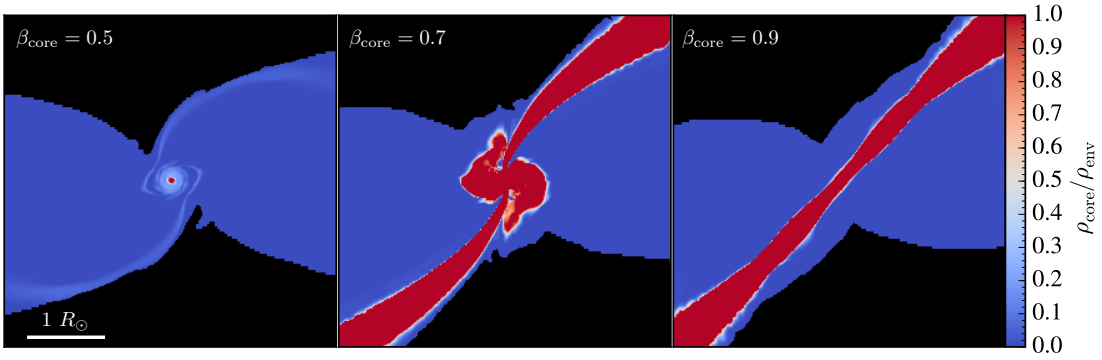

Figure 2.5: Panels from left to right show the mass fraction of core (red) versus envelope (blue) material for $\beta_{\rm core} = 0.5$, 0.7, and 0.9 encounters. These respectively correspond to a grazing encounter where just the envelope is stripped, an intermediate encounter, and full disruption. All slices are at $t = 96\ t_{\rm dyn}^{\rm core}$ after pericenter. Density below 10^{-4} g/cm^3 is shown in black.

(Colella & Woodward 1984). We refine the grid mesh on the value of the density, and derefine by one level every decade in density below $\rho = 10^{-4}$ g cm^{-3}. All of the simulations presented here are resolved by at least $R_\star/\Delta r_{\rm min} > 130$, where $\Delta r_{\rm min}$ is the size of the smallest cells. We note that adaptive mesh refinement is well suited for disruption calculations of an object with this core and envelope structure, as the envelope occupies a large volume yet has a very low mass fraction.

We perform our calculations in the rest-frame of the star to avoid introducing artificial diffusivity by moving the star rapidly across the grid structure. We solve the self-gravity of the star using a multipole expansion about the center of mass of the star with $l_{\rm max} = 10$. We then evolve the orbit based on the center of mass of the star and the position of a point-mass black hole (see the Appendix of Guillochon et al. 2011, for details). We use Newtonian gravity for the black hole, which is a reasonable approximation as our star's closest approach in any of our simulations is $> 10r_{\rm g}$, in the weak field regime. Cheng & Bogdanović (2014a) showed that general relativistic effects

in tidal disruption simulations should be small is this regime. Note that, because we use Newtonian gravity, by construction, the encounters we simulate are outside of our rapid circulation condition defined in Section 2.2. The effect of relativistic encounters is discussed in Section 2.7.2.

We run our simulations using the 0.17 $M_\odot$ He WD described above and a 10^5 $M_\odot$ BH. We input the MESA profile, matched as a nested polytrope (Figure 2.3), into FLASH. We use two different fluids in the simulation: one for the helium core and one for the hydrogen envelope. Both have the same equation of state, with a $\gamma_{\rm fluid} = 5/3$. This setup has an envelope composition of 100% hydrogen. More accurately, the envelope has a residual helium abundance that will migrate toward the core over time depending on the relative strength of mixing and gravitational settling. We relax the object onto the grid for 5 $t_{\rm dyn}$ before sending the BH toward it. We use an eccentricity $e \approx 1$, as most disrupted stars originate from orbits scattered from the sphere of influence (Magorrian & Tremaine 1999b; Wang & Merritt 2004b). As discussed in Guillochon & Ramirez-Ruiz (2013a), for a given stellar structure, we can understand the vast majority of disruptions by surveying in impact parameter $\beta = r_{\rm t}/r_{\rm p}$ as all other parameters obey simple scaling relations when relativistic effects are unimportant. Similar to the dynamical timescale, we can define β with respect to the tidal radius of the full star or the degenerate core. We survey in $\beta_{\rm full}$ from 1 to 10 in 12 runs. This corresponds to $\beta_{\rm core}$ of ≈ 0.1 to 1.2. We run our simulations for 21 $t_{\rm dyn}^{\rm full} = 500\ t_{\rm dyn}^{\rm core}$, well into the self-similar decay portion of the mass fallback rate.

2.5 Numerical Results

2.5.1 Phenomenology: Core versus envelope

Figure 2.4 shows the time evolution of the star for a $\beta_{\rm core} = 0.7$ encounter in 2D slices in density through the 3D simulation box, zoomed in on the star. Time is labeled in terms of the dynamical time of the core. In this moderately plunging encounter, the star is distorted through pericenter, evolving into a surviving remnant and two tidal tails—one bound and one unbound from the BH.

As we increase the impact parameter, the star is perturbed closer to its center. For mildly plunging encounters, only the hydrogen envelope is stripped, while the core survives intact. For more deeply plunging encounters, both the core and envelope are disrupted and fed to the BH. We can see this qualitatively in Figure 2.5, where we show slices through the simulation box zoomed in on the star for $\beta_{\rm core} = 0.5$, 0.7, and 0.9 encounters. We plot the ratio of the core material to envelope material density. The different spatial distributions of core and envelope material will result in different fall-back times to the BH, which will result in observed light curves dominated by material of different compositions at different times. Because of their different structures—the envelope has a steeper density gradient than the core—these two fluids react to losing mass in characteristically different ways, as we will see below.

2.5.2 Mass lost

Figure 2.6 shows the mass lost from the star as a function of impact parameter, calculated at the last timestep of our simulations. We run our simulations long enough

so that the mass lost calculated from this final timestep is asymptotically close to the final mass lost. Note that half of the lost mass will return to the black hole and half is ejected as an unbound debris stream. The object is smoothly disrupted with the impact parameter, albeit with two components from the envelope and the core. This is different from giant star disruptions (MacLeod et al. 2012a), where the core is never disturbed, and likely arises because the density contrast between the core and envelope is in general larger for giants than it is for He WDs.

A fitting formula from Guillochon & Ramirez-Ruiz (2013a, 2015c) for a $\Gamma = 5/3$ polytrope fits the mass lost from the core well. This is expected, as once the core has been penetrated, the envelope has negligible dynamical effect, and the disruption will proceed as if for a typical WD. Full disruption occurs at $\beta_{\rm core} \approx 0.9$.

This $n = 1.5$ polytrope has a lower critical β (for full disruption) compared to higher index polytropes, as the mass is distributed more evenly. In addition to this, a $n = 1.5$ polytrope has an inverse mass-radius relation, and so expands when mass is removed, making the object more vulnerable to disruption. We model the envelope, on the other hand, as an $n = 3.8$ polytrope, which reacts to mass removal by contracting—"protecting" itself. Because the envelope has a steeper density gradient, its critical β is higher than for a $\Gamma = 5/3$ polytrope. We can see this in the shallower slope of $\Delta M/M$ versus β for envelope material relative to core material.

2.5.3 Spread in binding energy and mass fallback rate

We calculate the spread in binding energy of the star's material to the BH, dM/dE versus E, over time. We compute the specific binding energy of the material in

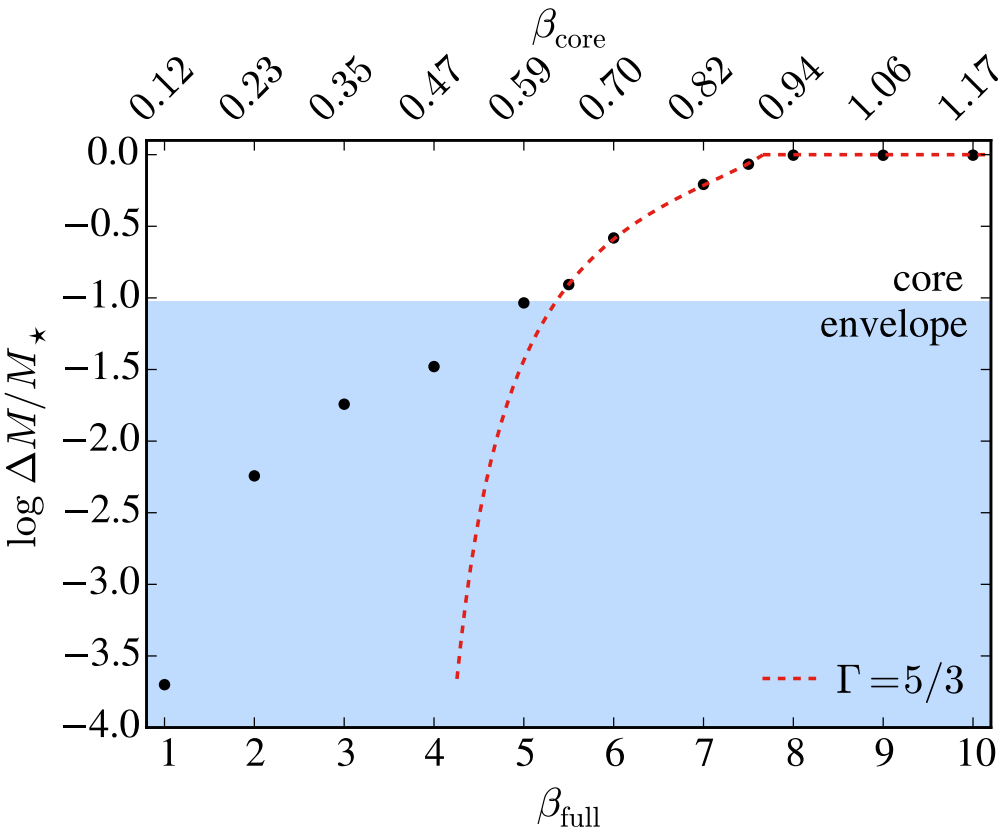

Figure 2.6: Mass lost versus impact parameter for the disruption of a 0.17 $M_\odot$ He WD with a 10^5 $M_\odot$ BH is shown in solid circles. The total mass of the envelope is shaded in blue. A fitting formula from Guillochon & Ramirez-Ruiz (2013a) for a $\Gamma = 5/3$ polytrope is shown in dashed red. Once the core begins to be disrupted as well, the single 5/3 polytrope yields the same amount of mass loss as the nested polytrope. The bottom x-axis shows the β of the full star (i.e., including the envelope), and the top x-axis shows the equivalent β of only the core.

each cell of the simulation, which depends on its distance and velocity relative to the center of mass of the star and to the black hole. Details of the calculation are presented in Guillochon & Ramirez-Ruiz (2013a). Only material that is bound to the BH and not bound to the star will contribute to the mass fallback onto the BH. We compute the specific binding energy of the material in each cell of the simulation, which depends on its distance and velocity relative to the center of mass of the star and to the black hole.

Figure 2.7 shows the spread in dM/dE over time for $\beta_{\rm core} = 0.5$, 0.7, and 0.9 encounters, with the contribution from material unbound to the star in solid black and contributions from the core and envelope of the remnant in red and blue. We see that impact parameter drastically changes the spread in binding energy through and following disruption, both for the bound and unbound material. Grazing encounters leave the core relatively unperturbed and are able to retain more envelope material, while deeper encounters leave a compact remnant that has been all but stripped of its envelope.

Given dM/dE and a pericenter distance, we can calculate the mass fallback rate onto the BH by Kepler's third law,

$$\frac{dM}{dt} = \frac{dM}{dE}\frac{dE}{dt} = \left(\frac{dM}{dE}\right)\frac{1}{3}\left(2\pi G M_{\rm bh}\right)^{2/3} t^{-5/3}. \tag{2.5}$$

The left panel of Figure 2.8 shows the spread in specific binding energy dM/dE versus E at the last timesteps of our simulations for all impact parameters. We verify that the binding energy has effectively "frozen in," or converged to its final distribution, by this timestep. The right panel shows dM/dE mapped onto dM/dt across time for

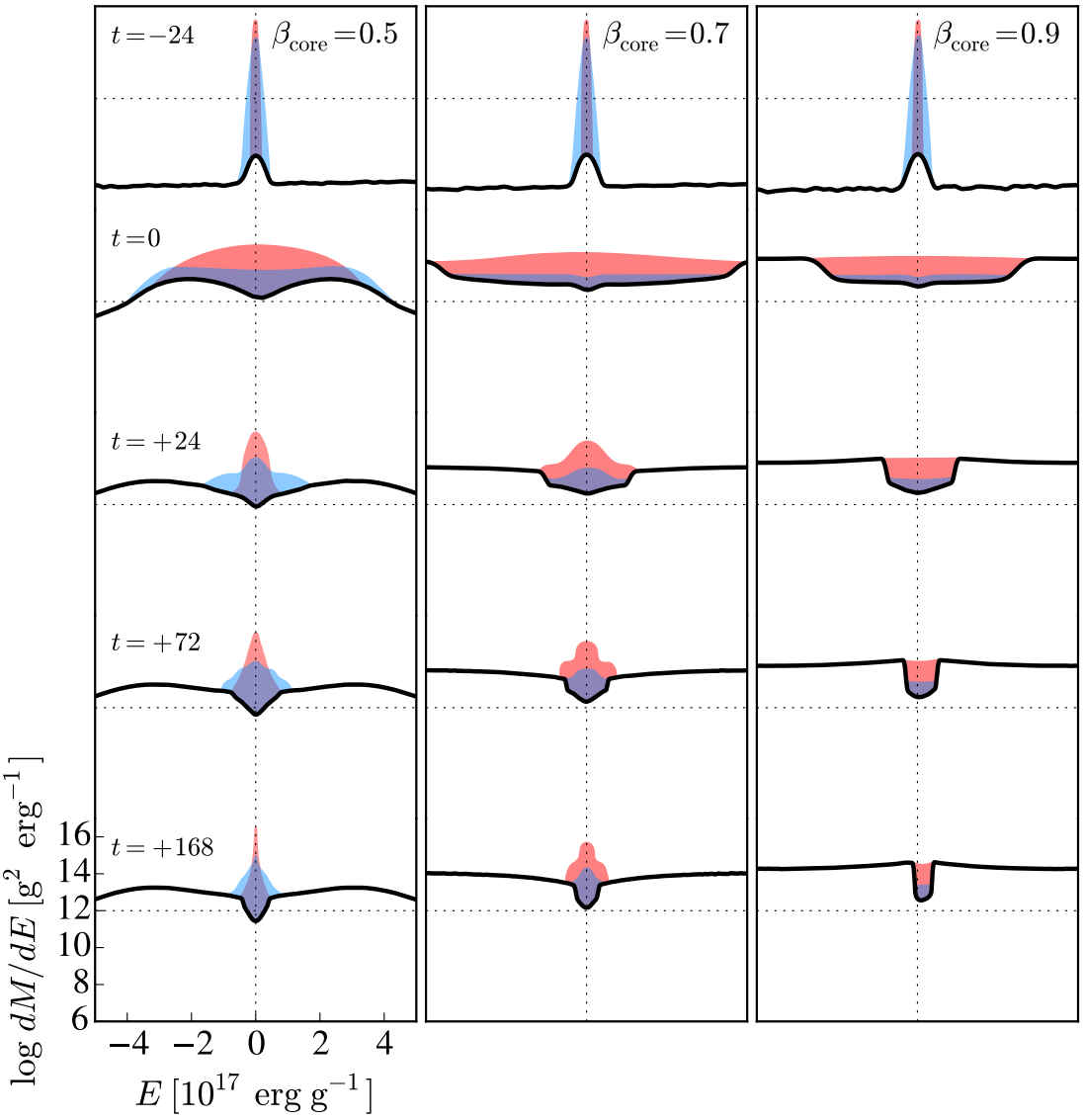

Figure 2.7: Panels from left to right show the spread in specific binding energy for $\beta_{\rm core} = 0.5$, 0.7, and 0.9 encounters (the same as shown in Figure 2.5). Time increases from top to bottom for each impact parameter and is labeled in terms of $t_{\rm dyn}^{\rm core}$. Material bound to the star (the remnant) is shown in red and blue, corresponding to core and envelope material, respectively. Material unbound to the star (the tidal tails) is shown by the black solid line. A vertical dashed line is shown for reference at $E = 0$, where material is moving with the center of mass of the star. A horizontal dashed line is shown for reference at $dM/dE = 10^{12}$ g^2 erg^{-1}. The binding energy of material both bound and unbound to the star varies widely with β. Material spreads out in binding energy through disruption, and higher impact parameters spread out the binding energy more effectively. Higher impact parameters also leave a more compact remnant. A grazing encounter retains some of the envelope, while a deeply plunging encounter loses nearly all of it.

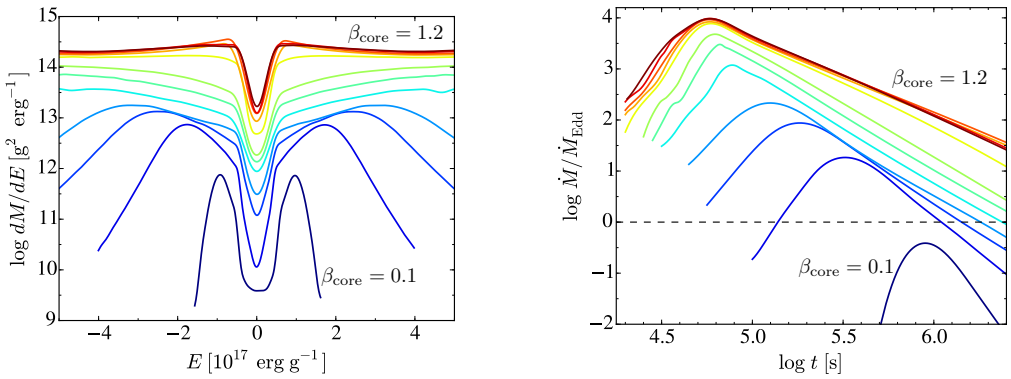

Figure 2.8: Left panel: spread in specific binding energy as a function of β for a 0.17 $M_\odot$ He WD disrupted by a 10^5 $M_\odot$ BH. Right panel: mass fallback rate $\dot{M}$ onto the BH versus time for the same impact parameters, with the Eddington limit for this BH shown in dashed black. Impact parameters range from $\beta_{\rm core} = 0.1$ to 1.2 in increments of roughly 0.1. See Figure 2.6 for the corresponding mass lost for each β.

the same impact parameters, with the Eddington limit for this BH shown in dashed black. We take $\dot{M}_{\rm Edd} = 0.02\ (\eta/0.1)\ (M_{\rm bh}/10^6\ M_\odot)\ {\rm M}_\odot/{\rm yr}$ with $\eta = 0.1$. Feeding rates peak at $t_{\rm peak} \sim 5 \times 10^4$ to 10^6 s ≈ 0.6 to 11 d depending on β. Weakly plunging encounters peak later, while deeply plunging encounter peak earlier. Note that $t_{\rm peak}$ evolves strongly with β (it spans more than an order of magnitude), in contrast to single polytrope solutions where the evolution in $t_{\rm peak}$ is much more gradual (e.g., Guillochon & Ramirez-Ruiz 2013a). This means that the He WD disruptions—and disruptions of other objects with this core and extended envelope structure—probe a much wider range of potential transient characteristics for a given BH mass. We see that even for very weakly plunging encounters, for which only a fraction of the envelope is stripped (see mass lost in Figure 2.6), the mass fallback rate is super-Eddington. Encounters only stripping the envelope appear to have a shallower slope in early-time mass fallback and smoother evolution near peak than encounters penetrating the core. This is due to

their different polytropic structures.

Guillochon & Ramirez-Ruiz (2013a) presented a fitting formula for the peak fallback rate of material onto the BH, where $\dot{M}_{\rm peak} = f(M_{\rm bh}, \beta, \gamma)$. Figure 2.9 shows $\dot{M}_{\rm peak}$ values from our simulations of the disruption of an 0.17 $M_\odot$ He WD compared with those from this fitting formula for a $\Gamma = 5/3$ non-hydrogen-envelope WD with a mass of 0.155 $M_\odot$, the mass of the core of the He WD. We expect this functional form to match for disruptions that penetrate the core. In low β encounters, the hydrogen envelope provides mass return rates that are unavailable to WDs without envelopes.

2.5.4 Composition of debris

We track the core and envelope material separately in our simulations, which allows us to track the composition of the debris falling onto the BH. In Figure 2.10 we show $\dot{M}$ as a function of time for $\beta_{\rm core} = 0.5$, 0.6, and 0.8, with absolute and fractional contributions from the helium core in red and the hydrogen envelope in blue. The mass fallback rate from weakly plunging encounters can be super-Eddington and hydrogen-dominated. In more deeply plunging encounters, the early rise of the mass fallback rate is fed almost entirely by the hydrogen envelope, while the peak and late time evolution are fed by the helium core; the nature of this transition depends on β. Note that the disruption turns the star inside out: the material that is removed first accretes first, and is then buried underneath the material that is removed last and accretes last. The diffuse envelope material feeds a qualitatively slower rise in the mass fallback curve compared to the core material.

The first evidence that a range of stellar or spectral properties might be rep-

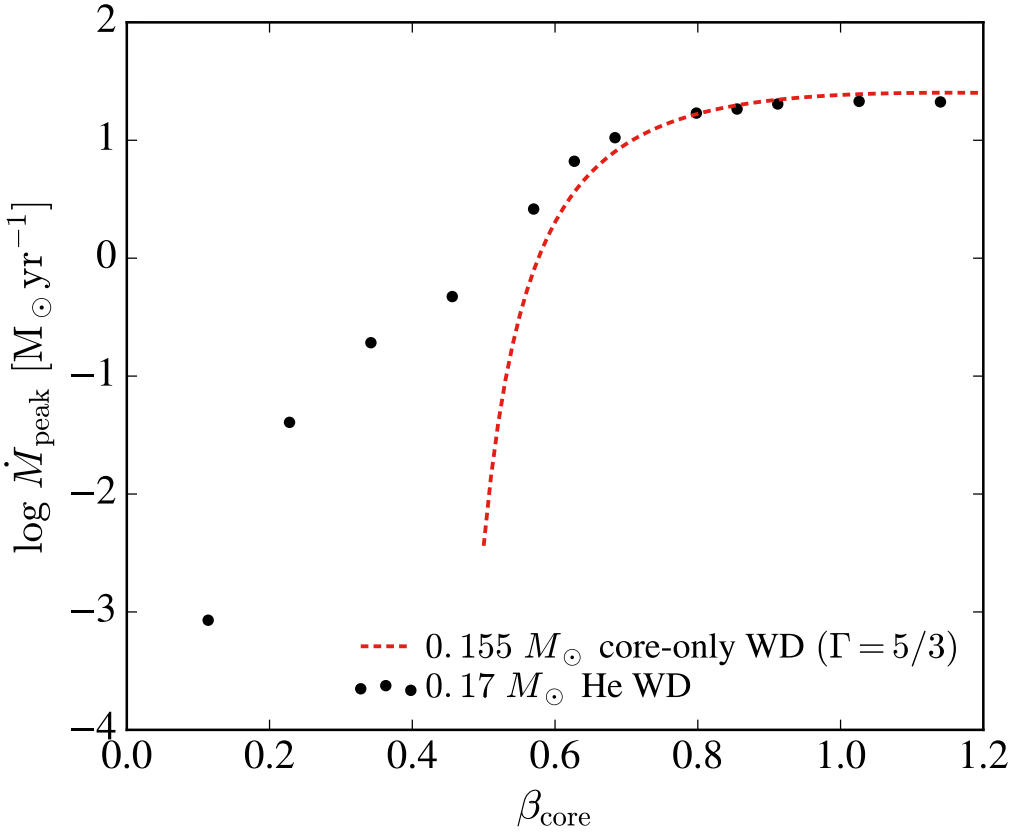

Figure 2.9: Black filled circles show the peak mass fallback rate, $\dot{M}_{\rm peak}$, versus β for the encounters shown in Figure 2.8. The $\dot{M}_{\rm peak}$ fitting formula from Guillochon & Ramirez-Ruiz (2013a) for a $\Gamma = 5/3$ polytrope with the mass of the core of this object, 0.155 $M_\odot$, is shown in dashed red. $\dot{M}_{\rm peak}$ values for encounters that penetrate the core are close to those of a non-hydrogen-envelope WD, while low β encounters provide fallback rates unavailable to WDs without envelopes.

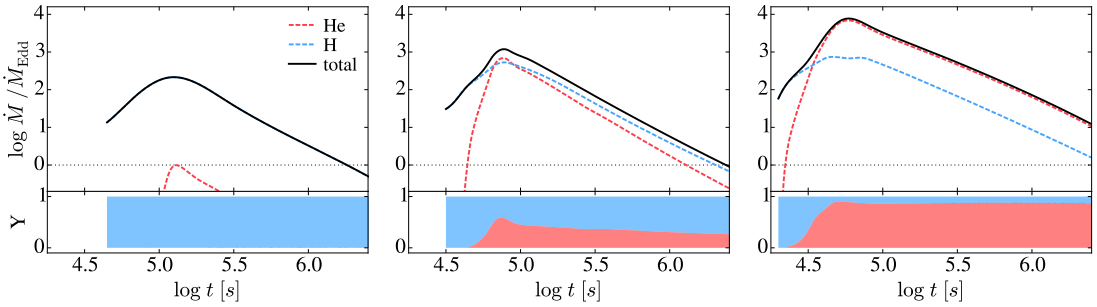

Figure 2.10: The tops of the panels from left to right show the mass fallback rate as a function of time for $\beta_{\rm core} = 0.5$, 0.6, and 0.8 encounters, respectively. The total $\dot{M}$ is shown in solid black, and the Eddington limit for this BH in dotted black. Contributions from the helium core and hydrogen envelope are shown in dashed red and blue, respectively. The bottoms of the panels show the mass fraction of $\dot{M}$ over time from helium and hydrogen. The mass fallback rate from weakly plunging encounters can be super-Eddington and hydrogen-dominated. In more deeply plunging encounters, there is a transition between envelope-fed fallback and core-fed fallback that depends on β.

resented in TDEs was the discovery of a helium-rich TDE, PS1-10jh (Gezari et al. 2012a). Gezari et al. explained its hydrogen-free spectrum as the result of the tidal disruption of the helium-rich core of a star, similar in structure to an He WD progenitor. Arcavi et al. (2014b) noted that TDEs observed thus far show a continuum of helium-rich to hydrogen-rich spectral features; there is an ongoing debate over the origin of the strong helium emission. Kochanek (2016a) found that stellar evolution can play a role in producing this spectral diversity. Roth et al. (2016) modeled the emission from TDEs through an extended, optically thick envelope formed from stellar debris. They find that due to optical depth effects, hydrogen Balmer line emission is often strongly suppressed relative to helium line emission. For MS stars, for example, it is possible for the hydrogen emission lines to be absent. Having said this, the specific composition of the material is expected to have consequences on the detailed line

ratios. Line diagnostics from disruptions of He WDs could transition from hydrogen to helium smoothly with β. An encounter stripping only the envelope could provide a rare, (nearly) pure hydrogen-powered mass fallback. If an optically thick reprocessing envelope exists, however, observational evidence of this type of encounter could be variable.

2.6 TDE Demographics

Here we explore the tidal disruption menu of BHs and disrupted objects in terms of the peak fallback rate and its associated peak timescale, and place our He WDs in context. Through Kepler's third law, we can write scalings of the peak mass fallback rate and its associated time of peak,

$$\dot{M}_{\rm peak} \propto M_{\rm bh}^{-1/2}\ M_\star^2\ R_\star^{-3/2} \tag{2.6}$$

$$t_{\rm peak} \propto M_{\rm bh}^{1/2}\ M_\star^{-1}\ R_\star^{3/2}, \tag{2.7}$$

where the $\dot{M}_{\rm peak} \propto M_\star^2$ scaling results when we assume that a constant fraction of the star's mass is lost in the disruption. Guillochon & Ramirez-Ruiz (2013a, 2015c) found fitting parameters for these scaling relations that depend on the polytropic Γ and impact parameter β. We use these below.

In Figure 2.11, we show $\dot{M}_{\rm peak}$ versus $t_{\rm peak}$ values for the He WD disruptions presented in this work, as well as for several representative disruptions of other objects: a 0.6 $M_\odot$ non-He WD, a 0.6 $M_\odot$ MS star, a 50 $M_{\rm Jup}$ brown dwarf (BD), a 1 $M_{\rm Jup}$

planet, and a 1.4 $M_\odot$, 10 $R_\odot$ red giant (RG). We use fitting parameters from Equations A1 and A2 of Guillochon & Ramirez-Ruiz (2013a) to calculate $\dot{M}_{\rm peak}$ and $t_{\rm peak}$ for the other objects, and to scale with BH mass. We use a polytropic Γ of 5/3 for the WD, MS star, BD, and planet (the values are similar if we use 4/3 for the MS star), and 4/3 for the RG. We show impact parameters that remove from $\Delta M/M_\star = 0.01$ to 1 from each object.

As in the tidal disruption menu shown in Figure 2.1, we only show encounters with BHs obeying our prompt circularization condition, $4GM_{\rm bh}/c^2 < r_{\rm t} < 10GM_{\rm bh}/c^2$. Here, flares resulting from the fallback of material onto the BH are both visible (disruption occurs outside the innermost bound circular orbit) and predominantly prompt (circularization of the debris is efficient). We color the encounters by BH mass.

There is a huge variety in the timescales and fallback rates with which stars feed MBHs following TDEs. Prompt flares separate into different timescale classes based on the stellar type and BH mass combination. Prompt flares also show relatively unique timescale/BH mass combinations—i.e., a timescale and a prompt flare can imply not only a stellar type but also a BH mass. The clean separations blur slightly if we allow for (1) the full distribution of masses and radii available for different classes of objects, which is especially important for He WDs, and (2) the effects of viscous delay, which smear the effective timescales and mass fallback rates.

In Figure 2.12 we show a fallback rate curve for each of the objects in Figure 2.11, scaled to disruptions with a 10^6 $M_\odot$ BH for comparison. Note that the 0.6 $M_\odot$ WD disruption would occur inside the event horizon for this BH mass. We show fallback

from a 1.4 $M_\odot$ RG at two different points along the giant branch: ascending the RG branch (RG1; $R \approx 10\ R_\odot$) and the tip of RG branch (RG2; $R \approx 100\ R_\odot$), from MacLeod et al. (2012a). We show a $\beta = 0.9$ encounter (full disruption) for the non-He WD, the MS star, and the planet, and a $\beta = 1.5$ encounter for the giant stars. We show two $\dot{M}$ curves for the He WD: one for a full disruption ($\beta_{\rm core} = 0.9$) and one for an envelope-stripping encounter ($\beta_{\rm core} = 0.5$). For a given BH mass, these objects offer distinct fallback rates and characteristic timescales.

Converting these fallback rates into luminosities is not straightforward. In this paper we have focused on rapidly circularized TDEs, where the accretion rate (and so the luminosity) is expected to closely follow the fallback rate. This is predicted to be true for emission both from the disk (Guillochon et al. 2014a) and from stream collisions (Dai et al. 2015), and is observed to be the case in the best-sampled, non-beamed UV/optical events (e.g., Gezari et al. 2012a; Guillochon et al. 2014a). However, it is not evident that the luminosity will always follow the fallback rate, in particular when circularization is inefficient or for BHs accreting at highly super-Eddington rates (Shiokawa et al. 2015; Piran et al. 2015b). For example, the event Sw J1644+57 (Bloom et al. 2011a) did not appear to follow a $t^{-5/3}$ luminosity evolution during its prompt decline phase. In addition, jetted emission may not be Eddington limited; its strength depends on the radiative efficiency of the (relativistic) flow. Even in the absence of a jet, McKinney et al. (2015) show that the radiative efficiency of super-Eddington accretion flows can be high under certain circumstances.

While most full disruptions are expected to provide super-Eddington accretion

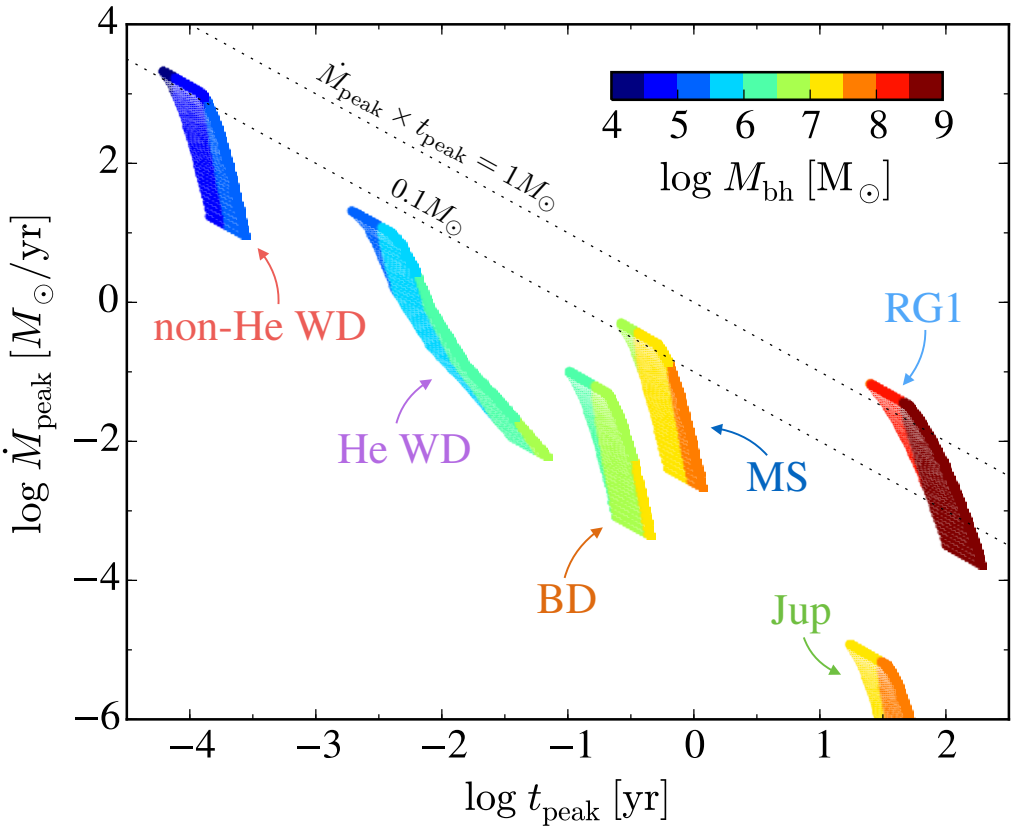

Figure 2.11: Peak mass fallback rate versus time of peak for a 0.6 $M_\odot$ non-He WD, a 0.17 $M_\odot$ He WD, a 0.6 $M_\odot$ MS star, a 50 $M_{\rm Jup}$ brown dwarf, a 1 $M_{\rm Jup}$ planet, and a 1.4 $M_\odot$ red giant at RG1 ($\approx 10\ R_\odot$). Encounters are colored by BH mass. Dotted lines show where $\dot{M}_{\rm peak} \times t_{\rm peak} = 0.1\ M_\odot$ and $1\ M_\odot$. We show only encounters obeying our circularization requirement, $4GM_{\rm bh}/c^2 < r_{\rm t} < 10GM_{\rm bh}/c^2$, favoring prompt flares. We show impact parameters that remove from $\Delta M/M_\star = 0.01$ to 1 from each object.

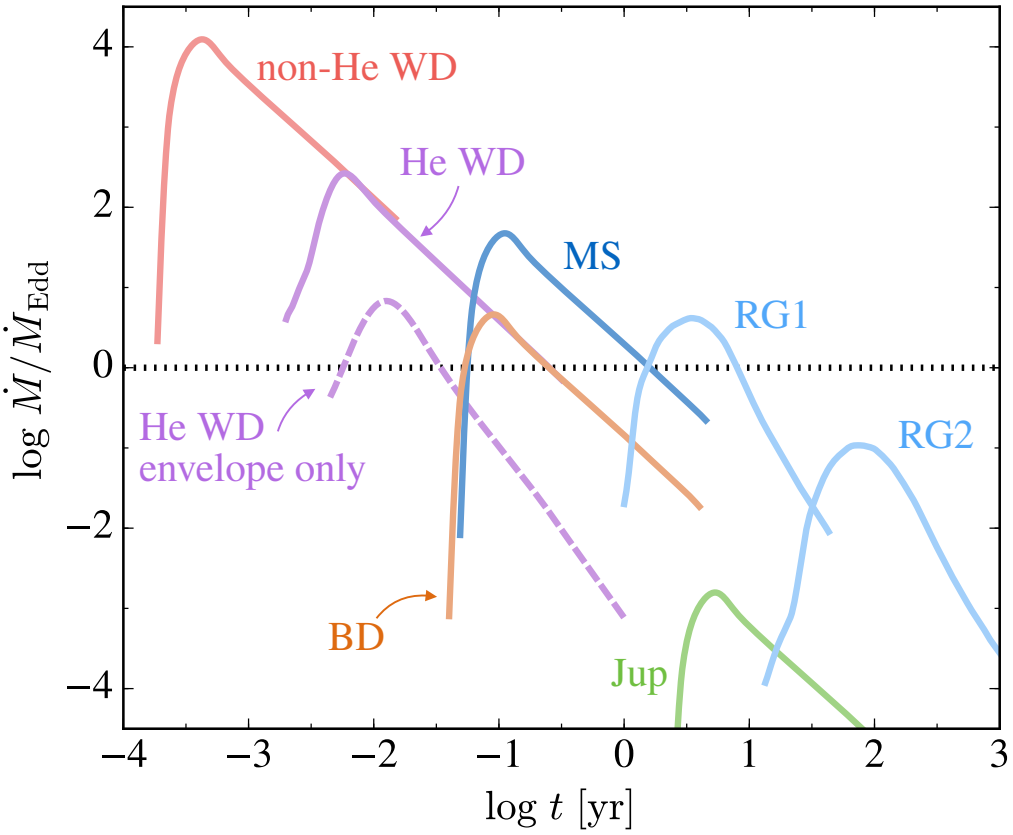

Figure 2.12: Mass fallback rate curves for the representative objects shown in Figure 2.11 scaled to a single BH mass (10^6 $M_\odot$) for comparison. Colors are the same as in Figure 2.1 menu. We show a 0.6 $M_\odot$ non-He WD in red, a 0.17 $M_\odot$ He WD in purple, a 0.6 $M_\odot$ MS star in blue, a 50 $M_{\rm Jup}$ brown dwarf in brown, a 1 $M_{\rm Jup}$ planet in green, and a 1.4 $M_\odot$ red giant at RG1 (≈ 10 $R_\odot$) and at RG2 (≈ 100 $R_\odot$) in light blue. We show a $\beta = 0.9$ encounter (full disruption) for the non-He WD, MS star, BD, and planet, and a $\beta = 1.5$ encounter for the giant stars. For the He WD, we show two $\dot{M}$ curves for comparison: the solid line shows a full disruption ($\beta_{\rm core} = 0.9$) and the dashed line shows an envelope-stripping encounter ($\beta_{\rm core} = 0.5$).

rates (Figure 2.12), the observed peak luminosities of UV/optical TDEs appear to be Eddington limited, or sub-Eddington (Hung et al. 2017a). Two possible solutions to this are (1) that the most commonly observed events are partial disruptions, where the fallback rate can be significantly lower (e.g., Guillochon & Ramirez-Ruiz 2013a) or (2) that the radiative efficiency is low (e.g., Piran et al. 2015a).

Constructing this menu—which spans many orders of magnitude in BH mass, fallback timescale, and fallback rate—is nonetheless a key step toward making meaningful comparisons with observations. We have only shown a few representative objects; the full phase space of luminosities and timescales, the effects of viscous delay, and a comparison to observations will be explored in future work.

2.7 Discussion

2.7.1 Possible Candidates for He WD Disruption

Here we compare $t_{\rm peak}$ values from simulations to those of two particularly rapidly rising TDE candidates, Dougie (Vinkó et al. 2015) and PTF10iya (Cenko et al. 2012a), accounting for luminosity and BH mass constraints. Vinkó et al. (2015) estimate Dougie's peak bolometric luminosity as $L_{\rm peak} \approx 5(\pm 1) \times 10^{44}$ erg s^{-1} and its rise time as $t_{\rm rise} \sim 10$ d. They estimate a central BH mass of a few 10^6 to 10^7 $M_\odot$ for Dougie's host galaxy. Cenko et al. (2012a) estimated 10iya's peak bolometric luminosity as $L_{\rm peak} \approx (1-5) \times 10^{44}$ erg s^{-1} and place a limit on its rise time of $t_{\rm rise} < 5$ d. They constrain the central BH mass via the observed bulge luminosity versus BH mass relation as $\log M_{\rm BH}/M_\odot \lesssim 7.5$.

In order to constrain the kinds of disruptions that can produce such rapid flares, we construct a histogram of $t_{\rm peak}$ for the 0.17 $M_\odot$ He WD disruptions presented in this work as well as for regular WDs, MS stars, BDs, and planets. We model regular WDs, MS stars, BDs, and planets with $M < 0.3\ M_\odot$ as $\Gamma = 5/3$ polytropes. We model MS stars with $M > 0.3\ M_\odot$ as $\Gamma = 4/3$ polytropes. The mass at which we transition from 5/3 to 4/3 does not affect our conclusions significantly, as their $t_{\rm peak}$ values overlap. Giant star disruptions have longer timescales than we are interested in here.

We draw from flat distributions in $M_{\rm obj}$, with white dwarf masses of $0.2\ M_\odot < M_{\rm WD} < 1\ M_\odot$, MS star masses of $0.085\ M_\odot < M_{\rm MS} < 3\ M_\odot$, BD masses of $13\ M_{\rm Jup} < M_{\rm BD} < 0.085\ M_\odot$, and planet masses of $1\ M_{\rm Jup} < M_{\rm pl} < 13\ M_{\rm Jup}$. We use only the one 0.17 $M_\odot$ He WD mass. We draw from a flat distribution in BH mass with $10^6 < M_{\rm bh}/M_\odot < 10^7$, roughly the BH mass constraints for Dougie and 10iya. We draw from a flat distribution in β, discarding encounters where $r_{\rm p} < r_{\rm ibco}$. We estimate the peak luminosity from each encounter as $L_{\rm peak} = \min\left(0.1\dot{M}_{\rm peak}c^2,\ L_{\rm Edd}\right)$ for the given BH, as these events were observed in the optical/UV and we expect accretion luminosity to be Eddington limited. We discard encounters with $L_{\rm peak} < 3 \times 10^{44}$ erg s^{-1}, which is comfortably below the errors in Dougie's peak luminosity.

In Figure 2.13, we show the outcome of the above exercise. We find that the only objects that satisfy the luminosity requirement are MS stars, BDs, and our prototypical He WD. MS stars and BDs, however, cannot reproduce the rapid timescales of Dougie and 10iya from $\dot{M}$ alone. Thermal TDEs such as PS1-10jh show a good correspondence between the observed luminosity and the fallback rate (Guillochon et al.

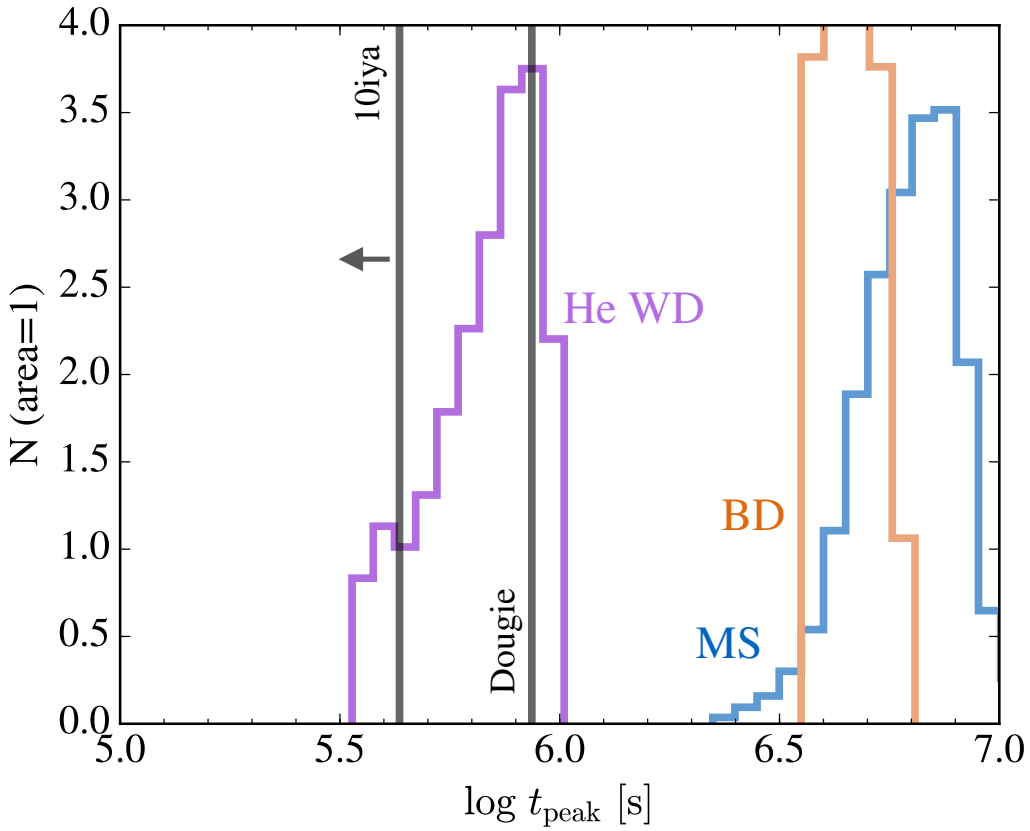

Figure 2.13: Histograms of peak timescales from the disruption of different types of objects, normalized to area=1, as compared to the peak timescales of two rapidly rising TDE candidates, Dougie and PTF10iya. We include non-He WDs, MS stars (in blue), brown dwarfs (in brown), planets, and the 0.17 $M_\odot$ He WD (in purple). We draw from flat distributions in object mass, BH mass, and β, as described in the text. Peak luminosities are Eddington limited, and we require $L_{\rm peak} > 3 \times 10^{44}$ erg s^{-1} in order to reproduce Dougie's peak luminosity.

2014a). This simplicity makes the disruption of He WDs an appealing explanation for rapidly rising nuclear transients.

In order to explain Dougie as a MS star disruption, models require a strong wind component with a functional form that may not directly reflect $\dot{M}$ (Vinkó et al. 2015). A wind that carries a significant amount of kinetic and thermal energy may be produced if the accretion rate onto the BH exceeds its Eddington limit (Strubbe & Quataert 2009a; Lodato & Rossi 2011; Metzger & Stone 2016; Jiang et al. 2016). While this scenario could explain Dougie and other rapidly rising TDEs such as PTF10iya, their timescales can be naturally explained by the $\dot{M}$ from He WD disruptions.

We note that Vinkó et al. (2015) found that Dougie appears offset ≈ 3.9 kpc from the photometric center of its host galaxy. This initially seems to disfavor a TDE interpretation. However, the photometric center of a galaxy is not necessarily its dynamical center. Vinkó et al. also noted that lower-mass off-center BHs are rare yet not unprecedented (e.g., Barth et al. 2008; Reines & Deller 2012), making the TDE hypothesis tenable.

2.7.2 Caveats

Our study focuses on a single example of the disruption of a prototypical 0.17 $M_{\odot}$ He WD. However, as we saw in Section 2.3.1, these objects can have a wide range of masses and radii, and the radius evolution even for a single mass is appreciable (see Figure 2.2). The inclusion of hydrogen-bearing He WDs with a larger range of core masses and envelope masses could potentially explain events with shorter or longer timescales than the prototypical encounters presented here.

In this work, we model the interaction between only a single He WD and a BH. We expect, however, that many He WDs will be in binary systems as they approach the BH, composed of either two He WDs or one He WD and one CO/ONe WD. This suggests that some disruptions of He WDs involve two stars instead of one (Antonini et al. 2011). The interaction of the binary with the BH can shift the distribution in binding energy of the debris, and cause the time of peak accretion to occur either earlier or later depending on the sign of the energy shift (a similar effect is seen in disruptions of stars on elliptical orbits; Hayasaki et al. 2012; Dai et al. 2013a). In extreme cases, this interaction can bind all of the material to the BH (as opposed to just half), allowing the BH to accrete the whole star; alternatively, all of the material can become unbound, preventing any accretion onto the BH. If the binary separation is of order the tidal radius, double tidal disruptions are possible (Mandel & Levin 2015). However, our single-star calculations are still applicable for double disruptions, as the hydrodynamics of the disruption are independent for each of the components of the binary. In cases where the outgoing debris streams from the two disrupted stars do not interact with one another, the fallback resulting from a binary disruption can be mimicked by applying simple shifts to the binding energy distribution of the debris of the single-star case.

We do not consider general relativistic effects in our disruption calculations—the gravitational potential of our point mass is purely Newtonian. Cheng & Bogdanović (2014a) investigated relativistic effects on the fallback rate of debris. For highly relativistic encounters, they found a more gradual rise and delayed peak of the fallback compared to the Newtonian result. For a 1 $M_\odot$, 1 $R_\odot$ MS star encounter with a 10^7 $M_\odot$

BH, where $r_{\rm p}/r_{\rm g} \approx 10$, they found a difference in $\dot{M}_{\rm peak}$ of $\approx 18\%$ and a difference in $t_{\rm peak}$ of $\approx 10\%$ between Newtonian and relativistic simulations. For a 0.6 $M_\odot$ WD encounter with a 10^5 $M_\odot$ BH, where $r_{\rm p}/r_{\rm g} \approx 4.6$, the difference in $\dot{M}_{\rm peak}$ is $\approx 69\%$ and the difference in $t_{\rm peak}$ is $\approx 49\%$.

For the He WD encounters presented in this work, the critical β of full disruption has $r_{\rm p}/r_{\rm g} \approx 12$, and the transition between an envelope-stripping encounter and one penetrating the core occurs at $r_{\rm p}/r_{\rm g} \approx 19$. Thus, relativistic corrections to our results should be small. In scaling to higher BH masses, however, our errors will increase. However, this will not weaken (and will in fact strengthen) our conclusions regarding the ability of He WDs to achieve the peak timescales of rapidly rising TDE candidates such as Dougie and PTF10iya though $\dot{M}$ alone, as the relativistic effect is to lengthen the peak fallback timescale.

We use a nested polytrope matched to a MESA profile of the He WD as the initial condition in our disruption calculations. We also track only two fluids—one for the core and one for the envelope—in the simulation, and make the simple choice to model the core as fully helium and the envelope as fully hydrogen. A more realistic treatment might use the MESA profile directly in the disruption calculations, and track the composition of the object more fully. For the particular object used in the simulations in this work, however, the gains in accuracy (aside from composition information) in using the MESA profile directly may be minimal, as the nested polytrope profile is very close to the true profile.

2.7.3 Conclusions

We have modeled the tidal disruption of a new class of object: the low-mass He WD with an extended hydrogen envelope. These objects are a missing link both hydrodynamically and in terms of BH masses probed through prompt tidal disruption flares. In summary, we find that:

1. Because of their lower density cores and extended envelopes, these objects extend the potential BH masses probed by single-star evolution WDs. In general, their peak fallback timescales will be longer that those of typical WDs and shorter than those of MS stars.

2. Grazing encounters that strip only the envelope will be hydrogen dominated, and—for a very small amount of mass removed—can provide high and often super-Eddington fallback.

3. Encounters penetrating the core generally have a fallback rate that is hydrogen-dominated in its rise and helium-dominated in its peak and decline, with relative composition versus time a function of impact parameter.

4. The typical peak accretion rate of He WD disruptions is a few times larger than that of a typical MS disruption. This likely makes these disruptions observable to larger distances, which would make them a larger fraction of the observed total than suggested by their relative population.

These objects are perhaps the last missing piece of a theoretical tidal disruption menu that includes WDs, MS stars, planets, and evolved stars. Constructing this menu is key

to better understanding tidal disruptions. The reader is referred to Figures 2.1, 2.11, and 2.12 for a summary of the phase space of the menu.

This work may have particular bearing on two puzzling observational aspects of TDEs that have emerged in the past few years. The first is their rates. There is a great deal of uncertainty in the properties of the nuclear star clusters from which stars are fed into disruptive orbits. Most calculations make standard assumptions of a spherical single-mass nuclear star cluster that feeds stars to the BH by a two-body relaxation-driven random walk in angular momentum space. These calculations predict disruption rates of $\gtrsim 10^{-4}$ yr^{-1} per galaxy (Magorrian & Tremaine 1999b; Wang & Merritt 2004b; Stone & Metzger 2016a), and are in general in tension with the lower observationally derived rates of roughly 10^{-5} yr^{-1} (e.g., van Velzen & Farrar 2014). However, there can be several complicating effects—such as secular relaxation, or the presence of a triaxial potential, rings or disks of stars, and/or a second massive body—and there is a lack of understanding of their relative importance in local galaxies. In addition, we need to better understand the mass spectrum of disrupted stars, in particular given mass segregation (e.g., MacLeod et al. 2016c).

The second puzzling observation is that a significant fraction of tidal disruptions may arise from unique stellar populations. We are learning that tidal disruption flares may occur preferentially in post-starburst galaxies (Arcavi et al. 2014b; French et al. 2016b), and that these types of galaxies are overrepresented as TDE hosts. This remains a mystery. Post-starburst galaxies are elliptical-type galaxies that have experienced a star formation burst that has stopped within the past ~ 1 Gyr, leaving these

galaxies with both old and very young stars.

If only certain types of stars (which are a small fraction of the population) produce prompt flares for BH masses of $\sim 10^6\ M_\odot$ due to circularization effects, this could alleviate some of the tension in the observed flaring versus disruption rate. As we have argued in Section 2.3.2, the rate of luminous flare production can be distinct from the disruption rate itself. We have shown in Section 2.2 and Section 2.6 that different stellar types probe distinct islands of BH mass when we consider prompt flares. This is strong evidence for a connection between stellar population details and the disruption flare rates. The post-starburst galaxy preference may be due to the production of particular stellar species in the nuclei of these galaxies, rather than in the dynamics of their nuclei. We caution, however, that the stellar population of a galaxy as a whole does not necessarily reflect its nuclear population.

In this work, we have argued that to effectively use TDEs to constrain the mass function of BHs, we need to acknowledge that not all disruptions produce luminous flares. Moving forward likely involves understanding the intersection of nuclear region stellar dynamics, stellar populations, and stellar evolution, along with the hydrodynamics of the disruptions themselves. Targeting the observational characteristics of certain TDEs might offer a way to identify BHs at the low end of the supermassive BH mass range.

Chapter 3

Tidal Disruption Event Host Galaxies in the Context of the Local Galaxy Population

Abstract

We study the properties of tidal disruption event (TDE) host galaxies in the context of a catalog of ∼500,000 galaxies from the Sloan Digital Sky Survey. We explore whether selection effects can account for the overrepresentation of TDEs in E+A/post-starburst galaxies by creating matched galaxy samples. Accounting for possible selection effects due to black hole (BH) mass, redshift completeness, strong AGN presence, bulge colors, and surface brightness can reduce the apparent overrepresentation of TDEs in E+A host galaxies by a factor of ∼4 (from ∼×100-190 to ∼×25-48), but cannot fully

explain the preference. We find that TDE host galaxies have atypical photometric properties compared to similar, "typical" galaxies. In particular, TDE host galaxies tend to live in or near the "green valley" between star-forming and passive galaxies, and have bluer bulge colors ($\Delta(g-r) \approx 0.3$ mag), lower half-light surface brightnesses (by $\sim$1 mag/arcsec^2), higher Sérsic indices ($\Delta n_{\rm g} \approx 3$), and higher bulge-to-total-light ratios ($\Delta B/T \approx 0.5$) than galaxies with matched BH masses. We find that TDE host galaxies appear more centrally concentrated and that all have high galaxy Sérsic indices and B/T fractions—on average in the top 10% of galaxies of the same BH mass—suggesting a higher nuclear stellar density. We identify a region in Sérsic index and BH mass parameter space that contains $\sim$2% of our reference catalog galaxies but $\geq 60\%$ of TDE host galaxies. The unique photometric properties of TDE host galaxies may be useful for selecting candidate TDEs for spectroscopic follow-up observations in large transient surveys.

3.1 Introduction

The cores of many galaxies undergo intense nuclear activity during their lifetimes. This activity inevitably leads to the growth of the central supermassive black hole (SMBH) but is short lived compared to galactic ages and was more prevalent when the universe was only $\sim$20% of its current age (Soltan 1982; Ho 2009). Quiescent SMBHs starved of fuel are common in the local universe (Greene & Ho 2007b) and are being discovered in nearby galaxies.

The presence of quiescent SMBHs in the nuclei of galaxies has been directly

inferred from the dynamics of the stars and/or gas near their centers (e.g., Kormendy & Ho 2013; McConnell & Ma 2013). For galaxies too distant to accurately resolve the nuclear stellar or gas kinematics, it is possible to probe the presence of an SMBH with the fate of the central, closely-packed stars. Each star within the nuclear star cluster traces out an intricate orbit under the combined influence of the SMBH and other stars. The orbits are gradually altered owing to the cumulative effect of encounters. As a result, stars that are scattered into orbits that pass too close to the central SMBH can be ripped apart by the black hole's tidal field in what is known as a tidal disruption event (TDE; Hills 1975b; Frank & Rees 1976a; Rees 1988b). After the star is disrupted, up to half of the stellar debris falls back and accretes onto the SMBH (Carter & Luminet 1982b; Evans & Kochanek 1989b; Lodato et al. 2009b; Guillochon & Ramirez-Ruiz 2013b). The accretion powers a flare that is a definitive sign of the presence of an otherwise quiescent SMBH.

TDEs are identified by a combination of a rapid increase in flux, proximity to a host galaxy's nucleus, and a decay in luminosity that loosely follows the canonical $t^{-5/3}$ law, though the most compelling events are those in which the rise, peak, and decay of the transient are observed with a frequent cadence (e.g., Komossa et al. 2004; Gezari et al. 2009, 2012b; Chornock et al. 2014a; Arcavi et al. 2014a; Holoien et al. 2014a; Miller et al. 2015). The (well-sampled) light curves of TDEs contain vital information about the disruption and can be used to constrain the properties of the SMBH and the stellar object that was disrupted (e.g., Guillochon et al. 2014b; Law-Smith et al. 2017b). A few dozen candidate TDEs have been observed in the optical, UV, and X-ray (for a

summary, see Komossa 2015b; Auchettl et al. 2017b). Future surveys such as the Large Synoptic Survey Telescope (LSST) will likely find hundreds to thousands more events (van Velzen et al. 2011).

The observed rates of TDEs and, in particular, the relative rates of flares in different galaxy hosts, hold important discriminatory power over both the dynamical mechanisms operating in galactic nuclei and the nature of their underlying stellar populations. However, the dynamical mechanisms that feed stars into disruptive orbits within nuclear star clusters remain highly uncertain. Stellar tidal disruption rates have typically been studied under the assumption of a spherical nuclear star cluster that feeds stars to the black hole (BH) through a two-body relaxation-driven random walk in angular momentum space (Magorrian & Tremaine 1999a; Wang & Merritt 2004a; Stone & Metzger 2016b). However, disks of stars and gas, if present, could feed stars to the BH at an enhanced rate through collisionless processes or secular instabilities (Lightman & Shapiro 1977; Rauch & Ingalls 1998; Magorrian & Tremaine 1999a; Madigan et al. 2009, 2011; Merritt & Vasiliev 2011; Vasiliev & Merritt 2013; Antonini & Merritt 2013). A second massive body, such as an inspiraling moderately massive BH, could also induce large-angle scatterings of stars (Ivanov et al. 2005; Chen et al. 2009). These processes and others could result in favorable conditions for TDEs and might manifest as enhanced rates within particular galaxy hosts (for a review, see Alexander 2017).

Understanding the host galaxies of TDEs is thus important; however, this understanding is in its infancy. Many uncertainties in the conditions necessary for tidal disruption will only be resolved through an understanding of the connection between

TDEs and their host galaxies. This connection will hopefully become clearer with a larger sample of TDE host galaxies, but the current sample already shows hints of being highly unusual.

TDEs appear to be observed preferentially in rare quiescent Balmer-strong galaxies (also known as post-starburst or K+A galaxies, or more restrictively as E+A galaxies; Arcavi et al. 2014a; French et al. 2016a). In a sample selected from the Sloan Digital Sky Survey (SDSS), French et al. (2016a) found that a particular selection of E+A galaxies contained only 0.2% of the sample but more than one-third of observed TDE host galaxies, implying a drastic rate enhancement. However, it is important to make a clear distinction between galaxies in which TDEs can occur and galaxies in which TDEs might be observable. We need to discern among (1) the intrinsic TDE rate based on stellar dynamics, (2) the rate of TDEs that produce luminous flares, and (3) the potential selection effects against detecting a TDE. In this paper, we seek to disentangle some of these issues.

We study the properties of TDE host galaxies in the context of a catalog of ∼500,000 galaxies from the SDSS. We consider first-order physical constraints and observational selection effects, and test whether they can account for the large preference for E+A/post-starburst galaxy hosts. To do this, we compare a sample of TDE host galaxies to matched control samples of galaxies in the local universe. We also find a new (photometric) observable that may be more broadly predictive of an enhanced TDE rate than E+A classification: the central light concentration, which is apparent in both galaxy Sérsic index and bulge-to-total-light ratio (B/T).

We take our sample of TDEs from the catalog presented in Auchettl et al. (2017b) and compile galaxy properties from the SDSS galaxy catalogs of Brinchmann et al. (2004), Simard et al. (2011), and Mendel et al. (2014). We explore several key properties of TDE host galaxies, including stellar mass, BH mass, redshift, star formation rate (SFR), bulge colors, surface brightness, Sérsic index, bulge-to-total-light ratio, and galaxy asymmetry. We also compare TDE host galaxies to active galactic nuclei (AGNs) and star-forming (SF) galaxies across these observables.

This paper is organized as follows. We describe our data in Section 3.2. We present the uniqueness of TDE host galaxies in Section 3.3. We explore selection effects in Section 3.4. We present a possible physical explanation for the overabundance of TDEs in E+A/post-starburst galaxies, as well as a new unique feature of all TDE host galaxies, in Section 3.5. We discuss and interpret our findings in Section 3.6. We study a few other properties of TDE host galaxies in Appendix 3.7 and show correlations between properties in Appendix 3.8.

3.2 Data

In this section, we describe our data sources as well as some conventions and definitions we use throughout the paper.

3.2.1 Reference Catalog

Our reference catalog is contained in the SDSS (York et al. 2000; Gunn et al. 1998, 2006) DR7 (Abazajian et al. 2009) and is based on the main galaxy sample (Strauss

et al. 2002). We make use of the MPA-JHU catalogs[2] (Brinchmann et al. 2004) of ∼700,000 galaxies, the Simard et al. (2011) catalog of bulge+disk decompositions and photometry for 1.12 million galaxies, and the Mendel et al. (2014) catalog of bulge, disk, and total stellar mass estimates for ∼660,000 galaxies.

We obtain redshift, bulge $g-r$, bulge and galaxy magnitude, galaxy half-light radius, galaxy Sérsic index (see Equation 3.4), bulge fraction (B/T), galaxy asymmetry indicator, and inclination measurements from the Simard et al. (2011) catalog. We obtain velocity dispersion, Hα equivalent width (EW), Lick Hδ_A, D$_n$(4000), and star formation rate (SFR) measurements from the MPA-JHU catalog. Here, we define Hα EW as `H_ALPHA_FLUX`/`H_ALPHA_CONT`. We obtain total and bulge stellar masses from the Mendel et al. (2014) catalog. We collate these measurements into a catalog of ∼610,000 galaxies.

We then apply the following quality control requirements. Following Scudder et al. (2012), we remove all galaxies with negative flux or continuum measurements as these are found to be unreliable. For consistency with the samples defined in French et al. (2016a), we require $z > 0.01$ (to prevent severe aperture bias), reliable Hα EWs (`H_ALPHA_EQW_ERR` > -1 in the MPA-JHU catalog), and median signal-to-noise ratio (S/N) per pixel of the integrated spectrum of greater than 10. Applying these selection criteria leaves us with a final catalog of ∼500,000 galaxies—we refer to this as our "reference catalog" throughout the paper. Unless otherwise specified, our quoted errors are those provided with the measurements from their respective catalogs.

We plan to compare our sample of TDE host galaxies to AGN and SF galaxies

[2] http://wwwmpa.mpa-garching.mpg.de/SDSS/DR7

within our reference catalog. The standard way of distinguishing AGN from SF galaxies is through the so-called BPT diagram of emission-line ratios of Baldwin et al. (1981); we use the empirical diagnostic of Kauffmann et al. (2003c) that is based on this approach. We classify AGN and SF galaxies as those with a minimum S/N of the four spectral lines used in the BPT classification—OIII (5007Å), Hβ, NII (6584Å), and Hα—of greater than 3. We classify low-S/N AGN and low-S/N SF galaxies as those with a minimum S/N of less than 3.

We use the $M_{\rm bh}$-σ_e scaling from Kormendy & Ho (2013) to estimate galaxy BH masses:

$$\frac{M_{\rm bh}}{10^9 M_\odot} = \left(0.309^{+0.037}_{-0.033}\right) \left(\frac{\sigma_e}{200 {\rm kms}^{-1}}\right)^{4.38\pm0.29}. \tag{3.1}$$

Equation 3.1 yields $M_{\rm bh}$ values with an intrinsic scatter of 0.29 dex. We use velocity dispersion measurements from the MPA-JHU catalog and perform an aperture correction to obtain the bulge/spheroidal velocity dispersion σ_e, using Equation (3) in Jorgensen et al. (1995):

$$\log \frac{\sigma_{\rm ap}}{\sigma_e} = -0.065 \log\left(\frac{R_{\rm ap}}{R_e}\right) - 0.013 \left[\log\left(\frac{R_{\rm ap}}{R_e}\right)\right]^2 \tag{3.2}$$

where R_e is the effective radius of the bulge or spheroid from the Simard et al. (2011) catalog, $R_{\rm ap}$ is the aperture radius (1.5″), and $\sigma_{\rm ap}$ is the velocity dispersion measured within the aperture. Our errors on BH mass include the error on velocity dispersion and the intrinsic scatter in the $M_{\rm bh}$-σ_e scaling, and are ∼0.4 dex. Our uncertainties on BH mass are relatively large, particularly for galaxies with low velocity dispersions (a few of our TDE host galaxies have velocity dispersions near or slightly below the

70 km s^{-1} SDSS instrumental resolution).[3] However, our analysis in this work is primarily concerned with differences between properties of TDE host galaxies and our reference catalog and so does not rely on accurate determinations of BH masses—only that they are determined homogeneously in the various samples we consider. Indeed, we often control for BH mass. We also performed our analysis using $M_{\star,\mathrm{bulge}}$ to determine BH masses using the scaling from Kormendy & Ho (2013),

$$\frac{M_{\mathrm{bh}}}{10^9 M_\odot} = \left(0.49^{+0.06}_{-0.05}\right)\left(\frac{M_{\mathrm{bulge}}}{10^{11} M_\odot}\right)^{1.16\pm0.08}, \tag{3.3}$$

and $M_{\star,\mathrm{bulge}}$ estimates from the Mendel et al. (2014) catalog, as well as using different scalings for M_{bh}-σ, and our conclusions are insensitive to these choices. In fact, if we replace BH mass with $M_{\star,\mathrm{total}}$ throughout our analysis, our conclusions remain the same.

When we study bulge quantities, such as the bulge color, bulge fraction (B/T), and bulge magnitude, obtained from the Simard et al. (2011) catalog of bulge+disk decompositions, we will show measurements from all galaxies in our reference catalog. Note that this will include galaxies where a second component is not statistically justified in the fit. We can isolate a relatively "pure" sample of bulges by including only galaxies for which the data support a bulge+disk decomposition compared to a single Sérsic fit (for example, by requiring $P_{pS} < 0.32$; see Simard et al. 2011). The size of this "pure" bulge sample depends mostly on the data quality and so it can be highly incomplete.

[3] We note that Wevers et al. (2017a) recently published the first homogeneously measured BH masses for a complete sample of 12 optical-/UV-selected TDE host galaxies. We use the SDSS velocity dispersions, even though they are less accurate, as our goal is to use consistent metrics in comparing between TDE hosts and our reference catalog. That being said, the TDE host galaxy BH masses we match on in this work are broadly consistent with the range found by Wevers et al. (2017a).

This sample includes roughly one-third of our reference catalog and only three of our TDE host galaxies (numbers 5, 7, and 8 in Table 3.1). Although the data quality cannot always statistically justify the bulge+disk decomposition, bulge measurements can be applied in a consistent way to our entire sample, and we find intriguing differences between the TDE host galaxies and our reference catalog (see Section 3.3).

The SDSS is biased in a few ways, and this leads to some sample limitations. Most importantly, the SDSS is inherently flux limited. This limits our sample to TDEs that are fairly low z, but since most observed TDEs are fairly low z, this is not a major problem. Our approach in this paper—of not just using the entire SDSS for our comparison, but selecting matched control samples on several parameters, forcing the parameter space to be the same—should mitigate most inherent biases in our sample.

Table 3.1: TDE Host Galaxies Used in This Work

#	Event Name	TDE Category[a]	Host Name	Host R.A.	Host Decl.	Redshift	Reference
1	ASASSN-14ae	Veiled	SDSS J110840.11+340552.2	11:08:40.116	34:05:52.23	0.0436	Holoien et al. (2014a)
2	ASASSN-14li	X-ray	SDSS J124815.23+174626.4	12:48:15.230	17:46:26.45	0.0206	Holoien et al. (2016b)
3	PTF-09ge	Veiled	SDSS J145703.17+493640.9	14:57:03.18	49:36:40.97	0.064	Arcavi et al. (2014a)
4	RBS 1032	Possible X-ray	SDSS J114726.69+494257.8	11:47:26.80	49:42:59.00	0.026	Maksym et al. (2014)
5	SDSS J1323	Likely X-ray	SDSS J132341.97+482701.3	13:23:41.973	48:27:01.26	0.08754	Esquej et al. (2007, 2008)
6	SDSS J0748	Veiled	SDSS J074820.67+471214.3	07:48:20.667	47:12:14.23	0.0615	Wang et al. (2012)
7	SDSS J1342	Veiled	SDSS J134244.41+053056.1	13:42:44.416	05:30:56.14	0.0366	Wang et al. (2012)
8	SDSS J1350	Veiled	SDSS J135001.49+291609.7	13:50:01.507	29:16:09.71	0.0777	Wang et al. (2012)
9	SDSS J0952	Veiled	SDSS J095209.56+214313.3	09:52:09.555	21:43:13.24	0.0789	Komossa et al. (2008)
10	SDSS J1201	Likely X-ray	SDSS J120136.02+300305.5	12:01:36.028	30:03:05.52	0.146	Saxton et al. (2012a)
a	PTF-09axc	Veiled	SDSS J145313.07+221432.2	14:53:13.08	22:14:32.27	0.1146	Arcavi et al. (2014a)
b	PTF-09djl	Veiled	SDSS J163355.97+301416.6	16:33:55.97	30:14:16.65	0.184	Arcavi et al. (2014a)
c	PS1-10jh	Veiled	SDSS J160928.27+534023.9	16:09:28.28	53:40:23.99	0.1696	Gezari et al. (2012b)
d	Swift J1644	X-ray	Swift J164449.3+573451	16:44:49.30	57:34:51.00	0.3543	Bloom et al. (2011b)
e	PTF-15af[b]	NA	SDSS J084828.13+220333.4	08:48:28.13	22:03:33.4	0.0790	French et al. (2016a)

[a]From Auchettl et al. (2017b).

[b]The discovery article for PTF-15af has not yet been published in the literature, but we include it here as it is included in the French et al. (2016a) sample and defines the boundary of their wF16 selection (see Figure 3.1).

Note. — TDE host galaxies 1-10 are in our reference catalog, and we use hosts 1-5 in our matching analysis (see text). Host galaxies a-e are not used in our analysis, but have published Hα EW and Lick Hδ_A measurements and are shown in Figure 3.1.

3.2.2 TDE Host Galaxies

We use the Auchettl et al. (2017b) catalog of 71 candidate TDEs as a parent sample of TDE host galaxies. We remove candidates with only one observation and those in the *Not a TDE* and *Unknown* categories, leaving us with 42 candidate TDEs. We use the R.A., decl., and z of these host galaxies to find matches in our reference catalog described above. Of the 42 candidate TDE host galaxies, 10 are in our reference catalog; the relatively low number of matches is mainly due to the redshift and magnitude limits of the various catalogs we draw from, as well as the fact that most galaxies require an SDSS spectrum for inclusion in these catalogs. These matches and their numbering (1-10) used throughout the paper are listed in Table 3.1, along with the relevant primary references.

We will use TDE host galaxies numbered 1-5 in our matching analysis of the extent of selection effects on the overrepresentation of TDEs in quiescent Balmer-strong galaxies (Section 3.4). TDE candidates 6-9 were not identified photometrically (i.e., by their light curves) but were instead proposed as TDE candidates due to their unique spectra: they are "extreme coronal line emitters," and are difficult to explain as standard AGNs. Numbers 9 and 10 are not in the MPA-JHU catalog, and so do not have velocity dispersion, Hα EW, Lick Hδ_A, or SFR measurements from this catalog. Additionally, No. 8 does not have a reliable velocity dispersion measurement from the MPA-JHU catalog (it is flagged with a negative error). We use the $M_{\rm bh}$-$M_{\star,\rm bulge}$ relation from Kormendy & Ho (2013), using $M_{\star,\rm bulge}$ measurements from the Mendel et al. (2014) catalog, to estimate BH masses for Nos. 8, 9, and 10—these BH masses do not enter

into the analysis and are only used to place these TDE host galaxies on our 2D plots versus BH mass. TDE hosts 1-5 are shown with red points and histograms throughout the paper, and TDE hosts 6-10 are shown with orange points. In our 1D stacked distributions, we will show the histograms for all TDE candidate with matches in our reference catalog (1-10) with dotted black lines. Finally, we will show Hα EW and Lick Hδ_A measurements for five TDE host galaxies (labeled a-e, see Table 3.1) not in our reference catalog in Figure 3.1. These last five are not used in our analysis, yet they provide additional evidence of an overrepresentation of TDEs in E+A/post-starburst galaxies. Although the small number of TDE host galaxies precludes performing detailed statistics, we are nonetheless able to draw compelling conclusions about the uniqueness of these galaxies.

The robustness of our conclusions may suffer from small numbers. Additionally, it is possible that the 10 TDE host galaxies (and ultimately the five used in our main analysis) are a special subset of TDE host galaxies and are not representative of the parent sample of 42 host galaxies. The 10 TDE host galaxies in our reference catalog are relatively low z and are not particularly faint, so that they are included in SDSS, and are therefore the most well-characterized in terms of their host properties. This is a potential source of bias in the TDE host sample.

Auchettl et al. (2017b) divide their candidate events into the categories *X-ray TDE*, *Likely X-ray TDE*, *Possible X-ray TDE*, and *Veiled TDE*. We provide this classification in Table 3.1, but the number of matches in each category is too small to make robust conclusions about differences in TDE host galaxies between categories.

The categorization is explained in detail in Auchettl et al. (2017b) but we summarize it here. Events in the *X-ray TDE* category have a well-defined and trustworthy X-ray light curve. Events in the *Likely X-ray TDE* category have very similar properties, yet with more limited data coverage. Events in the *Possible X-ray TDE* category have even more limited X-ray observations. Events in the *Veiled TDE* category have a well-defined optical/UV light curve but no X-ray emission near the peak.

3.3 Uniqueness of TDE Hosts

Following French et al. (2016a), we define the following selections in order to isolate quiescent Balmer-strong galaxies. We define the strong F16 (sF16) selection as $\mathrm{H}\delta_A - \sigma(\mathrm{H}\delta_A) > 4.0$ and $\mathrm{H}\alpha$ EW < 3.0. Here, $\sigma(\mathrm{H}\delta_A)$ is the error in the Lick $\mathrm{H}\delta_A$ index. $\mathrm{H}\alpha$ EW emission is an indicator of current star formation, and so this selects for galaxies with little ongoing star formation (i.e., with specific SF rates well below the main sequence of star-forming galaxies). $\mathrm{H}\delta_A$ absorption, from A stars, indicates star formation within the past $\sim$ Gyr. So, sF16 galaxies have had a strong starburst in the last $\sim$ Gyr. We define the weak F16 (wF16) selection as $\mathrm{H}\delta_A > 1.31$ and $\mathrm{H}\alpha$ EW $<$ 3.0. The looser cut on $\mathrm{H}\delta_A$ means that wF16 galaxies could have several possible star formation histories. Not accounting for selection effects, 0.2% of our reference catalog falls in the sF16 selection and 2.3% falls in the wF16 selection. Throughout this paper, we will define galaxies in the sF16 selection as "E+A" galaxies—we note that it is also common to define E+A galaxies with a stricter cut on $\mathrm{H}\delta_A$ (Goto 2007)—and galaxies in either the wF16 or sF16 selections more generally as "quiescent Balmer-strong" galaxies.

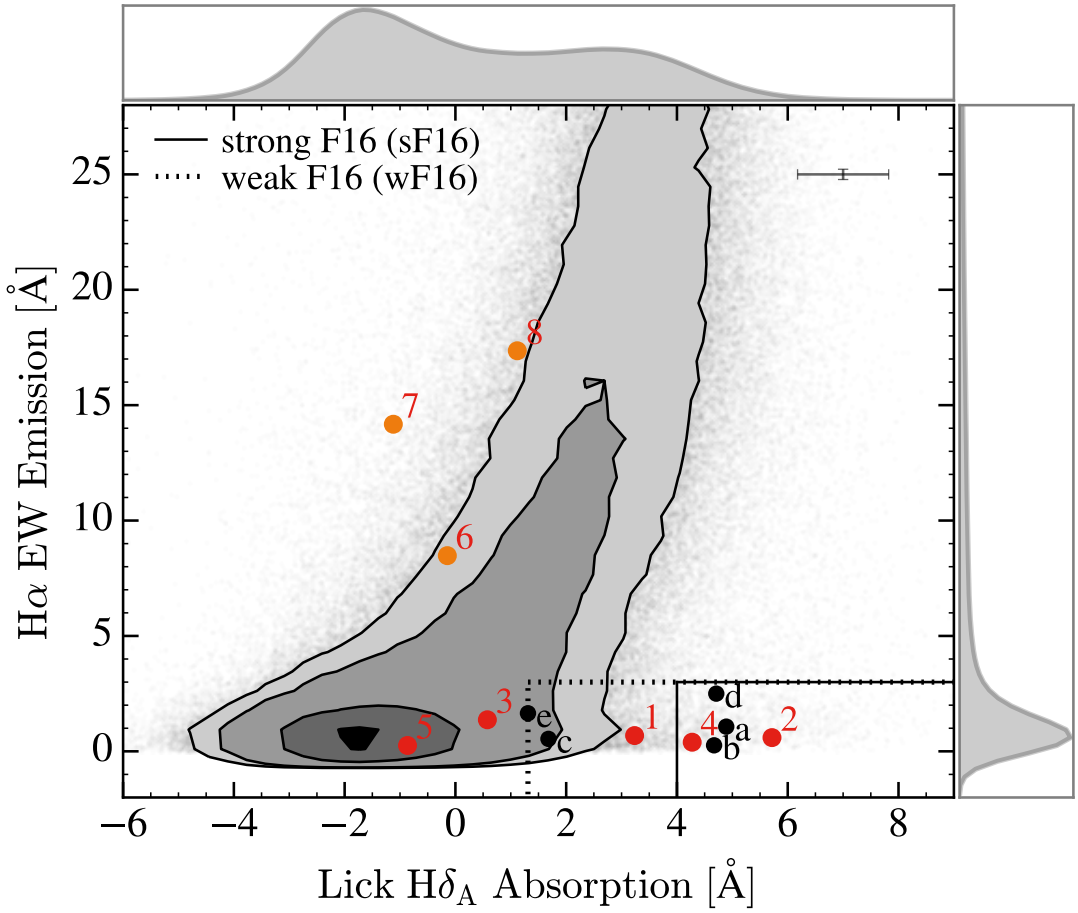

Figure 3.1: Hα equivalent width emission vs. Lick Hδ_A absorption, following French et al. (2016a), for TDE host galaxies (filled circles) and our reference catalog (contours). Galaxies numbered 1-5 are used in our matching analysis (see text). The solid-line selection (including errors on Lick Hδ_A; sF16, see text) contains 0.2% of the galaxies in our reference catalog and the dotted-line region (containing sF16; wF16) contains 2.3%. Contours are spaced by 0.5σ, with the darkest shading containing 0.5σ and the lightest shading containing 2σ. Median errors in the TDE host galaxy measurements are shown in the top right.

Figure 3.1 shows Hα EW emission versus Lick Hδ_A absorption, following French et al. (2016a), for TDE host galaxies and our reference catalog[4]. TDE hosts are numbered following Table 3.1. Excluding TDE candidates 6, 7, and 8 (not identified photometrically), and including candidates a-e, 3/10 = 30% of the TDE host galaxies fall in the sF16 selection[5] and 6/10 = 60% fall in the wF16 selection. TDEs thus remain significantly overrepresented in quiescent Balmer-strong galaxies. A straightforward comparison to all of the galaxies in our reference catalog suggests that TDEs are overrepresented in the sF16 selection by a factor of $\sim$150 (or $\sim$190, including only the optical/UV sample defined in French et al. (2016a)) and are overrepresented in the wF16 selection by a factor of $\sim$35. Of the five TDE hosts we use in our matching analysis, 1/5=20% are in the sF16 selection and 3/5=60% are in the wF16 selection. Restricting ourselves to these five TDE host galaxies does not allow us to claim as robust an overrepresentation in sF16 galaxies,[6] but that is not the direct aim of this work. Our aim is to compare a wide range TDE of host galaxy properties to a larger reference catalog using consistent metrics. Two (of four; two do not have measurements available) of the events in the Auchettl et al. (2017b) *X-ray TDE* category, ASASSN-14li and Swift J1644, appear to be in quiescent Balmer-strong galaxies, suggesting that X-ray TDEs share the same preference for these galaxies as do optical/UV TDEs.

Next, we show where AGN and SF galaxies fall in this Hα EW and Lick Hδ_A

[4]In this and other 2D plots that follow, we use contours to show our reference catalog galaxies. Note that for a 2D distribution, σ levels are defined differently from those for a 1D distribution. In two dimensions, the cumulative density function of a Gaussian is $F(x) = 1 - e^{-(x/\sigma)^2/2}$, meaning that "1$\sigma$" contains 39.3% of the volume and "2σ" contains 86.5% of the volume.

[5]Note that the sF16 selection includes the error on Lick Hδ_A, which excludes #4 and d.

[6]Though the binomial false-positive percentage here for 1/5 of the galaxies in a sample being sF16 is still relatively small, $\sim$1%; see Section 3.4.9.

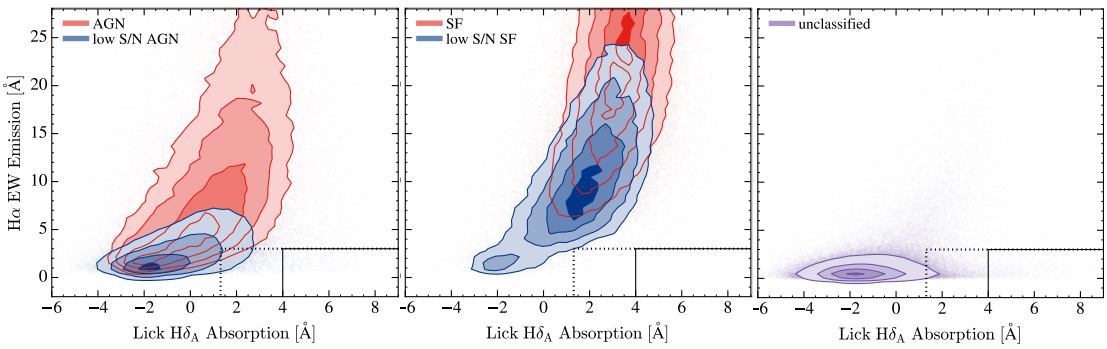

Figure 3.2: Hα EW vs. Lick Hδ_A as in Figure 3.1, for our reference catalog, but split according to AGN/SF classification following Kauffmann et al. (2003c). Low-S/N is taken as S/N < 3.0. Left panel: AGN in red, low-S/N AGN in blue. Middle panel: SF galaxies in red, low-S/N SF galaxies in blue. Right panel: unclassified galaxies. Contours are spaced by 0.5σ, with the darkest shading containing 0.5σ and the lightest shading containing 2σ. The distributions of each subsample are normalized separately, so the relative number in each of the categories is not represented (see Table 3.2 for this), only their relative distributions.

Table 3.2: Fraction of Reference Catalog Galaxies in the Strong and Weak F16 Selections According to AGN/SF Classification

Category	Number	% in sF16	% in wF16
TDE hosts (1-5)	5	20	60
TDE hosts (1-5, a-e)	10	30	80
Full reference catalog	500,707	0.20	2.29
AGN	52,613	0.09	0.60
Low-S/N AGN	93,304	0.36	4.02
SF	110,133	0.0	0.01
Low-S/N SF	42,616	0.01	0.20
Unclassified	202,041	0.30	3.61

parameter space. This is important, as there may be selection effects against detecting TDEs in some of these galaxies (in particular in galaxies hosting a strong AGN and in strongly SF galaxies), as discussed in Sections 3.4 and 3.6. Figure 3.2 shows our reference catalog split into AGN, low-S/N AGN, SF, low-S/N SF, and unclassified subsamples (see Section 3.2 for definitions). The low-S/N AGN scatter into the F16 selections more than the AGN. The unclassified galaxies also scatter into the F16 selections.

Table 3.2 shows the fraction of our reference catalog galaxies in the strong and weak F16 selections according to AGN/SF classification. Somewhat by construction, almost no SF or low-S/N SF galaxies are in the F16 selections. Importantly, however, if we restrict ourselves to only low-S/N AGN or unclassified galaxies, E+A/post-starburst galaxies are still rare, and TDE host galaxies remain overrepresented.

As a related metric of the uniqueness of TDE host galaxies, we show total star formation rate versus total stellar mass for TDE host galaxies and our reference catalog in the top panel of Figure 3.3. The solid blue line describes the star-forming main sequence (SFMS; Peng et al. 2010). We assume a 1σ scatter of 0.5 dex for the SFMS—this is the median scatter of the SFR measurements, shown by the dashed blue lines. We conservatively define the "green valley" or "transition region" in this diagram as being 1σ-3σ below the SFMS normalization (e.g., see Pandya et al. 2016, and references therein)—this is between the lower blue dashed line and the orange dashed line. It is immediately apparent from Figure 3.3 that none of our TDE host galaxies lie above the SFMS normalization[7]. Instead, all of our TDE hosts lie below the SFMS normalization, with some being within our assumed 1σ SFMS scatter and some inhabiting the green

[7]Though note that the errors on some of the TDE host galaxies extend above the SFMS.

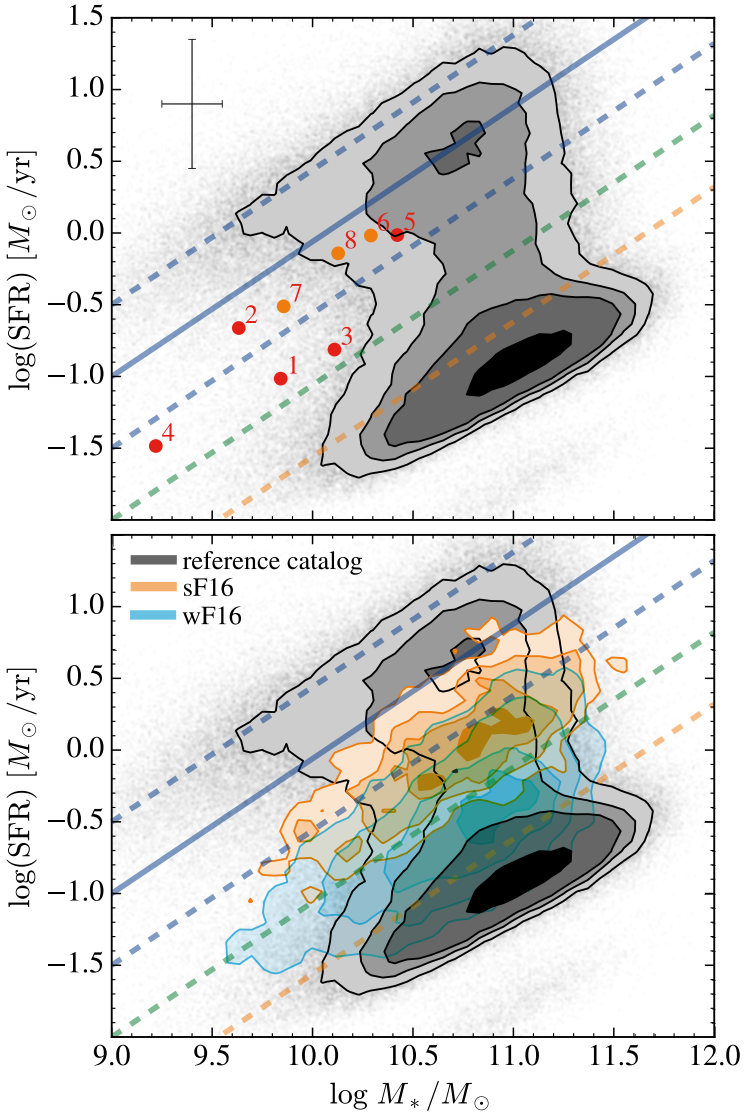

Figure 3.3: Top panel: total star formation rate vs. total stellar mass for TDE host galaxies (numbered points) and our reference catalog (contours). Galaxies 1-5 are used in our matching analysis. Median errors in the TDE host galaxy measurements are shown in the top left. The blue solid line describes the main sequence of SF galaxies (Peng et al. 2010), with dashed lines spaced by 0.5 dex (the median scatter of our SFR measurements) above and below. The green and orange dashed lines are also spaced by 0.5 dex, and indicate degrees of quiescence from the SFMS. Bottom panel: the distribution for galaxies in the sF16 selection (E+A galaxies) is shown in orange and for galaxies in the wF16 selection in light blue. sF16 galaxies account for 0.2% of our reference catalog and wF16 galaxies for 2.3%; their distributions are normalized separately. Contours are spaced by 0.5σ, with the darkest shading containing 0.5σ and the lightest shading containing 2σ.

valley. The location of the TDE host galaxies in this diagram suggests that they could be making a transition from the SFMS toward quiescence, but additional constraints on their stellar populations and star formation histories are needed to test this hypothesis (also see French et al. 2017a).

The distributions of sF16 and wF16 galaxies, separately normalized to the reference catalog's distribution, are shown in orange and light blue in the bottom panel of Figure 3.3. We calculate the fraction of quiescent Balmer-strong galaxies in our three bands of increasing degrees of quiescence below the SFMS (each spaced by 0.5 dex). Recall that the nominal percentage of sF16 (wF16) galaxies in our reference catalog is 0.2% (2.3%). Between the solid blue line and the dashed blue line, the percentage of sF16 (wF16) galaxies is 0.5% (0.9%). Between the dashed blue line and the dashed green line, the percentage of sF16 (wF16) galaxies is 1.1% (7.3%). Between the dashed green line and the dashed orange line, the percentage of sF16 (wF16) galaxies is 0.1% (7.8%). Outside of these three bands, the percentage of sF16 and wF16 galaxies drops well below nominal. If we restrict our reference catalog to galaxies with $\log(M_{\star,\mathrm{tot}}/M_{\odot}) < 10.5$, to match the $M_{\star,\mathrm{tot}}$ values of our TDE hosts, the fractions of quiescent Balmer-strong galaxies quoted above inside the three bands increase only slightly. Thus, quiescent Balmer-strong galaxies reside preferentially in the green valley, and the relative fraction of E+A/post-starburst galaxies in the band inhabited by TDE hosts 1, 3, and 4 is a factor of five greater than nominal.

3.4 TDE Selection Effects

As seen above, TDEs appear to show a distinct preference for quiescent Balmer-strong (and more restrictively E+A) galaxies. Much of this preference may in fact be due to physical and observational selection effects. In this section, we explore their extent.

3.4.1 Matching

Our strategy is to create matched comparison samples drawn from our SDSS reference catalog that are controls for the TDE host galaxies in various observables related to possible selection effects, and then to calculate the fraction of quiescent Balmer-strong galaxies in the controls. We use TDE host galaxies numbered 1-5 for this analysis, as these TDE candidates were photometrically identified and their hosts have measurements in our reference catalog of the properties we match. That the measurements are determined consistently between the TDE host galaxy sample and the reference catalog allows us to match and compare properties in an unbiased way. Our results are similar if we include TDE host galaxies 6-8 (which have Hα EW and Lick H$\delta_{\rm A}$ measurements in our reference catalog), and if we include 9 and 10 (which do not have Hα EW and Lick H$\delta_{\rm A}$ measurements in our reference catalog).

As we match only on five TDE host galaxies, we implement our matching as simple tolerances in each parameter. We match on BH mass, redshift, bulge colors, and half-light surface brightness (motivated and discussed below). The baseline tolerance used for matching is 1% of the "spread" (=$97.5^{\rm th} - 2.5^{\rm th}$ percentile) in each parameter,

which corresponds to roughly 0.0018 in z, 0.037 dex in BH mass, 0.028 mag in bulge color, and 0.074 mag/arcsec^2 in half-light surface brightness. We limit our control sample to a maximum of 10,000 matches per TDE host galaxy; if this is not reached, we increase the tolerance in intervals of 1%, up to a maximum of 5% of the "spread" in each parameter. We require the same number of matches per TDE host galaxy, limited by the TDE host with the fewest matches. We then calculate the fraction of quiescent Balmer-strong galaxies in the control. We do this matching for one parameter at a time and for several simultaneously. This allows us to control for possible selection effects in different observables without needing to understand the (likely complicated) exact form of the selection effect. Our results are relatively insensitive to the matching technique and absolute or fractional tolerances used.

Table 3.3: Fraction of quiescent Balmer-strong galaxies in control samples matched to TDE hosts 1-5. We tested all combinations of these properties, but only list combinations that (1) result in enough controls to compute a reliable fraction of sF16 or wF16 galaxies, (2) lead to an increase in these fractions, and (3) are interesting in comparison with similar combinations.

Properties matched	# Control	# sF16	% sF16	# wF16	% wF16
Full reference catalog	500707	996	0.2	11455	2.29
TDE hosts (1-5)	5	1	20	3	60
TDE hosts (1-5, a-e)	10	3	30	8	80
z	50000	82	0.16	1089	2.18
$M_{\rm bh}$	50000	63	0.13	1054	2.11
bulge $g-r$	50000	1026	**2.05**	2635	5.27
$\Sigma_{\rm hl,g}$	50000	117	0.23	1564	3.13
n_g	50000	76	0.15	1312	2.62
$(B/T)_g$	50000	169	0.34	1498	3.0
z, bulge $g-r$	28600	227	0.79	1294	4.52
z, $\Sigma_{\rm hl,g}$	1700	9	0.53	51	3.0
$M_{\rm bh}$, bulge $g-r$	16680	81	0.49	785	4.71
$M_{\rm bh}$, n_g	6240	39	0.63	496	7.95
$M_{\rm bh}$, $(B/T)_g$	3655	12	0.33	241	6.59
bulge $g-r$, $\Sigma_{\rm hl,g}$	14765	170	1.15	800	5.42
bulge $g-r$, n_g	41220	277	0.67	2328	5.65
bulge $g-r$, $(B/T)_g$	13120	322	**2.45**	1064	**8.11**

Table 3.3 (cont'd): Fraction of quiescent Balmer-strong galaxies in control samples matched to TDE hosts 1-5. We tested all combinations of these properties, but only list combinations that (1) result in enough controls to compute a reliable fraction of sF16 or wF16 galaxies, (2) lead to an increase in these fractions, and (3) are interesting in comparison with similar combinations.

Properties matched	# Control	# sF16	% sF16	# wF16	% wF16
$\Sigma_{\rm hl,g}$, $(B/T)_g$	17065	76	0.45	735	4.31
z, $M_{\rm bh}$, bulge $g-r$	8025	40	0.5	421	5.25
z, $M_{\rm bh}$, n_g	1485	6	0.4	129	**8.69**
z, $M_{\rm bh}$, $(B/T)_g$	1560	4	0.26	114	7.31
z, bulge $g-r$, n_g	4615	57	**1.24**	279	6.05
z, bulge $g-r$, $(B/T)_g$	3655	35	0.96	180	4.92
z, $\Sigma_{\rm hl,g}$, n_g	185	2	1.08	9	4.86
$M_{\rm bh}$, bulge $g-r$, $\Sigma_{\rm hl,g}$	1780	7	0.39	81	4.55
$M_{\rm bh}$, bulge $g-r$, n_g	4390	19	0.43	321	7.31
$M_{\rm bh}$, bulge $g-r$, $(B/T)_g$	2115	12	0.57	164	7.75
$M_{\rm bh}$, $\Sigma_{\rm hl,g}$, n_g	215	0	0.0	19	**8.84**
$M_{\rm bh}$, $\Sigma_{\rm hl,g}$, $(B/T)_g$	580	3	0.52	48	8.28
$M_{\rm bh}$, n_g, $(B/T)_g$	1580	10	0.63	125	7.91
bulge $g-r$, $\Sigma_{\rm hl,g}$, n_g	3065	24	0.78	166	5.42
bulge $g-r$, $\Sigma_{\rm hl,g}$, $(B/T)_g$	2235	46	**2.06**	161	7.2
bulge $g-r$, n_g, $(B/T)_g$	5760	66	1.15	378	6.56
z, $M_{\rm bh}$, bulge $g-r$, $\Sigma_{\rm hl,g}$	285	1	0.35	17	**5.96**

Table 3.3 (cont'd): Fraction of quiescent Balmer-strong galaxies in control samples matched to TDE hosts 1-5. We tested all combinations of these properties, but only list combinations that (1) result in enough controls to compute a reliable fraction of sF16 or wF16 galaxies, (2) lead to an increase in these fractions, and (3) are interesting in comparison with similar combinations.

Properties matched	# Control	# sF16	% sF16	# wF16	% wF16
z, $M_{\rm bh}$, bulge $g-r$, n_g	1105	4	0.36	91	8.24
z, $M_{\rm bh}$, n_g, $(B/T)_g$	440	0	0.0	40	**9.09**
z, bulge $g-r$, $\Sigma_{\rm hl,g}$, n_g	110	2	1.82	7	6.36
$M_{\rm bh}$, bulge $g-r$, n_g, $(B/T)_g$	945	3	0.32	79	8.36

Note. — $\Sigma_{\rm hl,g}$ is the g-band half-light surface brightness, $n_{\rm g}$ is the galaxy Sérsic index, and $(B/T)_g$ is the g-band bulge-to-total-light ratio. Bold numbers highlight particularly large enhancements in the fraction of sF16 or wF16 galaxies.

Table 3.4: Fraction of quiescent Balmer-strong galaxies in samples created with simple cuts on the reference catalog; simultaneous matching (as in Table 3.3) on these combinations of parameters returns few controls. These cuts are chosen to include TDE host galaxies 1, 2, and 4 (all quiescent Balmer-strong).

Sample	# Control	# sF16	% sF16	# wF16	% wF16
Full reference catalog	500,707	996	0.20	11455	2.29
TDE hosts (1-5)	5	1	20	3	60
TDE hosts (1-5, a-e)	10	3	30	8	80
Cut A:[a] $5.5 < \log(M_{\rm bh}/M_\odot) < 7.0$, $z < 0.09$, bulge $g-r < 0.51$, $\Sigma_{\rm hl,g} > 2.05$	4301	33	0.77	118	2.74
Cut B: cut A plus no S/N>5 AGN	4054	32	0.79	117	2.89
Cut C: cut B plus $n_g > 2.24$	1662	28	1.68	85	5.11
Cut D: cut B plus $(B/T)_g > 0.55$	1807	25	1.38	78	4.32

Note. — $\Sigma_{\rm hl,g}$ is the g-band half-light surface brightness, $n_{\rm g}$ is the galaxy Sérsic index, and $(B/T)_g$ is the g-band bulge-to-total-light ratio.

[a]Of the three TDE hosts (in 1-5) that pass cut A, one of three are sF16 and three of three are wF16. All of these also pass cuts B, C, and D.

Table 3.5: Medians of 1D Distributions in Samples Matched in BH Mass to TDE Host Galaxies 1-5

Parameter	Control	TDE hosts (1-5)	TDE hosts (1-10)	sF16	wF16
Bulge $g-r$ [mag]	$0.78^{+1.03}_{-0.44}$	$0.46^{+0.16}_{-0.11}$	$0.49^{+0.32}_{-0.19}$	$0.42^{+0.18}_{-0.08}$	$0.67^{+0.19}_{-0.15}$
$\Sigma_{\rm hl,g}$ [mag/arcsec^2]	$0.98^{+1.55}_{-0.68}$	$2.06^{+2.07}_{-0.46}$	$1.95^{+2.7}_{-0.45}$	$1.58^{+8.28}_{-1.0}$	$1.45^{+2.42}_{-1.04}$
Galaxy Sérsic index	$1.21^{+1.29}_{-0.45}$	$4.03^{+0.92}_{-1.55}$	$4.3^{+1.05}_{-1.92}$	$4.33^{+2.8}_{-1.71}$	$2.88^{+2.58}_{-1.19}$
$(B/T)_g$	$0.06^{+0.37}_{-0.06}$	$0.56^{+0.25}_{-0.06}$	$0.54^{+0.26}_{-0.22}$	$0.6^{+0.18}_{-0.25}$	$0.44^{+0.29}_{-0.27}$
$M_{g,\rm galaxy}$ [mag]	$-19.78^{+1.05}_{-0.9}$	$-19.24^{+0.7}_{-0.59}$	$-19.81^{+1.01}_{-0.49}$	$-19.79^{+1.2}_{-0.52}$	$-19.22^{+1.03}_{-0.76}$
$M_{g,\rm bulge}$ [mag]	$-17.52^{+2.09}_{-1.36}$	$-18.59^{+0.38}_{-0.35}$	$-18.56^{+0.91}_{-0.88}$	$-19.16^{+1.51}_{-0.43}$	$-18.05^{+1.28}_{-1.09}$
Galaxy $g-r$ [mag]	$0.56^{+0.18}_{-0.16}$	$0.63^{+0.11}_{-0.07}$	$0.68^{+0.09}_{-0.11}$	$0.57^{+0.08}_{-0.07}$	$0.74^{+0.09}_{-0.09}$
Inclination	$49.18^{+21.14}_{-22.61}$	$38.48^{+26.15}_{-22.4}$	$40.83^{+19.56}_{-24.86}$	$40.01^{+16.08}_{-23.61}$	$47.69^{+22.33}_{-24.25}$

Note. — $\pm$ values indicate 84th and 16th percentiles. $\Sigma_{\rm hl,g}$ is the g-band half-light surface brightness, $(B/T)_g$ is the g-band bulge-to-total-light ratio, and M_g is the g-band absolute magnitude. Results for r-band are similar.

3.4.2 Overview of Selection Effect Matching Results

Table 3.3 lists the fraction of quiescent Balmer-strong galaxies in our control samples for both individual and simultaneous matches. This table also includes results from matching on galaxy Sérsic index (n_g) and bulge-to-total-light ratio (B/T), discussed in Section 3.5. We find that matching individually on redshift or BH mass slightly decreases the fraction of quiescent Balmer-strong galaxies. Matching on bulge colors increases the fraction of E+A galaxies by a factor of $\sim$10 (from 0.2% to 2%). Matching on half-light surface brightness increases the fraction of quiescent Balmer-strong galaxies only slightly. Matching on several parameters simultaneously can increase the fraction of quiescent Balmer-strong galaxies by a factor of $\sim$4. The number of controls within our tolerances is often too few to compute a reliable sF16 fraction when matching on more than three parameters—we address this with a simple cut-based approach later in this section, and the results of these cuts are listed in Table 3.4.

Figure 3.4 shows 2D distributions of redshift, bulge colors, and half-light surface brightness versus BH mass as well as their 1D distributions matched on the BH masses of TDE hosts 1-5 and split into different subsamples. This figure includes measurements for TDE hosts numbered 6-10, though the matching analysis (resulting in Table 3.3) uses only TDE host galaxies 1-5. The 1D distributions are all smoothed and normalized to equal area. These are shown for presentation purposes only—the smoothing does not enter into or affect our analysis. Red distributions correspond to TDE host galaxies 1-5. We show the unsmoothed histograms for TDE hosts 1-5 in solid red and those for hosts 1-10 in dotted black. The different subsamples shown on the

right-hand side of Figure 3.4 are, from top to bottom, the TDE host galaxies, quiescent Balmer-strong galaxies (sF16 and wF16 selections), and AGNs and low-S/N AGNs. We compare to AGNs both to better understand the connection between TDEs and AGNs (see, e.g., Auchettl et al. 2017c), and because there may be a bias against detecting TDEs in galaxies hosting a strong AGN, as discussed later in this section. Table 3.5 lists the medians and spreads of these 1D distributions matched on BH mass, as well as for some properties considered in Section 3.5 and Appendix 3.7.

3.4.3 BH Mass

The first selection effect we consider is BH mass. As presented in the tidal disruption menu of Law-Smith et al. (2017b), most main sequence (MS) stars cannot be disrupted outside the innermost bound circular orbit of BHs of $M_{\rm bh} \gtrsim 10^{7.5} M_{\odot}$[8]. Giant stars can be disrupted by higher-mass BHs, but their relative disruption rate is lower and their flares last on the order of years (MacLeod et al. 2012b) and may not be seen in current surveys. BHs with $M_{\rm bh} \lesssim 10^{6} M_{\odot}$, on the other hand, may inefficiently circularize the debris from the majority of MS star disruptions (Guillochon & Ramirez-Ruiz 2015b), leading to a delayed flare that is more difficult to detect due to a lower luminosity and longer timescale (Hayasaki et al. 2013b; Dai et al. 2013b; Cheng & Bogdanović 2014b; Bonnerot et al. 2016b). These lower-mass BHs can disrupt denser objects such as white dwarfs, but we do not expect this to be a significant contribution to the current sample of observed TDEs (MacLeod et al. 2016b).

[8]Though combinations of rapid BH spin and favorable orbital orientation can permit MS disruption by BHs with masses of up to a few $\times 10^{8} M_{\odot}$ (Kesden 2012b).

BH mass is thus a primary physical constraint in whether a TDE can be observed in a given galaxy, and we control for it by creating matched samples with similar distributions in BH mass to the observed TDE host galaxies. We obtain BH masses from velocity dispersions, though our conclusions are insensitive to the exact method used to derive BH masses (see Section 3.2). As long as BH mass is determined homogeneously between the different samples we consider, the effect of our uncertainty on BH mass is largely mitigated; i.e., we do not rely on accurate determinations of BH mass for our conclusions. In fact, if we simply replace BH mass with $M_{\star,\mathrm{tot}}$ throughout our analysis, our conclusions remain the same. Matching on only BH mass to TDE hosts 1-5 (see Table 3.3) slightly decreases the fraction of quiescent Balmer-strong galaxies in our reference catalog.

We expect (and find; see Figure 3.4, or Wevers et al. (2017a) for TDE hosts not in our reference catalog) nearly all currently observed TDEs to occur in the BH mass range of $10^{5.5} < M_{\mathrm{bh}}/M_{\odot} < 10^{7.5}$. TDE host galaxies thus have significantly lower BH masses than the bulk of our reference catalog. We plot each of the properties discussed below versus BH mass on the left-hand side of Figure 3.4, and we control for BH mass (matching on TDE hosts 1-5) in the stacked 1D distributions on the right-hand side.

3.4.4 Redshift Completeness

The second selection effect we consider is redshift completeness. The luminosity of a tidal disruption flare depends on the stellar mass, stellar radius, BH mass, impact parameter, and circularization efficiency of the debris. For a typical TDE, however, the maximum peak luminosity does not vary by more than an order of magnitude,

and most observed TDEs have peak luminosities of 10^{43} to 10^{44} erg s^{-1}. Additionally, most TDEs appear to be sub-Eddington or Eddington limited for their BHs (Hung et al. 2017b).

A typical TDE can thus only be observed out to a redshift that depends on the detection limits of the telescope and, especially if the flare is Eddington limited, the mass of the BH. Strubbe & Quataert (2009b) and Kochanek (2016c) studied the dependence of TDE rates on BH mass and redshift in detail; generally, they found that detection rates decrease rapidly with redshift, but that future surveys such as LSST could be sensitive to a sizable number of TDEs at $z > 1$. TDE detectability is a strong function of redshift, and we control for this by creating samples matched on redshift to the TDE host galaxies in our sample. Matching on only redshift (see Table 3.3) slightly decreases the fraction of quiescent Balmer-strong galaxies in our reference catalog.

We show redshift versus BH mass for TDE host galaxies and our reference catalog in the top-left panel of Figure 3.4. All but one of the TDE hosts in our sample have $z < 0.1$. The top-right panel of Figure 3.4 shows that, after controlling for BH mass, the redshift distributions of the TDE host galaxies, sF16 and wF16 galaxies, and both low- and high-S/N AGNs are similar to that of our reference catalog. We note that the "sF16" classification of E+A galaxies is likely to change with redshift if it is based on a single slit width. Although this is a small effect for galaxies with $z < 0.1$, it is sizable when comparing to galaxies at $z > 0.2$. The fraction of sF16 galaxies in our reference catalog as a function of redshift bin (we took $\Delta z = 0.01$), for $z \lesssim 0.1$, is relatively constant at the nominal $\simeq$0.2%, but for $z \gtrsim 0.25$, it can be >5%.

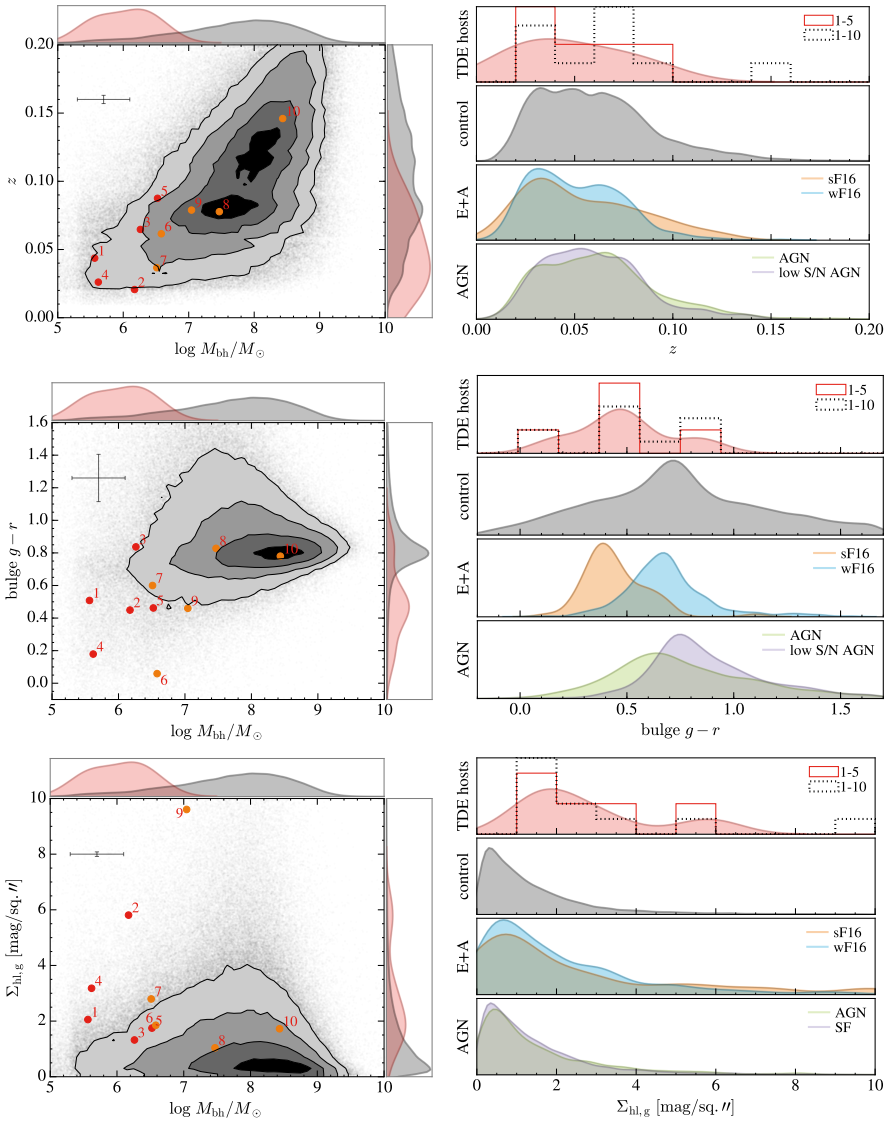

Figure 3.4: Left panels, top to bottom: redshift, bulge $g-r$, and half-light surface brightness vs. BH mass for TDE host galaxies (numbered points) and our reference catalog (contours). Galaxies 1-5 are used in our matching analysis. BH masses for 8, 9, and 10 are determined via $M_{\star,\mathrm{bulge}}$. Contours are spaced by 0.5σ, with the darkest shading containing 0.5σ and the lightest shading containing 2σ. Median errors in the TDE host galaxy measurements are shown in the top left. Right panels: 1D distributions in these properties in different subsamples, matched on BH mass of TDE hosts 1-5. From top to bottom in each panel, the subsamples are: TDE host galaxies (1-5 in red, showing both smoothed and actual distributions, and 1-10 in dotted black), our reference catalog (black), the strong F16 selection (orange), weak F16 selection (light blue), AGN (green), and low-S/N AGN (purple). In the bottom-right panel, we show SF galaxies, rather than low-S/N AGN, in purple, as these have a very similar distribution to the AGN. All 1D histograms are smoothed and normalized to equal area.

3.4.5 Bulge Colors

The third selection effect we consider is the color of the galaxy bulge,[9] as dusty, red bulges might obscure TDEs. Indeed (see below), TDE hosts have bluer bulge colors than most galaxies. We thus control for this possible selection effect by creating samples matched in bulge $g-r$ to TDE host galaxies 1-5. Controlling for only bulge $g-r$ (see Table 3.3) results in a large increase in the fraction of E+A galaxies in our reference catalog: compared to the nominal percentage of 0.2% sF16 galaxies, the matched sample has 2% sF16 galaxies, a factor of $\sim$10 increase. The fraction of wF16 galaxies increases by a factor of two, from 2.3% to 5.3%. Recall that $1/5 = 20\%$ of the TDE host galaxies used in our matching analysis (or $3/10 = 30\%$ including hosts not in our reference catalog) are in the sF16 selection and 3/5 (or 8/10) are in the wF16 selection.

The middle-left panel of Figure 3.4 shows bulge $g-r$ color versus BH mass for the TDE host galaxies and our reference catalog. In the middle-right panel (where we have controlled for BH mass), we see that TDE hosts have bluer bulge $g-r$ colors than the reference catalog, suggesting a preference against observing TDEs in redder bulges. This is also seen clearly in the sF16 sample but only very weakly in the wF16 sample. The AGN and low-S/N AGN samples appear similar to the reference catalog, with the low-S/N AGN sample showing slightly bluer bulge colors than the AGN sample. TDE hosts 1-5 have a median bulge $g-r$ of 0.46 mag, and TDE hosts 1-10 of 0.49 mag. After matching in BH mass to TDE hosts 1-5, the reference catalog has a median bulge $g-r$ of 0.78 mag, and sF16 galaxies of 0.42 mag. This is also listed in Table 3.5. So both

[9]The color of the core/nucleus may be more relevant for TDE detectability but this measurement is not available for nearly as many galaxies as in our catalog drawn from SDSS.

TDE hosts and E+A/post-starburst galaxies have median bulge colors ∼0.3 mag bluer than the control sample.

3.4.6 Half-light Surface Brightness

The fourth selection effect we consider is on surface brightness, as image subtraction for transients might be more challenging for high surface brightness galaxies. We define the half-light surface brightness, $\Sigma_{\rm hl}$, as half the galaxy apparent magnitude divided by the galaxy half-light size in square arcseconds. Using the Simard et al. (2011) measurements, this is $\Sigma_{\rm hl,g} = (g_{g2d} + 0.75254)/\pi\theta_{\rm hl}^2$, where g_{g2d} is the g-band apparent magnitude of the GIM2D output pure Sérsic model, $g_{g2d} + 0.75254$ yields half the flux, and $\theta_{\rm hl} = R_{\rm chl,g}/{\rm Scale}$. $R_{\rm chl,g}$ is the circular half-light radius in the g band, and Scale is the physical scale in kpc/arcsec^2 at redshift z. We use only g band, as results for r band, or a combination of both g and r bands, are similar. Controlling for $\Sigma_{\rm hl,g}$ (see Table 3.3) increases the fraction of quiescent Balmer-strong galaxies in our reference catalog slightly, from 2.3% to 3.1% for wF16 galaxies.

The bottom-left panel of Figure 3.4 shows the half-light surface brightness versus BH mass for the TDE host galaxies and our reference catalog. It is evident that TDEs are found preferentially in galaxies with lower half-light surface brightnesses. In the right panel (controlled for BH mass), we see that sF16 and wF16 galaxies have slightly lower half-light surface brightnesses than the reference catalog, and that AGN and SF[10] galaxies have higher half-light surface brightnesses than either TDE hosts

[10]Low-S/N AGNs have a distribution in $\Sigma_{\rm hl,g}$ that is indistinguishable from that of AGNs here, so we show SF galaxies instead.

or quiescent Balmer-strong galaxies. TDE host galaxies 1-5 have a median half-light surface brightness of 2.06 mag/arcsec^2, and TDE hosts 1-10 of 1.95 mag/arcsec^2. After matching in BH mass to TDE hosts 1-5, the reference catalog has a median half-light surface brightness of 0.98 mag/arcsec^2, and sF16 galaxies of 1.58 mag/arcsec^2; this is also shown in Table 3.5. So, TDE hosts and sF16 galaxies have median half-light surface brightnesses $\sim$1 mag/arcsec^2 and $\sim$0.6 mag/arcsec^2 fainter than the control sample, respectively.

3.4.7 Galaxies Hosting a Strong AGN

We also consider a possible selection effect based on the presence of a strong AGN. Observational identification of TDEs is biased against galaxies with strong AGN, as it is difficult to distinguish a TDE signal from regular variability in a strong AGN. Galaxies with a strong AGN are often not considered for spectral follow-up on potential TDEs. As a first-order exploration of this selection effect, we performed a cut on all AGNs with S/N>5 (we also tried S/N>3) from our reference catalog. Applying this cut—both individually and in combination with controlling for other parameters—has a relatively small effect, but does slightly increase the fraction of quiescent Balmer-strong galaxies in our control samples. We do not show this high-S/N AGN cut in Table 3.3 for clarity, as its effect is generally small, but we show its effect in combination with other simple cuts (described below) in Table 3.4.

3.4.8 Cumulative Effect

Individually, controlling for BH mass or redshift slightly decreases the fraction of quiescent Balmer-strong galaxies in our control sample, controlling for half-light surface brightness slightly increases this fraction, and controlling for bulge $g-r$ increases the fraction of sF16 galaxies by a factor of $\sim$10 and of wF16 galaxies by a factor of $\sim$2. Table 3.3 also lists the effect of controlling for these parameters simultaneously. Note that this table also includes results from matching on two indicators of central light concentration: the galaxy Sérsic index ($n_{\rm g}$) and bulge-to-total-light ratio (B/T); we discuss these parameters in Section 3.5. We summarize our major findings with respect to matching on $M_{\rm bh}$, z, bulge $g-r$, and $\Sigma_{\rm hl,g}$ below. Of these four observables, bulge $g-r$ is the most important in increasing the fraction of quiescent Balmer-strong galaxies in our control samples. However, its effect is largest on the fraction of sF16 galaxies (and remains similar for wF16 galaxies) when matched on individually. Matching simultaneously on z, $M_{\rm bh}$, and bulge $g-r$ increases the percentage of sF16 galaxies by a factor of 2.5, to 0.5%. Matching simultaneously on all four parameters results in too few controls to calculate the fraction of sF16 galaxies but increases the fraction of wF16 galaxies by a factor of 2.6, to 6%. Recall that 1/5=20% of the TDE host galaxies used in our matching analysis (or 3/10=30% including galaxies not in our reference catalog) are sF16 galaxies, and 3/5=60% (or 8/10=80%) are wF16 galaxies.

As matching simultaneously on z, $M_{\rm bh}$, bulge $g-r$, and $\Sigma_{\rm hl,g}$ results in too few controls to calculate the fraction of sF16 galaxies, we perform simple cuts on our full reference catalog as a cruder probe of the extent of these selection effects; this

is shown in Table 3.4. We chose cuts that are consistent with the properties of our quiescent Balmer-strong TDE host galaxies: $5.5 < \log(M_{\rm bh}/M_{\odot}) < 7.0$, $z < 0.09$, bulge $g - r < 0.51$, and $\Sigma_{\rm hl,g} > 2.05$. This results in a sample with 0.77% sF16 galaxies (a factor of $\sim$4 increase from the nominal 0.2%) and 2.74% wF16 galaxies (a factor of 1.2 increase from the nominal 2.3%). Further removing all S/N>5 AGNs increases these numbers slightly.

In summary, the selection effects we considered in this section may reduce the apparent overrepresentation of TDEs in E+A galaxies by a factor of $\sim$4 (quoting the result from simple cuts; Table 3.4) and in quiescent Balmer-strong host galaxies more generally by a factor of $\sim$2.5 (quoting the matching results; see Table 3.3, where we have enough wF16 galaxies to calculate a reliable fraction). Comparing to TDE host galaxies numbered 1-5 used in the matching, this reduces the TDE rate enhancement in sF16 galaxies to a factor of $\sim$25 (from $\sim$100) and in wF16 galaxies to a factor of $\sim$10 (from $\sim$26). Comparing to TDE host galaxies 1-5 and a-e (a-e are not in our reference catalog and so we did not match on their properties), this reduces the TDE rate enhancement in sF16 galaxies to a factor of $\sim$38 (from $\sim$150) and in wF16 galaxies to a factor of $\sim$13 (from $\sim$35).

3.4.9 Small Sample Size

As mentioned, only 1/5 of the TDE hosts we use in our matching analysis is in the sF16 selection. This is too sensitive to small number statistics to claim a true overrepresentation in sF16 galaxies using this sample alone. However, the sF16 overrepresentation increases with the larger sample of 10 photometrically identified TDE

hosts with available Hα EW and Lick Hδ_A measurements, and so it appears robust. Restricting ourselves to the five TDE hosts we use in the matching, however, we can test the probability of having 1/5 sF16 galaxies (i.e., the extent to which this is due to small number statistics) in a Monte Carlo approach. We create 10,000 samples of five galaxies drawn from our full catalog and matched in $M_{\rm bh}$ and z to the five TDE hosts. For each of these 10,000 samples of five galaxies, we count the number (if any) that fall in the sF16 selection. The percentage of the samples that have 1/5 or more sF16 galaxies is 1.0%; this is the chance likelihood of having 1/5 sF16 galaxies in our sample.

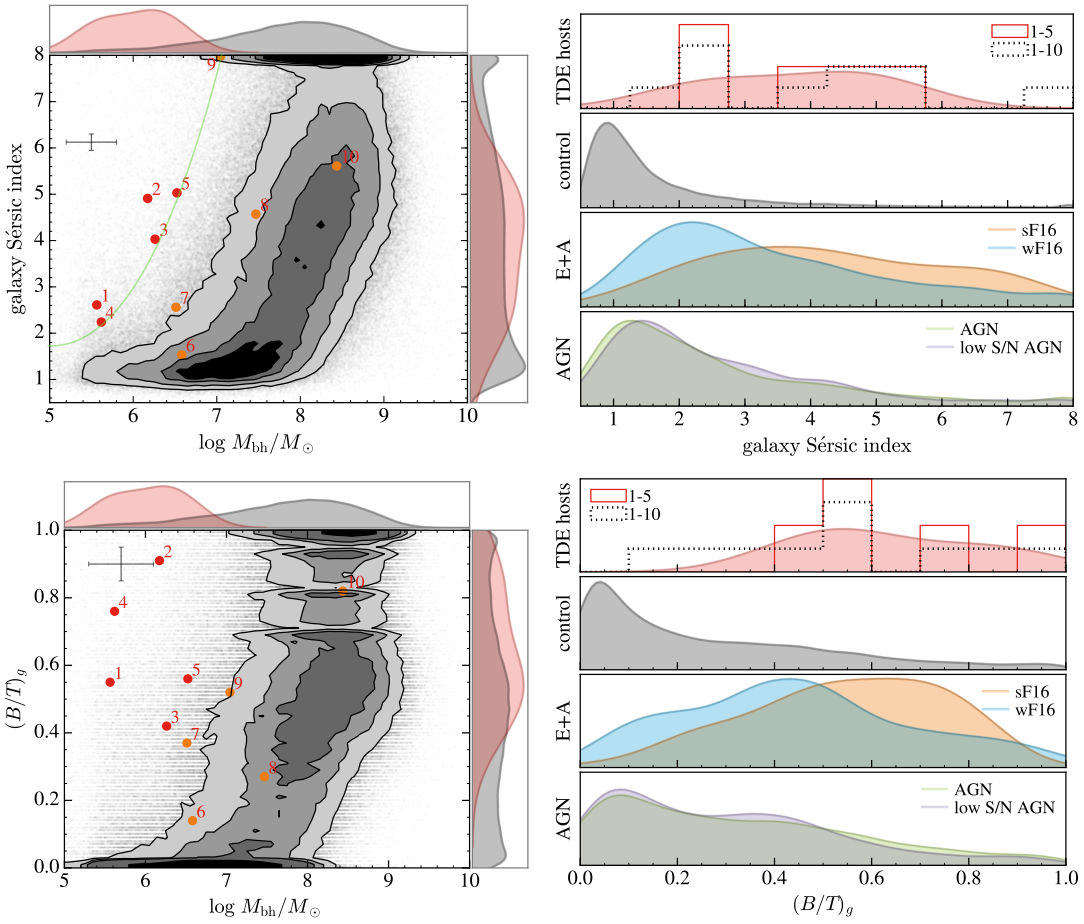

Figure 3.5: Top-left panel: galaxy Sérsic index vs. BH mass for TDE host galaxies and our reference catalog. We use TDE hosts 1-5 in our matching analysis. BH masses for TDE hosts 8, 9, and 10 are determined via $M_{\star,\rm bulge}$. Contours are spaced by 0.5σ, with the darkest shading containing 0.5σ and the lightest shading containing 2σ. Average errors in the TDE host galaxy measurements are shown in the top left. The region above the light green line contains $\sim$2% of our reference catalog galaxies but 5/5 (or 6/10) of our TDE host galaxies. Top-right panel: galaxy Sérsic index distribution in different subsamples, matched on BH mass of TDE hosts 1-5. 1D histograms are smoothed and normalized to equal area. Unsmoothed 1D histograms are also shown for TDE hosts 1-5 in solid red and for TDE hosts 1-10 in dotted black. Bottom panels: g-band bulge-to-total-light ratio (bulge fraction); similar description to that above. Results are similar for r band.

3.5 Physical Enhancements to the TDE Rate

In this section, we consider two possible alternative (physical) explanations for the enhanced frequency of TDEs in quiescent Balmer-strong galaxies: (1) higher central stellar densities and (2) a recent merger. In exploring the first, we find a new unique property of all TDE host galaxies, regardless of E+A or quiescent Balmer-strong classification.

3.5.1 Higher Central Stellar Densities

Sérsic Index

It is expected that a higher stellar density in the nuclear star cluster surrounding an SMBH leads to a higher tidal disruption rate, as there are more dynamical encounters between stars and therefore more scatterings into the loss cone (e.g., Magorrian & Tremaine 1999a). The galaxy Sérsic index is a broad indicator of the steepness of a galaxy's light profile and thus (to a certain extent) its stellar density profile. A Sérsic profile has the form

$$\ln I(R) = \ln I_0 - kR^{1/n}, \tag{3.4}$$

where I is the intensity, I_0 is the intensity at $R = 0$, k is a constant, and n is the Sérsic index. The higher the Sérsic index, the more centrally concentrated the galaxy's light profile.

The top panel of Figure 3.5 shows the galaxy Sérsic index[11] versus BH mass

[11]This is for a single Sérsic fit, also referred to as n_g throughout the paper. We show galaxy rather than bulge Sérsic index here, as only a fraction of our TDE host galaxies and the reference catalog have high enough resolution data to justify (see Section 3.2) free-n Sérsic fits to their bulges. We note,

for TDE hosts and our reference catalog. Note that the Sérsic index fits are allowed to vary from 0.5 to 8 (see Simard et al. 2011). The region above the light green line contains ∼2% of our reference catalog galaxies but 5/5 of TDE host galaxies 1-5 (or 6/10 including the "extreme coronal line emitters" 6-9 and 10 with a BH mass determined via $M_{\star,\mathrm{bulge}}$)[12]. We compute the fraction of reference catalog galaxies that have a higher Sérsic index than each TDE host galaxy at its BH mass (in a bin of width 0.02 dex); we find that all of the TDE host galaxies have high Sérsic indices for their BH masses. On average, TDE hosts 1-5 have galaxy Sérsic indices in the top 10% of those of reference catalog galaxies at their BH masses. Including TDE host galaxies 6-10 results in an average Sérsic index in the top 15%.

In the top-right panel of Figure 3.5, we create a sample matched on the BH masses of TDE hosts 1-5 and compare distributions between different subsamples. TDE hosts have a much broader (toward higher values) distribution of Sérsic indices than the control sample. The distribution for sF16 galaxies is similarly weighted toward high Sérsic indices, and wF16 galaxies show a similar but weaker effect. AGNs and low-S/N AGNs show a fairly similar distribution to the reference catalog, though with a slight preference for higher Sérsic indices. TDE host galaxies 1-5 have a median galaxy Sérsic index of 4.03, and TDE hosts 1-10 of 4.30. After controlling for BH mass, our reference catalog has a median galaxy Sérsic index of 1.21, and sF16 galaxies of 4.33. This is also listed in Table 3.5. So both TDE host galaxies and E+A/post-starburst galaxies have relatively high galaxy Sérsic indices, especially after controlling for BH mass.

however, that in this justified free-n_{b} sample, Simard et al. (2011) find that galaxies with low and high n_{b} values also have low and high n_{g} values.

[12]Note that this region is drawn to include these TDE host galaxies.

Importantly, all of our TDE host galaxies, regardless of E+A or quiescent Balmer-strong classification, have high galaxy Sérsic indices for their BH masses. We have thus identified a photometric criterion (Sérsic index) that may predict an enhanced TDE rate more broadly than a spectroscopic criterion (E+A classification).

Bulge-to-total-light Ratio

The relatively high central concentration of light in TDE host galaxies is also apparent in their bulge-to-total-light ratios. We show the g-band bulge fraction, $(B/T)_g$, in the bottom panel of Figure 3.5. Results are similar for r band. Similarly to above, we compute the fraction of reference catalog galaxies that have a higher $(B/T)_g$ than each TDE host galaxy at its BH mass. Again, we find that all of the TDE host galaxies have high bulge fractions for their BH masses: on average in the top 10% for TDE host galaxies 1-5, and in the top 20% for TDE hosts 1-10. Controlling for BH mass (right panel), we see that both TDE host galaxies and quiescent Balmer-strong galaxies have significantly higher bulge fractions than our reference catalog. This is related to our galaxy Sérsic index result: observed TDEs show a preference for centrally concentrated, bulge-dominated galaxies (and/or tend to avoid disk-dominated galaxies). The bulge fraction and the Sérsic index are correlated—see Figure 14 of Simard et al. (2011) or our Figure 3.11. TDE host galaxies 1-5 have a median $(B/T)_g$ of 0.56 (0.54 for TDE hosts 1-10). Matched on BH mass to TDE hosts 1-5, the reference catalog has a median $(B/T)_g$ of 0.06, and sF16 galaxies of 0.60. This is also listed in Table 3.5.

Can Sérsic Index or B/T Explain the Quiescent Balmer-strong Overrepresentation?

We perform matches on galaxy Sérsic index and bulge fraction, as we did for the selection effects considered in Section 3.4, and compute the fraction of quiescent Balmer-strong galaxies in the matched samples. The results of this matching (using TDE hosts 1-5 as before) are listed in Table 3.3; we will summarize below. We tested all combinations of the properties we studied, but only list combinations that (1) result in enough controls to compute a reliable fraction of sF16 or wF16 galaxies, (2) lead to an increase in these fractions, and (3) are interesting in comparison with similar combinations. Matching only on Sérsic index slightly decreases the fraction of sF16 galaxies in our control sample, while matching only on $(B/T)_g$ increases the fraction of sF16 and wF16 galaxies by a factor of $\sim$1.5. Matching simultaneously on $n_{\rm g}$ or B/T in combination with the selection effects we considered in Section 3.4 can increase the fraction of quiescent Balmer-strong galaxies in our reference catalog by a factor of 3-10 depending on the combination. The highest increase in the fraction of sF16 galaxies—from 0.2% to 2.45%—is given by matching on bulge $g-r$ and $(B/T)_g$. The highest increase in the fraction of wF16 galaxies—from 2.3% to 9.1%—is given by matching on z, $M_{\rm bh}$, $n_{\rm g}$, and $(B/T)_g$.

Simultaneously matching on either Sérsic index or B/T and on all of the four parameters we considered earlier returns too few controls to compute the fraction of quiescent Balmer-strong galaxies. We perform simple cuts on our full reference catalog as a cruder probe of the effect of controlling for five of these properties; these are listed in

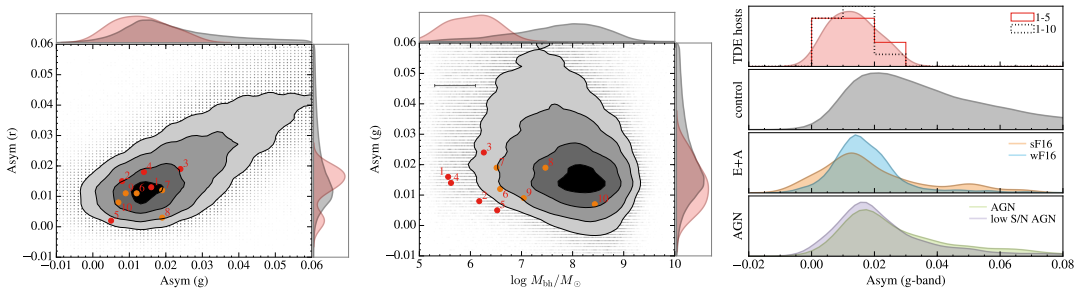

Figure 3.6: Left panel: galaxy asymmetry indicators in the g and r bands for TDE host galaxies and our reference catalog. Middle panel: asymmetry indicator in the g band vs. BH mass. The r band is similar. BH masses for TDE hosts 8, 9, and 10 are determined via $M_{\star,\mathrm{bulge}}$. Contours are spaced by 0.5σ, with the darkest shading containing 0.5σ and the lightest shading containing 2σ. Average errors in the TDE host galaxy measurements are shown in the top left (asymmetry indicators do not have associated errors in our catalog). Right panel: asymmetry indicator distribution in the g band in different subsamples, matched on BH mass of TDE hosts 1-5. The r band is similar. 1D histograms are smoothed (we also show the true histogram for the TDE hosts 1-5 in red and 1-10 in dotted black) and normalized to equal area.

Table 3.4. We chose cuts that are consistent with the properties of our quiescent Balmer-strong TDE host galaxies: $5.5 < \log(M_{\mathrm{bh}}/M_{\odot}) < 7.0$, $z < 0.09$, bulge $g - r < 0.51$, $\Sigma_{\mathrm{hl,g}} > 2.05$, and $n_{\mathrm{g}} > 2.24$ and/or $(B/T)_g > 0.55$. These result in samples with ∼1.7% sF16 galaxies (a factor of ∼8 increase from the nominal 0.2%) and ∼5.1% wF16 galaxies (a factor of 2.2 increase from the nominal 2.3%).

Higher galaxy Sérsic indices and/or higher bulge-to-total-light ratios could therefore partially explain the enhanced TDE rate in quiescent Balmer-strong galaxies; we discuss this further in Section 3.6.

3.5.2 Merger Indicators

Galaxy mergers might also enhance the TDE rate if they trigger binary BH inspiraling. To study this, we use the *RA*1_2 galaxy asymmetry indicators output from

GIM2D (as defined in Simard et al. 2002, 2009) in the g and r bands. For recent major mergers, the asymmetry indicators can be $\gtrsim 0.04$ (e.g., Patton et al. 2016). The asymmetry indicators are shown plotted against each other as well as against BH mass for TDE host galaxies and our reference catalog in Figure 3.6. In the right two panels, we show only g-band measurements; results are similar for r band. Interestingly, our TDE host galaxies have small asymmetry indicators, suggesting that they are not the products of recent major mergers. It is important to note that a small SDSS asymmetry indicator does not necessarily correspond to the lack of a merger. The major limitation here is the SDSS resolution, along with the fact that asymmetries in mergers tend only to be high for major mergers and gas-rich galaxies (Lotz et al. 2010; Ji et al. 2014). In the right panel (controlled for BH mass), we see that TDE host galaxies and quiescent Balmer-strong galaxies both have a narrower distribution in asymmetry indicator compared to the reference catalog. They do not share the reference catalog's tail toward high asymmetry indicators.

3.5.3 Summary of TDE Host Galaxy Properties; SDSS Images

In summary, TDE host galaxies tend to have bluer bulges, lower half-light surface brightnesses, and more centrally concentrated light profiles (in Sérsic index and bulge fraction) than "typical" galaxies at their BH masses. As an illustrative example of this, in Figure 3.7, we show SDSS images[13] of TDE host galaxies 1-5 as well as, for each TDE host galaxy, a randomly selected galaxy matched in BH mass and redshift to

[13]Though higher resolution imaging is available for several of these galaxies, we show SDSS photometry here as this is what was used to derive the photometric galaxy properties in our reference catalog.

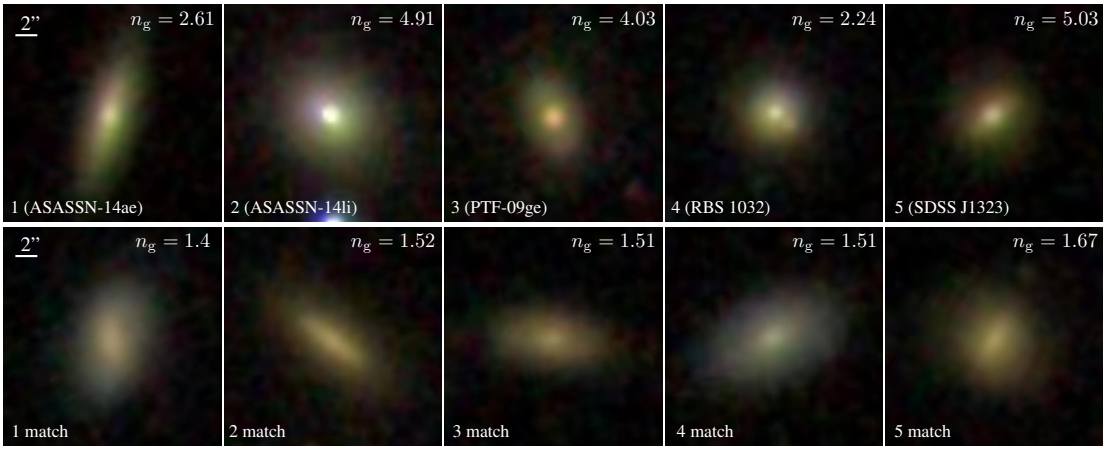

Figure 3.7: Top panels: SDSS *gri* images of TDE host galaxies 1-5. Bottom panels: for each TDE host galaxy, a randomly selected galaxy matched in BH mass and redshift to the TDE host galaxy, but with a galaxy Sérsic index, bulge $g-r$, and half-light surface brightness very close to the median values of our reference catalog at that BH mass. Images are $20'' \times 20''$. The galaxy Sérsic index of each galaxy is listed in the top right of each image.

the TDE host galaxy, but with a galaxy Sérsic index, bulge $g-r$, and half-light surface brightness very close to the median values of our reference catalog at that BH mass. The galaxies in the bottom panels are thus "typical" galaxies in a few of the parameters we considered above, but matched in BH mass and redshift to the TDE host galaxies. The higher central concentration of these TDE host galaxies is visually apparent. The galaxy Sérsic index of each galaxy is listed in the top right of each image.

3.6 Discussion

In this section, we discuss (1) whether there is a selection effect against detecting TDEs in SF galaxies, (2) if the observed time delay between SF and AGN activity can help us understand the nature of the post-starburst TDE delay, (3) if the quiescent Balmer-strong enhancement can be understood in terms of Sérsic indices in the green

valley, and (4) the implications of higher central light concentrations on the TDE rate. Before discussing these issues, we list a summary of our key findings.

3.6.1 Summary

We studied TDE host galaxies in the context of a catalog of ∼500,000 SDSS galaxies. Our main conclusions are:

1. Controlling for (by creating matched samples) selection effects due to BH mass, redshift completeness, bulge color, and half-light surface brightness reduces the apparent overrepresentation of TDEs in E+A host galaxies by a factor of ∼4 (from ∼×100-190 to ∼×25-48 in sF16 galaxies), but cannot fully explain the preference.

2. Controlling for BH mass, TDE host galaxies have bluer bulge $g - r$ colors (by ∼0.3 mag) and fainter half-light surface brightnesses (by ∼1 mag/arcsec^2) than galaxies in our reference catalog. TDE host galaxies have low galaxy asymmetry indicators, suggesting that they are not the result of a recent major merger.

3. TDE hosts and E+A galaxies have high galaxy Sérsic indices and high B/T for their BH masses, suggesting a higher stellar density in their cores. On average, our TDE host galaxies have galaxy Sérsic indices and bulge fractions in the top 10% of those of reference catalog galaxies at their BH masses. We identify a region in galaxy Sérsic index versus BH mass space that contains ∼2% of our reference catalog galaxies but 5/5 (or 6/10) of our TDE host galaxies.

We also note that Graur et al. (2017a) appeared on arXiv after submission of this work and is an independent and complementary analysis of TDE host galaxy

properties. They study a smaller set of host galaxy properties, but, importantly, find that TDE host galaxies have high stellar surface mass densities. This is similar to our finding that TDE host galaxies appear more centrally concentrated, with higher galaxy Sérsic indices and B/T. They control for the type of galaxy in which the TDE is found (quiescent or star-forming) and find that this result is driven particularly by the star-forming hosts.

3.6.2 Is There a Selection Effect Against Detecting TDEs in SF Galaxies?

In order to understand the TDE rate enhancement in quiescent Balmer-strong galaxies, it is important to know whether there is a selection effect against detecting TDEs in SF galaxies. As SF galaxies are (by definition) not quiescent Balmer-strong galaxies, if there is a bias against observing TDEs in SF galaxies, quiescent Balmer-strong galaxies are less rare as hosts.

First, we consider whether the dust and gas associated with SF may obscure TDEs. Certainly, starbursting galaxies have significant dust attenuation (e.g., Casey et al. 2014), especially in the optical/UV bands where the SF occurs. Del Moro et al. (2013) study a robust sample of 51 "hidden" radio-excess AGNs in SF galaxies, and find that half of these are not detected in deep *Chandra* X-ray data, indicating that they might be heavily obscured. As a case study, the Seyfert 2 galaxy NGC 4968 is found to have heavy obscuration and circumnuclear SF, as well as SF-associated gas that may increase the covering factor of the enshrouding gas and play a role in obscuring the AGN (LaMassa et al. 2017). If a TDE occurred in NGC 4968, the large column density

($N_{\rm H} > 1.25 \times 10^{24}$ cm^{-2}) would prevent X-ray—and optical/UV, for dust-to-gas ratios similar to the Milky Way—identification.

Although difficult to detect, AGNs are often found in SF galaxies[14] (Bongiorno et al. 2012; Ellison et al. 2016). Nuclear activity in SF galaxies might be fairly common, and it is possible that TDEs are missed in these galaxies primarily due to selection effects. We note that Tadhunter et al. (2017) discovered a TDE in a nearby ultraluminous infrared galaxy.[15] The galaxy features suggest that there is an unusually clear view of the nuclear star-forming region, whose obscuration is known to have a complex structure (e.g., Buchner & Bauer 2017). Two galaxies in our TDE host galaxy sample, SDSS J0748 and SDSS J1342 (Wang et al. 2012), are in SF galaxies. We note, however, that both events were classified as TDEs in a search for extreme coronal line emitters, and in both cases were not identified based on their light curve properties.

Second, we recognize that there could be a bias against TDE identification in SF galaxies, as TDE characterization for nuclear transients is not done systematically. In addition, current TDE host galaxies have relatively low half-light surface brightnesses, while SF galaxies have relatively high half-light surface brightnesses (see Figure 3.4). If image subtraction is less robust for these galaxies, this could help explain the lack of TDEs in SF galaxies.

[14]Though we caution that this strongly depends on how the AGN is selected (see e.g., Ellison et al. 2016).

[15]This galaxy is not in our sample as it is not in the SDSS catalogs we draw from.

3.6.3 Time Delay between SF and AGN/TDEs

If TDEs occur preferentially in post-starburst galaxies, then the TDE rate is time dependent and, in particular, depends on the recent SF history of the galaxy. If the starburst was caused by a galaxy merger, the second inspiraling BH could certainly enhance the TDE rate; we discuss this further below, but first we consider the relationship between the SF and the TDE. After a starburst occurs, the gas is transported inwards on some timescale and may drive an enhanced TDE rate (possibly through contributing to disk instabilities; Madigan et al. 2017).

This transport timescale is also seen in AGN activity, and there is an intriguing connection between AGN activity and SF episodes. AGN activity appears to be triggered by the same gas that drives SF episodes (Trump et al. 2015), but with a time delay, presumably due to the transport timescale of gas to the BH. The post-starburst timescale in TDE hosts appears tantalizingly similar to this observed AGN activity–SF episode delay.

Wild et al. (2010) study a sample of 400 galaxies with BH masses of $10^{6.5}$-$10^{7.5} M_{\odot}$ that have experienced a starburst in the past 600 Myr. They find that the average rate of accretion of matter onto the BH rises steeply $\approx$ 250 Myr after the starburst begins. Similarly, Davies et al. (2007) study the nuclei of nine AGNs at spatial scales of $\approx$ 10 pc and find a hint of a delay of 50-100 Myr between the onset of star formation and accretion onto the BH. This delay is strikingly reminiscent of the post-starburst timescale inferred for TDE hosts, which have post-starburst ages of

10-1000 Myr (French et al. 2017a)[16].

LaMassa et al. (2013) study the connection between AGN activity and star formation with a sample of $\approx$ 28,000 obscured active galaxies. They find that circumnuclear star formation is associated with increased BH activity and that angular momentum transfer through the disk limits the efficiency of mass inflow onto the BH. Mullaney et al. (2012b) also suggest that the same secular processes that drive the bulk of star formation are responsible for the majority of SMBH activity, which gives further credence to the idea that the majority of moderate nuclear activity is fueled by internal mechanisms rather than violent mergers (Mullaney et al. 2012a). If the connection between SF history and the TDE rate is analogous to the SF episode–AGN activity connection, this could help explain the quiescent Balmer-strong galaxy preference.

3.6.4 The Green Valley, Sérsic Index, and E+A/Post-Starburst Galaxies

In Figure 3.3, we saw that our TDE host galaxies lie below the SFMS, but not by more than 1.0 dex (some are in the green valley and some appear near it), and that E+A/post-starburst galaxies inhabit a similar region. In the left panel of Figure 3.8, we show SFR versus $M_{*,\mathrm{tot}}$ for our TDE host galaxies and the reference catalog, similarly to Figure 3.3, but color-coded by galaxy Sérsic index; this shows the evolution of galaxy surface density profiles in this parameter space. TDE host galaxies clearly inhabit a transition region in Sérsic index.

In the right panel of Figure 3.8, we show normalized histograms of Sérsic

[16]Though note that only 4/8 of their sample have post-starburst ages of <250 Myr.

index for different subsamples of the reference catalog: the band from the SFMS to 0.5 dex below the SFMS (band 1), the band 0.5 dex below this, from the dashed to the dotted line (band 2), and galaxies in the sF16 selection. Though their population is small, E+A galaxies have much higher Sérsic indices relative to the larger population of galaxies in the green valley. If we restrict our reference catalog to galaxies with $\log(M_{\star,\mathrm{tot}}/M_{\odot}) < 10.5$, to match the TDE hosts, as well as to galaxy Sérsic indices of > 2.0, the percentage of sF16 (wF16) galaxies in band 2 is 1.9% (16%). Further restricting to galaxies with Sérsic indices > 4.0 results in 3.8% sF16 galaxies and 23% wF16 galaxies in band 2. This cut also results in 4.9% sF16 galaxies in band 1. So, E+A galaxies are a subset of green valley galaxies with high Sérsic indices. If, due to their higher intrinsic rates in these galaxies, TDEs are preferentially found in post-starburst galaxies with high central densities, then E+A/post-starburst galaxies are relatively less rare as TDE hosts.

3.6.5 On the TDE Rate Enhancement

The increased TDE rates in E+A/post-starburst galaxies might be explained by mergers and/or by higher nuclear stellar densities.

A merger is thought to increase the disruption rate by many orders of magnitude (e.g., Ivanov et al. 2005). But these rate enhancements are short lived (less than 1 Myr), so that the fraction of TDEs resulting from merging BHs is expected to be low (Wegg & Nate Bode 2011). The asymmetry indicators for TDE hosts are comparatively small, meaning that they show no obvious signs of recent major mergers. However, TDE hosts could be the product of high mass ratio mergers. Indeed, unequal mass ra-

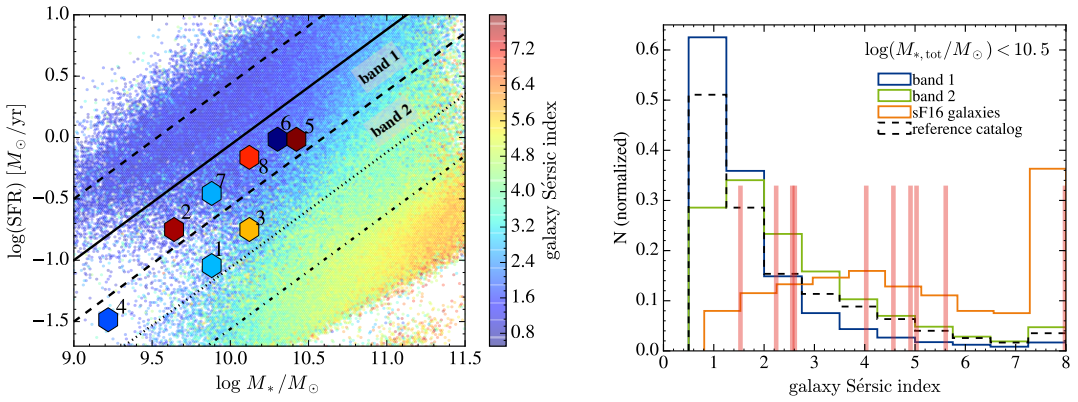

Figure 3.8: Left panel: total star formation rate vs. total stellar mass for our reference catalog and TDE host galaxies 1-8. Color corresponds to galaxy Sérsic index, ranging from 0.5 (blue) to 8 (red); for the reference catalog galaxies, this is the mean within each hexagonal bin. Right panel: normalized histograms of galaxy Sérsic index for our reference catalog (dashed black), galaxies between the SFMS and 0.5 dex below the SFMS (band 1; blue), galaxies between the SFMS − 0.5 dex and the SFMS − 1.0 dex (band 2; green), and galaxies in the sF16 selection (orange). Sérsic indices of our TDE hosts are indicated by the red vertical lines. Here, we restrict all samples to $\log(M_{\star,\mathrm{tot}}/M_\odot) < 10.5$ to roughly match the range of TDE host galaxy values.

tio mergers are more effective at enhancing the TDE rate as stars are scattered into the loss cone of disruptive orbits more efficiently (Chen et al. 2009). French et al. (2017a) find that the post-starburst ages of TDE hosts, if the starburst arose from a galaxy merger, are consistent with mergers of mass ratios more equal than 12:1 for most hosts, which is still consistent with our findings.

Additionally, higher resolution observations could reveal signs of mergers that the asymmetry indicators miss. Using MUSE integral field unit (IFU) spectroscopy observations, Prieto et al. (2016) find that the host galaxy of ASASSN-14li shows asymmetric and filamentary structures—signs of a recent merger—yet this galaxy has a small $RA1\_2$ asymmetry indicator (0.008 and 0.015 in the g and r bands, respectively).

Higher Sérsic indices and bulge-to-total-light ratios for both TDE host galaxies

and E+A/post-starburst galaxies (see Figure 3.5) provide a natural explanation for the enhanced disruption rates in these galaxies. Stone & Metzger (2016b) were the first to predict that the enhanced rate in E+A/post-starburst galaxies might be due to their large central stellar densities, as per-galaxy TDE rates scale roughly as $\dot{N}_{\rm TDE} \propto \rho_\star^2$. We caution that our galaxy Sérsic indices were derived using measurements that typically do not resolve the nuclear regions of the galaxy and, as such, the density of the sphere of influence of the BH cannot be directly constrained. We note, however, that Simard et al. (2011) isolate a subsample of ∼53,000 galaxies with justified free-n Sérsic fits to their bulges, and they find that galaxies with low and high $n_{\rm bulge}$ values also have low and high $n_{\rm g}$ values.

There is also some direct evidence that E+A galaxies have higher central stellar densities. Stone & van Velzen (2016) find that the E+A galaxy NGC 3156 is centrally overdense, leading to an estimated TDE rate via two-body relaxation of $\sim 10^{-3}$ yr^{-1}, an order of magnitude higher than for other galaxies with similar BH masses. Pracy et al. (2012) study a sample of seven local E+A galaxies with IFU spectroscopy and find that they have compact young cores and stellar population gradients that are predicted from models of mergers and tidal interactions that funnel gas into the galaxy core. This suggests that these galaxies are being seen in the late stage of a merger where the nuclei have already coalesced.

Importantly—and separate from understanding the E+A galaxy preference—we are able to identify a photometric criterion (light concentration, given by either the Sérsic index or bulge fraction) that may predict a TDE overabundance more broadly

than a spectroscopic criterion (E+A classification). For upcoming transient surveys where there may be up to $\sim 10^5$ transients discovered each year, a photometric host galaxy selection criterion could be extremely useful for focusing limited follow-up resources. For instance, choosing nuclear transients in high-Sérsic galaxies could significantly increase the success of confirming TDEs.

3.7 Other TDE Host Galaxy Properties

Here, we discuss a few other properties of the host galaxies of TDEs. The top-left panel of Figure 3.9 shows $D_n(4000)$ versus BH mass for TDE host galaxies and our reference catalog. $D_n(4000)$ corresponds to the strength of the 4000Å break and is an indicator of the age of the galaxy stellar population: no break means a young galaxy and a strong break means an old galaxy. Following Kauffmann et al. (2003a,b) and Brinchmann et al. (2004), the peak in $D_n(4000)$ at ~ 1.3 corresponds to galaxies with r-band weighted mean stellar ages of $\sim$1-3 Gyr and mass-weighted mean ages a factor of ~ 2 larger. The peak in $D_n(4000)$ at ~ 1.85 corresponds to older elliptical galaxies with mean stellar ages of $\sim$10 Gyr. The TDE host galaxies lie roughly in between these two peaks, with a peak in $D_n(4000)$ at ~ 1.5, indicating that they have mean stellar ages in between those of these two populations. Note that this measurement is only sensitive to the dominant stellar population and does not reveal multiple stellar populations. In the right panel, where we match on BH mass to TDE hosts 1-5, we see that sF16 galaxies exhibit a younger mean stellar age than wF16 galaxies. AGNs exhibit a younger mean stellar age than low-S/N AGNs. We note that $D_n(4000)$ is not as effective a metric

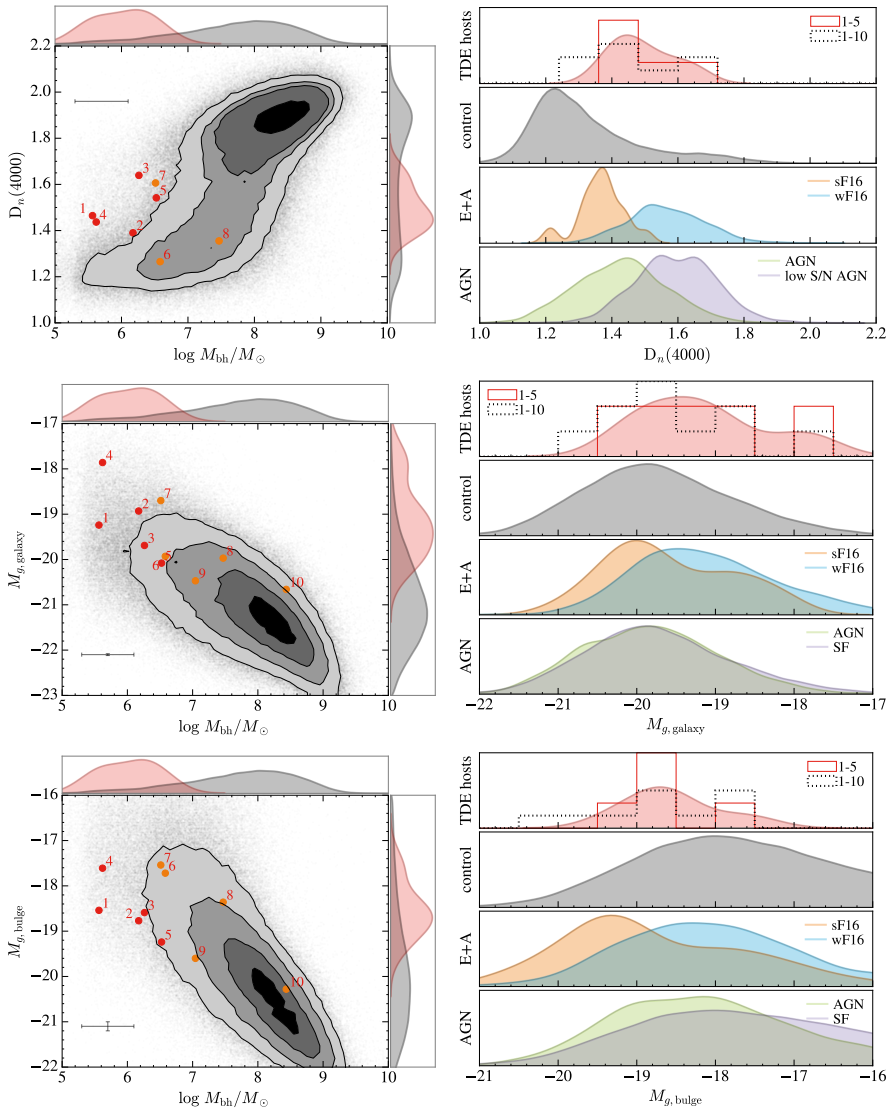

Figure 3.9: Left panels, top to bottom: $D_n(4000)$, g-band galaxy absolute magnitude, and g-band bulge absolute magnitude vs. BH mass for TDE host galaxies and our reference catalog. For galaxy and bulge magnitudes, the results are similar for the r-band. BH masses for TDE hosts 8, 9, and 10 are determined via $M_{\star,\rm bulge}$. Contours are spaced by 0.5σ, with the darkest shading containing 0.5σ and the lightest shading containing 2σ. Average errors in the TDE host galaxy measurements are shown in the top or bottom left. Right panels: 1D distributions of these properties in different subsamples, matched on BH mass of TDE hosts 1-5. All 1D distributions are smoothed and normalized to equal area. Unsmoothed 1D histogram for TDE hosts 1-5 is shown in solid red, and for TDE hosts 1-10 in dotted black.

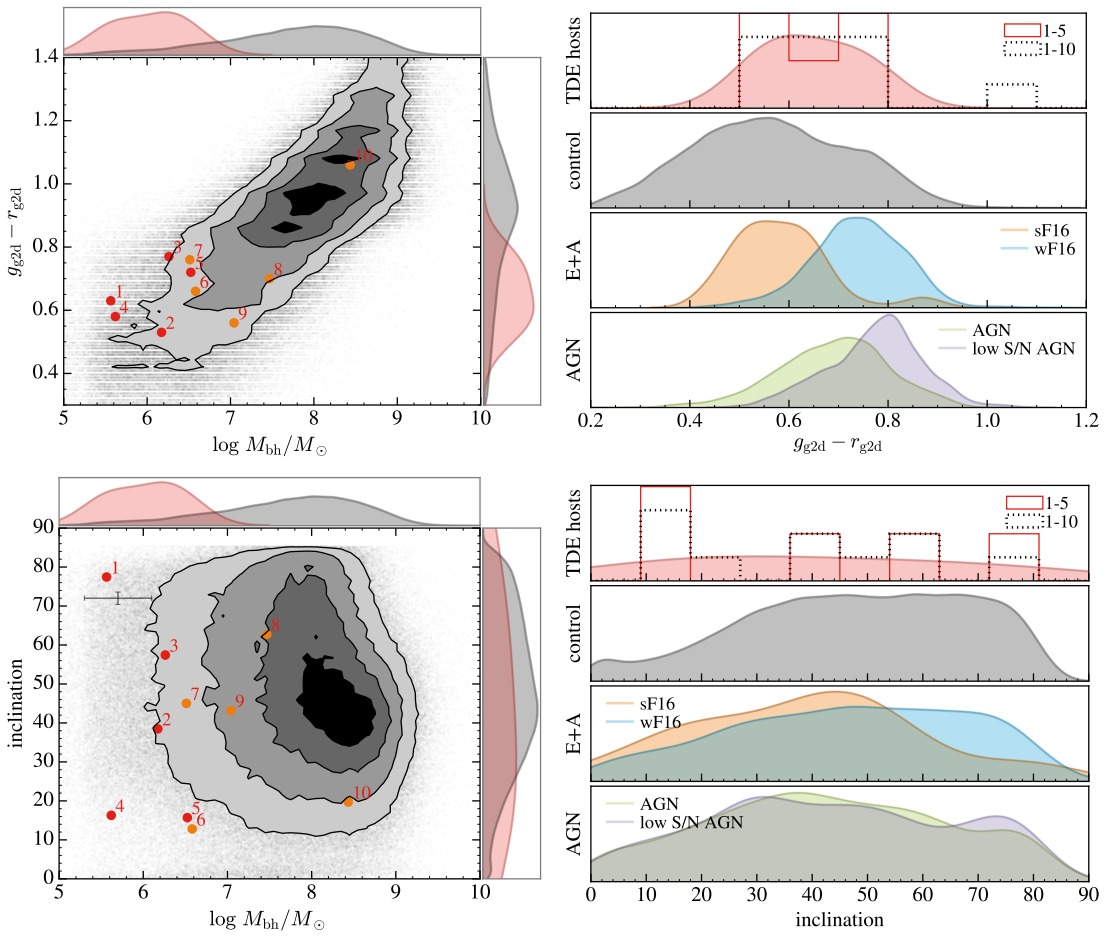

Figure 3.10: Same description as in Figure 3.9, but galaxy $g - r$ in the top panel and inclination (face-on is 0°, maximum of 85°) in the bottom panel.

as the Hα EW and Lick Hδ_A metric (Figure 3.1) in isolating quiescent Balmer-strong galaxies.

The middle-left panel of Figure 3.9 shows g-band galaxy absolute magnitude versus BH mass for TDE host galaxies and our reference catalog. Results are similar for r band. Controlling for BH mass (right panel), TDE hosts are slightly fainter than the catalog galaxies, and sF16 galaxies are slightly brighter than wF16 galaxies. The AGN and SF samples have very similar distributions. The bottom panel of Figure 3.9 shows bulge g-band absolute magnitude. Results are similar for r band. Here, controlling for BH mass, both TDE host galaxies and (to a somewhat greater extent) sF16 galaxies have brighter bulge magnitudes than the reference catalog. Medians and spreads on the distributions of the galaxy and bulge absolute magnitudes are given in Table 3.5.

Lastly, we show galaxy $g - r$ in the top panel of Figure 3.10, and galaxy inclination (face-on is 0°) in the bottom panel. Controlling for BH mass, the galaxy $g - r$ colors for TDE host galaxies and our reference catalog appear fairly similar. sF16 galaxies have bluer colors than wF16 galaxies. The inclinations of TDE hosts appear fairly uniform, with a hint of a preference for lower inclinations. Interestingly, the inclination distribution of sF16 galaxies appears different from that of the reference catalog, with a preference for $20 \lesssim i \lesssim 65$ in contrast to the catalog's preference for $40 \lesssim i \lesssim 80$. Medians and spreads on the distributions of galaxy colors and inclinations are given in Table 3.5.

3.8 Correlations

We show correlations between many of the properties explored in this paper in Figure 3.11. We show BH mass, total stellar mass, redshift, half-light surface brightness, bulge $g - r$, galaxy Sérsic index, and bulge-to-total-light ratio. The total stellar mass behaves very similarly to BH mass in this diagram, which, in addition to it being a more physically relevant parameter for tidal disruptions, is why we use BH mass in our analysis. However, as mentioned in the text, if we simply replace BH mass with $M_{\star,\mathrm{tot}}$ in our analysis, our conclusions remain the same.

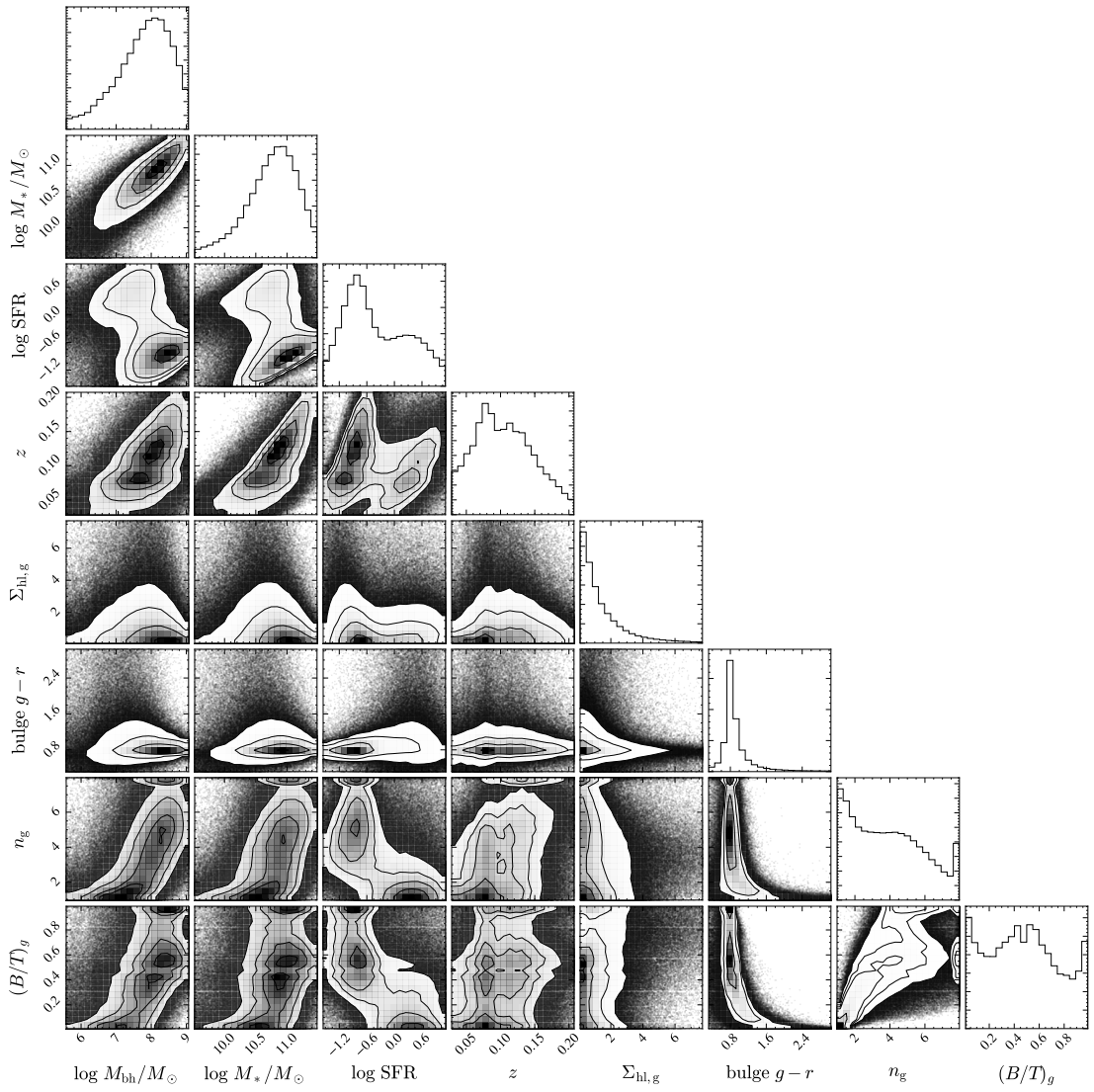

Figure 3.11: Correlations between many of the properties explored in this paper for our reference catalog of ∼500,000 galaxies. From left to right along the bottom row, the properties are BH mass, total stellar mass, total star formation rate (in $M_\odot$ yr^{-1}), redshift, g-band half-light surface brightness (in mag/arcsec^2), bulge $g-r$, galaxy Sérsic index ($n_{\rm g}$), and g-band bulge-to-total-light ratio $(B/T)_g$. Each panel contains 95% of the points.

Chapter 4

Tidal Disruptions of Main Sequence Stars of Varying Mass and Age: Inferences from the Composition of the Fallback Material

Abstract

We use a simple framework to calculate the time evolution of the composition of the fallback material onto a supermassive black hole arising from the tidal disruption of main sequence stars. We study stars with masses between 0.8 and 3.0 $M_{\odot}$, at

evolutionary stages from zero-age main sequence to terminal-age main sequence, built using the Modules for Experiments in Stellar Astrophysics code. We show that most stars develop enhancements in nitrogen (^{14}N) and depletions in carbon (^{12}C) and oxygen (^{16}O) over their lifetimes, and that these features are more pronounced for higher mass stars. We find that, in an accretion-powered tidal disruption flare, these features become prominent only after the time of peak of the fallback rate and appear at earlier times for stars of increasing mass. We postulate that no severe compositional changes resulting from the fallback material should be expected near peak for a wide range of stellar masses and, as such, are unable to explain the extreme helium-to-hydrogen line ratios observed in some TDEs. On the other hand, the resulting compositional changes could help explain the presence of nitrogen-rich features, which are currently only detected after peak. When combined with the shape of the light curve, the time evolution of the composition of the fallback material provides a clear method to help constrain the nature of the disrupted star. This will enable a better characterization of the event by helping break the degeneracy between the mass of the star and the mass of the black hole when fitting tidal disruption light curves.

4.1 Introduction

Tidal disruption events (TDEs) offer a way to study both galactic supermassive black holes (SMBHs) and the dense stellar clusters that surround them. In these clusters, each star traces out a complicated orbit under the combined influence of the SMBH and all the other stars. The orbits slowly diffuse as a result of the cumulative effect of

stellar encounters (Magorrian & Tremaine 1999b). There is a chance that one of these interactions will rapidly shift a star onto a nearly radial orbit, bringing it close to the SMBH. If a star wanders too close to the SMBH it can be violently ripped apart by the SMBH's tidal field (e.g., Rees 1988a). As a result, for a full disruption, about half of the disrupted material eventually falls back and accretes onto the SMBH. This accretion is expected to power a flare that contains vital information about the disruption and can be used to constrain the properties of the SMBH and the disrupted object (Frank & Rees 1976b).

The disruption of stars by SMBHs has been linked to tens of flares in the cores of previously quiescent galaxies (Auchettl et al. 2017a; Komossa 2015a). Transient surveys such as the Palomar Transient Factory (PTF), the All-Sky Automated Survey for Supernovae (ASAS-SN) and the Panoramic Survey Telescope and Rapid Response System (Pan-STARRS) are now finding increasing numbers of these events, especially at early times (Arcavi et al. 2014b; Holoien et al. 2014b; Gezari et al. 2012a). By capturing the rise, peak, and decay of the flares, and with the addition of spectroscopic information, these events are starting to provide significant information about the underlying mechanisms (e.g., Guillochon et al. 2014a).

Modeling TDEs properly requires a prediction of the rate of mass return to the SMBH after a disruption. While previous numerical results have provided reasonably precise models for the fallback resulting from the disruption of stars (e.g., Guillochon & Ramirez-Ruiz 2013a), they are incomplete in that they do not directly examine the predicted compositional changes.[17] Additionally, many previous studies have focused

[17]Except for the specific case of a helium white dwarf with hydrogen envelope (Law-Smith et al.

on stars of a single structural profile, usually selected to match the Sun. However, typical stellar mass functions in TDE host galaxies predict that tidal disruptions should commonly involve evolved main sequence stars (Arcavi et al. 2014b; French et al. 2016b, 2017b; Law-Smith et al. 2017c; Graur et al. 2017b) whose internal structures are very diverse.

Given that the accretion time is inferred to be significantly shorter than the period of the returning debris in most events, the fallback rate is expected to track the flare luminosity relatively closely (Evans & Kochanek 1989a; Strubbe & Quataert 2009a; Ramirez-Ruiz & Rosswog 2009; Guillochon et al. 2014a). As the number of observed disruptions increases, and as the cadence and quality of data continues to improve, it has become increasingly important to improve models of the fallback material for disruptions of all kinds.

The presence or absence of particular emission line features in the spectra of TDEs might be used as a probe of the nature of the disrupted star (Wyrzykowski et al. 2017; Cenko et al. 2016; Brown et al. 2018, 2017, 2016a; Holoien et al. 2016a,c; Leloudas et al. 2016; Merloni et al. 2015; Brown et al. 2015; Holoien et al. 2014b; Arcavi et al. 2014b; Cenko et al. 2012b; Saxton et al. 2012b; Gezari et al. 2012a). Motivated by this, in this paper, we expand upon work by Kochanek (2016a) to further characterize the rate of fallback and, in particular, the composition of the fallback debris. Our results predict what happens when stars of different masses and evolutionary states are tidally disrupted, and what composition a distant observer might be able to infer as the signature of such events.

2017a).

In Section 7.2, we briefly review the calculation of the mass accretion rate, $\dot{M}$, onto the SMBH, originally derived by Lodato et al. (2009a), and propose a simple generalization that allows $\dot{M}$ to be estimated from realistic stars. In Section 7.3, using this new framework, we present the accretion rate for stars ranging in mass from 0.8–3.0 $M_\odot$ and in evolutionary state from zero-age main sequence to terminal-age main sequence. In Section 7.4, we summarize our findings and discuss how our models can help inform the emission models of tidal disruption events by providing detailed predictions of the abundance of the radiating material.

4.2 Methods

4.2.1 The Mass Accretion Rate

If a star with mass $M_\star$ and radius $R_\star$ is on a parabolic orbit around a SMBH of mass $M_{\rm bh}$ with pericenter distance, $r_{\rm p}$, less than the tidal radius, $r_{\rm t} = R_\star(M_{\rm bh}/M_\star)^{1/3} = R_\star q^{-1/3}$, the star will be tidally disrupted. Here $q \equiv M_\star/M_{\rm bh}$ is the mass ratio.

When a star is disrupted, the debris moves on approximately ballistic trajectories, with a spread in specific orbital energy that is roughly frozen at $r_{\rm t}$. This spread arises because at the time of disruption, the leading portions of the star are deeper in the potential of the SMBH than the trailing portions, which are farther away. The spread in specific energy of the debris, $E_{\rm t}$, can be approximated by taking the Taylor expansion of the SMBH's potential at the star's location:

$$E_{\rm t} = GM_{\rm bh}R_\star/r_{\rm t}^2 = q^{-1/3}E_\star, \tag{4.1}$$

where $E_\star = GM_\star/R_\star$ is the specific self-binding energy of the star. Because most stars that are tidally disrupted in galactic nuclei approach the SMBH on nearly zero energy orbits, E_t determines the fallback timescale for the most tightly bound debris

$$\begin{aligned} t_\mathrm{t} &= \frac{\pi}{M_\star}\left(\frac{M_\mathrm{bh}R_\star^3}{2G}\right)^{1/2} \\ &= 0.1\ \mathrm{yr}\left(\frac{M_\mathrm{bh}}{10^6 M_\odot}\right)^{1/2}\left(\frac{M_\star}{M_\odot}\right)^{-1}\left(\frac{R_\star}{R_\odot}\right)^{3/2}. \end{aligned} \tag{4.2}$$

In order to form an accretion flow, the bound stellar debris must lose a significant amount of energy by viscous dissipation (Guillochon & Ramirez-Ruiz 2015a; Hayasaki et al. 2016; Bonnerot et al. 2016a; Shiokawa et al. 2015). If the viscosity is large enough to allow accretion onto the SMBH on a timescale shorter than t_t, the luminosity of the flare is expected to follow the rate of mass fallback $\dot{M} = (dM/dE)(dE/dt) \propto t^{-5/3}$, where $dM/dE = M_\star/(2E_\mathrm{t})$ for a star on an initially parabolic orbit and $q \ll 1$ (Rees 1988a; Phinney 1989). The $t^{-5/3}$ dependence of TDE light curves relies on the assumption that the specific energy distribution of stellar debris dE/dM is roughly flat with orbital specific energy, which is only valid at late times (Guillochon & Ramirez-Ruiz 2013a). At early times, the assumption of constant dM/dE is incorrect and depends sensitively on the structure of the disrupted star (Lodato et al. 2009a; Ramirez-Ruiz & Rosswog 2009) and the strength of the tidal interaction (Laguna et al. 1993; Guillochon et al. 2009; Guillochon & Ramirez-Ruiz 2013a).

Lodato et al. (2009a) and Kesden (2012a) moved beyond this simple description by constructing models that explicitly calculate the energy distribution of the disrupted stellar debris to $\mathcal{O}(q^{1/3})$ for stars described by a self-gravitating, spherically symmetric,

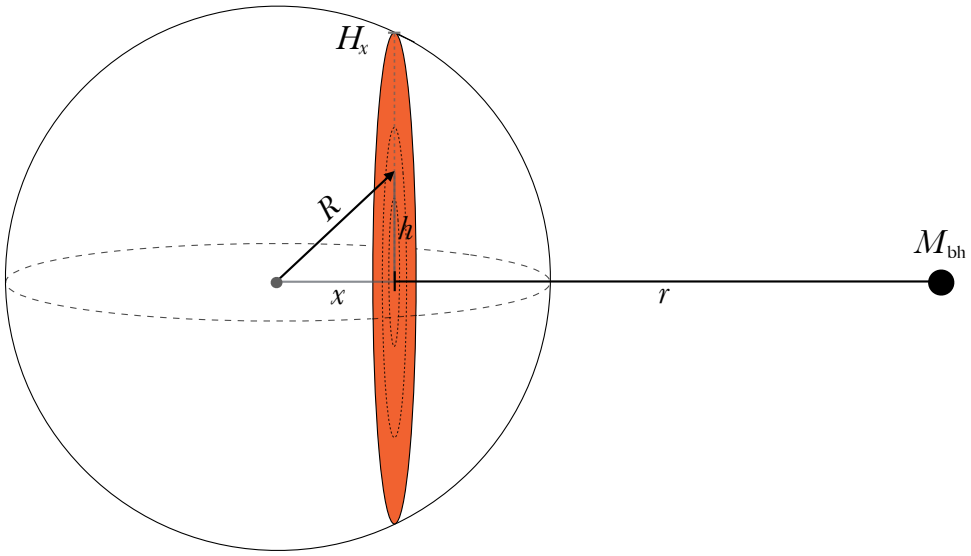

Figure 4.1: The geometry of the disrupted star and how it can be used to calculate dM/dE. The orange slice represents an equal orbital binding energy surface, which can be approximated as an equal fallback time surface. Here x is the distance from the center of the star along the star's orbital plane and H_x is the maximum radius of the particular slice. When calculating the equal arrival time surfaces it is common to neglect any azimuthal or polar deviations. These can be safely neglected given that $(R_\star/r_{\rm t}) = q^{1/3} \ll 1$.

polytropic fluid. By solving the Lane-Emden equation they determined the density profile of the star, which in turn allowed them to calculate dM/dE. In this paper we build on their work and show how their formalism can be easily extended to estimate the rate at which the debris falls back to pericenter and is subsequently accreted for tidally disrupted stars with realistic profiles.

The geometrical setup envisioned here is shown in Figure 4.1. To calculate $\dot{M}$

we begin by using the standard assumption that the star *freezes in* at the moment of disruption at $r_{\rm t}$. The specific binding energy of a fluid element in this case depends on its position, and dM/dE can be expressed in terms of the star's initial density profile $\rho_\star$. The mass of a slice of stellar debris dM, defined here as having the same orbital energy, is found by integrating

$$\frac{dM}{dx} = \int_0^{H_x} \rho_\star(h) 2\pi h \; dh, \tag{4.3}$$

where x is measured from the center of the star, H_x is the radius of the slice at a given x, and h is the rescaled height coordinate. If the orbital period t of a given slice is given in terms of its orbital binding energy dE/dx, then the rate dM/dt at which mass falls back to pericenter can be calculated by numerically integrating equation (4.3). Using this framework, we calculate the accretion rate history for a large number of realistic stars, whose density profiles we generate using the Modules for Experiments in Stellar Astrophysics (MESA) code. The reader is referred to Subsection 4.2.2 for a description of our MESA setup.

The use of this analytic method allows for an extensive study of $\dot{M}$ arising from the disruption of different stars. While this formalism leads to a large reduction in computational expense, it is nonetheless restricted as it relies on the assumption of a spherically symmetric star at the time of disruption. Contrary to what can be predicted by the simple analytical models used in this paper, the rate at which material falls back depends strongly on the strength of the encounter, which can be measured by the penetration factor $\beta \equiv r_{\rm t}/r_{\rm p}$.

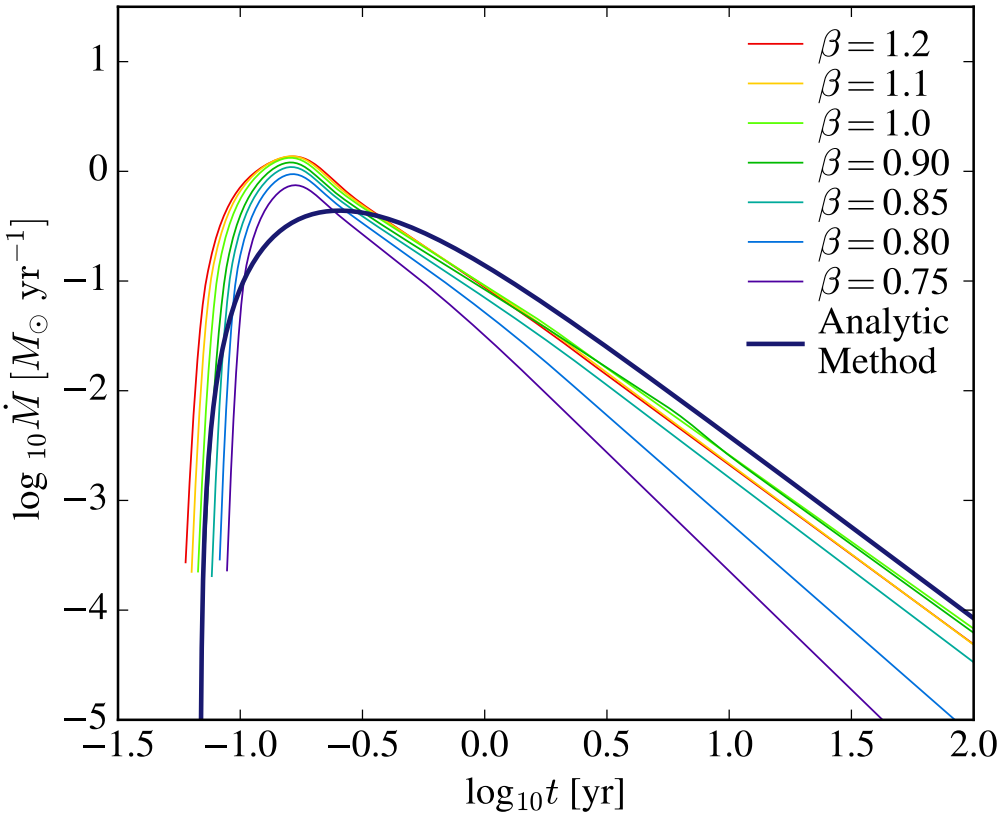

Figure 4.2: The rate of fallback of stellar debris to pericenter as a function of time from the disruption of a $1M_\odot$ star calculated using the analytic framework used in this work (*thick dark blue* line), which assumes a full disruption, compared to those calculated by Guillochon & Ramirez-Ruiz (2013a) using hydrodynamical calculations for different β values (*thin colored* lines). Both calculations use $M_{\rm bh} = 10^6 M_\odot$ and a star that is constructed as a self-gravitating, spherically symmetric, polytropic fluid with $\gamma = 5/3$.

This is because varying β changes the amount of mass lost by the star, which affects the rate at which the liberated stellar debris returns to pericenter (e.g., Law-Smith et al. 2017a). In Figure 4.2 we compare fallback curves calculated using the analytical model (*thick dark blue* line) to those calculated using simulations (*thin colored* lines). For the purpose of comparison, both models use a $1M_\odot$ star with adiabatic index $\gamma = 5/3$ and a $10^6 M_\odot$ SMBH. We find that the broad features of $\dot{M}$ are reasonably well captured by the simple model (the same holds true for stars constructed with $\gamma = 4/3$), as also argued by Lodato et al. (2009a) and Kesden (2012a). This fact is extremely powerful in that it permits a reasonable characterization of TDE signatures without the need to run many computationally expensive simulations on the large set of stars we study here.

What is more, for a fixed β, the time evolution of the forces applied is identical, regardless of the ratio of the star's mass to the mass of the SMBH. This is because the ratio of the time the star takes to cross pericenter to the star's own dynamical time depends only on β. Therefore, as long as $q \ll 1$, the tidal disruption problem is self-similar, and our results can be scaled to predict how the time (Equation 4.2) of peak accretion rate, $t_{\rm peak}$, and its corresponding magnitude $\dot{M}_{\rm peak}$ change with $M_{\rm bh}$, $M_\star$ and $R_\star$:

$$\dot{M}_{\rm peak} \propto M_{\rm bh}^{-1/2} M_\star^2 R_\star^{-3/2}, \tag{4.4}$$

and

$$t_{\rm peak} \propto M_{\rm bh}^{1/2} M_\star^{-1} R_\star^{3/2}. \tag{4.5}$$

This fact is extremely powerful in that it permits us to completely characterize the properties of a disruption of a given star with one calculation. An exception to these simple scalings is if the star penetrates deeply enough such that $r_{\rm p}$ is comparable to the Schwarzschild radius $r_{\rm g}$. In this case, general relativistic effects can alter the outcome, especially if the black hole is spinning (Laguna et al. 1993; Kesden 2012a).

We remind the reader that the exact value of the time of peak accretion rate $t_{\rm peak}$ and its corresponding magnitude $\dot{M}_{\rm peak}$ are not precisely determined. Most of these differences arise from how the problem was originally formulated, in which the star's self-gravity is ignored, and only the spread in binding energy across the star at pericenter is assumed to be important to determining $\dot{M}$. Our primary goal in this paper is to develop a robust formalism for calculating the rate of fallback and its associated chemical composition as well as conducting a preliminary survey of the key stellar evolution parameters associated with this problem. The formalism presented in this section is well suited to this goal.

4.2.2 Stellar Models

We use the open source MESA code (Paxton et al. 2011) to calculate the structure and composition of the stars that will be disrupted. We generated 192 solar metallicity stellar profiles ranging in mass from 0.8–3.0 $M_{\odot}$ and evolutionary state from zero-age main sequence (ZAMS) to near terminal-age main sequence (TAMS). Profiles are spaced in intervals of 0.05 in central hydrogen fraction.

The MESA setup used here is described below.[18] We begin with a pre-MS

[18]Inlists are available upon request.

model, use the `mesa_49` nuclear network with the `jina` rates preference, the Asplund et al. (2009) abundances (X=0.7154, Y=0.2703, and Z=0.0142), and `mixinglengthalpha=2.0`. The final profile, which we call TAMS, is at a central hydrogen fraction of 10^{-3}. Time steps are limited to a maximum change in central hydrogen fraction of 1%.

We consider the mass range of 0.8–3.0 $M_{\odot}$ as stars with masses below 0.8 $M_{\odot}$ will not evolve appreciably over the age of the universe, and stars with masses above 3 $M_{\odot}$, with MS lifetimes $<$ 300 Myr, are unlikely to be disrupted (the relaxation time for most galactic nuclei is $\gg$ 300 Myr).

We do not consider evolved stars for two reasons. First, the contribution of evolved stars to the current and near-future tidal disruption population is expected to be modest (MacLeod et al. 2012a). Second, studies of the tidal disruption of evolved stars such as MacLeod et al. (2012a) have shown that even for large β, giant stars are effective at retaining envelope mass and effectively retaining their cores (where the differences in composition arise from MS and post-MS evolution). In this paper we are interested in the evolved material in the inner-most layers of stars that can be reasonably revealed during a TDE and thus we do not focus on significantly evolved stars.

4.2.3 Salient Model Features

Here we briefly discuss the stellar evolution features that are central to our study; these arise from changes in mass and evolutionary state along the MS. The two main burning processes in MS stars, the p-p chain and the CNO cycle, are highly sensitive to interior temperatures (Kippenhahn et al. 2012) and contribute differently to stars of varying mass. The p-p chain, which increases the abundance of ^{4}He in

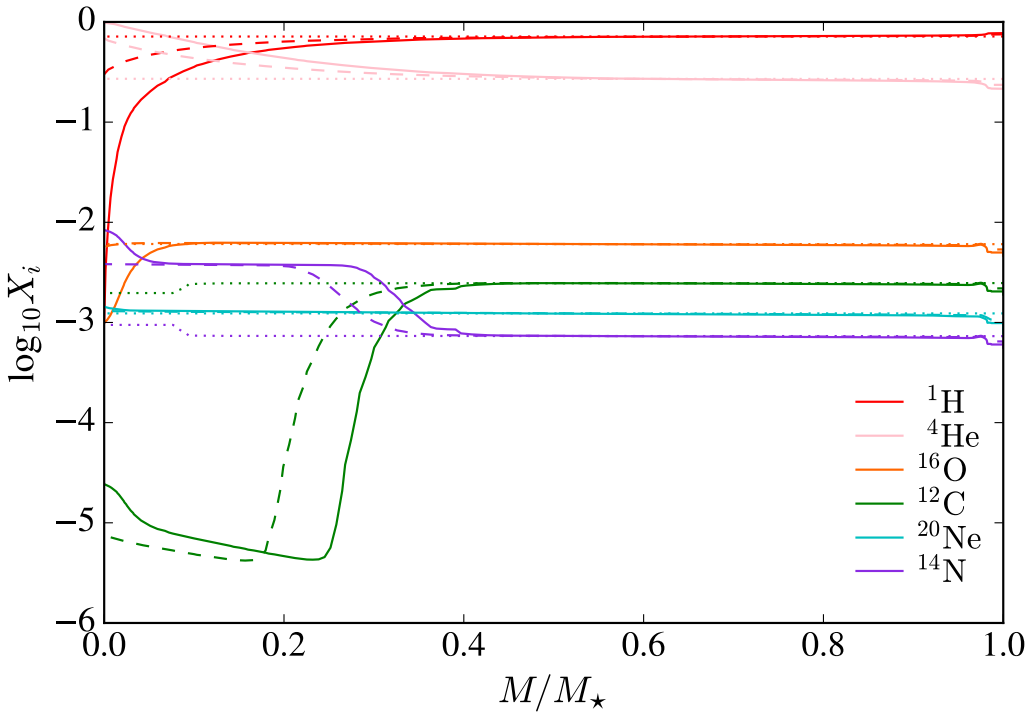

Figure 4.3: Compositional abundance as a function of enclosed mass in a $1M_\odot$ star at three different evolutionary stages during its MS lifetime. In this paper, we characterize evolutionary stages by $f_{\rm H}$, the fraction of central hydrogen that has been burned. Here we show the stellar profiles for $f_{\rm H} = 0.0 = f_{\rm ZAMS}$ (*dotted*), $f_{\rm H} = 0.60$ (*dashed*), and $f_{\rm H} = 0.99$ (*solid*), respectively. A $1M_\odot$ star disrupted at later stages in its evolution should reveal abundance anomalies: an increase in nitrogen and depletion of oxygen, as previously argued by Kochanek (2016a).

stars, roughly dominates for masses $\lesssim 1.5\ M_\odot$. For masses $\gtrsim 1.5\ M_\odot$ the CNO cycle dominates. During the CNO cycle, fusing hydrogen to helium results in an increase (decrease) of ^{14}N (^{16}O) abundance, with ^{12}C acting as a catalyst for the entire cycle. As argued by Kochanek (2016a), strong compositional variations are expected in the fallback material of MS stars. In this paper we trace the abundance variations of the following elements: ^{1}H, ^{4}He, ^{16}O, ^{12}C, ^{20}Ne, and ^{14}N. These elements make up at least 99.6% of each star's total mass. The ^{34}S contribution and abundance ratio is very similar to that of ^{20}Ne and is thus not explicitly shown in this paper. In what follows, we present abundances relative to solar.

As an example, in Figure 4.3 we show the compositional variations along the MS for a $1M_\odot$ star with solar abundance at ZAMS. The differently styled lines correspond to different stellar ages as defined by $f_{\rm H}$, the fraction of central hydrogen burned. A star will have $f_{\rm H} = 0$ at ZAMS and $f_{\rm H} = 0.99$ near the end of its MS lifetime. At ZAMS the star has solar composition (*dotted* lines) and is roughly homogeneous. After 4.8 Gyr (*dashed* lines), when more than half of the central hydrogen has been processed ($f_{\rm H} = 0.60$), the following abundance variations are seen: a significant increase of ^{14}N, a modest increase (decrease) of ^{4}He (^{1}H), a significant decrease of ^{12}C, and a roughly unchanged abundance of ^{20}Ne and ^{16}O. At TAMS (*solid* lines), where most of the central hydrogen has been processed ($f_{\rm H} = 0.99$), a depletion in ^{16}O abundance is also observed. At this late stage, there is also a secondary increase in ^{14}N in the core of the star.

In summary, we see that ^{1}H, ^{4}He and ^{16}O abundances evolve gradually, slowly

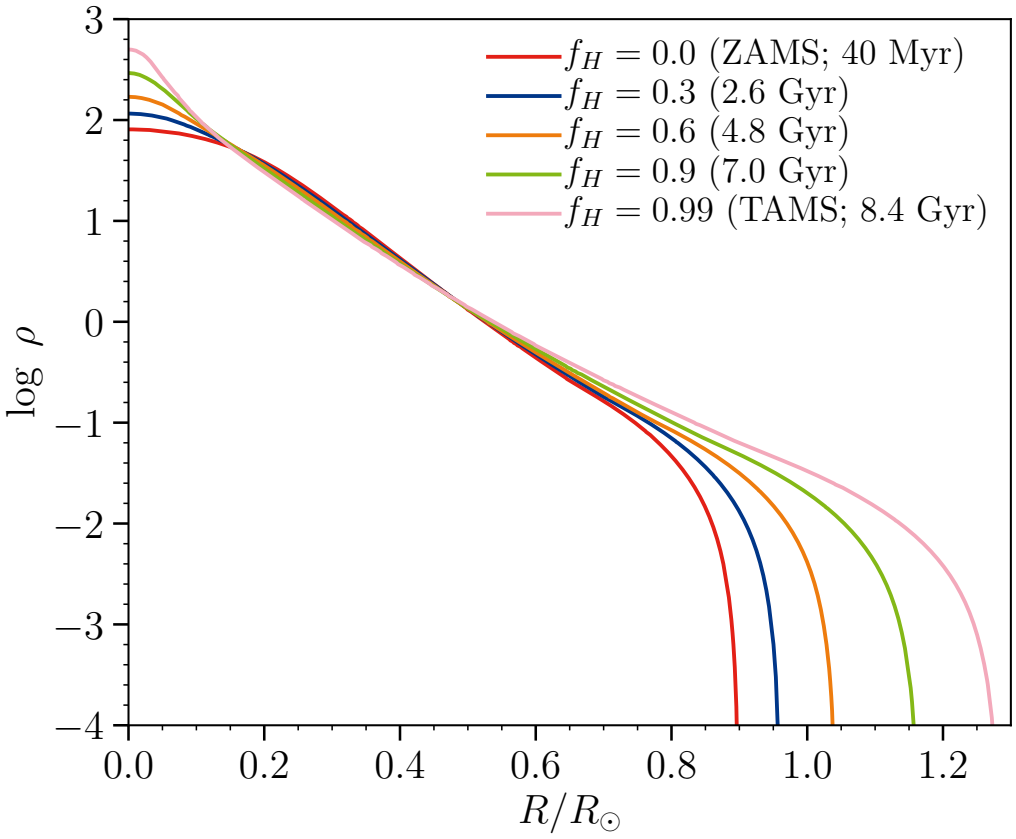

Figure 4.4: Density profiles for a $1M_\odot$ star at different times along its MS evolution. The *red* line corresponds to ZAMS with a central density of 81 g cm^{-3} and the *pink* line corresponds to a central hydrogen fraction of 10^{-3} with a central density of 500 g cm^{-3}. These different density profiles result in different r_t and thus exhibit different vulnerability to disruption.

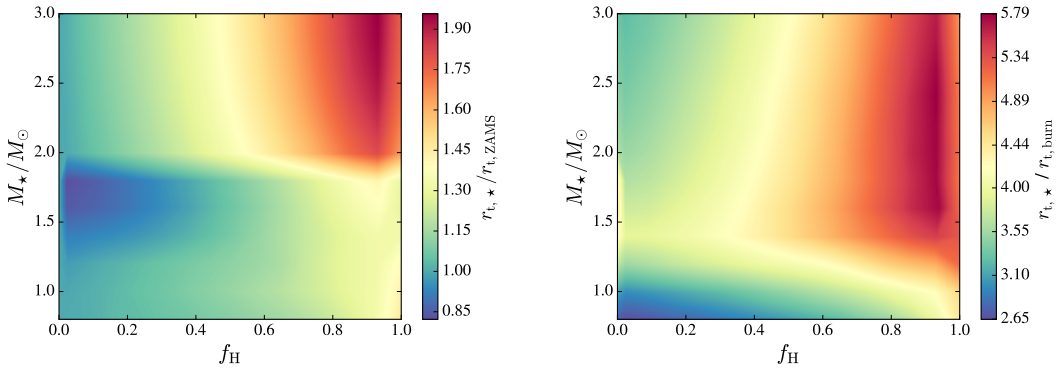

Figure 4.5: In both panels, the color scale shows the tidal radius of the disrupted star. *Left panel*: Plotted are the ratio of the star's tidal radius to the tidal radius of that same star at ZAMS ($f_{\rm H} = 0.0 = f_{\rm ZAMS}$). This shows that the star's vulnerability to disruption increases with age. This effect is stronger for more massive stars. *Right panel:* Plotted are the ratio of the tidal radius to $r_{\rm t,burn}$. Here $r_{\rm t,burn}$ is defined as the tidal radius of the star's core undergoing active nuclear burning, where the specific power from nuclear reactions is greater than 1 erg $\rm g^{-1}s^{-1}$. This shows that all of the stars in our study require deeper encounters to strip mass from their burning regions.

extending to larger parts of the star and encompassing larger radii, while ^{12}C and ^{14}N abundances evolve rapidly across the burning region. All stars follow a similar trend. The most massive star in this study ($3M_\odot$) has, at TAMS, large compositional changes across roughly half of its mass (or about 20% of its radius). As discussed by Kochanek (2016a), in the fallback material from a TDE we expect ^{12}C and ^{14}N abundance anomalies to be more noticeable and appear at earlier times than the other elemental anomalies.

As a star evolves along the MS, its average density, $\bar{\rho}_\star$, decreases and its core density, $\rho_{\rm core}$, increases. This is illustrated in Figure 4.4, where we show the evolution of the density profile for a $1M_\odot$ star with initial solar abundance from ZAMS to TAMS. Since the star's radius increases with age while its mass remains nearly constant, $\bar{\rho}_\star$ decreases with age. The effects of $\bar{\rho}_\star$ on the star's vulnerability to tidal deformations

can be readily seen by rewriting $r_{\rm t}$ as $r_{\rm t} \cong M_{\rm bh}^{1/3} \bar{\rho}_{\star}^{-1/3}$. This scaling implies that as the star evolves, it becomes progressively more vulnerable to tidal deformations and mass loss. However, this scaling is unable to accurately capture the exact impact parameter required to fully disrupt a star. This is because as the star evolves a denser core, a surviving core is likely to persist for a disruption at $r_{\rm t}$ ($\beta = 1$), which is the penetration factor assumed for the analytical calculations. Nonetheless, we expect the time and magnitude of the peak accretion rate to be reasonably well captured by the simple formalism described here.

4.3 The Disruption of Evolved MS Stars

4.3.1 Tidal Vulnerability

Here we analyze how the tidal radius, $r_{\rm t,\star}$, evolves with stellar mass and age along the MS for the stars in our study. The left panel of Figure 4.5 shows $r_{\rm t,\star}$ normalized to the tidal radius of the same star at ZAMS, $r_{\rm t,ZAMS}$. We plot this ratio as a function of $f_{\rm H}$, the fraction of central hydrogen burned, and stellar mass $M_{\star}$. As expected, we find that the tidal radius increases with age and evolves more dramatically with $f_{\rm H}$ throughout the lifetime of more massive stars. For example, the tidal radius of a $3 M_{\odot}$ star increases by roughly a factor of two over its MS lifetime. As stars move along the MS, they become progressively more vulnerable to tidal dissipation and mass stripping.

Next, we discuss how the vulnerability of regions with processed element abundances compares to that of the entire star. The right panel of Figure 4.5 shows the ratio of $r_{\rm t,\star}$ to $r_{\rm t,burn}$, where $r_{\rm t,burn}$ is defined as the tidal radius of material within the re-

gions of a star that exhibit active nuclear burning. This region of active nuclear burning is defined to be where the specific power from nuclear reactions is greater than 1 erg $g^{-1}s^{-1}$. This is a consistent way for defining the burning region throughout all of the stellar profiles calculated here. As expected, this region is located at small radii where the density is much higher than $\bar{\rho}_\star^{-1/3}$ and thus deeper penetrations are required in order to observe the evolved element abundances in the fallback material. Also, as this region is located within the innermost layers of the star, the processed elements will be revealed in the fallback material only at later times.

4.3.2 The Disruption of a Sun-like Star

Figure 4.6 shows the mass fallback rate arising from the full disruption of a $1M_\odot$ star at two different evolutionary states: at ZAMS (*dotted* lines) and after 4.8 Gyr (*dashed* lines), when more than half of the central hydrogen has been processed ($f_{\rm H} = 0.60$). These curves are normalized to the peak fallback rate and peak time of the corresponding ZAMS star: $\dot{M}_{\rm peak,ZAMS}$ and $t_{\rm peak,ZAMS}$, respectively. The compositions of the stars before disruption are shown in Figure 4.3 as *dotted* (ZAMS) and *dashed* ($f_{\rm H} = 0.60$) lines. The disruption of the TAMS $1M_\odot$ star, whose composition is shown by the *solid* lines in Figure 4.3, is expected to be similar in shape to the disruption of the $f_{\rm H} = 0.60$ star, with an enhancement in ^{14}N and depletion in ^{12}C.

The smooth behavior of the fallback rates for all the plotted elements during the disruption of the ZAMS star (*dotted* lines in Figure 4.3) is the result of the nearly homogeneous elemental composition within the star. The fallback rates for the $f_{\rm H} = 0.60$ star (*dashed* lines in Figure 4.3), on the other hand, contain information about the

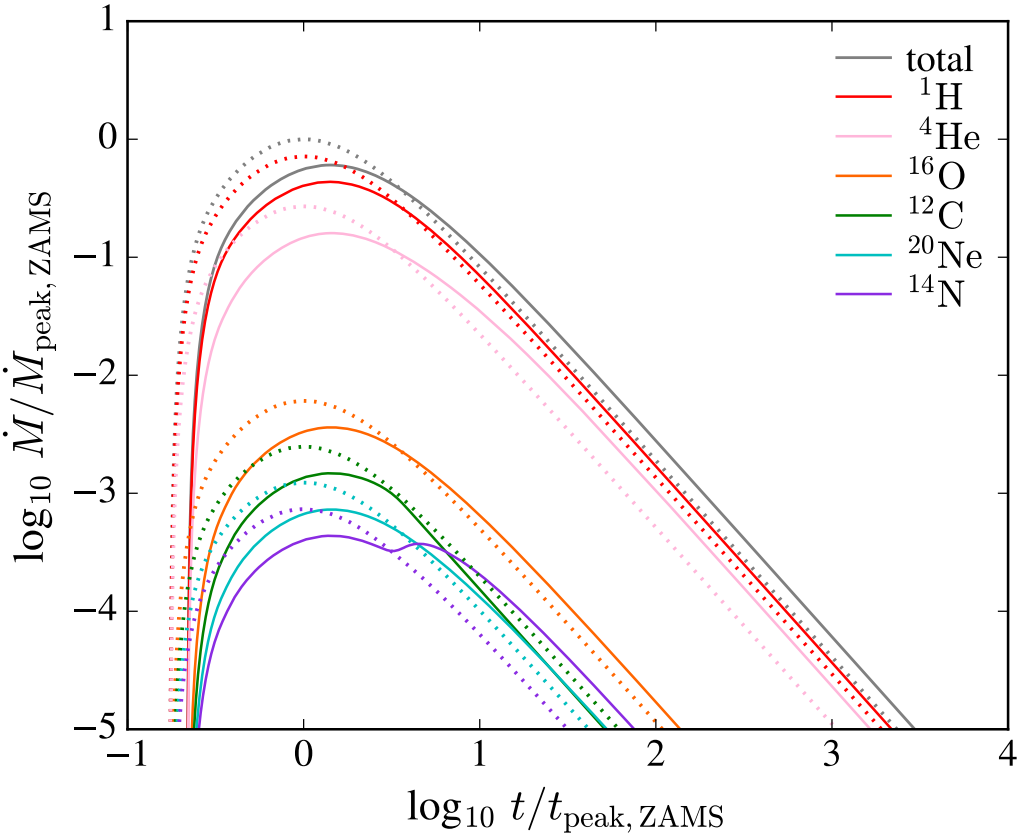

Figure 4.6: Mass fallback rates for elements that make up 99.6% of the mass of a $1M_{\odot}$ tidally disrupted star at two different evolutionary stages. The star aged nearly 5 Gyr from the *dotted* lines ($f_{\rm H} = 0.0 = f_{\rm ZAMS}$) to the *solid* lines ($f_{\rm H} = 0.60$). $\dot{M}$ for the total mass of the star is shown by the *gray* curves. All curves are normalized to $\dot{M}_{\rm peak}$ and $t_{\rm peak}$ for the corresponding ZAMS star. The main changes in fallback rates as the star evolves along the MS are an increase in nitrogen and a decrease in carbon after $t_{\rm peak}$ due to CNO activity in the core.

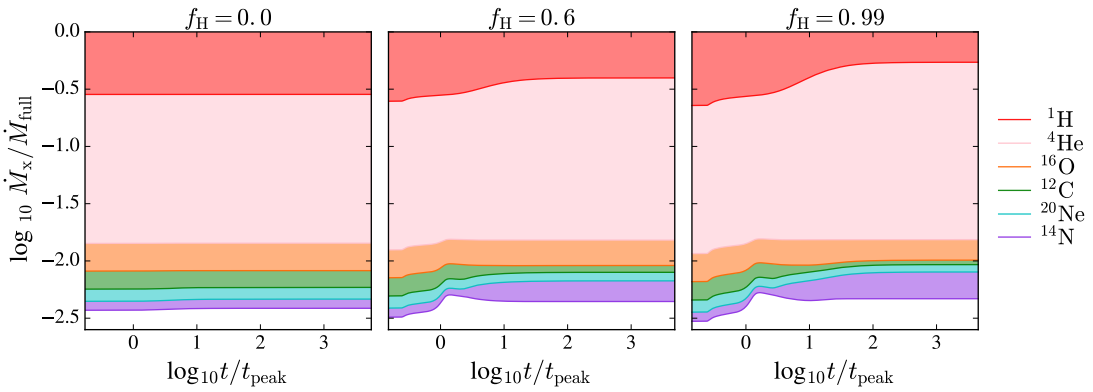

Figure 4.7: The fallback rate for different elements, $\dot{M}_{\rm X}$, following the disruption of a $1M_{\odot}$ star at three different evolutionary stages. The *left* and *center* panels correspond to the *dotted* and *solid* lines shown in Figure 4.6, respectively. The *right* panel shows $\dot{M}$ for the same star but at $f_{\rm H} = 0.99$, which corresponds to an age of 8.3 Gyr. Time is in units of $t_{\rm peak}$. As the star ages we see an increase in nitrogen and a decrease in carbon abundance but only after $t_{\rm peak}$.

varying nature of its elemental composition. In the fallback rates we can see an obvious increase in ^{14}N, decrease in ^{12}C, and a slight increase in ^{4}He, which is consistent with the compositional structure of the star before disruption. These results are in agreement with Kochanek (2016a). We note that the fallback curves for the $f_{\rm H} = 0.60$ star have no abundance variations at $t \lesssim t_{\rm peak}$. These compositional anomalies might provide insight into the nature of the progenitor star near or after the most luminous time of the tidal disruption flare.

In Figure 4.7 we show the fractional contribution to the total fallback rate arising from each element during the disruption of a $1M_{\odot}$ star at three different evolutionary stages. From left to right, these panels correspond to the ZAMS (*dotted*), $f_{\rm H} = 0.60$ (*dashed*), and TAMS (*solid*) composition profiles in Figure 4.3, respectively. In each panel we calculate the ratio of the fallback rate for each element, $\dot{M}_{\rm X}$, to the total mass fallback rate, $\dot{M}_{\rm full}$.

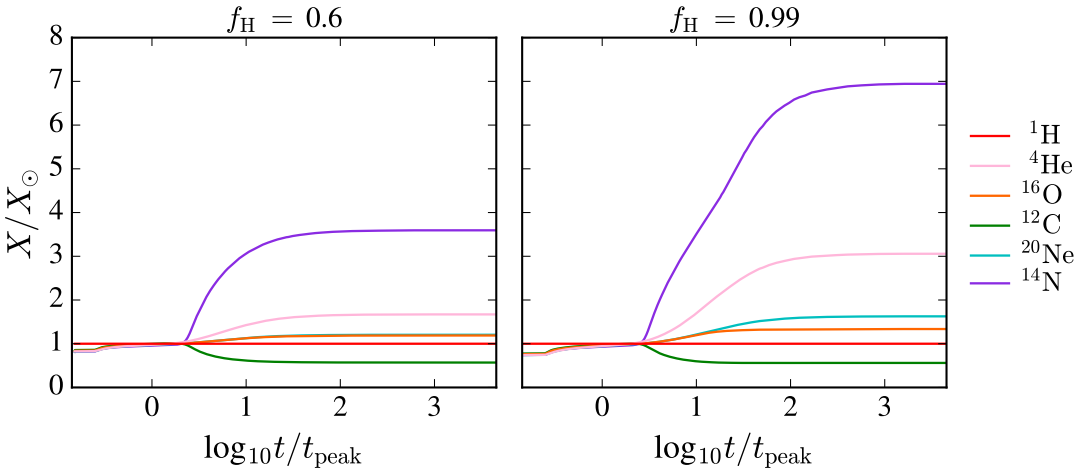

Figure 4.8: Elemental abundance of the fallback material relative to solar following the disruption of a $1M_\odot$ at two different evolutionary stages: $f_{\rm H} = 0.60$ (*left* panel) and TAMS (*right* panel). A rapid evolution of ^{14}N and ^{12}C abundance relative to the other elements is clearly seen. The solar ratios clearly illustrate the significance of the variations in the abundances of ^{16}O, ^{4}He, and ^{20}Ne.

For the disruption of a $1M_\odot$ star, it might be challenging to distinguish its evolutionary stage using spectral information if it is only obtained at $t \lesssim t_{\rm peak}$ (although the exact values of $\dot{M}_{\rm peak}$ and $t_{\rm peak}$ are expected to be distinct; Figure 4.12). This is, however, not the case after $t_{\rm peak}$.

Figure 4.8 shows the abundance of the fallback material relative to solar following the disruption of a $1M_\odot$ at two different evolutionary stages: $f_{\rm H} = 0.60$ (*left* panel) and TAMS (*right* panel). Elemental abundances relative to solar are calculated here using

$$\frac{X}{X_\odot} = \frac{\dot{M}_{\rm X}/\dot{M}_{\rm H}}{M_{\rm X}/M_{\rm H,\odot}}, \tag{4.6}$$

where $\dot{M}_{\rm X}$ is the fallback rate for a selected element, $\dot{M}_{\rm H}$ is the fallback rate of ^{1}H, and $M_{\rm X}/M_{\rm H,\odot}$ is the abundance mass ratio relative to solar of element X. The disruptions

of a $f_{\rm H} = 0.60$ and a TAMS star each show a significant increase in ^{14}N and ^{4}He after $t_{\rm peak}$. As expected, these features are more prominent for the TAMS star. Near $t = 10t_{\rm peak}$, Figure 4.8 shows steeper abundance gradients in the *right* panel compared to the *left* in all elements except ^{12}C. We note that these values are relative to ^{1}H. This is important in the case of ^{16}O and ^{20}Ne where we see an increase in their abundance. This is because while ^{1}H is depleted at every evolutionary stage, ^{16}O and ^{20}Ne abundance remain relatively constant for a star of this mass, which results in higher solar ratios. However, this behavior is also altered by the mass of the star as we discuss in the following section.

4.3.3 Disruption of MS stars

For reasons discussed previously, it seems likely that the evolutionary state of a star might be revealed by charting the compositional evolution of the fallback material, which might be inferred from particular features in the spectra of the resulting luminous flare. The association of a significant fraction of TDEs with post-starburst galaxies (Arcavi et al. 2014b; French et al. 2016b, 2017b; Law-Smith et al. 2017c) has suggested the likely presence of evolved stars in the nuclei of TDE hosts, or at least a subset thereof. Much of our effort in this section will thus be dedicated to determining the state of the fallback material after the tidal disruption of stars of a wide range of ages and masses.

In Figure 4.9 we show the relative abundances of the fallback material for three representative MS star disruptions. The *first row* of panels shows the abundance of the fallback material for a $0.8M_{\odot}$ star tidally disrupted at three different evolutionary

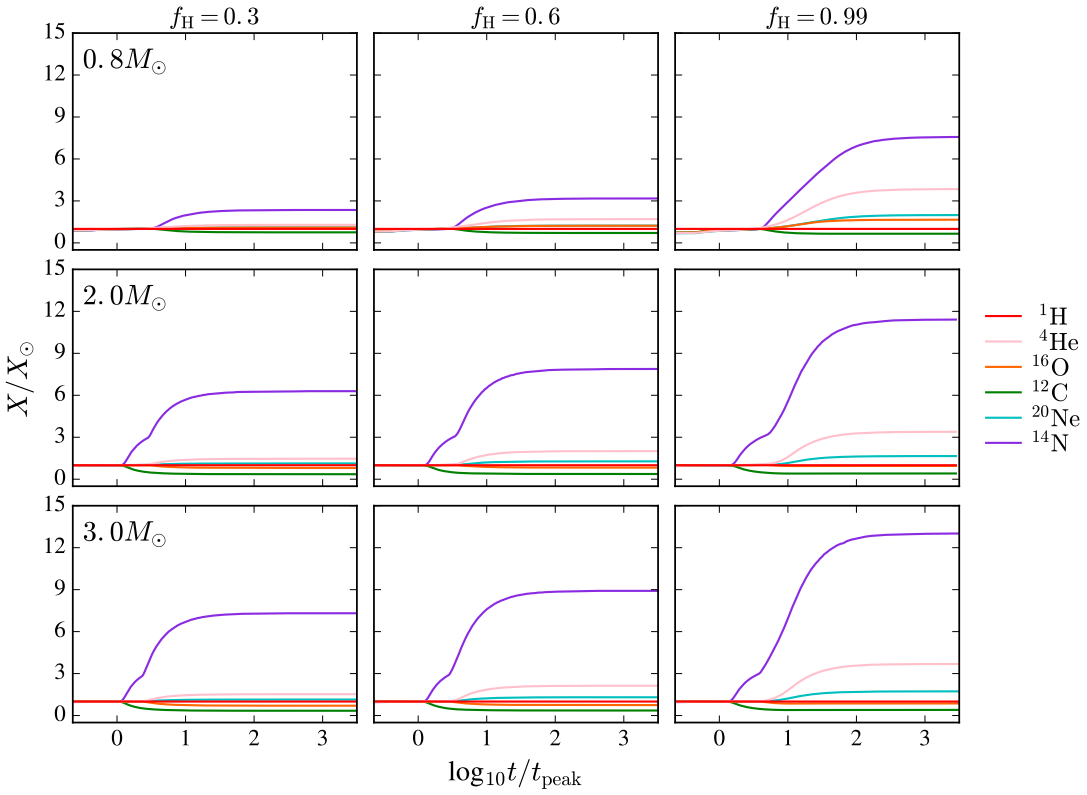

Figure 4.9: The relative abundance of stellar debris as a function of fallback time arising from the disruption of $0.8M_\odot$ (*top* row), $2.0M_\odot$ (*middle* row) and $3.0M_\odot$ (*bottom* row) stars at three different evolutionary stages ($f_{\rm H} = 0.3, 0.6$ and 0.99). The change in abundance relative to solar is observed to increase with mass and age but only after $t_{\rm peak}$. These anomalies appear at earlier times for higher mass stars.

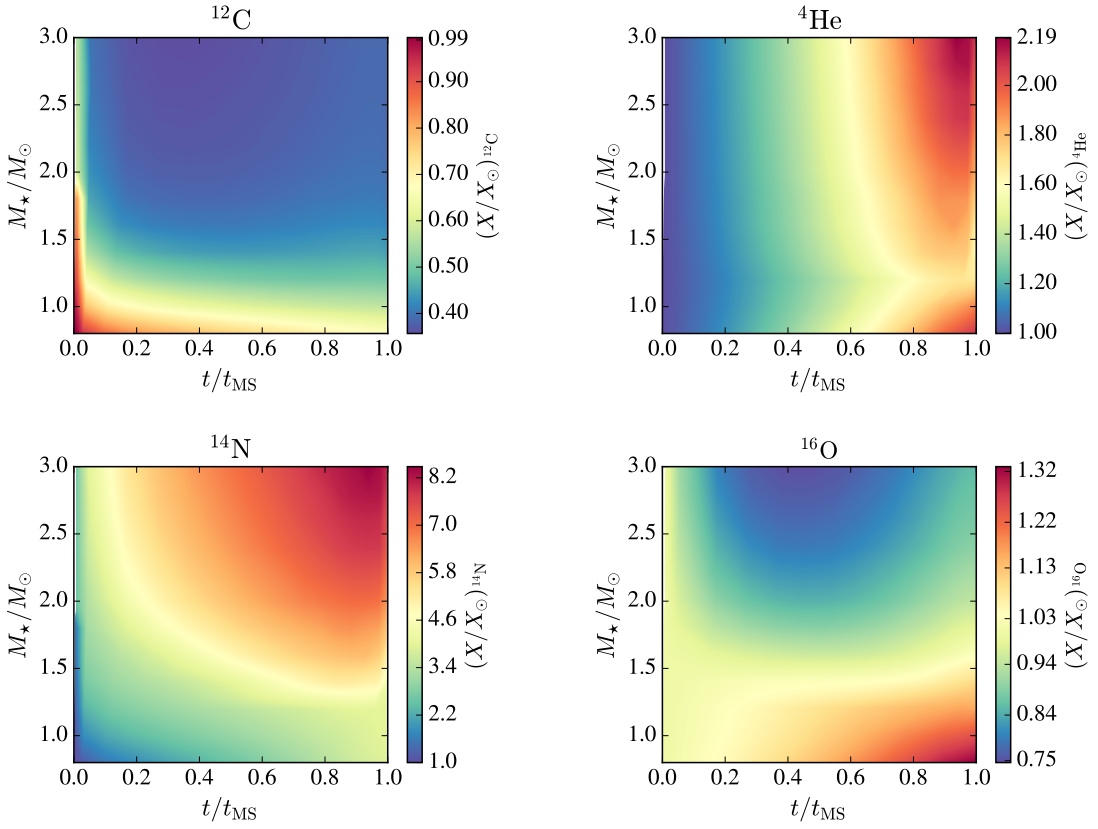

Figure 4.10: Elemental abundances relative to solar at the time the mass fallback rate has reached one tenth of its peak value, $t_{0.1} > t_{\rm peak}$, for all of the stellar masses and ages in our sample. Elements of interest are ^{12}C, ^{4}He, ^{14}N and ^{16}O. Values are shown as a function of the star's fractional main sequence lifetime and stellar mass. We find carbon abundances to be more indicative of stellar mass for $M_\star \lesssim 1.5 M_\odot$, while helium abundances are correlated with stellar age for all masses. $(X/X_\odot)_{^{14}\rm N} \gtrsim 5.0$ occurs only for masses greater than $1.5 M_\odot$ and develops early in the star's evolution. We also find oxygen abundances to be primarily stellar mass dependent.

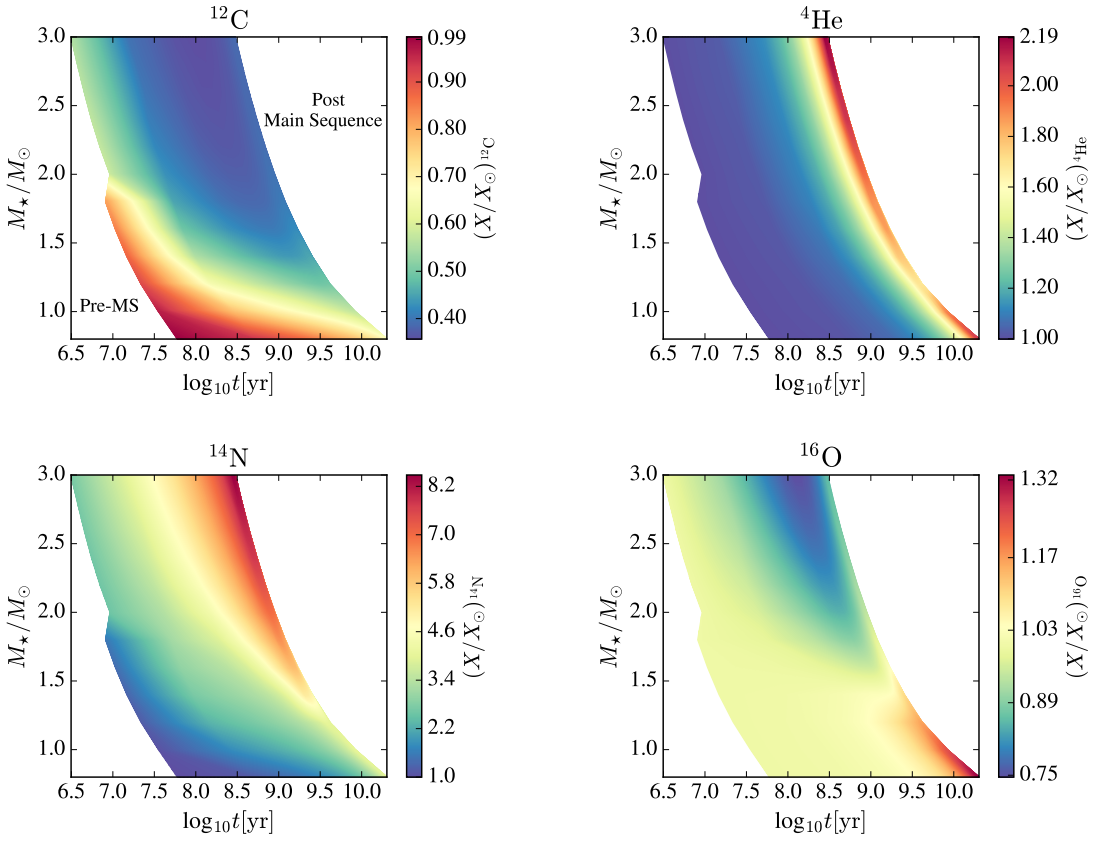

Figure 4.11: Same as Figure 4.10 but presented with stellar age in years (x-axis). The white regions correspond to pre-MS (*left*) or post-MS (*right*).

stages: $f_{\rm H} = 0.3$, $f_{\rm H} = 0.6$, and $f_{\rm H} = 0.99$. The abundances shown are similar to those shown in Figure 4.8 for a $1M_{\odot}$ star. At these low masses, we expect the abundance anomalies to be present in the fallback material at a few times $t_{\rm peak}$.

The *second* row of panels in Figure 4.9 shows the relative abundances of the fallback material for a disrupted $2M_{\odot}$ star. The abundance patterns are broadly similar to those seen for the $0.8M_{\odot}$ and $1M_{\odot}$ stellar disruptions. However, there are three main differences. First, in contrast to the observed increase of ^{16}O seen in the $0.8M_{\odot}$ and $1.0M_{\odot}$ disruptions, a significant decrease in ^{16}O abundance is observed. This is an indication of the increased CNO activity in the $2M_{\odot}$ star. Second, two distinct bumps are seen in the evolution of the ^{14}N abundance, contrary to its steady increase in the smaller mass disruptions. The first increase in ^{14}N abundance (and the corresponding ^{12}C depletion) is due to the local maximum of CNO burning that is located at roughly 20% of the star's radius. There is also significant CNO and p-p chain activity in the star's core, which is revealed at later times in the fallback material, and leads to the relatively delayed increase in ^{4}He and ^{20}Ne, the corresponding decrease of ^{16}O, and a secondary increase in ^{14}N. Third, abundance variations are observed significantly closer to $t_{\rm peak}$ in the $2M_{\odot}$ disruptions than in the $0.8M_{\odot}$ disruptions. This is a result of the more extended burning region within the star, whose material is revealed at earlier times following the disruption.

In the *bottom* row of panels in Figure 4.9 we show the composition of the fallback material following the disruption of a $3M_{\odot}$ star. The abundance variations in these fallback curves closely resemble those for the $2M_{\odot}$ star, but with larger variations

appearing at earlier times. The abundance variations presented in Figure 4.9 for the few representative stars accurately describe the overall trends in our sample. These trends are illustrated in Figure 4.10, in which various elemental abundances are shown at the time that the mass fallback rate has reached one tenth of its peak value, $t_{0.1} > t_{\rm peak}$.

The fallback abundances at $t_{0.1}$ are plotted in Figure 4.10 as a function of the star's fractional main sequence lifetime, $t/t_{\rm MS}$, and stellar mass. In Figure 4.11 we show the same abundance values as in Figure 4.10 but presented with the evolutionary age of the star in years. Some key points should be emphasized. We find carbon decrements to be indicative of stellar mass, while helium enhancements are indicative of age. $(X/X_{\odot})_{^{14}\rm N} \gtrsim 5.0$ occurs only for masses greater than $1.5M_{\odot}$ and develops early in the star's evolution. This is due to the enhanced CNO activity inside the more massive stars in our sample. We also find oxygen abundances to be primarily dependent on stellar mass.

The processes discussed here suggest that TDEs may have a more complex spectrum and time-structure than simple models suggest. The effects are especially interesting when the accretion rate is high, as this gives rise to high luminosities, and thus can more readily offer clues to the nature of the disrupted star. The specific values of $\dot{M}_{\rm peak}$ and $t_{\rm peak}$ can further aid in distinguishing the properties of the progenitor star before disruption. This is illustrated in Figure 4.12 where we show abundances of carbon, helium, nitrogen and oxygen (relative to solar) in the fallback debris as a function of $\dot{M}_{\rm peak}$ and $t_{\rm peak}$. Each panel in Figure 4.12 corresponds to a different element, the different lines correspond to different stars in our study ($0.8M_{\odot}$, $1.0M_{\odot}$,

$1.2M_\odot$, $1.4M_\odot$, $2.0M_\odot$, and $3.0M_\odot$), the points are different stages in the stars' evolution on the MS (roughly equally spaced in time), and the color of the points is the abundance of the fallback debris at the time that $\dot{M}$ falls to one tenth of its peak value, $t_{0.1}$. We used the fitting formulas presented in Guillochon & Ramirez-Ruiz (2013a), which give $\dot{M}_{\rm peak}$ and $t_{\rm peak}$ given β, γ, $M_\star$, and $R_\star$. We used $\gamma = 4/3$ and its corresponding penetration factor for full disruption ($\beta = 1.85$) given by Guillochon & Ramirez-Ruiz (2013a). The values of $M_\star$ and $R_\star$ were taken from the MESA profiles and we have assumed $M_{\rm bh} = 10^6 M_\odot$ (the reader is referred to equations 4.4 and 4.5 for the scalings of $\dot{M}_{\rm peak}$ and $t_{\rm peak}$ with $M_{\rm bh}$, respectively). The abundance values are the same as in Figure 4.10.

The variation in elemental abundances is accompanied by a wide range in $\dot{M}_{\rm peak}$ and a moderate range in $t_{\rm peak}$; a combination of these different pieces of information can help characterize the progenitor stars of TDEs. For example, the disruption of a $3M_\odot$ star has similar $t_{\rm peak}$ values to that of a $2M_\odot$ star. While their ^{12}C and ^{16}O abundances are very similar, the $3M_\odot$ star's disruption results in a higher abundance in ^{14}N and ^{4}He at every stage in its evolution, along with a higher $\dot{M}_{\rm peak}$. In the lower mass stars (0.8–$1.4M_\odot$) there are many degeneracies in $\dot{M}_{\rm peak}$ and $t_{\rm peak}$ values. Here, the ^{14}N, ^{16}O, and ^{4}He abundances are similar (over the age of the universe) but the ^{12}C abundances vary at the early stages in these stars' MS evolution. Compositional information, combined with reprocessing and radiative transfer calculations (e.g., Roth et al. 2016), can thus be used to discern the stellar mass and age of the disrupted star.

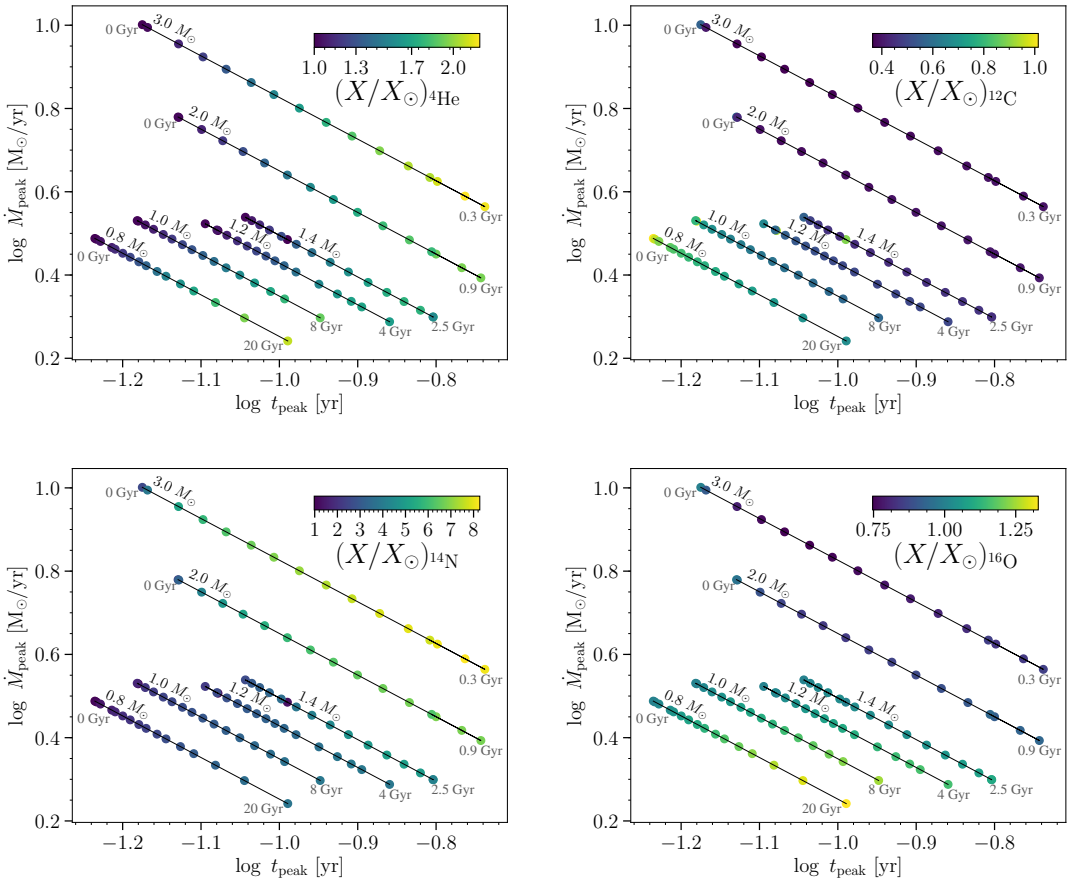

Figure 4.12: Fallback abundance at $t_{0.1}$ of ^{4}He, ^{12}C, ^{14}N, and ^{16}O (clockwise from top left) for the disruption (by a $M_{\rm bh} = 10^6 M_\odot$ SMBH) of $0.8M_\odot$, $1M_\odot$, $1.2M_\odot$, $1.4M_\odot$, $2.0M_\odot$, and $3.0M_\odot$ stars along their MS evolution. Abundances are at $t_{0.1}$, but points are placed at $\dot{M}_{\rm peak}$ and $t_{\rm peak}$ for the disruption of each star. Abundances are quoted relative to solar. Points are roughly equally spaced in time for each mass, with the top-left-most point being ZAMS and the bottom-right-most point being TAMS. (This is not strictly true for the ZAMS point of the $1M_\odot$, $1.2M_\odot$, and $1.4M_\odot$ stars as their radius slightly decreases at the very beginning of their MESA evolution, but all other points for these stars proceed left to right with age as the star subsequently evolves.)

4.4 Discussion

4.4.1 Summary of Key Results

Motivated by the work of Kochanek (2016a), we have modeled the tidal disruption of MS stars of varying mass and age. We adopted the analytic formalism originally presented in Lodato et al. (2009a) to study, for the first time, the time evolution of the composition of the fallback debris onto the SMBH. We compared the analytic method to hydrodynamic simulations in Figure 4.2 and found, similarly to Lodato et al. (2009a) and Kesden (2012a), that the broad features of the fallback curves are reasonably well captured by it.[19] We quantify the variations in composition arising from the disruption of 12 different stars with masses of 0.8–3.0$M_\odot$ at 16 different evolutionary stages along the MS. The main results of our study are the following.

1. We predict an increase in nitrogen and depletion in carbon abundance in the fallback debris with MS evolution for all stars in our sample (in agreement with Kochanek 2016a). We find a decrease in oxygen with MS evolution for $M_\star \gtrsim 1.5M_\odot$, and an increase for $M_\star < 1.5M_\odot$.

2. For all of the TDEs modeled in this study, we find that the time during the fallback rate curve when anomalous abundance features are present, $t_{\rm burn}$, is *after* the time of time of peak fallback rate $t_{\rm peak}$.

3. Abundance variations are more significant and $t_{\rm burn}/t_{\rm peak}$ is smaller for stars of larger mass.

[19] This work should, however, be taken only as a guide for the expected compositional trends in the fallback material, as hydrodynamical simulations are needed to accurately predict the evolution and characteristics of the flares.

4. Some key variations in the compositional evolution are highlighted, along with the types of observation that would help to discriminate between different stellar disruptions. In particular, we find carbon and oxygen abundances to strongly dependent on stellar mass for $M_\star \lesssim 2M_\odot$, while helium abundances are found to be correlated with stellar age for all masses. $(X/X_\odot)_{^{14}\mathrm{N}} \gtrsim 5.0$ occurs only for masses greater than $1.5M_\odot$ and is observed early in the star's evolution.

5. Studying the compositional variation in the fallback debris provides a clear method for inferring the properties of the progenitor star before disruption.

4.4.2 Implications for Observations and Models

It is evident from the results described above that the evolution of the interior structure of stars during their MS lifetimes is very rich. Even in the simplest case of a Sun-like star, complex behavior with multiple abundance transitions in the fallback material may be observed. The resulting TDE spectra are expected to depend fairly strongly on the abundance properties of the fallback material (Roth et al. 2016). This implies that if one can be very specific about the times at which we expect to see such transitions in the observed emission, one can better constrain the properties of the disrupted star.

Motivated by this, in Figure 4.13 we plot the fallback time t_{burn}, relative to t_{peak}, at which we expect to see anomalous abundance variations. Here t_{burn} is defined as the time at which the abundances of ^{12}C and ^{14}N in the fallback material, as presented in Figures 4.8 and 4.9, both deviate from unity. $t_{\mathrm{burn}}/t_{\mathrm{peak}}$ is shown in Figure 4.13 as

a function of stellar mass and age (characterized by $f_{\rm H}$). At fixed $f_{\rm H}$ we see that non-solar abundances in the fallback debris begin to appear systemically closer to $t_{\rm peak}$ as stellar mass increases. For the $3.0M_{\odot}$ star, $t_{\rm burn} \approx 1.2t_{\rm peak}$ for $f_{\rm H} \lesssim 0.3$. For constant $M_{\star}$, $t_{\rm burn}/t_{\rm peak}$ increases mildly with $f_{\rm H}$ for stars with $M_{\star} > 1.6M_{\odot}$. For stars with $M_{\star} < 1.6M_{\odot}$, this ratio remains fairly constant throughout the star's evolution. In summary, $t_{\rm burn}$ depends strongly on $M_{\star}$ but has a relatively weak dependence on stellar age. It is important to note that independently of the mass and age of the disrupted star, no anomalous abundances are expected to be observed before $t_{\rm peak}$.

Information regarding the nature of the disrupted star should be imprinted on the properties of the TDE light curve (e.g., $t_{\rm peak}$ and $\dot{M}_{\rm peak}$) and spectrum (particularly at $t \gtrsim t_{\rm burn}$). Current observations of TDEs show clear differences in their rise and decay properties as well as in their spectral evolution. Peculiar emission features have been observed in their spectra, which include an array of helium, hydrogen, and nitrogen broad line emission features. The origin of these features as well as their associated line ratios have caused significant debate. The extreme helium to hydrogen line ratio observed in the transient event PS1-10jh was initially proposed to be the result of the tidal disruption of a helium-rich star (Gezari et al. 2012a). However, such line ratios have also been shown to arise from the reprocessing of radiation through the fallback debris of a disrupted Sun-like star (Roth et al. 2016). As for the additional presence of rare nitrogen features, Kochanek (2016a) first proposed that the disruption of MS stars with evolved stellar compositions could lead to enhanced nitrogen (as well as anomalous helium and carbon abundances).

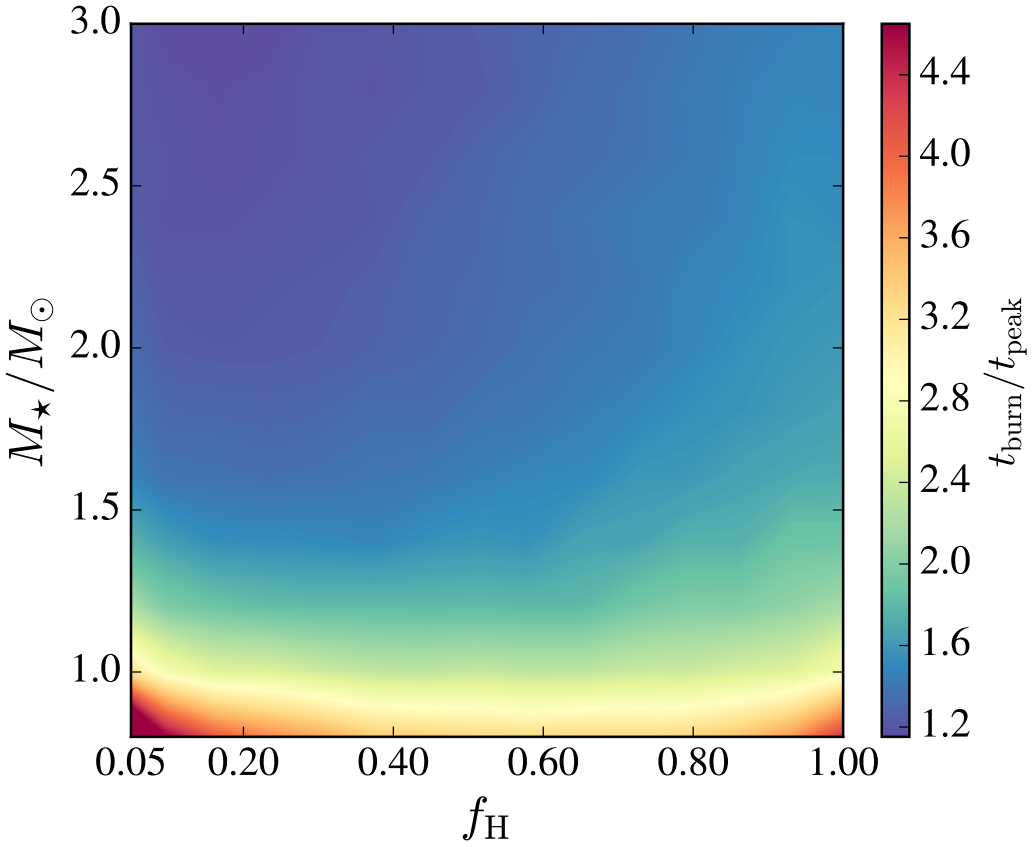

Figure 4.13: The ratio of $t_{\rm burn}$ to $t_{\rm peak}$ as a function of $f_{\rm H}$ and stellar mass. Here $t_{\rm burn}$ is the time when non-solar abundance ratios begin to appear in the fallback material, specifically when the abundance of ^{12}C and ^{14}N deviate from solar. We have explicitly excluded $f_{\rm H} \lesssim 0.05$ from this plot, given that these stars experience some mild contraction early in their MESA evolution. The ratio ($t_{\rm burn}/t_{\rm peak}$) reaches a maximum (minimum) value of 7.6 (1.15) for a $0.8 M_\odot$ ($3 M_\odot$) star at $f_{\rm H} = 0.05$ ($f_{\rm H} = 0.23$).

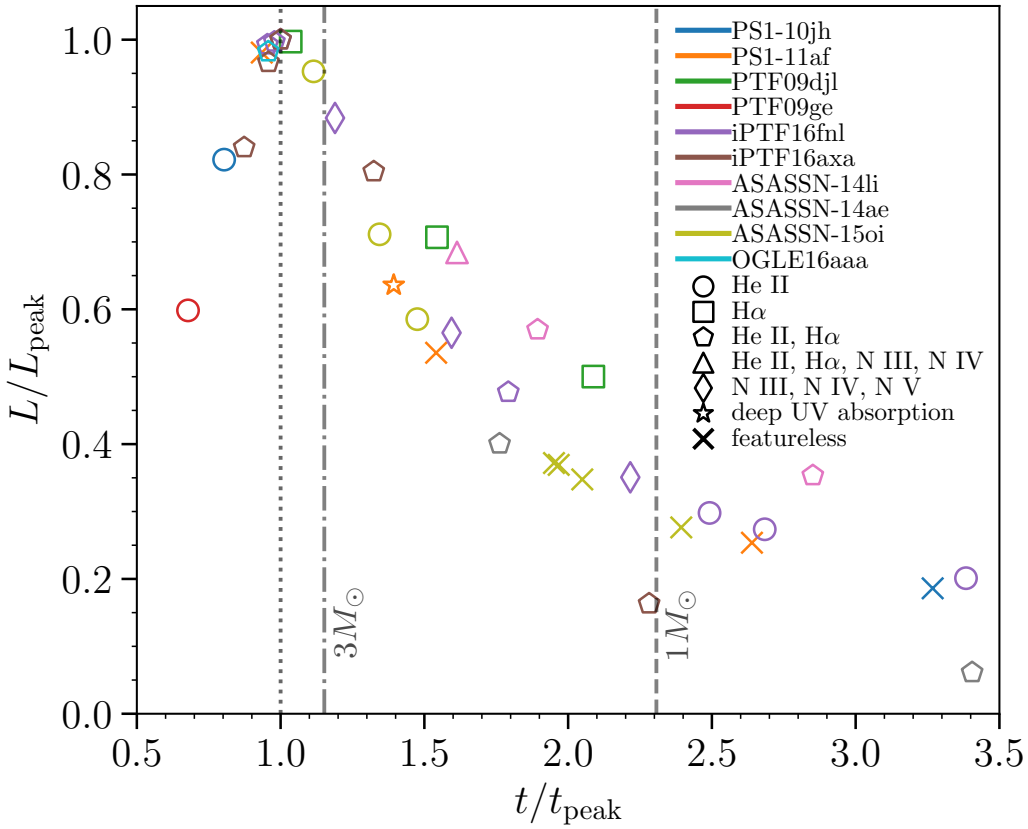

Figure 4.14: Compositional features in the spectra of well-sampled tidal disruption events with existing spectroscopic observations. The y- and x-axes show luminosity and time relative to peak respectively, with different colors corresponding to distinct events, and different symbols corresponding to different spectral features. We show the minimum values of $t_{\rm burn}/t_{\rm peak}$ (Figure 4.13) as derived from our study for a $1M_\odot$ (*dashed* line) and $3M_\odot$ (*dash-dotted* line) star.

In Figure 4.14, we show compositional features in the spectra of ten observed TDEs. We place each spectrum in the light curve of each event, relative to its peak luminosity and peak time. Symbols indicate features present in the spectra. Bolometric light curve fits for each event are from Mockler et al. (2018). Data is taken from Gezari et al. (2012a, 2015); Chornock et al. (2014b); Arcavi et al. (2014b); Brown et al. (2018); Blagorodnova et al. (2017b); Hung et al. (2017c); Holoien et al. (2014b, 2016a,c); Cenko et al. (2016); Brown et al. (2016a, 2017); Wyrzykowski et al. (2017). Note that this figure shows TDEs with well-sampled light curves and existing spectroscopic observations. Several TDE spectra show compositional features at or near the peak in their light curve. Our calculations (in particular see Section 4.3.3 and Figure 4.13) predict no compositional abundance changes (relative to solar) in the fallback material at or near peak due to the star. This implies that the strong suppression of hydrogen Balmer line emission relative to helium line emission should occur even at solar composition, as argued by Roth et al. (2016), due to optical depth effects alone. For observations at $t > t_{\rm burn}$, we expect the reprocessing material to be enhanced in helium, yet the optical depth effects are expected to be less important (Guillochon et al. 2014a). As such, radiation transfer calculations are needed before firm conclusions can be derived from observations of evolving line ratios in a given TDE.

Nitrogen emission lines, on the other hand, are only currently detected at $t \gtrsim 1.2 t_{\rm peak}$. If their presence is primarily attributed to a drastic increase in nitrogen abundance, then based on the results shown in Figures 4.12 and 4.13, one would conclude that $M_\star \gtrsim 1.8 M_\odot$ for the star whose disruption triggered the ASASSN-14li flaring event

and $M_\star \gtrsim 3.0 M_\odot$ for the star whose disruption triggered iPTF16fnl. However, early UV spectra that show a lack of nitrogen emission lines at early times are needed to support constraints such as these. In addition, the line ratio variability of, for example, CIII and NIII, can be used to infer the abundance evolution (as these lines have similar ionization potentials). The timescale for chemical enrichment (i.e., $t_{\rm burn}$) can thus provide a direct observational test of which stars are being disrupted by the central SMBH.

Much progress has been made in understanding how the feeding rate onto a SMBH proceeds after the disruption of a particular star, and in deriving the generic properties of the flares that follow from this. There still remain a number of mysteries, especially concerning the identity of the star, the nature of the energy dissipation mechanism, and the time scales involved. The modeling of the flare itself (i.e., the dissipation mechanism and the radiation processes) is a formidable challenge to theorists and to numerical techniques. It is also a challenge for observers, in their quest to detect fine details in distant, fading sources. The class of models we have presented here predict that the spectral properties of the fading signals will turn out to be even more telling and fascinating that initially anticipated.

Future work will include a more detailed exploration of the parameters governing the abundance of the fallback material, including hydrodynamical calculations (e.g., Law-Smith et al. 2017a) as well as radiative transfer calculations (e.g., Roth et al. 2016) evolved over time for different properties of the reprocessing material. Studies of this sort, in comparison with improved spectral observations of TDEs, will undoubtedly help clarify the physics governing these transient sources.

Chapter 5

The Tidal Disruption of Sun-like Stars by Massive Black Holes

Abstract

We present the first simulations of the tidal disruption of stars with realistic structures and compositions by massive black holes (BHs). We build stars in the stellar evolution code MESA and simulate their disruption in the 3D adaptive-mesh hydrodynamics code FLASH, using an extended Helmholtz equation of state and tracking 49 elements. We study the disruption of a $1M_{\odot}$ star and $3M_{\odot}$ star at zero-age main sequence (ZAMS), middle-age, and terminal-age main sequence (TAMS). The maximum BH mass for tidal disruption increases by a factor of $\sim$2 from stellar radius changes due to MS evolution; this is equivalent to varying BH spin from 0 to 0.75. The shape of the mass fallback rate curves is different from the results for polytropes of Guillochon

& Ramirez-Ruiz (2013a). The peak timescale $t_{\rm peak}$ increases with stellar age, while the peak fallback rate $\dot{M}_{\rm peak}$ decreases with age, and these effects diminish with increasing impact parameter β. For a $\beta = 1$ disruption of a $1M_{\odot}$ star by a 10^6 $M_{\odot}$ BH, from ZAMS to TAMS, $t_{\rm peak}$ increases from 30 to 54 days, while $\dot{M}_{\rm peak}$ decreases from 0.66 to 0.14 $M_{\odot}$/yr. Compositional anomalies in nitrogen, helium, and carbon can occur before the peak timescale for disruptions of MS stars, which is in contrast to predictions from the "frozen-in" model. More massive stars can show stronger anomalies at earlier times, meaning that compositional constraints can be key in determining the mass of the disrupted star. The abundance anomalies predicted by these simulations provide a natural explanation for the spectral features and varying line strengths observed in tidal disruption events.

5.1 Introduction

The tidal disruption of a star by a massive black hole (BH) occurs when a star is knocked onto a nearly radial "loss-cone" orbit toward the BH by a chance encounter with another star. The flares resulting from the disruption can offer insight into otherwise quiescent massive BHs, the nuclear stellar populations that surround them, the physics of super-Eddington accretion, and the dynamical mechanisms operating in galactic centers. A detailed theoretical understanding of tidal disruptions is required to pry this information from observations. Pioneering theoretical work includes Hills (1975a), Carter & Luminet (1983), Rees (1988a), and Evans & Kochanek (1989a).

In this Letter, we present the first simulations of tidal disruptions of stars with

realistic structures and compositions. We build stars using the 1D stellar evolution code MESA (Paxton et al. 2011) and calculate their disruption in the 3D adaptive-mesh hydrodynamics code FLASH (Fryxell et al. 2000). We track the elemental composition of the debris that falls back onto the black hole. We study the disruption of a $1M_{\odot}$ star and $3M_{\odot}$ star at three different ages.

A few dozen tidal disruption event (TDE) candidates have been observed thus far; see Komossa (2015a) and Auchettl et al. (2017a) for a review of observations. Nearly all of their light curves (luminosity vs. time) are well fit by a simple scaling of mass fallback rate predictions from simulations (e.g., Mockler et al. 2019), suggesting that circularization of the debris is prompt, and that the mass fallback rate has important discriminatory power in determining the key properties of an observed disruption (Ramirez-Ruiz & Rosswog 2009).

The shape of the mass fallback rate curve depends on the properties of the BH (mass, spin), the properties of the star (structure, mass), and the parameters of the disruption (impact parameter, orientation). Guillochon & Ramirez-Ruiz (2013a) studied the impact of stellar structure and impact parameter on the mass fallback rate using $\gamma = 4/3$ and $\gamma = 5/3$ polytropic stellar structures. Gafton & Rosswog (2019a) performed a parameter space study of relativistic tidal disruptions with spinning BHs for a $\gamma = 5/3$ stellar structure. Goicovic et al. (2019) recently simulated the disruption of a zero-age main sequence (ZAMS) star using moving-mesh hydrodynamics and studied the evolution of the stellar remnant, but did not track composition or study non-ZAMS stars.

Besides the shape of the light curve, spectroscopic information can provide clues as to the nature of the disrupted star. Kochanek (2016a) predicted abundance anomalies in TDEs resulting from evolved stars. Gallegos-Garcia et al. (2018) developed a simple framework, based on the work of Lodato et al. (2009a) and Kochanek (2016a), to calculate the mass fallback rate for the disruption of stars of many masses and ages and to track the composition of the mass fallback. This is a useful framework that can be used to interpret spectroscopic observations of TDEs, but, as we discuss here, the simulations presented in this Letter make several different predictions from it.

An outstanding mystery in the field is that TDEs appear to occur preferentially in a rare type of galaxy (Arcavi et al. 2014b; French et al. 2016b; Law-Smith et al. 2017c; Graur et al. 2018). If we can determine the exact type of star that was disrupted in a TDE and build a demographic sample, we may be able to better understand this peculiar host galaxy preference. Separate from this, we may eventually be able to study the nuclear stellar populations in other galactic centers through tidal disruption.

TDEs can be used to obtain BH masses with comparable precision to the M–σ relation (e.g., Mockler et al. 2019). Simulations of tidal disruption using realistic stellar models will provide a better backbone for these fitting routines and a more accurate determination of all of the properties of the disruption.

A diversity of stellar types can contribute to tidal disruptions from 10^5–$10^9 M_\odot$ BHs; see the tidal disruption menu presented in Law-Smith et al. (2017a). It is important to build a library of realistic tidal disruption simulations in order to extract the most information from the diversity of incoming and existing observations. The simu-

lation framework we present in this Letter enables one to simulate the tidal disruption of any object that can be constructed in a stellar evolution code, allowing for the development of a library of tidal disruption simulations of stars with realistic structures and compositions.

This Letter is organized as follows. In Section 7.2 we discuss our methods. In Sections 5.3 and 5.4 we discuss our results with regard to stellar structure and composition respectively. In Section 7.5 we summarize and conclude.

5.2 Methods

We build stars using the 1D stellar evolution code MESA and simulate their tidal disruption using FLASH, a 3D grid-based adaptive mesh refinement hydrodynamics code. For this study, we focus on the disruption of a $1M_{\odot}$ star at ZAMS (0 Gyr), middle-age (4.8 Gyr), and TAMS (terminal-age main sequence; 8.4 Gyr), and a $3M_{\odot}$ star at ZAMS (0 Gyr) and TAMS (0.3 Gyr). We simulate an encounter with a $10^6 M_{\odot}$ BH (for non-relativistic encounters, other BH masses will simply scale the properties of the disruption; see e.g. Guillochon & Ramirez-Ruiz 2013a) at a range of impact parameters from grazing encounters to full disruptions.

We use the following MESA setup[20]: we start with a pre-MS model, use the Asplund et al. (2009) abundances (X=0.7154, Y=0.2703, and Z=0.0142), the `mesa_49` nuclear network with the `jina` nuclear reaction rates preference (from Cyburt et al. 2010), and `mixinglengthalpha=2.0` (this is the MESA default, and corresponds to

[20]Inlists are available upon request.

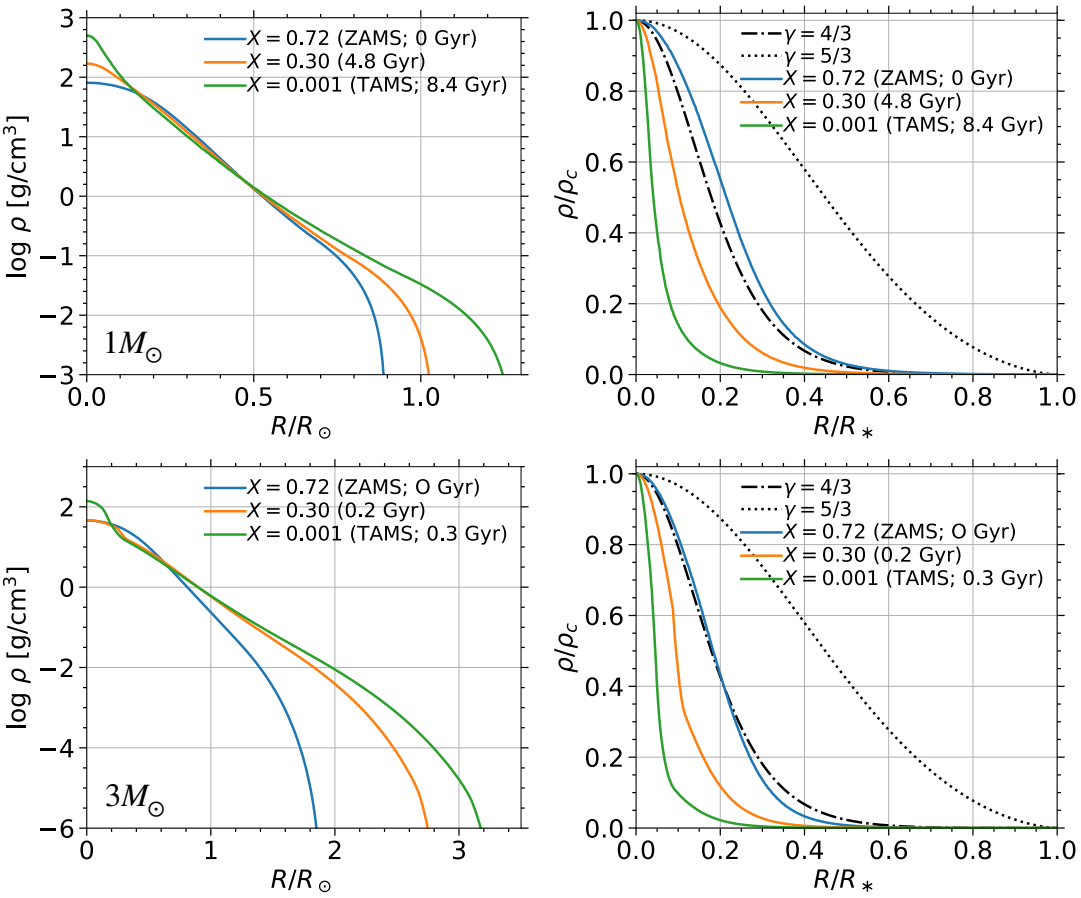

Figure 5.1: MESA density profiles for a $1M_\odot$ star (top panels) and $3M_\odot$ star (bottom panels) along their main sequence lifetimes. X is the central hydrogen mass fraction. Left panels: density vs. radius. Right panels: normalized to central density and stellar radius. Dashed and dotted lines show profiles for $\gamma = 4/3$ and $\gamma = 5/3$ polytropes respectively.

setting the mixing length equal to twice the local pressure scale height[21]). We define TAMS as a central hydrogen fraction of 10^{-3}. We track 49 elements, but in our results only show a few representative elements that have relatively high mass fractions. Full composition (and other) results will be made publicly available with the release of our tidal disruption library (in prep.).

[21] Moore & Garaud (2016) show that this is accurate for stellar masses up to $3M_\odot$.

We map the 1D profiles of density, pressure, temperature, and composition from MESA onto a 3D grid in FLASH, with initially uniform refinement. Some of the details of our FLASH setup are explained in Guillochon & Ramirez-Ruiz (2013a). The important differences from this setup are that (1) we use an extended Helmholtz equation of state[22] rather than a polytropic equation of state, (2) we map a MESA profile onto the FLASH grid, and (3) we track the elemental composition of the debris for 49 elements. Our setup is Eulerian, centered on the rest frame of the star. Our domain is $1000R_\star$ on a side, and we run our simulations until the stellar debris leaves the domain, typically 60-100 $t_{\rm dyn}$ after the start of the simulation (the dynamical time of the star is defined as $t_{\rm dyn} = \sqrt{R_\star^3/GM_\star}$). This corresponds to 23-65 hours depending on the star and impact parameter. Note that the period of the most tightly bound debris in our simulations is (at shortest) $\approx$ 110 hours, so no stream-stream collisions occur. At initial maximum refinement, we have 131 cells across the initial diameter of the star. This is a factor of $\approx$ 2.6 times better initial resolution than Guillochon & Ramirez-Ruiz (2013a), which had $\approx$ 50 cells across the initial diameter. The simulation retains this maximum refinement through pericenter and derefines as the debris spreads out. We refine based on density, relative to the maximum density in the simulation. All cells within 10^{-5} of the maximum density have the same refinement (are maximally refined). The simulations presented in this Letter have a maximum total number of blocks of 4.8×10^4. There are $8^3 = 512$ cells per block, so this translates to 2.5×10^7 maximum cells in the simulation.

[22]This is an extension of the default FLASH Helmholtz table, based on Timmes & Swesty (2000), and is available at http://cococubed.asu.edu/code_pages/eos.shtml.

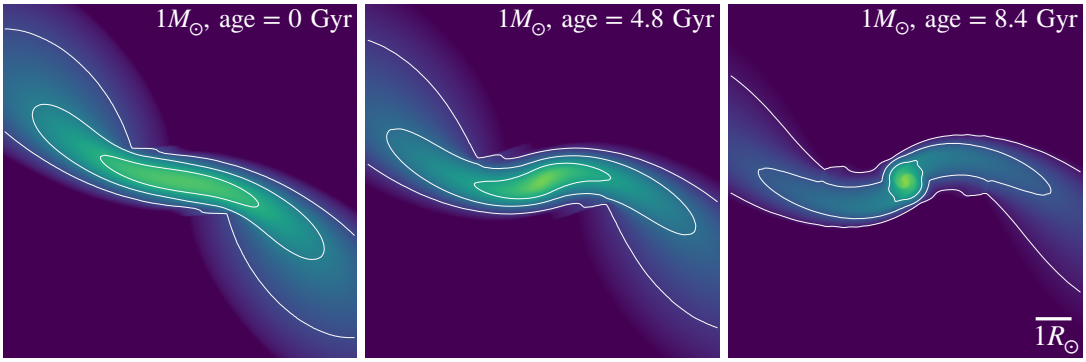

Figure 5.2: 2D slices in the orbital plane of a $\beta = 2$ encounter with a $10^6 M_\odot$ BH for a $1M_\odot$ star at ZAMS, middle-age, and TAMS, at $\approx 3\ t_{\rm dyn}$ after pericenter. Color corresponds to density and contours are equally spaced in the logarithm of the density (at $\rho = 1, 10^{-1}, 10^{-2}$ g/cm^3). Videos of the simulations are available at this URL.

The impact parameter $\beta \equiv r_{\rm t}/r_{\rm p}$ is defined as the ratio of the tidal radius,

$$r_{\rm t} \equiv (M_{\rm BH}/M_\star)^{1/3} R_\star, \tag{5.1}$$

to the pericenter distance, $r_{\rm p}$. Note that the tidal radius is defined using the stellar radius (not necessarily $1R_\odot$ for a $1M_\odot$ star), so that the same impact parameter for different stellar ages corresponds to different pericenter distances. The most relativistic encounter shown in this work is a $\beta = 3$ disruption of a ZAMS Sun; here $r_{\rm p} \simeq 14GM_{\rm BH}/c^2$. In this regime, relativistic effects on the rate of return of the fallback material are minor (Tejeda et al. 2017b; Stone et al. 2019). Note also that in our simulations the tidal radius is $100R_\star$, meaning that the BH enters the computational domain as it moves through pericenter. This does not lead to any issues vis-a-vis capture by the event horizon, as the star's deformation through pericenter only extends to a few $R_\star$, and further, the pericenter passage takes place on the star's dynamical timescale. Put more precisely, the minimum angular momentum of the tidal debris is much greater

than the threshold for capture. We begin the simulations at $r = 10\ r_{\rm t}$, where tidal effects are negligible.[23] We then relax the star onto the grid for 5 $t_{\rm dyn}$ before beginning the parabolic BH orbit evolution. We verify that the stellar profiles after this relaxation process are very similar to the intial input MESA profiles (see also e.g. Law-Smith et al. 2017a).

We calculate the mass fallback rate ($\dot{M}$) to the BH by first calculating the spread in binding energy dM/dE of each cell in our simulation. We smooth the dM/dE distribution with a Gaussian filter, as it is noisy due to our fine binning, then convert this distribution to an $\dot{M}$ curve through Kepler's third law. Our $\dot{M}$ curves are derived at the last time at which all of the stellar debris is within the domain, 40-80 $t_{\rm dyn}$ after pericenter; Figure 10 of Guillochon & Ramirez-Ruiz (2013a), which shows $\dot{M}$ curves up to 550 $t_{\rm dyn}$ after pericenter, demonstrates that our $\dot{M}$ curves are accurate for the timescales we are interested in for this work. We tested that our setup can reproduce the Guillochon & Ramirez-Ruiz (2013a) $\dot{M}$ and ΔM results for polytropes at a few different impact parameters. We verified the resolution convergence of our results by running a subset of our simulations with twice or four times the maximum number of blocks stated above, finding no appreciable difference.

5.3 Stellar Structure

In this section we consider the structure evolution of a $1M_\odot$ star and $3M_\odot$ star along their main sequence lifetimes as representative examples. Stars with $M \gtrsim 3M_\odot$

[23] Cf., for example, Goicovic et al. (2019), whose simulations start at 5 $r_{\rm t}$.

will be very rare as TDEs due to their short main sequence lifetimes; stars with $M \lesssim 0.6M_\odot$, on the other hand, will not significantly evolve over the age of the universe.

Figure 7.1 shows density profiles from MESA for a $1M_\odot$ star and $3M_\odot$ star along their main sequence lifetimes. From ZAMS to TAMS, the Sun's central density increases by a factor of ≈ 6, from 80 g/cm^3 to 500 g/cm^3, and its radius increases by a factor of ≈ 1.4, from $0.9R_\odot$ to $1.3R_\odot$. A $3M_\odot$ star's radius increases by a factor of 1.75 over its MS lifetime. Normalized to central density and stellar radius, the profile of a $\gamma = 4/3$ polytrope is in rough agreement with that of a ZAMS Sun and in better agreement with that of a ZAMS $3M_\odot$ star, though is not a good match for non-ZAMS stars.

The density profile of a star determines its susceptibility to tidal disruption. Figure 5.2 shows 2D slices in the orbital plane from simulations of the disruption of the Sun at three different ages (ZAMS, middle-age, and TAMS) at the same impact parameter ($\beta = 2$). For the ZAMS Sun this is a full disruption, whereas for the TAMS Sun this is a grazing encounter in which a core survives.

As the density profile of a star changes, so does the mass fallback rate to the BH resulting from its disruption. Panels (a), (b), and (c) of Figure 5.3 show the mass fallback rate $\dot{M}$ to the BH as a function of time for the disruption of the Sun for three impact parameters at three different ages (results here for the $3M_\odot$ star show similar trends). Panels are grouped by impact parameter.

Older stars are more centrally concentrated and thus more difficult to fully disrupt, resulting in higher critical impact parameters for full disruption. At a fixed β,

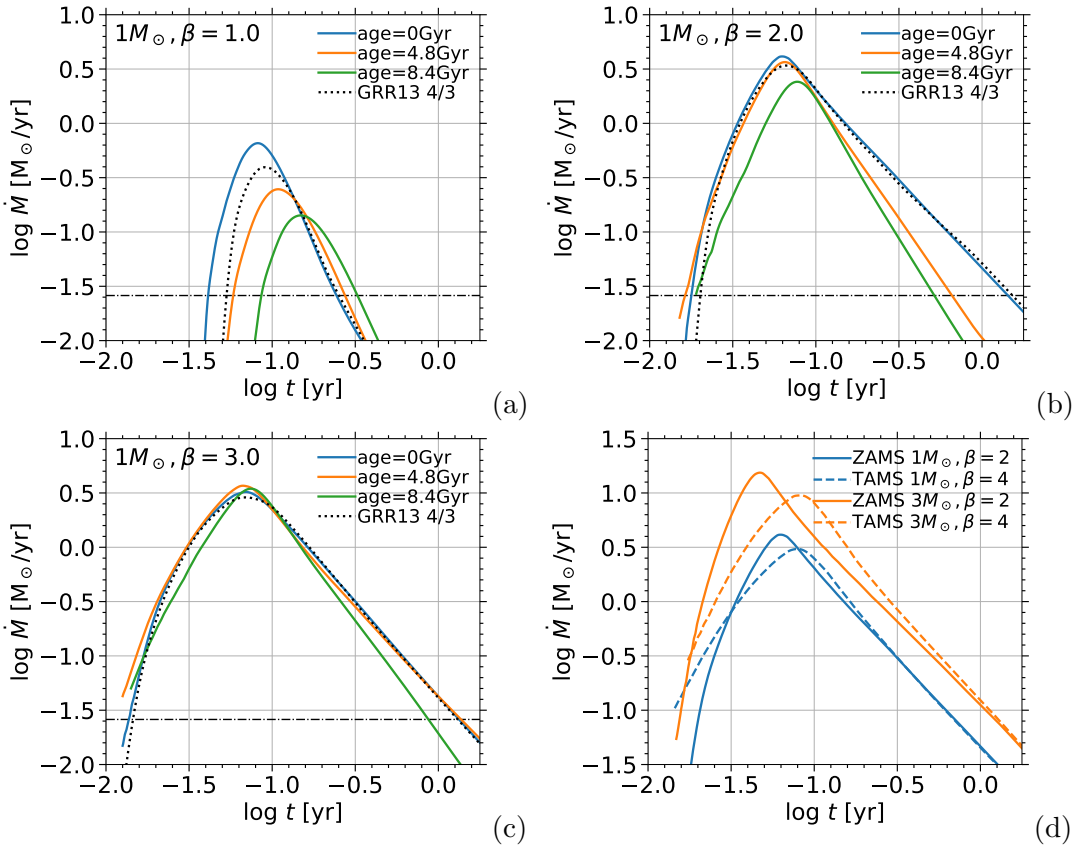

Figure 5.3: Panels (a), (b), (c): mass fallback rate to the BH as a function of time for the disruption of a $1M_\odot$ star at three different ages and impact parameters by a $10^6 M_\odot$ BH. Panels are grouped by impact parameter β. The result for a $\gamma = 4/3$ polytrope from Guillochon & Ramirez-Ruiz (2013a), scaled to the radius of the ZAMS Sun, is in dotted black. The Eddington limit for this BH, assuming a radiative efficiency of $\epsilon = 0.1$ and an electron scattering opacity of $\kappa = 0.34$ cm^2 g^{-1}, is shown by the dot-dashed line. Panel (d): mass fallback rate for full disruptions of a $1M_\odot$ star and $3M_\odot$ star at ZAMS and TAMS.

the amount of mass lost ΔM decreases with stellar age.[24] The shape of the $\dot{M}$ curve also changes: at a fixed β (for the β's shown in this work), the slope of the $\dot{M}$ curve after peak becomes steeper with stellar age—this is mostly easily seen for the $\beta = 2$ disruptions. This behavior was also observed for partial disruptions of a given polytrope in Guillochon & Ramirez-Ruiz (2013a).

The time of peak of the mass fallback rate, $t_{\rm peak}$, increases with stellar age (i.e., younger stars can provide faster flares) and this effect diminishes with increasing β. The peak mass fallback rate, $\dot{M}_{\rm peak}$, decreases with stellar age and this effect diminishes at high β. For $\beta = 1$, from ZAMS to TAMS for the Sun, $t_{\rm peak}$ increases from 30 days to 54 days, while $\dot{M}_{\rm peak}$ decreases from 0.66 $M_\odot$/yr to 0.14 $M_\odot$/yr. For $\beta = 2$, $t_{\rm peak}$ increases from 23 to 28 days, while $\dot{M}_{\rm peak}$ decreases from 4.1 $M_\odot$/yr to 2.4 $M_\odot$/yr. For $\beta = 3$, the peak properties for the three ages are more similar. Fitting formulae will be provided with a more extensive parameter study in impact parameter, mass, and age in future work.

We compare to the simulation results of Guillochon & Ramirez-Ruiz (2013a) for a $\gamma = 4/3$ polytrope (the $\gamma = 5/3$ simulations are more dissimilar), scaled to the radius of the ZAMS Sun. For $\beta = 1$, the $\gamma = 4/3$ simulation is in rough agreement but does not match any of the ages particularly well. For $\beta = 2$, the $\gamma = 4/3$ simulation more closely matches the ZAMS Sun, but does not capture the shape of the $\dot{M}$ curve for the middle-age or TAMS Suns. For $\beta = 3$, the $\gamma = 4/3$ simulation is a better approximation of the general shape for all three ages, but is a worse match for the

[24]Note however that at *fixed pericenter distance* $r_{\rm p}$, because older stars have larger radii, for low-β partial disruptions the mass lost is larger for older stars.

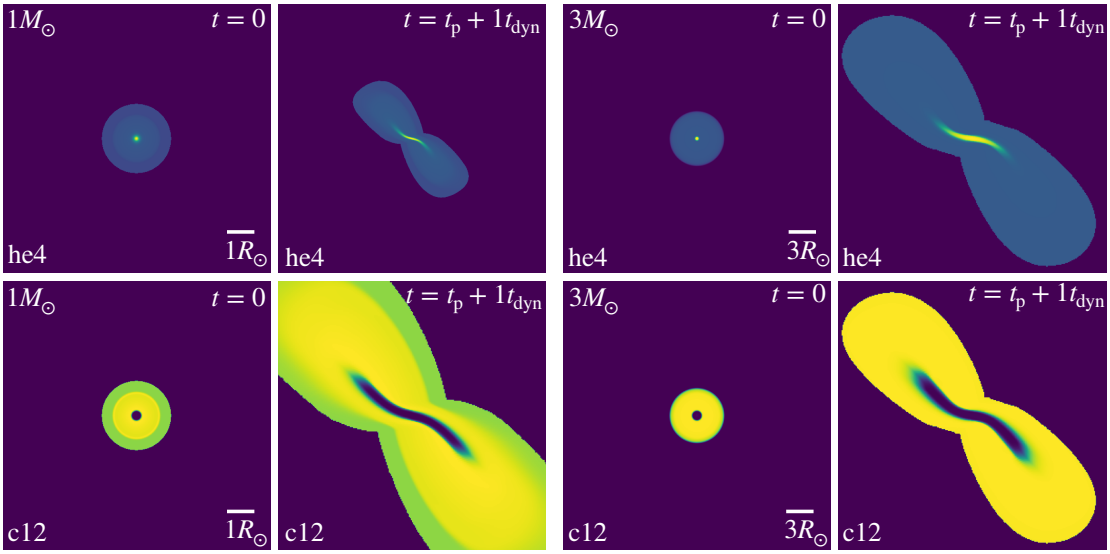

Figure 5.4: 2D slices in the orbital plane of the mass fractions of helium and carbon for a $\beta = 4$ disruption of a TAMS $1M_\odot$ and $3M_\odot$ star, at the start of the simulation and at $\approx 1\ t_{dyn}$ after pericenter. Color corresponds to the mass fraction of the element, with yellow being higher. The panels are normalized separately. The right panels in each group of four have a density cut of 10^{-4} g/cm^3.

TAMS Sun.

The shape of the $\dot{M}$ curve is useful in determining the properties of the disruption when fitting to observed events (e.g., Mockler et al. 2019), and a full library of tidal disruption simulations using realistic stellar profiles will improve these determinations. However, there are certain difficulties and degeneracies which can be resolved by incorporating more information. For example, for full disruptions, there is not a large variation in t_{peak} with the mass of the star. In panel (d) of Figure 5.3, we compare the mass fallback rate for full disruptions[25] of a $1M_\odot$ star and $3M_\odot$ star at ZAMS and TAMS. At a given evolutionary state, the normalization of the $\dot{M}$ curve changes with mass but the peak timescale does not vary much: it decreases by ≈ 5 days from a

[25]We conducted a preliminary parameter-space study to determine the approximate impact parameters for full disruption (these are $\beta \approx 2$ for ZAMS $1M_\odot$, $\beta \approx 3$ for middle-age $1M_\odot$, $\beta \approx 4$ for TAMS $1M_\odot$, $\beta \approx 2$ for ZAMS $3M_\odot$, and $\beta \approx 4$ for TAMS $3M_\odot$, with approximate uncertainty ± 0.5).

ZAMS $1M_\odot$ to $3M_\odot$ star. Age can increase the spread: from a ZAMS to TAMS $3M_\odot$ star, $t_{\rm peak}$ increases by ≈ 12 days. This implies that determinations of BH masses are expected to be relatively robust, as the uncertainties associated with stellar mass and age do not greatly alter the shape of the resultant $\dot{M}$ curves. On the other hand, using light curves alone might be insufficient to effectively identify the nature of the disrupted star. Using compositional information as a second axis can significantly improve our determinations of the properties of the disruption and it is to this issue that we now turn our attention.

5.4 Composition

Tracking compositional information in our hydrodynamical simulations captures the mixing of previously sequestered regions within a star. This mixing affects the timing and composition of the debris returning to the BH. Figure 5.4 shows 2D slices of the mass fractions of helium and carbon for a $\beta = 4$ disruption of a TAMS $1M_\odot$ and $3M_\odot$ star. Both the helium enhancement and the depletion of carbon in the stars' cores are mixed into the tidal tails. Note that while nuclear burning occurs primarily via the pp chain in the $1M_\odot$ star and the CNO cycle in the $3M_\odot$ star, carbon is similarly depleted in the cores of both of the stars; this is primarily because carbon is depleted during pre-MS evolution for the $3M_\odot$ star.

Figure 5.5 shows the composition of stellar material returning to pericenter as a function of time for three full disruptions: a $\beta = 3$ disruption of a middle-age Sun, a $\beta = 4$ disruption of a TAMS Sun, and a $\beta = 4$ disruption of a TAMS $3M_\odot$ star. We

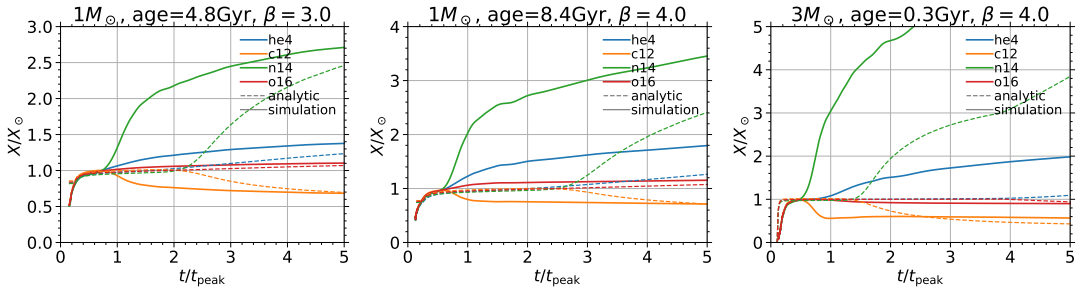

Figure 5.5: Composition (relative to solar) of the fallback material to pericenter as a function of time (relative to the peak of the mass fallback rate). The panels from left to right show full disruptions of a middle-age Sun, a TAMS Sun, and a TAMS $3M_\odot$ star. Solid lines are hydrodynamic simulation results and dashed lines are analytic results from Gallegos-Garcia et al. (2018).

define

$$\frac{X}{X_\odot} = \frac{\dot{M}_X/\dot{M}_{\rm H}}{M_X/M_{{\rm H},\odot}}, \tag{5.2}$$

where X is a given element, H refers to hydrogen, and the denominator is the abundance of X relative to hydrogen in the Sun. Refer to Figure 3 of Gallegos-Garcia et al. (2018) for the compositional evolution of the Sun along its main sequence lifetime.

For a ZAMS Sun, for all impact parameters, $X/X_\odot \simeq 1$ for all elements as a function of time. This follows from the fact that a $1M_\odot$ star is nearly perfectly homogeneous at ZAMS. This is not, however, true of a ZAMS $3M_\odot$ star (see below). For stars that have evolved along the MS, $X/X_\odot$ can be ≈ 1 for low-β (grazing) encounters that only strip the outside layers of the star unaffected by nuclear burning. Deeper encounters of non-ZAMS stars show non-solar fallback abundances. In general, abundance variations manifest as an increase in nitrogen and helium and a decrease in carbon over time, with an increase or decrease in oxygen depending on the mass of the star. Other elements, such as neon, sodium, and magnesium, show an increase over time. The rel-

ative strength and timing of these anomalies is a function of the mass and age of the star and the impact parameter of the disruption. More massive stars, older stars, and deeper encounters result in stronger abundance anomalies at earlier times.

For full disruptions of a middle-age Sun, TAMS Sun, and TAMS $3M_\odot$ star, abundance anomalies appear before the time of peak fallback rate. Helium, carbon, nitrogen, and oxygen (among many other elements with lower mass fractions) can all be enhanced or depleted before $t_{\rm peak}$. Abundance anomalies can also appear before peak for partial disruptions—for example, this occurs for a $\beta = 3$ disruption of a TAMS Sun. These early variations are particularly encouraging for observations of the signatures of these kinds of disruptions. Additionally, the N/C ratio shows even stronger variations than the above individual elements. Though not shown here, nitrogen, helium, and oxygen abundances continue to rise/decrease for more than one year after peak (for the disruption of a $1M_\odot$ star by a $10^6 M_\odot$ BH, until ≈ 6 years after peak). That is, at late times, the elemental abundances asymptote to fixed values (this late-time behavior was also predicted in our analytic framework, Gallegos-Garcia et al. 2018).

Focusing on the time at which nitrogen is enhanced by a factor of 3 as a diagnostic of the timing of abundance anomalies: this occurs at $\approx 10\ t_{\rm peak}$ for a middle-age Sun, at $\approx 3\ t_{\rm peak}$ for a TAMS Sun, and at $\approx t_{\rm peak}$ for a TAMS $3M_\odot$ star. There is a similar trend in other elements—for example, for a TAMS $3M_\odot$ star, carbon is depleted by a factor of ≈ 2 at $t_{\rm peak}$. Though not shown here, the full disruption of a ZAMS $3M_\odot$ star exhibits abundance variations in nitrogen and carbon, but at a lower level than for the TAMS star. A TAMS $3M_\odot$ star shows stronger abundance variations

at earlier times compared to a $1M_\odot$ star; thus, abundance anomalies increase with age and $M_\star$ at a fixed $t/t_{\rm peak}$. If TDEs occur (on average) for stars of the same age in a given nuclear stellar cluster, then more massive stars will provide stronger abundance anomalies. Another determinant of mass is oxygen: oxygen is enhanced for the $1M_\odot$ star but depleted for the $3M_\odot$ star.

If strong abundance variations are observed at early times in a TDE (in the simple picture that abundance variations beget spectral features), this is a sign of a higher-β disruption of a higher-mass star. Note, however, that the prospect of identifying the nature of the disrupted star is further complicated by β. For example, if more modest abundance variations are observed, it may be difficult to discern between a low-β disruption of a higher-mass star and a high-β disruption of a lower-mass star. A full library of simulations with fitting formulae will help break this degeneracy.

We also compare our results to predictions from the analytic framework of Gallegos-Garcia et al. (2018). The simulations show stronger abundance variations at early times. We note that over longer timescales ($t \gtrsim 10\ t_{\rm peak}$), the analytic framework is in good general agreement with the simulations, but we focus on timescales near peak here, as these are the most relevant to current observations. The analytic framework is useful for predicting broad features of the composition of the fallback material for many stellar masses and ages, but is limited in that it cannot probe the β parameter space (as it is only applicable to full disruptions) and more importantly, it does not capture the deformation and spin-up of the star at pericenter (it assumes that the star arrives intact to pericenter, at which point the binding energy is "frozen-in"). The fact that

at pericenter, the star is typically spun-up to a large fraction of its breakup angular velocity and has a highly distorted shape, as well as the subsequent mixing of debris as the disruption evolves, account for the differences between the analytic model and the simulations. See Steinberg et al. (2019) for a more detailed examination of the differences between the "frozen-in" model and hydrodynamical simulations.

5.5 Conclusion

We built stars with realistic stellar profiles and elemental compositions in MESA and simulated their tidal disruption in FLASH, using a Helmholtz equation of state and tracking the composition of the debris. The shape of the mass fallback rate curves and the tidal susceptibility for a star at different ages along its main sequence lifetime differ from results for polytropes from Guillochon & Ramirez-Ruiz (2013a). $t_{\rm peak}$ increases with stellar age, while $\dot{M}_{\rm peak}$ decreases with age, and these effects diminish with increasing impact parameter. Significant mixing and rotation of the debris occurs during disruption, leading to abundance anomalies appearing before the peak of the mass fallback rate for some disruptions. In the fallback debris for non-ZAMS stars, nitrogen and helium are enhanced and carbon is depleted relative to solar. Abundance variations are stronger at earlier times for older and more massive stars.

Strong nitrogen and a lack of carbon (C III) features, and in two cases strong oxygen features, have been observed in the four TDEs with UV spectra extending to these wavelengths: ASASSN-14li (Cenko et al. 2016), iPTF16fnl (Brown et al. 2018), iPTF15af (Blagorodnova et al. 2019), and AT 2018dyb (Leloudas et al. 2019a). These

features are naturally explained by our simulations as the tidal disruptions of non-ZAMS stars. A stronger N/C ratio at an earlier time relative to peak (such as the nitrogen feature observed at $t \approx 1.2\ t_{\rm peak}$ in iPTF16fnl) indicates that a flare arose from the disruption of a more massive star. Time-resolved spectroscopy extending into the UV will be very useful for fitting to simulations and determining the mass of the disrupted star.

It is important to note that stellar evolution along the MS leads to significant changes in the density profile of the star, but also in its radius. The Sun's radius changes from $0.9R_\odot$ to $1.3R_\odot$ from ZAMS to TAMS. The maximum black hole mass for disruption (assuming the same β) increases by a factor of 1.75. A $3M_\odot$ star's radius changes from 1.9 to 3.3 $R_\odot$ from ZAMS to TAMS; the maximum BH mass increases by a factor of 2.3. So the uncertainty on maximum BH mass from stellar evolution is ~ 2. From Figure 1 of Kesden (2012c), a factor of ~ 2 in maximum BH mass is equivalent to a change in black hole spin of 0 to 0.75 (from a spin of 0.75 to 1, the maximum BH mass changes by a factor of 4). The uncertainty from stellar evolution can therefore be of the same order as the uncertainty from BH spin—this is important as it is BH spin that determines the cutoff of the TDE rate as a function of BH mass in Figure 4 of Kesden (2012c) (this is also Figure 4 of Stone et al. 2019).

We plan to construct a library of tidal disruption simulations of stars built in MESA, for different stellar masses and ages, tracking composition information. As the present study shows, these simulations can reveal important behavior not captured by earlier models. Now that the sample of TDEs with high quality observations has grown

to a few dozen (and continues to grow), it is very important to construct a library of tidal disruption simulations of realistic stars with fitting formulae for important disruption quantities. In using simulations such as these to fit light curve and spectral information, it may be possible to accurately determine the mass of the disrupted star, as well as provide more accurate fits for all of the other properties of the disruption (BH mass, spin, efficiency, etc.).

Additionally, the framework developed in this Letter can be used to study the surviving remnants of tidal disruption. These objects can have unique compositions and internal dynamics. For example, the late-time checkpoint of the surviving star could be used as an input to MESA for future stellar evolution calculations.

Chapter 6

Stellar Tidal Disruption Events with Abundances and Realistic Structures (STARS): Library of Fallback Rates

Abstract

We present the STARS library, a grid of tidal disruption event (TDE) simulations interpolated to provide the mass fallback rate (dM/dt) to the black hole for a main-sequence star of any stellar mass, stellar age, and impact parameter. We use a one-dimensional stellar evolution code to construct stars with accurate stellar structures and chemical abundances, then perform tidal disruption simulations in a three-

dimensional adaptive-mesh hydrodynamics code with a Helmholtz equation of state, in unprecedented resolution: from 131 to 524 cells across the diameter of the star. The interpolated library of fallback rates is available on GitHub (github.com/jamielawsmith/STARS_library) and version 1.0.0 is archived on Zenodo; one can query the library for any stellar mass, stellar age, and impact parameter. We provide new fitting formulae for important disruption quantities ($\beta_{\rm crit}, \Delta M, \dot{M}_{\rm peak}, t_{\rm peak}, n_\infty$) as a function of stellar mass, stellar age, and impact parameter. Each of these quantities varies significantly with stellar mass and stellar age, but we are able to reduce all of our simulations to a single relationship that depends only on stellar structure, characterized by a single parameter $\rho_c/\bar{\rho}$, and impact parameter β. We also find that, in general, more centrally concentrated stars have steeper dM/dt rise slopes and shallower decay slopes. For the same ΔM, the dM/dt shape varies significantly with stellar mass, promising the potential determination of stellar properties from the TDE light curve alone. The dM/dt shape depends strongly on stellar structure and to a certain extent stellar mass, meaning that fitting TDEs using this library offers a better opportunity to determine the nature of the disrupted star and the black hole.

6.1 Introduction

Near the region of influence of a galactic massive black hole (BH), a star scattered onto an orbit that brings it close to the BH can be tidally disrupted by the BH's gravitational field—this is a tidal disruption event (TDE). The stellar material that remains bound to the BH produces a flare that is the signature of this event.

TDEs were first explored theoretically with pioneering studies by Lidskii & Ozernoi (1979), Hills (1975a), Carter & Luminet (1983), Rees (1988a), and Evans & Kochanek (1989a).

Several dozen such flares have been observed at the centers of other galaxies (for reviews of observations, see e.g. Komossa 2015a; Auchettl et al. 2017a; Hung et al. 2017c; van Velzen et al. 2020), with observations now regularly capturing both the rise (e.g., Holoien et al. 2019a) and decay (e.g., Holoien et al. 2018; van Velzen et al. 2019) of the transient in great detail, and even signatures of an accretion disk (e.g., Holoien et al. 2019b; Hung et al. 2020). Fitting theoretical models to observed TDEs allows one, in principle, to extract the properties of the disruption: BH mass, BH spin, stellar mass, stellar age, impact parameter, and radiative efficiency. The first attempt to systematically extract BH masses from TDEs (Mockler et al. 2019) was remarkably successful, obtaining errors of order that of the M–σ relationship. However, determination of other parameters is made difficult by degeneracies between stellar properties and BH properties. One needs better theoretical models of TDEs in order to extract more accurate information from observed events.

A combination of detailed theoretical modeling and high resolution observations can turn TDEs into unique tools to probe several astrophysical questions: (1) the BH mass function and in particular the possible existence of a cutoff in the BH mass function at low masses ($M_{\rm BH} \lesssim 10^5 M_\odot$), (2) the BH spin distribution, (3) the radiative efficiency of BH accretion and other questions of accretion physics, (4) the stellar populations (stellar masses and ages) in galactic centers, as the stars at the centers of

distant galaxies are exposed through their disruption and accretion, (5) the dynamics operating in galactic centers; e.g., which mechanisms (two-body, resonant relaxation, secular effects, etc.) dominate how stars and BHs interact.

At the order-of-magnitude level, tidal disruption occurs when a star crosses the tidal disruption radius

$$r_{\rm t} = \left(\frac{M_{\rm BH}}{M_\star}\right)^{1/3} R_\star \propto \bar{\rho}_\star^{-1/3}, \tag{6.1}$$

at which point a star's self-gravity is smaller than the tidal acceleration across its radius. The pericenter passage time of the star is approximately equal to the star's dynamical time, $t_{\rm p} \sim r_{\rm p}/v_{\rm p} \sim \sqrt{R_\star^3/GM_\star} = t_{\rm dyn,\star}$. The star is spun-up to a large fraction of its breakup angular velocity, and a quadrupole tidal distortion develops across its surface. These two effects are what tidally disrupt a star, and (again, at the order-of-magnitude level) they occur over the star's dynamical timescale, so the star does not have time to react hydrodynamically. The impact parameter of the encounter

$$\beta \equiv \frac{r_{\rm t}}{r_{\rm p}} \tag{6.2}$$

is the ratio of the tidal radius to the pericenter distance; it is an order-of-magnitude measure of the "strength" of the tidal interaction. The critical impact parameter $\beta_{\rm crit}$ is defined as the smallest impact parameter of full disruption (i.e., where the entire star's mass is disrupted), below which are partial disruptions and above which are "post-critical" encounters.

The mass fallback rate $dM/dt \equiv \dot{M}_{\rm fb}$ of debris to pericenter is a central quantity of interest as it appears to track the Optical/UV luminosity evolution of observed TDEs closely (e.g., Gezari et al. 2012a; Guillochon et al. 2014a; Mockler et al. 2019).[26] For non-relativistic disruptions, one can scale mass fallback rate and time of return to pericenter with BH mass as follows:

$$\dot{M}_{\rm peak} \propto M_{\rm BH}^{-1/2}\ M_\star^2\ R_\star^{-3/2} \tag{6.3}$$

$$t_{\rm peak} \propto M_{\rm BH}^{1/2}\ M_\star^{-1}\ R_\star^{3/2} \tag{6.4}$$

where the $\dot{M}_{\rm peak} \propto M_\star^2$ scaling results when we assume that a constant fraction of the star's mass is lost to the BH in the disruption. Note that these formulae are for the peak quantities of the mass fallback rate, but can be applied to scale the entire dM/dt curve.

Because the tidal radius depends inversely on the average density of the star (Eq. 6.1), there is a maximum BH mass for disruption outside the innermost-bound spherical orbit for different types of stars. See Figure 1 of Law-Smith et al. (2017a) for the phase space in $M_{\rm object}$ and $M_{\rm BH}$ of stellar objects (from planets to evolved stars) that are expected to produce bright tidal disruption flares. We expect that most observed TDEs will be from MS stars, and that the mass function of TDEs is relatively flat for $M_\star \lesssim M_\odot$ (Kochanek 2016b) (see more detailed discussion in Section 7.5). Thus, it is important to have a library of MS star simulations with which to fit observed events. This work is aimed to be the definitive library of the MS star parameter space. One can

[26] In present model fitting, this is true provided a few additional free parameters (mostly related to the photosphere size).

extend this library to include relativistic encounters, but these are rarer, and account for a small fraction of MS star disruptions (see discussion in Section 7.5).

Our own Galactic Center's nuclear star cluster is host to young, massive stars, giant-branch stars, and an old population of main sequence stars (e.g., Schödel et al. 2007). Stars in the Galactic Center also exhibit a range of metallicities, from metal-rich to metal-poor (Feldmeier-Krause et al. 2017). In nuclear clusters outside our galaxy, there is evidence for a diversity of stellar ages and types (Seth et al. 2010) and a wide range of star formation histories (Georgiev & Böker 2014). Additionally, TDEs appear to be observed preferentially in post-starburst galaxies (Arcavi et al. 2014b; French et al. 2016b; Law-Smith et al. 2017c; Graur et al. 2018). Thus, we expect some TDEs to be sourced by more massive stars and also by stars of varying ages and compositions. Observations of TDEs suggest that many disruptees are non-ZAMS stars (spectra show metal lines that evolve with time; e.g., Leloudas et al. 2019b) as is expected (this was first argued for in Kochanek 2016a). However, the theoretical modelling of TDEs thus far has largely ignored the stellar evolution aspect of the problem.

A brief (incomplete) summary of recent theoretical work, where we highlight features relevant to or differing in significant ways from this work, is below. Before discussing the simulation work, we mention the so-called "frozen-in" approximation, studied in detail by Lodato et al. (2009a), in which the star arrives intact to pericenter. One can then integrate across the star in equal-orbital-energy slices and determine the mass fallback rate to the BH as a function of time analytically. In this framework, only the structure of the star matters. This approximation can only handle full disruptions (a

single impact parameter). Kochanek (2016a) investigated abundance anomalies using this framework and 1D stellar evolution models from MESA. Gallegos-Garcia et al. (2018), following the above two works, developed an analytic framework to study the composition as a function of time following disruption, using MESA stars. In a recent significant extension to Lodato et al. (2009a), Coughlin & Nixon (2019) developed an analytic framework to determine the asymptotic power-law slope of the fallback rate, finding $\propto t^{-5/3}$ for full disruptions and $\propto t^{-9/4}$ for partial disruptions, in general (but not detailed) agreement with simulations.

Despite the success and usefulness of the "frozen-in" approximation in calculating TDE properties, we have learned from hydrodynamical simulations that the star arrives at pericenter significantly distorted and spinning (for a detailed discussion see Steinberg et al. 2019). Nolthenius & Katz (1982) performed the first 3D tidal disruption simulations, of a $\gamma = 5/3$ polytropic stellar structure. Khokhlov et al. (1993b,a) were the first to study stars with different stellar structures ($\gamma = (5/3, 1.5, 4/3)$) numerically. Ramirez-Ruiz & Rosswog (2009) studied the tidal disruption and initial disk formation for $\gamma = 5/3$ and $\gamma = 1.4$ polytropes in 3D hydrodynamics. Guillochon & Ramirez-Ruiz (2013a) performed the first systematic parameter-space study of the effect of both stellar structure and impact parameter, exploring $\gamma = 4/3$ and $\gamma = 5/3$ polytropes and a wide range of impact parameters. The effect of impact parameter made it clear that tidal disruptions are a 3-dimensional nonlinear hydrodynamical problem that needs to be studied by simulations, at least to a certain extent. Laguna et al. (1993) were the first to explore relativistic tidal disruptions, on a Schwarzchild met-

ric. Diener et al. (1997) studied the disruption of a $\gamma = 5/3$ polytrope by a rotating BH on a Kerr metric. Haas et al. (2012) simulated the disruption of a white dwarf by a spinning BH. Cheng & Bogdanović (2014a) and Tejeda et al. (2017b) compared relativistic simulations to Newtonian simulations in detail, finding good agreement for non-relativistic encounters. Gafton & Rosswog (2019b) performed a grid of general-relativistic simulations for a $\gamma = 5/3$ polytrope, exploring higher impact parameters and spinning BH's, providing new fitting formulae for the relativistic regime, and again finding good agreement for non-relativistic encounters. See also Stone et al. (2019) for a review of the status of TDEs in general relativity. Rosswog et al. (2008a,b, 2009) studied the tidal disruption of white dwarfs in detail for the first time, while MacLeod et al. (2012a) were the first to study the tidal disruption of giant stars, whose highly segregated density profiles did not allow them to be fully disrupted. Law-Smith et al. (2017a) performed a case-study simulating realistic stellar structures and compositions, with a hydrogen-envelope helium-core white dwarf. Golightly et al. (2019a) studied the stellar spin dependence of fallback rates for a $\gamma = 5/3$ polytrope. Goicovic et al. (2019) ran moving-mesh simulations of a ZAMS $1M_{\odot}$ star with MESA stellar structure. Their results were consistent with the $\gamma = 4/3$ result from Guillochon & Ramirez-Ruiz (2013a). Golightly et al. (2019b) ran simulations with MESA stellar structures, for three stellar masses and ages, at one impact parameter $\beta = 3$, and argued that the inferred BH mass from fitting TDEs to polytropic hydrodynamical simulations can be incorrect at the order-of-magnitude level. Law-Smith et al. (2019) performed simulations with MESA stellar structures and a Helmholtz EOS, tracking chemical abundances for 49

elements in the 3D hydrodynamical simulations for the first time. They found significant differences with the polytropic results of Guillochon & Ramirez-Ruiz (2013a) and also significant differences with the analytic predictions of the fallback-rate composition of Gallegos-Garcia et al. (2018). Ryu et al. (2020a,b,c,d) recently posted results of a parameter-space study using a fully general-relativistic framework, for a range of stellar masses, impact parameters, and BH masses, and at a single stellar age (see Sections 7.2 and 7.5 for comparisons).

A number of theoretical studies have focused on the disk formation process (e.g., Ayal et al. 2000; Hayasaki et al. 2013a; Guillochon et al. 2014a; Shiokawa et al. 2015; Piran et al. 2015b; Guillochon & Ramirez-Ruiz 2015a; Dai et al. 2015; Hayasaki et al. 2016; Bonnerot et al. 2016a; Lu & Bonnerot 2020; Bonnerot & Lu 2020). At present, the emission mechanism(s) responsible for the Optical/UV emission in TDE flares is an open question—the main candidates are (1) rapid disk circularization and accretion emission or (2) stream self-intersections and disk-formation-process emission—, but it is clear that the Optical/UV luminosity evolution of TDEs (the "light curve") tracks the mass fallback rate to the BH (dM/dt, the main output of the simulations in this work) very closely (see references above). This means that the fallback rate, which, as we show in this paper, is nearly solely determined by stellar structure, is a useful output.

In this paper, we study the disruption of main-sequence (MS) stars in a grid of stellar mass, stellar age, and impact parameter. Previously published systematic studies have used polytropic stellar structures, where $P = K\rho^{\gamma} = K\rho^{(n+1)/n}$. This work is a

parameter space study using realistic internal stellar structures, chemical abundances, and equations of state (EOS). We significantly expand upon the stellar structure study of Guillochon & Ramirez-Ruiz (2013a) by considering a wide range of density profiles derived from more accurate stellar models (as compared to polytropes): we study 14 distinct stellar structures, corresponding to different stellar masses and ages. The EOS is incorporated via the Helmholtz EOS, consistent with the MESA EOS of the stellar models. We find (see Appendix) that the EOS contribution to the pressure support is small, and we argue that one can predict many of the properties of tidal disruption from stellar structure and impact parameter alone. In order to reduce our simulations into one relationship for various tidal disruption quantities, we parameterize the stellar structure by the single parameter $\rho_c/\bar{\rho}$, the ratio of the star's central density to its average density. The simulations presented in this work have a full Helmholtz EOS tracking 49 elements; however, we study the chemical abundance of the fallback debris in a followup paper.

This paper is organized as follows: Section 7.2 describes our methods, Section 7.3 describes our results, Section 7.5 concludes, and the Appendix describes the interpolated `STARS_library` tool, as well as several other issues.

6.2 Methods

We use the 1D stellar evolution code MESA (Paxton et al. 2011) to run a grid of models from $0.1M_\odot$ to $10M_\odot$, from pre-MS to zero-age main-sequence (ZAMS) to terminal-age main-sequence (TAMS). We define TAMS as a central hydrogen mass

fraction of 10^{-3}. We use the `mesa_49.net` nuclear network, including 49 elements. See also Gallegos-Garcia et al. (2018) and Law-Smith et al. (2019) for details on the MESA setup. Table 6.3 in the Appendix lists relevant or non-standard parameters for the MESA simulations. Stars with $M_\star \lesssim 0.8 M_\odot$ have a MS lifetime longer than the age of the universe; thus, for these stars, the oldest model we use in our tidal disruption calculations is at 10 Gyr, rather than TAMS.

We then map the 1D stellar density profiles and chemical abundances into the 3D adaptive-mesh refinement (AMR) hydrodynamics code FLASH (Fryxell et al. 2000). We use the Helmholtz EOS and an extended Helmholtz table[27] that spans $10^{-12} \leq \rho$ [g/cm^3] $\leq 10^{15}$ and $10^3 \leq T$ [K] $\leq 10^{13}$. This Helmholtz EOS is the backbone of the EOS module in MESA, so our mapping is self-consistent. In FLASH, we use the sinks module to integrate trajectories and to track the position of the BH relative to the star, as in Guillochon & McCourt (2017). This is also an update from Guillochon & Ramirez-Ruiz (2013a). We begin the simulations at $r = 10 r_{\rm t}$, where tidal effects are negligible.[28] In the multipole gravity solver, we use a maximum angular number of the multipole expansion of $l_m = 20$. Our 3D box is $1000 R_\star$ on a side and we set the background density to 10^{-11} g/cm^3. This is such that the mass of the box is typically $\ll 0.1\%$ of the stellar mass. We use the following hydrodynamics parameters: the interpolation order is 3rd order, the slope limiter is the "hybrid" one, and we use the hybrid Riemann solver. We have no magnetic fields ($B = 0$). As in Guillochon & Ramirez-Ruiz (2013a), in calculating the binding energy of each cell in the simulation

[27] Available at `http://cococubed.asu.edu/code_pages/eos.shtml`.
[28] For comparison, Goicovic et al. (2019) begin at $r = 5 r_{\rm t}$.

with respect to the BH and stellar debris, we shift the center of mass of the star to be on a parabolic orbit (this is equivalent to centering the dM/de distribution at $e = 0$). Note that in this paper e denotes the specific orbital energy and not eccentricity. Guillochon & Ramirez-Ruiz (2013a) show that, because of the magnitude of this shift, it only affects the dM/dt for $t > 100$ yrs. For the vast majority of events, the star is expected to approach on a parabolic or nearly-parabolic orbit (Hayasaki et al. 2018). See also Guillochon et al. (2009), Guillochon et al. (2011), Guillochon & Ramirez-Ruiz (2013a), and Law-Smith et al. (2019) for details on the FLASH setup. Table 6.4 in the Appendix lists several additional FLASH parameters, including the background grid values.

The simulations in this paper are run with 1.5×10^8 maximum cells. This is a higher maximum cell count than in Law-Smith et al. (2019). We choose the maximum initial refinement based on the central concentration of the stellar density profile. We use 131 cells across the diameter of the star for less centrally concentrated stars ($\rho_c/\bar{\rho} \lesssim 150$) and 524 cells across the diameter of the star for more centrally concentrated stars ($\rho_c/\bar{\rho} \gtrsim 150$). In a few test simulations, results are nearly identical if we use 262 or 524 cells across the diameter of the star for the less centrally concentrated stars as well. See Section 6.13 for our numerical convergence study. For comparison, the simulations in Guillochon & Ramirez-Ruiz (2013a) had ≈50 cells across the initial diameter, so our simulations have a factor of 2.6X to 10.5X higher initial resolution. The moving-mesh simulations of Goicovic et al. (2019) have a maximum of 2.4×10^5 cells, thus initially ≈60 cells across the diameter of the star. The simulations of Ryu et al. (2020a,b,c,d) initially have ≈50 cells across the diameter of the star and, in an important difference,

the final box size is $17 \times 9 \times 14 R_\star$.

Table 6.1: FLASH simulation grid in stellar mass, stellar age, and impact parameter. The simulations in this grid are interpolated in each of these dimensions in order to produce the library. Scaled results are indicated by $*$ for polytropes and † for our simulations (see text). The ratio of the central to average density $\rho_c/\bar{\rho}$, the dynamical time of the star $t_{\rm dyn}$, and the corresponding $r_{\rm p}/r_{\rm g}$ for each β is also listed.

$M_\star$	$R_\star$	stellar age	$\rho_c/\bar{\rho}$	$t_{\rm dyn}$	$\beta \equiv r_{\rm t}/r_{\rm p}$	$r_{\rm p}/r_{\rm g}$
0.1 $M_\odot$	0.1214 $R_\odot$	0 Gyr	5.5	213 s	0.5–1.2*	25–10
	0.1215 $R_\odot$	10 Gyr	5.5	213 s	0.5–1.2*	25–10
0.3 $M_\odot$	0.2814 $R_\odot$	0 Gyr	5.8	434 s	0.6, 0.7, 0.8, 0.9, 1.0, 2.0	33, 28, 25, 22, 20, 10
	0.2989 $R_\odot$	10 Gyr	5.8	475 s	0.6, 0.7, 0.8, 0.9, 1.0, 2.1	35, 30, 26, 23, 21, 10
0.5 $M_\odot$	0.4452 $R_\odot$	0 Gyr	11	669 s	0.6, 0.8, 1.0, 1.15, 1.4, 2.6	44, 33, 26, 23, 19, 10
	0.4564 $R_\odot$	10 Gyr	12	715 s	0.6, 0.8, 1.0, 1.2, 1.4, 2.8	46, 35, 28, 23, 20, 10
0.7 $M_\odot$	0.6485 $R_\odot$	0 Gyr	23	994 s	0.75, 1.0, 1.25, 1.5, 3.4	46, 34, 28, 23, 10
	0.6793 $R_\odot$	10 Gyr	36	1065 s	0.8, 1.0, 1.15, 1.3, 1.5, 1.7, 3.6	45, 36, 31, 28, 24, 21, 10
1.0 $M_\odot$	0.9012 $R_\odot$	0 Gyr	42	1362 s	1.0, 1.25, 1.5, 1.75, 2.0, 4.2	42, 34, 28, 24, 21, 10
	1.0455 $R_\odot$	4.8 Gyr	138	1702 s	1.0, 1.5, 2.0, 2.5, 3.0, 3.5, 4.9	49, 33, 24, 20, 16, 14, 10
	1.2872 $R_\odot$	8.4 Gyr	756	2325 s	1.0, 1.5, 2.0, 3.0, 4.0, 4.5, 5.0, 6.0	60, 40, 30, 20, 15, 13, 12, 10
1.5 $M_\odot$	1.6275 $R_\odot$	0 Gyr	128	2699 s	1.0, 1.5, 2.0, 2.75, 6.7	67, 51, 34, 24, 10
	2.0805 $R_\odot$	2 Gyr	1697	3901 s	2.0, 4.0, 6.0, 8.6	43, 21, 14, 10
3.0 $M_\odot$	1.8896 $R_\odot$	0 Gyr	73	2387 s	0.6–4.0*	103–15
	3.3192 $R_\odot$	0.3 Gyr	1198	5558 s	1.5, 2.0, 3.0, 4.0, 4.5, 5.0, 7.0, 10.8	72, 54, 36, 27, 24, 22, 16, 10
10 $M_\odot$	3.6870 $R_\odot$	0 Gyr	38	3564 s	1.0–4.2†	80–19

Table 6.1 (cont'd): FLASH simulation grid in stellar mass, stellar age, and impact parameter. The simulations in this grid are interpolated in each of these dimensions in order to produce the library. Scaled results are indicated by $*$ for polytropes and † for our simulations (see text). The ratio of the central to average density $\rho_c/\bar{\rho}$, the dynamical time of the star $t_{\rm dyn}$, and the corresponding $r_{\rm p}/r_{\rm g}$ for each β is also listed.

$M_\star$	$R_\star$	stellar age	$\rho_c/\bar{\rho}$	$t_{\rm dyn}$	$\beta \equiv r_{\rm t}/r_{\rm p}$	$r_{\rm p}/r_{\rm g}$
	8.4232 $R_\odot$	0.02 Gyr	1292	12307 s	1.5–10.8†	123–17

Table 6.1 lists the parameter space in stellar mass, stellar age, and impact parameter studied in this work. For each star, we run a range of impact parameters β (the ratio of the tidal radius to the pericenter distance) from grazing partial disruptions to post-critical disruptions. The lowest β for a given star corresponds to 1% to 10% mass lost (unbound) from the star in the encounter. We run one very-post-critical (post-full-disruption) β for each star such that $r_{\rm p} = 10r_{\rm g}$ for this highest β encounter, where $r_{\rm g} \equiv GM/c^2$ in this paper. This is for the purpose of interpolating our grid of dM/dt curves in the maximum applicable range. We also plan to extend this library with relativistic simulations (applicable to the small fraction of very relativistic encounters) in future work. For comparison, the most relativistic encounter in Guillochon & Ramirez-Ruiz (2013a) was the $\beta = 4$ for the $\gamma = 4/3$ star, which was $r_{\rm p} = 11.8r_{\rm g}$.

Table 6.1 also lists several other quantities, such as the ratio of the star's central density to average density $\rho_c/\bar{\rho}$ (a parameterization of the central concentration of the star that we use extensively later on), the dynamical time of the star, defined in this paper as $t_{\rm dyn} \equiv \sqrt{R_\star^3/GM_\star}$, and the ratio of pericenter distance to gravitational radius, $r_{\rm p}/r_{\rm g}$, corresponding to each β. In order to extend the range of the interpolated fallback rate library (see Appendix), we include a few results scaled from simulations where the stellar structures are nearly identical. We scale $\gamma = 5/3$ results for the $0.1M_\odot$ stars, $\gamma = 4/3$ results for the ZAMS $3M_\odot$ star, our ZAMS $1M_\odot$ results for the ZAMS $10M_\odot$ star, and our TAMS $3M_\odot$ results for the TAMS $10M_\odot$ star. Note that we do perform a $10M_\odot$, $\beta = 1.5$ simulation in Section 6.11 in our "stellar structure vs. EOS" study.

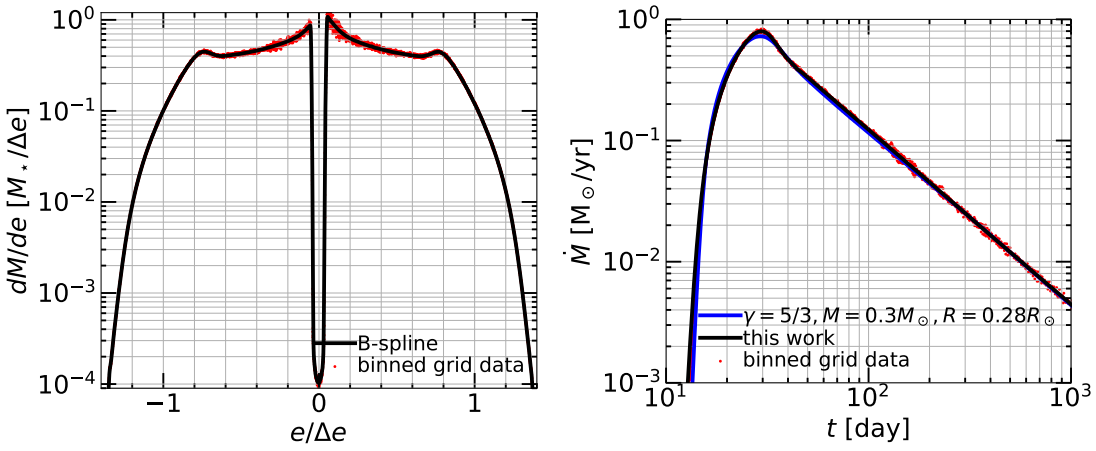

Figure 6.1: Specific binding energy distribution, dM/de, and resulting mass fallback rate to the BH, dM/dt, for a $0.3M_\odot$ ZAMS star constructed in MESA in a $\beta = 0.9$ encounter with a $10^6 M_\odot$ BH; this is a full disruption. The finely binned hydrodynamical grid data is shown in red and the B-spline fit (this work) in black. The x- and y-axis of the dM/de plot are normalized to the characteristic spread in binding energy, Δe (see text). The dM/dt plot also compares to a $\gamma = 5/3$ polytropic simulation for this β from Guillochon & Ramirez-Ruiz (2013a), scaled to the same mass and radius as this star, in blue. It is expected to match quite closely as the stellar structure of a $0.3M_\odot$ ZAMS star is well approximated by a $\gamma = 5/3$ polytrope (see Figure 6.17).

We run at a single BH mass of $M_{\rm BH} = 10^6 M_\odot$. Our simulations are directly applicable to any non-relativistic encounter with a different BH mass, to leading order in the "tidal approximation" ($R_\star/r \ll 1$), because of the scaling of t and dM/dt with $M_{\rm BH}$ in Eq. (6.4). See Figure 6.20 in the Appendix for the range of applicability of our simulations. This grid of simulations applies to tidal disruptions from most stellar masses, ages, impact parameters, and BH masses. For $r_{\rm p} > 10 r_{\rm g}$, the difference in dM/dt's between Newtonian and relativistic simulations is $\lesssim 10\%$ (see more detailed discussion in Section 7.5).

At the last timestep before debris begins to leave the computational domain, we calculate the specific binding energy of every cell in the simulation relative to the BH and the star (if any self-bound mass remains), including only material bound to the BH and excluding material bound to the star or unbound from the BH. From this spread in specific binding energy distribution, or dM/de, we calculate the mass return rate to the BH (more accurately, to pericenter) as a function of time, using Kepler's third law:

$$\frac{dM}{dt} = \frac{dM}{de}\frac{de}{dt} = \frac{dM}{de}\frac{1}{3}(2\pi G M_{\rm BH})^{2/3} t^{-5/3}. \tag{6.5}$$

We run the simulations to a maximum time of $100 t_{\rm dyn}$ and the star reaches pericenter at approximately $20 t_{\rm dyn}$ into the simulation. For moderate β's, the debris remains inside the box for $100 t_{\rm dyn}$, but for high β's the debris begins to leave the box earlier—for the most extreme β's we study this is at approximately $50 t_{\rm dyn}$. So dM/de distributions are calculated at 30–$80 t_{\rm dyn}$ after pericenter. Guillochon & Ramirez-Ruiz (2013a) studied fallback rates at up to $550 t_{\rm dyn}$ after pericenter, showing that the

resulting shape is identical to those calculated at earlier times as we do. By not having a large enough box to follow the entire debris for $t > 100t_{\rm dyn}$, we do not sacrifice any accuracy in the final result, but instead gain precision as a smaller box allows for higher resolution. Note that however, unlike in Ryu et al. (2020a,b,c,d), where debris leaves the computational domain after a few dynamical timescales, the debris in our simulations remains in the box for many dynamical timescales after pericenter. The effect this difference has on fallback rate determinations is unclear.

As an example of our analysis method, Figure 6.1 shows the specific binding energy distribution and resulting mass return rate to the BH for a $0.3M_\odot$ ZAMS star in a $\beta = 0.9$ encounter with a $10^6 M_\odot$ BH. dM/de is plotted in units of $M_\star/\Delta e$, where $\Delta e = GM_\star^{2/3} M_{\rm BH}^{1/3}/R_\star$, an order-of-magnitude estimate of the range in fluid binding energies (Stone et al. 2013). The x-axis is normalized similarly. The hydrodynamical grid data from the simulation is binned and then fit with a B-spline. The dM/dt is extended by finding the average slope of the last 10–20% of the dM/dt. The extended section is not visible on this plot as it is for $t \gtrsim 10^4$ s. The result for a $\gamma = 5/3$ polytrope, for this β, scaled to the same mass and radius as this star, is also shown. It is expected to match quite closely as the stellar structure of a $0.3M_\odot$ ZAMS star is well approximated by a $\gamma = 5/3$ polytrope (see Figure 6.17 in the Appendix).

The small differences between the polytropic and MESA initial condition simulations are likely due to differences in resolution, numerical method, and smoothing algorithm between the two works. The B-splines applied to smooth the dM/de distributions in this work have been examined and calibrated in detail for the dM/de result

from each simulation, and so the resulting dM/dt curves in this work have higher fidelity to the raw hydrodynamical grid data.

6.3 Results

6.3.1 Stellar structure

Figure 6.2 shows the ratio of central density to average density $\rho_c/\bar{\rho}$ for MS stars, interpolated based on a finely-spaced MESA grid (more finely spaced than for our TDE simulations; Table 6.1). This shows the range of stellar structures on the main sequence. We perform TDE simulations in FLASH for structures at the extremes and interpolate the resulting dM/dt's in stellar mass and stellar age in between these extremes. For some regions one can use polytropic stellar structures rather than MESA initial conditions (e.g., for $M_\star \lesssim 0.3 M_\odot$).

The top panels show $\rho_c/\bar{\rho}$ in the space of stellar age vs. stellar mass. Here one sees that lower-mass stars ($\lesssim 0.8 M_\odot$), whose main-sequence lifetimes are $\gtrsim$ the age of the universe, evolve slowly and have roughly constant stellar structures over 10 Gyr. More massive stars ($\gtrsim 0.8 M_\odot$) have shorter lifetimes and evolve through different stellar structures more rapidly. We expect a wide variety of stellar masses and stellar ages to source observed TDEs; see Section 7.5 for discussion.

The bottom panels show normalized density profiles colored by $\rho_c/\bar{\rho}$, both individually for the stars we simulate in FLASH and interpolated on a more finely-spaced grid of MESA stars. One can see that $\rho_c/\bar{\rho}$ maps nearly 1-1 onto the stellar density profile, at least for the main sequence. This makes it a very good single-value

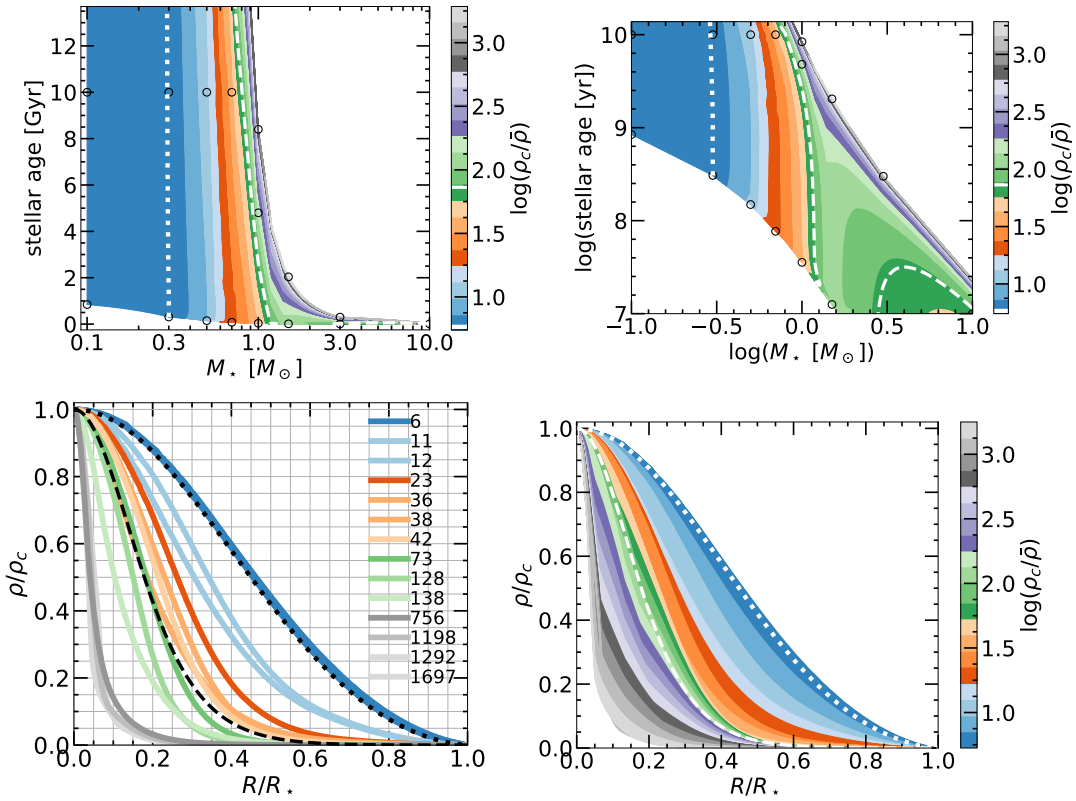

Figure 6.2: Stellar structure, parameterized by the ratio of central density to average density. Top: as a function of stellar mass and stellar age for MS stars, based on finely-spaced MESA grid. x-axis is log scale. y-axis is linear scale on left panel and log scale on right panel and its maximum is 13.8 Gyr. Dotted line corresponds to $\gamma \approx 5/3$ polytrope ($\rho_c/\bar{\rho} = 5.8$, from a ZAMS 0.3 $M_\odot$ star) and dashed line corresponds to $\gamma \approx 4/3$ polytrope ($\rho_c/\bar{\rho} = 73$, from a ZAMS 3 $M_\odot$ star). Black circles are stars for which we have done tidal disruption simulations in FLASH (note we run multiple β's for each star). Bottom: density profiles for MS stars, normalized to central density and stellar radius. Left panel is stars we have disrupted in FLASH (numbers in legend are $\rho_c/\bar{\rho}$) and right panel is based on finely-spaced MESA grid. Dotted and dashed lines are $\gamma = 5/3$ and $\gamma = 4/3$ polytropes respectively.

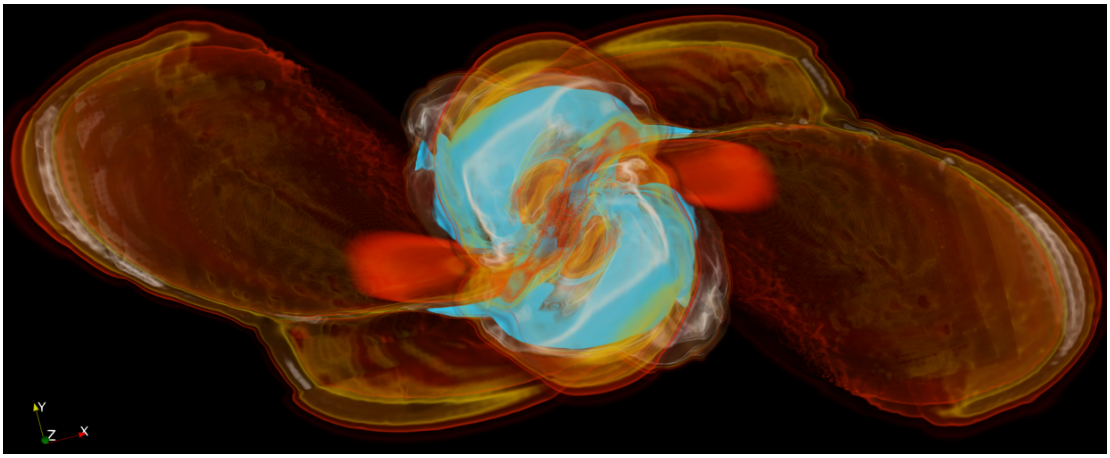

Figure 6.3: Volume rendering of a $1M_\odot$ ZAMS star at $t - t_\mathrm{p} \approx 3t_\mathrm{dyn}$ in a $\beta = 1$ encounter with a $10^6 M_\odot$ BH. Color corresponds to density, and the colorbar and transfer function are chosen to qualitatively highlight the stratified density structure of the debris. Videos of the simulations are available at https://www.youtube.com/channel/UCShahcfGrj5dOZTTrOEqSOA.

parameter to describe the stellar structure, and we use it to reduce our simulations into a single relationship and to provide fitting formulae for each TDE quantity.

For comparison, for giant stars, $\rho_c/\bar{\rho} \gtrsim 10^6$. In MacLeod et al. (2012a), due to numerical limitations, the authors use $\rho_\mathrm{core}/\bar{\rho} \approx 2 \times 10^3$ for the hydrodynamical simulations. They are unable to fully disrupt the giant stars, due to the highly segregated density profile (much more centrally concentrated than that of MS stars despite the artificial value of $\rho_\mathrm{core}/\bar{\rho}$) and extended envelope structure.

Figure 6.17 in the Appendix shows density profiles for each star we simulate as compared to $\gamma = 5/3$ and $\gamma = 4/3$ stellar structures. Also see Figure 1 in Law-Smith et al. (2019) for the stellar structure evolution of a $1M_\odot$ and $3M_\odot$ star over their MS lifetimes (also compared to polytropic stellar profiles). Only a few stars correspond closely to polytropic stellar structures; for all others, MESA initial conditions are significantly

more accurate.

6.3.2 Qualitative tidal disruption results

As an example of one of our FLASH simulations, Figure 6.3 shows a volume rendering of the disruption of a $1M_\odot$ ZAMS star at $t - t_\mathrm{p} \approx 3t_\mathrm{dyn}$ in a $\beta = 1$ encounter with a $10^6 M_\odot$ BH (where t_p is the pericenter time and t_dyn is the dynamical time of the star). Color corresponds to density. One can see the stratified structure following the disruption of a star with an accurate internal stellar structure. This encounter is a partial disruption in which a core survives. Note that this snapshot is zoomed in on the star in order to highlight the density structure of the debris a few dynamical times after pericenter, but that our computational domain is $1000R_\star$ on a side (roughly 100 times the size of this volume rendering), and the debris eventually expands to fill this.

As an example of the range of vulnerability to tidal disruption of our grid, Figure 6.4 shows 2D density slices of the disruption of several different stars at different impact parameters, all at $\approx 2t_\mathrm{dyn}$ after pericenter. The axes are arranged such that β increases from left to right, and central concentration ($\rho_c/\bar{\rho}$) increases from top to bottom. The white contours correspond to absolute values of density (1, 10^{-1}, and 10^{-2} g/cm^3), illustrating the different stellar structures and also the amount the different layers of the star are spun up. Increasing β both increasingly distorts the star and spins it up. The more centrally concentrated stars have "layers" that are more differentiated. This leads to the outer layers being torqued more than the inner layers, and the core remaining sequestered and undisturbed at higher β's for more centrally concentrated stars. Increasing central concentration allows the star to survive higher-β encounters.

For example, a ZAMS $0.3M_\odot$ star has a larger fraction of its mass at larger radii, and is thus fully disrupted by a $\beta = 1$ encounter, whereas a TAMS $1M_\odot$ star has only a small fraction of its mass at larger radii from its sequestered core, and is thus relatively undisturbed by a $\beta = 1$ encounter.

6.3.3 Mass lost

Figure 6.5 shows fractional mass lost from the star $\Delta M/M_\star$ as a function of impact parameter β. The x-axis in the top left panel is the raw β and the x-axis in the top right panel is normalized to the critical β for full disruption for each star. Generally, more massive stars and stars further along in their MS evolution are more centrally concentrated, and thus must be disrupted deeper relative to their nominal "tidal radii" in order to lose the same amount of fractional mass. One can see that the mass-loss prescriptions for $\gamma = 5/3$ and $\gamma = 4/3$ polytropes are inadequate to describe the more centrally concentrated stars, which have critical impact parameters of $\beta_{\rm crit} > 2$.

The bottom panels have a scaled x-axis,

$$x = \exp\left[(\beta/\beta_{\rm crit})^\alpha - 1\right], \quad \alpha = (\rho_c/\bar{\rho})^{-1/3}, \tag{6.6}$$

constructed by trial-and-error in order to reduce all of the simulations into a single relationship. The physical meaning of the functional form of x is unclear at present, but the sharp 1/3 factor suggests at least a partial physically-motivated origin as this number appears in basic TDE theory. This formula accounts for the dependence of ΔM vs. β on stellar structure. The fact that we are able to express all of the simulations

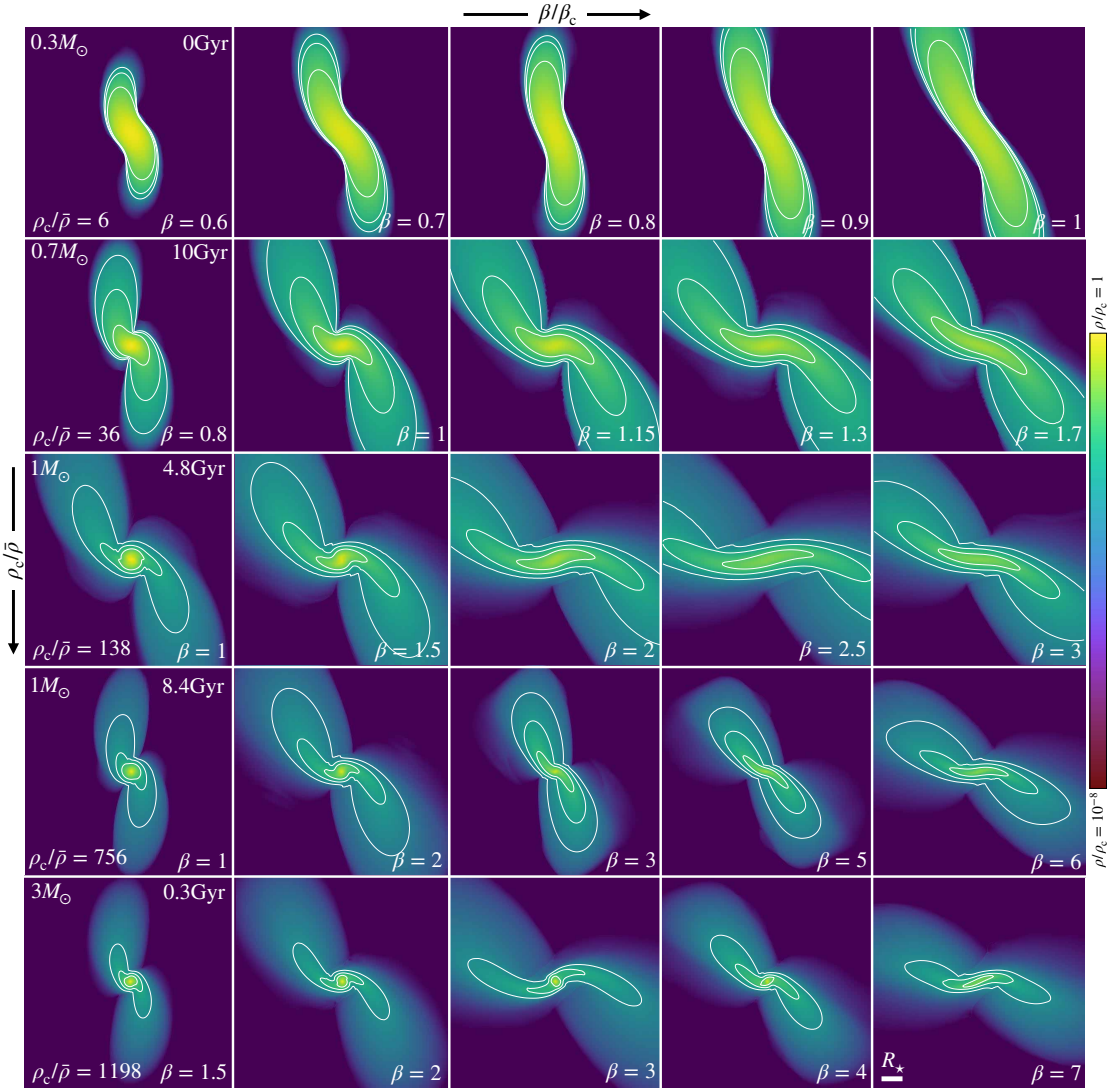

Figure 6.4: 2D density slices of a few different simulations. The axes of this plot grid are central concentration ($\rho_c/\bar{\rho}$) vs. impact parameter (β/β_c). Each row is a different star and each panel is a different impact parameter. β increases from left to right and $\rho_c/\bar{\rho}$ increases from top to bottom. Color is the logarithm of density and is normalized to the initial central density of the star, extending to 10^{-8} of this value. Each panel has width $10R_\star$. All panels are at $t - t_\mathrm{p} \approx 2t_\mathrm{dyn}$. White contours correspond to densities of 1, 10^{-1}, and 10^{-2} g/cm^3.

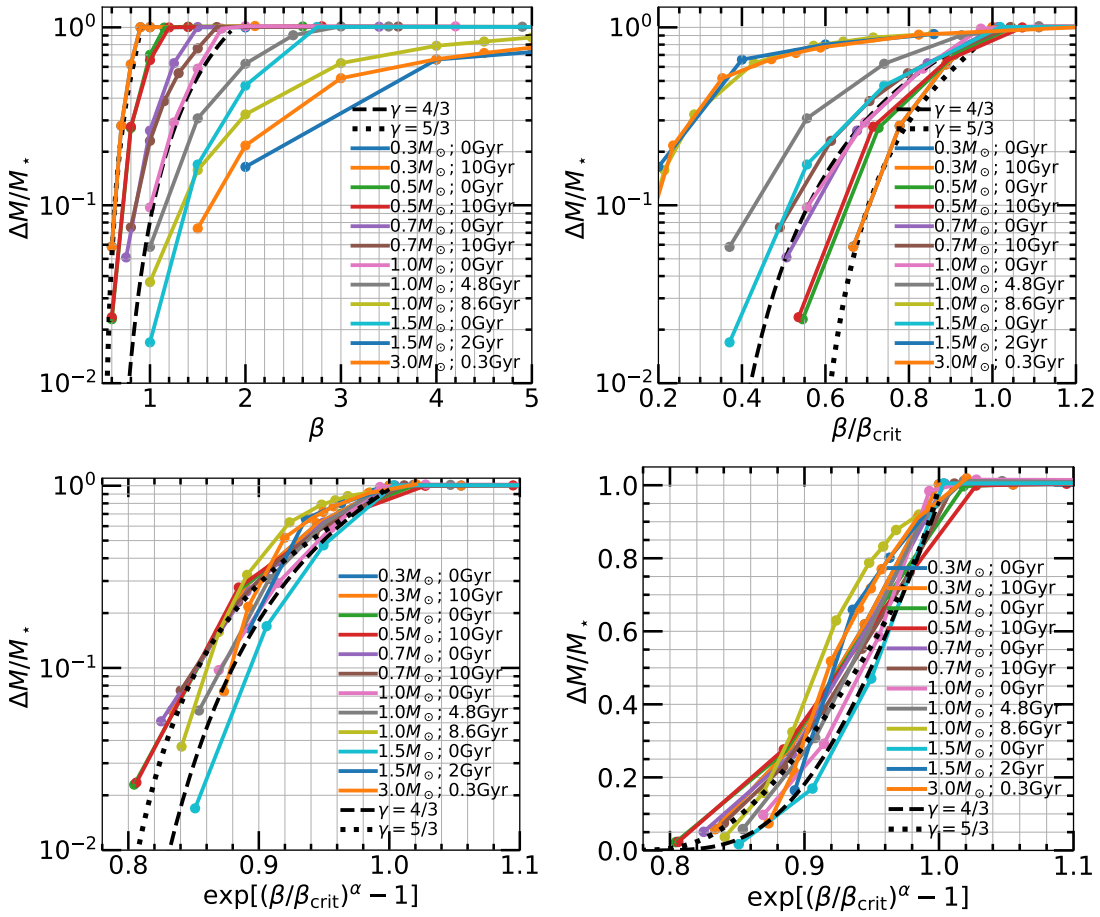

Figure 6.5: Top left: fractional mass lost $\Delta M/M_\star$ vs. impact parameter β. Top right: x-axis is normalized to the critical impact parameter for each star (see Table 6.2). Bottom left: x-axis is scaled with a structural parameter, $\alpha = (\rho_c/\bar{\rho})^{-1/3}$ (see text). Bottom right: linear y-axis. Results from Guillochon & Ramirez-Ruiz (2013a) for a $\gamma = 5/3$ and $\gamma = 4/3$ polytrope are shown by the dotted and dashed lines respectively.

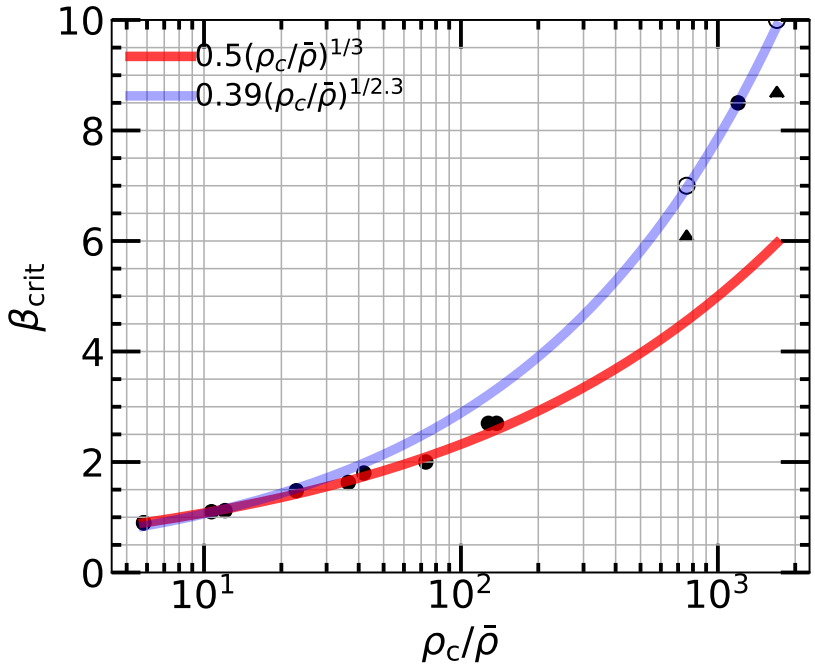

Figure 6.6: Critical impact parameter for full disruption $\beta_{\rm crit}$ vs. ratio of stellar central density to average density $\rho_c/\bar{\rho}$. Triangle markers indicate lower limits and open circles indicate extrapolation. Simple fits in red and purple. See Table 6.2 as well as Figure 6.19 in Appendix for dependence of $\beta_{\rm crit}$ and $(r_p/r_g)_{\rm crit}$ with stellar mass.

in a single relationship implies that ΔM depends only on $\rho_c/\bar{\rho}$ and β. Analytic and B-spline fits for this relation, allowing one to obtain the mass lost for any stellar mass, stellar age, and impact parameter, are provided in the Appendix. The simulations in this work all reduce to a single relation for other disruption quantities as well (see below in this section).

6.3.4 Critical impact parameter

We did not sample finely enough in β to find the exact critical impact parameter for full disruption for each star, but we estimate this within the bounds associated with our spacing in β and the mass lost as a function of β for the star. Figure 6.6 shows

the critical β as a function of $\rho_c/\bar{\rho}$. For nearly all stars, the critical β is well-fit by a simple relation,[29]

$$\beta_{\rm crit} \approx 0.5 \left(\frac{\rho_c}{\bar{\rho}}\right)^{1/3}, \quad \rho_c/\bar{\rho} \lesssim 500. \tag{6.7}$$

At the highest central concentrations ($\rho_c/\bar{\rho} \gtrsim 500$), the critical β is higher than predicted with this relation, and is instead better fit by a steeper relation,

$$\beta_{\rm crit} \approx 0.39 \left(\frac{\rho_c}{\bar{\rho}}\right)^{1/2.3}, \quad \rho_c/\bar{\rho} \gtrsim 500. \tag{6.8}$$

Equation (6.7) and Equation (6.8) allow one to predict the approximate critical impact parameter for full disruption for any main-sequence star. We note that already for $\rho_c/\bar{\rho} \gtrsim 100$, Equation (6.7) slightly underpredicts $\beta_{\rm crit}$, and that there is likely a smooth transition between the two power-law relationships, but we fit only two equations for simplicity. All one needs is $\rho_c/\bar{\rho}$ for that star, obtained from, e.g., a MESA model directly or pre-computed grids such as the MIST models (Choi et al. 2016). So the ability to fully disrupt a star is a simple function of this ratio of densities.

Note that for 2 points at the highest central concentrations, the quoted $\beta_{\rm crit}$ is obtained through extrapolation, as the maximum β simulated for that star did not fully disrupt it. The lower limits obtained from our simulations are also shown. We note also that the resolution (in term of maximum number of cells in the simulation) required to precisely determine $\beta_{\rm crit}$ becomes significantly higher for these most centrally concentrated stars. At the end of the simulation when the debris has expanded, and

[29] We note that this formula (for stars with lower central concentrations, $\rho_c/\bar{\rho} \lesssim 500$), is very similar to that found by Ryu et al. (2020b).

thus the linear resolution has decreased from the initial maximum level of refinement (in order to resolve the same number of cells in the simulation box), the highest density "core" of the star—for the stars with $\rho_c/\bar{\rho} \gtrsim 10^3$—becomes smaller than a grid cell and so is not resolved. However, the aim of this study is not to precisely determine the critical impact parameter for these most centrally concentrated stars, but rather to determine the mass fallback rate to the BH following their disruption.

Table 6.2 lists the critical impact parameter $\beta_{\rm crit}$ for full disruption for all stars studied. Errors represent the grid spacing and so are overestimates. We also list the corresponding physical pericenter distance in gravitational radii $r_{\rm p}/r_{\rm g}$. For stars that do not evolve significantly in structure over 10 Gyr, their $\beta_{\rm crit}$'s remain the same or very similar. For stars that evolve significantly over < 10 Gyr, the $\beta_{\rm crit}$ increases dramatically over a star's lifetime. For example, for a $1M_\odot$ star, the $\beta_{\rm crit}$ increases from $\approx$1.8 to $\approx$7.0, a factor of 3.9X, over its main-sequence lifetime, a result of its $\rho_c/\bar{\rho}$ increasing from 42 to 756. This corresponds to the critical $r_{\rm p}/r_{\rm g}$ for full disruption decreasing by a factor of 2.7X, from 23.4 to 8.6. Thus, a TAMS $1M_\odot$ star must approach 2.7X closer the BH in order to be fully disrupted compared to its ZAMS self. Similar trends are seen for the $1.5M_\odot$ and $3M_\odot$ stars, where the critical $r_{\rm p}/r_{\rm g}$ decreases by a factor >2X from ZAMS to TAMS. Thus, for higher-mass stars ($M_\star \gtrsim 0.8M_\odot$), at the same pericenter distance, the ZAMS star is roughly 2X as vulnerable to tidal disruption and associated mass loss as the TAMS star. For lower-mass stars ($M_\star \lesssim 0.8M_\odot$), the critical $r_{\rm p}/r_{\rm g}$ is roughly constant over 10 Gyr. See the Appendix for the dependence of $\beta_{\rm crit}$ and the associated $r_{\rm p}/r_{\rm g}$ with stellar mass.

Table 6.2: Critical impact parameter for full disruption $\beta_{\rm crit}$ and the corresponding physical pericenter distance in gravitational radii $r_{\rm p}/r_{\rm g}$. † indicates extrapolation and $*$ indicates polytropic result. See also Figure 6.6, Figure 6.19.

$M_\star$	$R_\star$	stellar age	$\beta_{\rm crit}$	$r_{\rm p}/r_{\rm g}$
0.3 $M_\odot$	0.2814 $R_\odot$	0 Gyr	0.9 ± 0.1	22.0
	0.2989 $R_\odot$	10 Gyr	0.9 ± 0.1	23.4
0.5 $M_\odot$	0.4452 $R_\odot$	0 Gyr	1.1 ± 0.1	24.0
	0.4564 $R_\odot$	10 Gyr	1.1 ± 0.1	24.7
0.7 $M_\odot$	0.6485 $R_\odot$	0 Gyr	1.5 ± 0.2	23.2
	0.6793 $R_\odot$	10 Gyr	1.6 ± 0.1	22.1
1.0 $M_\odot$	0.9012 $R_\odot$	0 Gyr	1.8 ± 0.1	23.4
	1.0455 $R_\odot$	4.8 Gyr	2.7 ± 0.2	18.1
	1.2872 $R_\odot$	8.4 Gyr	$7.0^\dagger$	8.6
1.5 $M_\odot$	1.6275 $R_\odot$	0 Gyr	2.7 ± 0.5	23.5
	2.0805 $R_\odot$	2 Gyr	$10^\dagger$	8.6
3.0 $M_\odot$	1.8896 $R_\odot$	0 Gyr	$2.0^* \pm 0.25$	30.8
	3.3192 $R_\odot$	0.3 Gyr	8.5 ± 1.5	12.7

As $\rho_c/\bar{\rho}$ increases, the star's expansion in response to mass loss decreases. As a result, the star becomes less vulnerable to tidal disruption and thus the critical impact parameter for full disruption monotonically increases with increasing $\rho_c/\bar{\rho}$. For example, note the transition in critical impact parameter from $\beta_{\rm crit} = 0.9 < 1$ for the $0.3M_\odot$ star to $\beta_{\rm crit} = 1.1 > 1$ for the $0.5M_\odot$ star. The $0.3M_\odot$ star corresponds to a $\gamma = 5/3$ polytrope (see Figure 6.17) and the $0.5M_\odot$ star has an intermediate structure in between a $\gamma = 5/3$ and $\gamma = 4/3$ polytrope. In the most extreme cases, for example for giant stars (MacLeod et al. 2012a) with a sequestered core-envelope structure, the remaining envelope contracts and thus its disruption requires increasingly higher β's for the same amount of mass loss (in fact, these stars are unable to be fully disrupted by massive BHs).

6.3.5 Mass fallback rates

All encounters

Figure 6.7 shows mass fallback rates dM/dt for all of our simulations, grouped by star. Each panel is a particular stellar mass and age, and shows all impact parameters β for that object. One can perhaps pick out trends in the shape of the dM/dt curves that we will explore in more detail below. Higher β generally corresponds to shifting the dM/dt curve upwards and to the left, giving a shorter peak timescale and higher peak fallback rate. After the critical β for full disruption, the dM/dt curve flattens, particularly near the peak. The rise and decay slopes also vary with stellar mass, stellar age, and impact parameter.

The top panels of Figure 6.8 show dM/dt's for a single stellar mass, $1M_{\odot}$, for all β's and stellar ages, in order to demonstrate the effect of stellar age. Note that the β's are not the same for each stellar age (see Table 6.1 or Figure 6.7). The left panel shows the raw curves and the right panel is normalized to the peak fallback rate ($\dot{M}_{\rm peak}$) and the associated peak fallback time ($t_{\rm peak}$) in order to focus on the rise and decay slopes. In the left panel, the curves largely overlap, demonstrating the degeneracy between stellar structure and β. This is similar to the shifting of dM/dt's from $\gamma = 5/3$ and $\gamma = 4/3$ polytropes to lie on top of each other demonstrated in Guillochon & Ramirez-Ruiz (2013a). This is why there is a degeneracy in the `MOSFiT` TDE fitting between stellar mass and impact parameter (and so radiative efficiency) (Mockler et al. 2019; Mockler & Ramirez-Ruiz 2020). In the right panel, one sees that the rise and decay slopes also largely overlap for a single stellar mass at multiple ages.

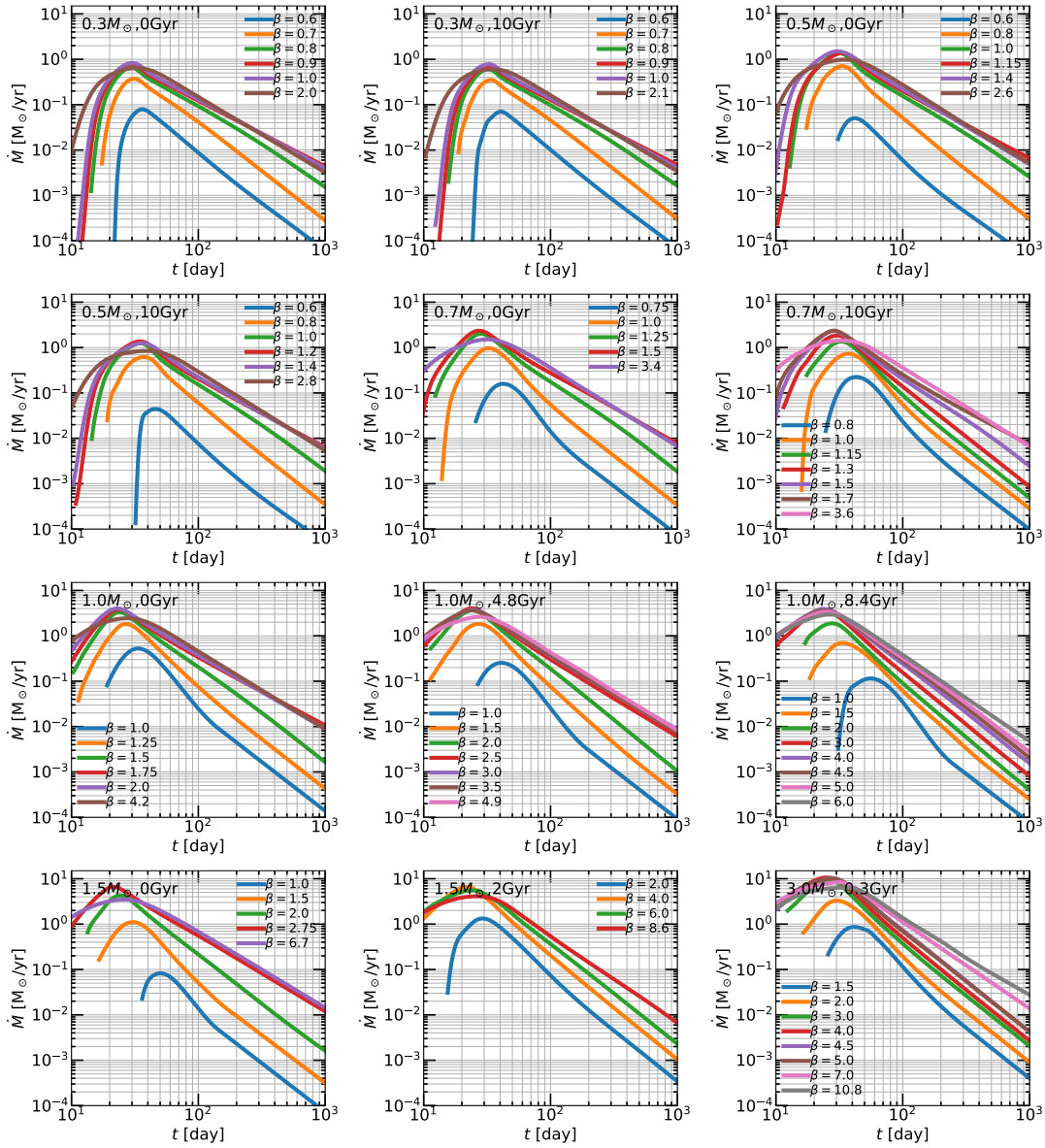

Figure 6.7: Mass fallback rate dM/dt to the BH as a function of time for all of our simulations. Each panel is a different star (stellar mass and stellar age, labeled in top left). Colors correspond to different impact parameters β.

Thus, it is more challenging to identify the age of the star by the light curve alone, due to the degeneracy introduced by β. However, stars of different age have significantly different compositions, and thus the stellar debris will have different chemical abundances. This is a promising avenue to distinguish stellar age, and indeed also stellar mass, if one can tie the composition of the fallback debris to observed spectral features. See Law-Smith et al. (2019) for a first study of the chemical abundance of the debris.

The middle and bottom panels of Figure 6.8 show dM/dt's for all of our simulations. The middle panels are colored by stellar mass, with multiple stellar ages and β's for each mass. From the middle left panel, evidently, more massive stars produce dM/dt curves with higher normalizations than less massive stars, but the peak timescales are similar if BH mass is constant. This in principle would offer a way to determine stellar mass in an observed TDE, but there is a degeneracy between stellar mass and efficiency in the current fitting of TDE observations (e.g., Mockler et al. 2019; Mockler & Ramirez-Ruiz 2020). One can have more efficient conversion of matter to radiation with a smaller total stellar debris mass, or a less efficient conversion of matter to radiation with a larger total stellar debris mass.

From the middle right panel, one sees that, generally, the rise slope is shallower with increasing stellar mass and (though this is more difficult to see) the decay slope is steeper with increasing stellar mass. The rise slope is a stronger trend, whereas the decay slope appears to mainly be a function of the fact that for more massive stars, a higher fraction of encounters studied in this work are partial disruptions. Indeed, with

lower β encounters being more likely, it is more likely to have a steeper decay slope for a more massive star. We also tabulate the asymptotic power law indices n_∞ later on in this section.

The bottom panels are colored by $\rho_c/\bar{\rho}$. In the bottom right panel, one can see that more centrally concentrated stars have shallower rise slopes and (though it is difficult to see because of the density of lines) steeper decay slopes. The fact that more centrally concentrated stars have slower rises can be understood by thinking about (1) the density profile of the star and (2) the hydrodynamics of disruption. First, stars with higher values of $\rho_c/\bar{\rho}$ have relatively more extended, lower density envelopes. Just considering the undisturbed spherically-symmetric profile (see Figure 6.17), the material that will be most bound to the BH has a slower transition in density, leading to a shallower rise slope. Stars with lower values of $\rho_c/\bar{\rho}$, on the other hand, have more uniform density profiles, and their outer layers exhibit a sharper transition in density, leading to a steeper rise slope. Second, there is a hydrodynamical effect that, for a more centrally concentrated star, the outer layers are more vulnerable to tidal disruption and this material is thus further stretched out post-disruption (compare the density contours in Figure 6.4). This results in a greater difference in rise slopes than might be predicted from the undisturbed density profiles alone. This can be seen more clearly in Figure 6.9, which shows only full disruptions and has fewer profiles plotted. The fact that more centrally concentrated stars have faster decays relates to the survivability of the core. While full disruptions decay closer to $\propto t^{-5/3}$, the presence of a surviving core changes the binding energies of the material bound to the BH (Guillochon & Ramirez-Ruiz

2013a). This results in a steeper decay slope when there is a surviving core (Coughlin & Nixon 2019, discuss this effect in more detail). See also Ryu et al. (2020c) for further discussion. The transition between partial disruptions and full disruptions occurs at higher β's with increasing $\rho_c/\bar{\rho}$; thus, more centrally concentrated stars are more likely to exhibit steeper decays.

The structure of the star is imprinted on the shape and slope of the fallback curve. It is thus easier to determine the stellar structure of the disrupted star in an observed TDE than more degenerate properties such as stellar mass and stellar age. This also hints that in principle, there may be a mapping from a single structural parameter such as $\rho_c/\bar{\rho}$, in combination with β, to the shape of the dM/dt. One can imagine a mapping in which $M_\star$ gives the normalization of the dM/dt while $\rho_c/\bar{\rho}$ gives the "tilt" corresponding to the rise and decay slopes.

Full disruptions

Figure 6.9 shows only critical (full) disruptions for all stellar masses and ages. These encounters thus all have the same fractional mass lost $\Delta M/M_\star \approx 1$. Here the trends are more evident than in Figure 6.8, though the decay slopes are relatively similar, as all full disruptions give $n_\infty \approx -5/3$ (see below in the section). The top panels show a single stellar mass $M_\star = 1 M_\odot$ in order to highlight the stellar age dependence. Here the actual amount of mass unbound from the star ΔM and thus the mass eventually fed to the BH, $\approx \Delta M/2$, is identical between the stars. The rise slopes are shallower with increasing stellar age.

The middle panels are colored by stellar mass. In the left panel one primarily

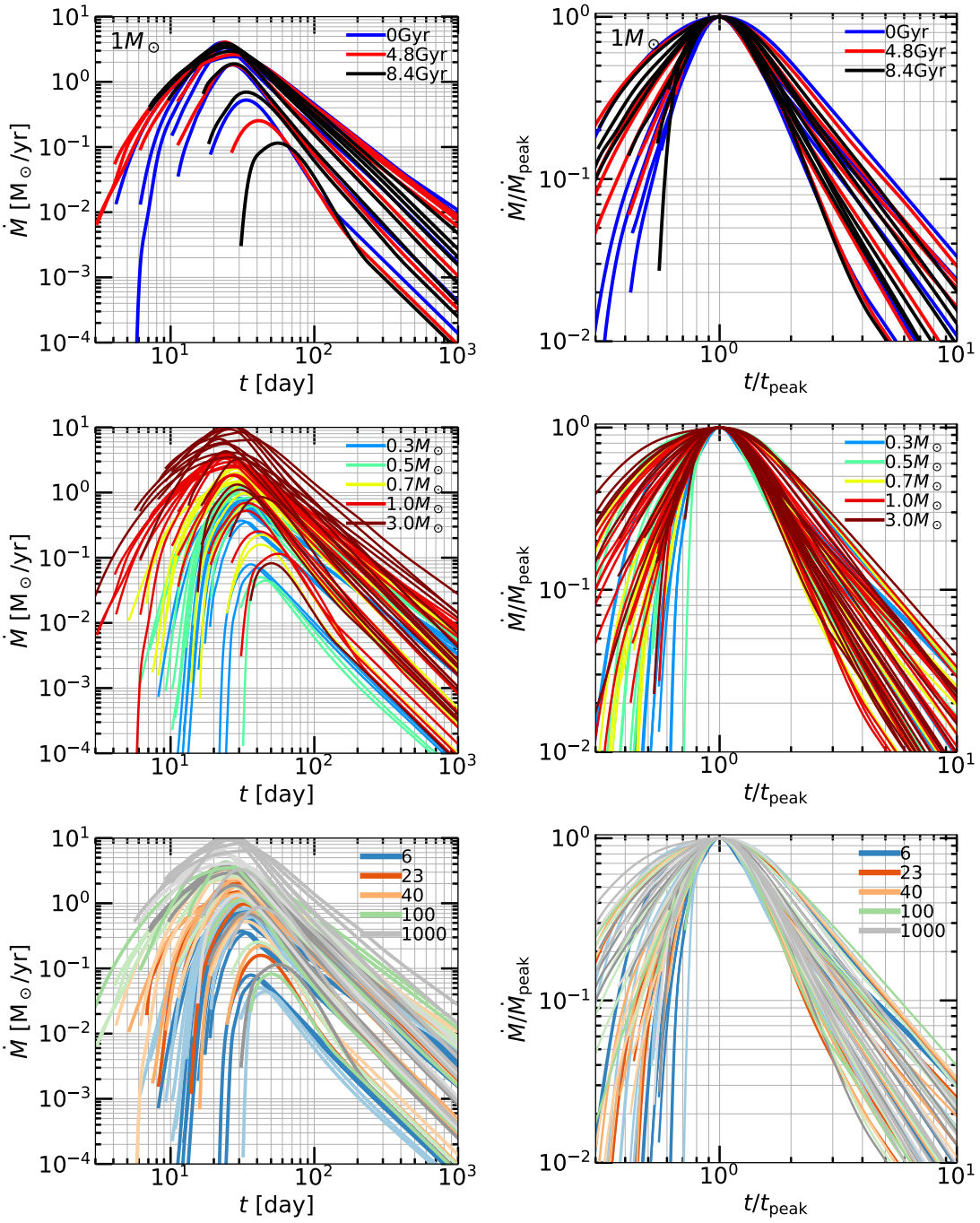

Figure 6.8: Mass fallback rate to the BH as a function of time for all of our simulations. Left panels: raw; right panels: normalized to peak. Top: only $M_\star = 1M_\odot$, all β's, 3 stellar ages. Middle: color corresponds to $M_\star$. Bottom: color corresponds to $\rho_c/\bar{\rho}$ for the star (with the same colors as in Figure 6.2) and the legend indicates a few reference values.

sees the normalization to dM/dt given by $M_\star$. With increasing $M_\star$, the dM/dt curve is shifted upwards and slightly to to the left. In the right panel, one sees that the rise slopes are shallower with increasing stellar mass. There is a weak trend towards steeper decay slopes with increasing stellar mass.

The bottom panels are colored by $\rho_c/\bar{\rho}$. Here one sees perhaps most clearly the trends discussed above, as we are coloring by the key physical parameter. It appears that, for the same $\Delta M/M_\star$, $\rho_c/\bar{\rho}$ nearly uniquely determines the rise slope of dM/dt (this is also true for the decay slope, but is more clear when we study n_∞ vs. β below). Increasing central concentration leads to shallower rise slopes, and, for full disruptions, similar decay slopes. See discussion above for the physical intuition behind this effect.

At fixed mass lost

Figure 6.10 shows a comparison of dM/dt curves at fixed mass lost ΔM. This allows one to compare fallback rates for the same amount of total material supplied to the BH. We compare at $\Delta M = (0.1, 0.3, 0.5, 0.7, 1.0)M_\odot$; half of this unbound material returns to the BH. Of course, some values of ΔM are inaccessible to some stellar masses. To do this, we construct a very finely interpolated grid (see Appendix) of impact parameters for each star, and select the β for which the dM/dt integrates to the given ΔM.

The top five panels show stars at 0 Gyr (ZAMS) and the bottom five panels show stars at 10 Gyr (or TAMS for $M_\star \geq M_\odot$). If the efficiency of conversion of matter to light is relatively constant, then the total energy radiated in a TDE is determined by ΔM. Thus, this figure shows dM/dt's from a stellar population at a single age, and

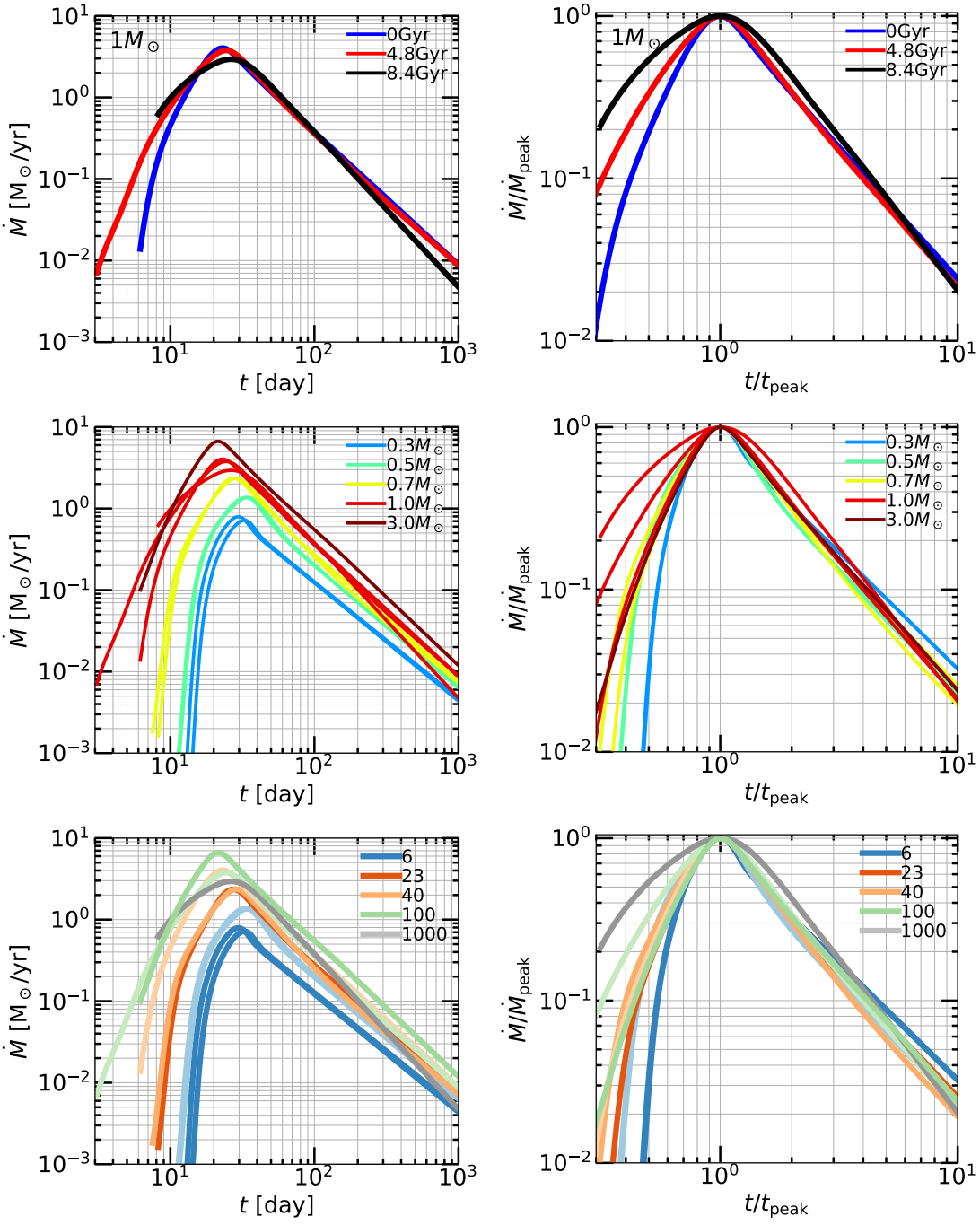

Figure 6.9: Same as Figure 6.8, but only critical (full) disruptions. Top: only $M_\star = 1M_\odot$, colored by stellar age. Middle: colored by stellar mass. Bottom: colored by $\rho_c/\bar{\rho}$.

(assuming constant efficiency) for a given radiated energy.

At fixed ΔM, the shape of the dM/dt's vary significantly with stellar mass. The peak fallback rate, the peak timescale, and the rise and decay slopes all vary significantly. Most strikingly, for both stellar age populations, the decay slopes are steeper with increasing stellar mass. This is because for the same ΔM, the encounter is more of a partial disruption for higher stellar masses. Higher stellar masses also correspond to higher $\dot{M}_{\rm peak}$ values (by up to a factor of $\approx$5) at fixed ΔM. The differences in the shape of the dM/dt's are not particularly more or less significant for different values of ΔM. These differences suggest that fitting TDEs with this library of fallback rates will allow for better determination of stellar properties, and perhaps that the nature of the disrupted star can be determined from the light curve alone.

6.3.6 Derived quantities

Peak timescale and fallback rate

Next we discuss quantities derived from the $\dot{M}_{\rm fb}$ results. The top panels of Figure 6.11 show the peak mass fallback rate $\dot{M}_{\rm peak}$ and the associated peak time $t_{\rm peak}$ as a function of impact parameter β. The $t_{\rm peak}$'s are plotted with a linear y-axis and so may appear to vary significantly, but nearly all $t_{\rm peak}$ values are $\approx$20–40 days. This is because the mass-radius relationship of main sequence stars nearly cancels out the $M_\star$ and $R_\star$ dependence ($M_\star^{-1}R_\star^{3/2}$) in Equation (6.4). The general trend is that $t_{\rm peak}$ decreases sharply with β until full disruption and then increases more slowly post critical-β.

The $\dot{M}_{\rm peak}$ values show a marked $M_\star$ dependence, and span several orders of

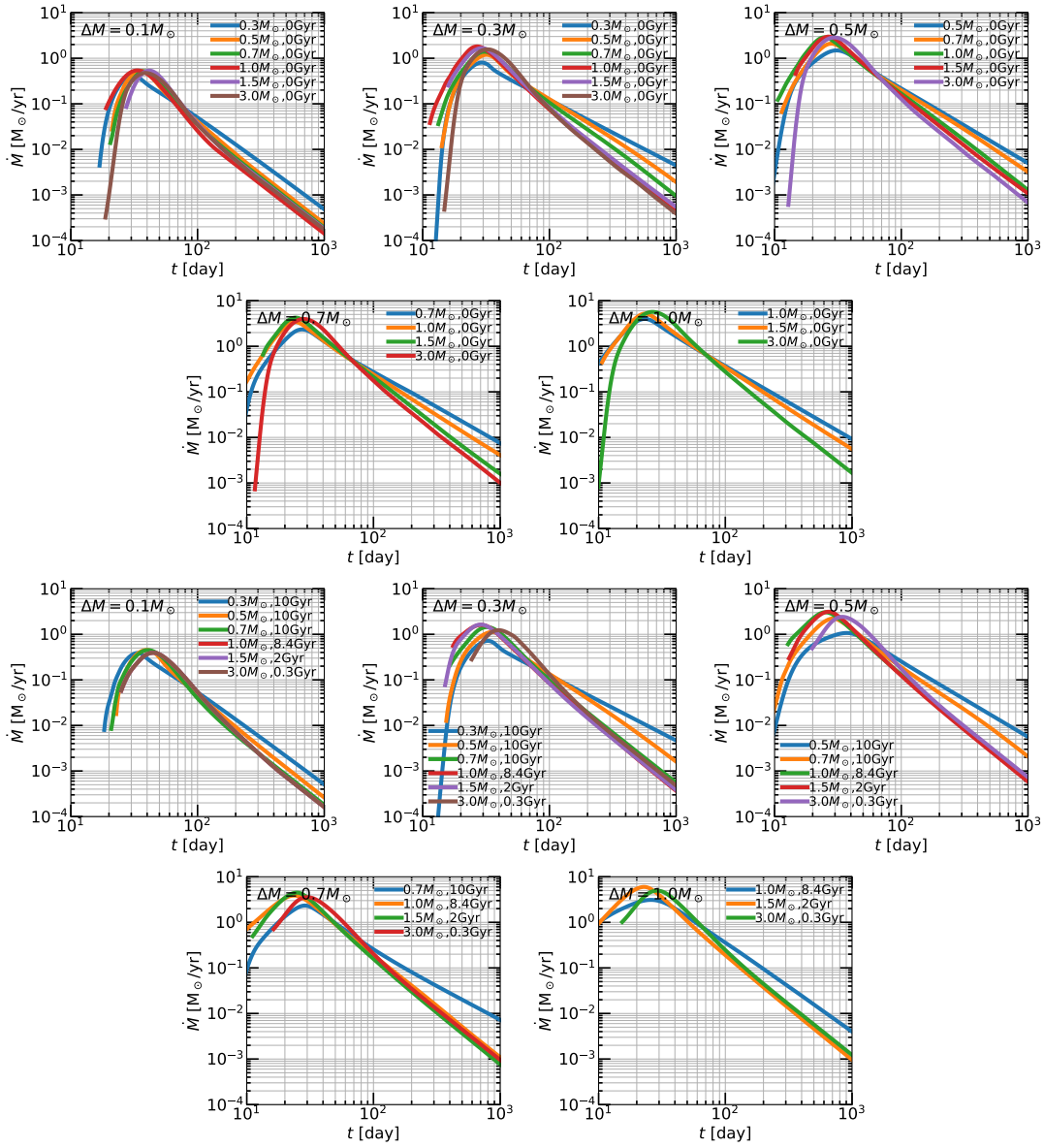

Figure 6.10: Comparison of dM/dt curves at a fixed mass lost ΔM. Top 5 panels are stellar ages of 0 Gyr and bottom 5 panels are stellar ages of 10 Gyr (or TAMS for $M_\star \geq M_\odot$). These are interpolated dM/dt curves at the particular β for each star that corresponds to the ΔM in the top left of each panel.

magnitude. We can understand this because of the $M_\star$ and $R_\star$ dependence ($M_\star^2 R_\star^{-3/2}$) in Equation (6.4) has a higher power on $M_\star$ than in the $t_{\rm peak}$ scaling. The general trend is that $\dot{M}_{\rm peak}$ increases sharply with β until full disruption and then decreases more slowly post critical-β. Trends for both $t_{\rm peak}$ and $\dot{M}_{\rm peak}$ are qualitatively similar to the Guillochon & Ramirez-Ruiz (2013a) simulations, but our study spans a wider range due to the many different stellar structures. Focusing on the $1 M_\odot$ star at 3 ages for comparison, at the same β, the more centrally concentrated (older) star peaks later and has a lower peak fallback rate.

In the bottom panels of Figure 6.11, the x-axis is scaled with the structural parameter $\alpha = (\rho_c/\bar{\rho})^{-1/3}$ in the same way as in Figure 6.5. Here $\dot{M}_{\rm peak}$ is also normalized by the stellar mass. Note that unlike for $\Delta M/M_\star$ in Figure 6.5, the y-axes of these two plots are not normalized to be unitless, and so have some spread (note that $t_{\rm peak}$ appears to have more spread, but it is on a linear scale). Despite this, nearly all of the simulations collapse into one coherent relationship. Fitting formulae for $t_{\rm peak}$ and $\dot{M}_{\rm peak}$ are provided in the Appendix, such that one can obtain the $t_{\rm peak}$ and $\dot{M}_{\rm peak}$ for any stellar mass, stellar age, and impact parameter.

Figure 6.12 shows the quantity $\dot{M}_{\rm peak} \times t_{\rm peak}/M_\star$ vs. β scaled with structural parameter as above. To order-of-magnitude, $\dot{M}_{\rm peak} \times t_{\rm peak}/M_\star \approx \Delta M_{\rm bound}/M_\star \approx \Delta M/2M_\star$, so this relation is similar to the bottom left panel of Figure 6.5. This is a good internal consistency check. Note that the integrated dM/dt is only approximately equal to the product of its peak values (e.g., for full disruptions $\Delta M/2M_\star = 0.5$, while $\dot{M}_{\rm peak} \times t_{\rm peak}/M_\star$ asymptotes to $\approx$0.25).

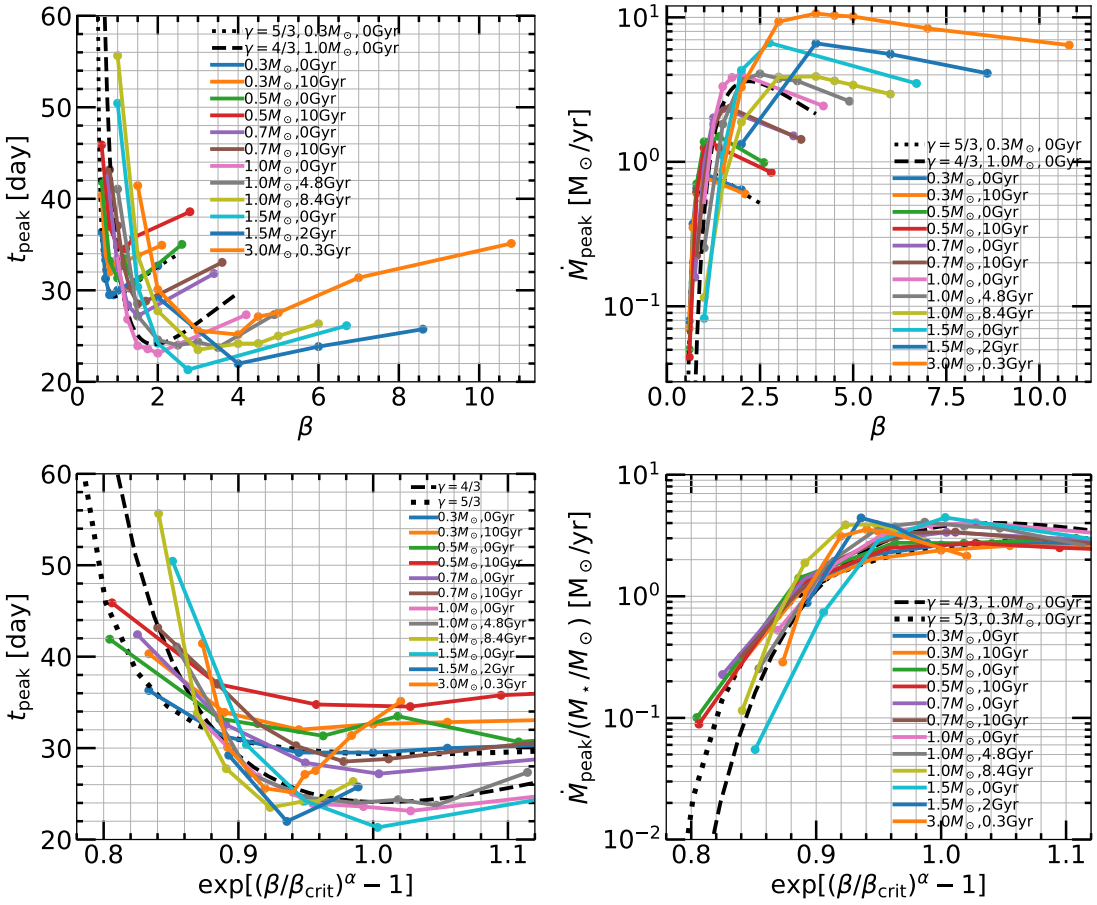

Figure 6.11: Time of peak (left panels) and peak mass fallback rate (right panels) as a function of impact parameter. Results from Guillochon & Ramirez-Ruiz (2013a) for a $\gamma = 5/3$ and $\gamma = 4/3$ polytrope are shown by the dotted and dashed lines respectively. Bottom panels are where x-axis is scaled with a structural parameter, $\alpha = (\rho_c/\bar{\rho})^{-1/3}$. In the bottom right panel, $\dot{M}_{\rm peak}$ is normalized by the stellar mass.

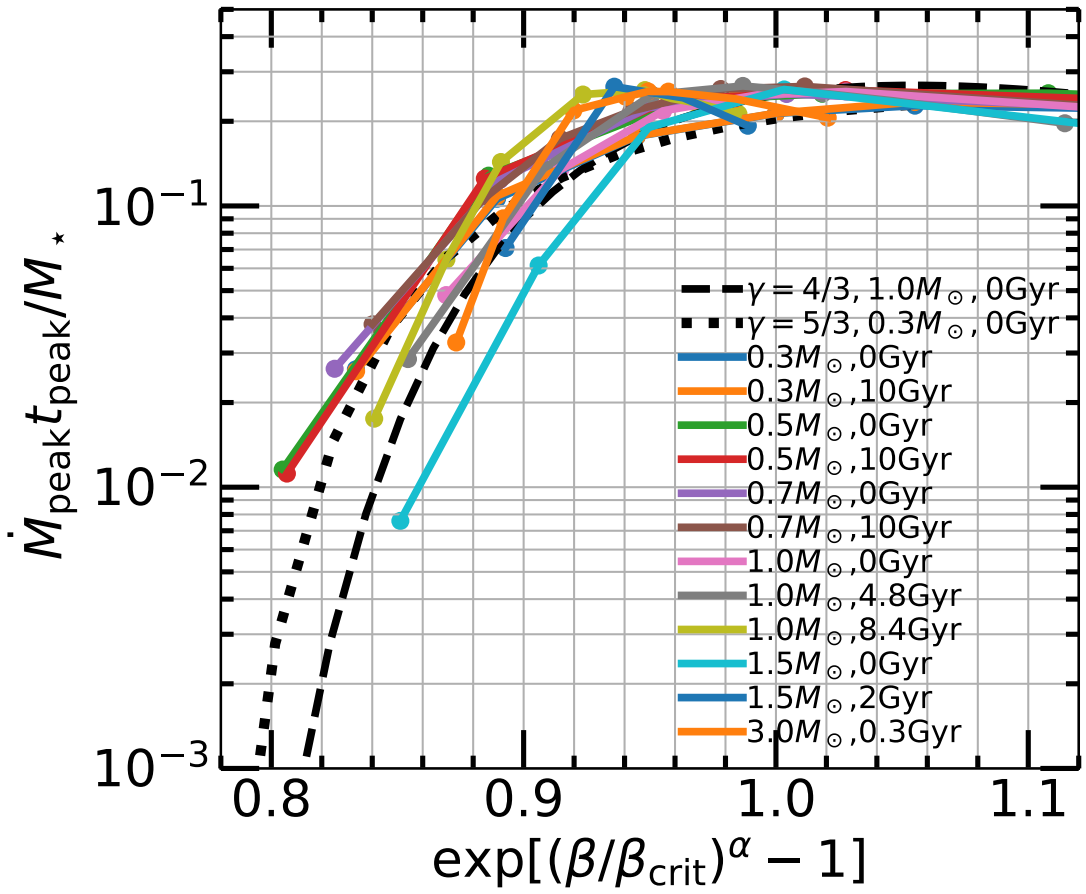

Figure 6.12: $\dot{M}_{\rm peak} \times t_{\rm peak}/M_\star$ as a function of β scaled with structural parameter $\alpha = (\rho_c/\bar{\rho})^{-1/3}$.

Power law indices

The top panels of Figure 6.13 show the instantaneous power law index $n(t)$ of the mass fallback rate as a function of time. The top left panel shows the parameter space occupied by tidal disruptions of MS stars for a $10^6 M_\odot$ BH in absolute units. The x-axis in the top right panel is normalized by the peak time, and we also compare to the results of Guillochon & Ramirez-Ruiz (2013a) for $\gamma = 5/3$ and $\gamma = 4/3$ polytropes. The regions are comparable, but this work covers more parameter space, as expected by the larger range of stellar structures studied. The different range of β's sampled may also account for some differences.

The bottom panels of Figure 6.13 show the asymptotic decay power law index n_∞ for individual stars as a function of β, and as a function of the scaled x-axis incorporating stellar structure familiar from earlier figures. Partial disruptions generally have $n_\infty \approx -2.2$ ($\approx 9/4$; Coughlin & Nixon 2019), while full and post-critical disruptions generally have $n_\infty \approx -5/3$, though the β-dependence is more nuanced than this. For example, n_∞ peaks near the critical β for full disruption, then falls slightly for post-critical disruptions. There is also a small region at small β where there is a sharp transition from higher n_∞ to $n_\infty \approx -2.2$—this was better captured in Guillochon & Ramirez-Ruiz (2013a), who sampled β more finely in this region.

In the bottom left panel, one can see that the more centrally concentrated stars (which correspond roughly to the more massive stars) have $n_\infty \approx -2.2$ for progressively higher β's. Aside from fitting individual TDEs, one can use this information with a statistical population of TDEs: given that the TDE rate depends inversely on β to

some power (see Section 7.5 for more detailed discussion), one can use n_∞ as a probe of the stellar structure and more indirectly the stellar mass and age. More specifically, the lower-mass stars spend only a small portion of β parameter space at $n_\infty \approx -2.2$, while the higher-mass stars spend much more of β parameter space here, especially when weighted inversely by β to some power. If the stellar mass function of TDEs is roughly flat for $M_\star \lesssim M_\odot$ (Kochanek 2016b), and especially if mass segregation in galactic centers is important (see Section 7.5) then if an $n_\infty \approx -2.2$ is observed, it is more likely due to the partial disruption of a more massive star. Less massive stars are more likely to be full disruptions, and thus if $n_\infty \approx -5/3$ is observed, it is more likely due to the full disruption of a lower-mass star.

In the bottom right panel, after rescaling the x-axis with $\rho_c/\bar{\rho}$, the simulations reduce into a single relationship describing n_∞ for any star and impact parameter. We provide a B-spline fit to this relation in the Appendix, so that one can obtain the n_∞ for any stellar mass, stellar age, and impact parameter.

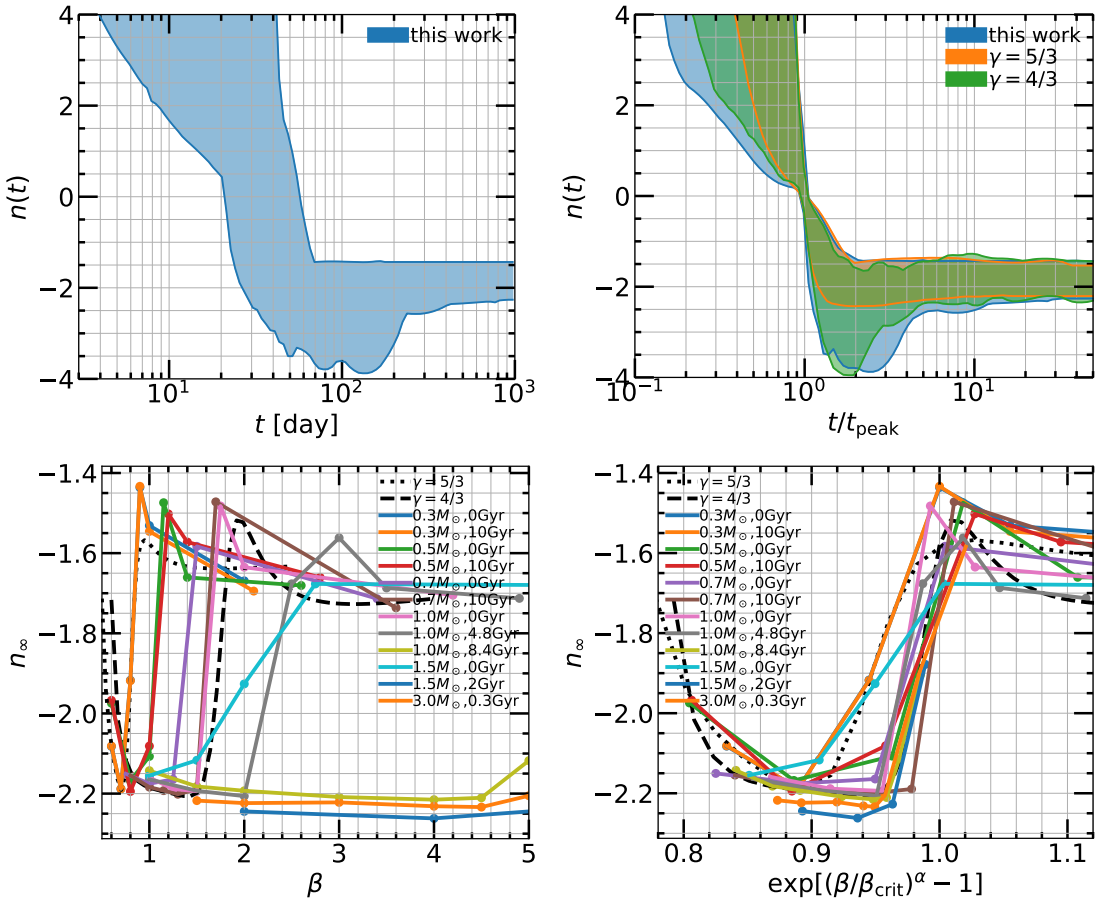

Figure 6.13: Top panels: instantaneous power law index $n(t)$ of the mass fallback rate as a function of time. Top left: absolute units; top right: x-axis normalized by the peak time. Blue regions correspond to this work, while orange and green regions correspond to results from Guillochon & Ramirez-Ruiz (2013a) for $\gamma = 5/3$ and $\gamma = 4/3$ polytropes. Bottom panels: asymptotic decay power law index n_∞ as a function of impact parameter. (In case of confusion due to the repeated colors, the $0.3M_\odot$ stars follow the $\gamma = 5/3$ polytrope.) The bottom right panel has x-axis scaled with the critical impact parameter and a structural parameter $\alpha = (\rho_c/\bar{\rho})^{-1/3}$.

6.4 Conclusion

6.4.1 Comparison to other work

We compare with Guillochon & Ramirez-Ruiz (2013a) throughout, but perhaps the most salient point is that, as we stress in this paper, every tidal disruption quantity that we have calculated depends primarily on the stellar structure, parameterized by $\rho_c/\bar{\rho}$, and impact parameter β. Thus, the study of Guillochon & Ramirez-Ruiz (2013a) is only directly applicable to stars with exactly $\gamma = 5/3$ or $\gamma = 4/3$ stellar structures, which do not represent the range of stellar masses and stellar ages involved in TDEs. This work offers a significant improvement upon the Guillochon & Ramirez-Ruiz (2013a) grid of simulations, and applies to any main-sequence stellar mass and stellar age. The fitting formulae (see Appendix) we find for key disruption quantities can be used to predict the disruption quantities for any star, provided one knows the $\rho_c/\bar{\rho}$. Additionally, the `STARS_library` tool (Law-Smith et al. 2020, see Appendix) allows one to retrieve the dM/dt for any stellar mass and age.

Our results are consistent with the hydrodynamical simulations of Goicovic et al. (2019), Gafton & Rosswog (2019b) in the non-relativistic limit, and Golightly et al. (2019b) for the impact parameters and stars they consider. The asymptotic decay power law indices we find are broadly consistent with the analytic predictions of Coughlin & Nixon (2019) ($n_\infty = -9/4$ for partial disruptions, $n_\infty = -5/3$ for full disruptions), though our results indicate a more nuanced β dependence (see Figure 6.13 and associated discussion). We note that we find $n_\infty \approx -2.2$ for partial disruptions, slightly larger than the $n_\infty = -2.25$ found by Coughlin & Nixon (2019).

Our results are broadly consistent with those of Ryu et al. (2020a,b,c,d), though we note some differences. Rather than comparing dM/dt's in detail, we note that the critical impact parameters we find for full disruption differ slightly. This is partly due to the fact that Ryu et al. (2020a,b,c,d) study a single stellar age (MAMS), whereas we study 2 or 3 stellar ages for each star, so a direct comparison of results for a given stellar mass is misleading, as the stellar structures differ. See Figure 6.19 in the Appendix for a comparison. One disagreement is at the 15% level in our $\beta_{\rm crit} = 0.9$ result for the 0.3 $M_\odot$ star (which has an identical profile to a $\gamma = 5/3$ polytrope) for $M_{\rm BH} = 10^6 M_\odot$; Ryu et al. (2020a,b,c,d) argue that this discrepancy is due to GR effects at $r_{\rm p} = 22 r_{\rm g}$. The difference is modest, but we note that our $\beta_{\rm crit} = 0.9$ result has been independently found by other authors for polytropic stellar models, and the non-relativistic regime is one in which our grid-based adaptive-mesh FLASH framework has also been independently verified with two other numerical methods (SPH and moving-mesh) and resolutions by other authors (Guillochon & Ramirez-Ruiz 2013a; Mainetti et al. 2017; Goicovic et al. 2019; Golightly et al. 2019b; Gafton & Rosswog 2019b).

6.4.2 Caveats/extensions

Our calculations are Newtonian, and thus do not capture the minority of encounters in which relativistic effects significantly alter the dM/dt. Cheng & Bogdanović (2014a), Tejeda et al. (2017b), and Gafton & Rosswog (2019b) (for a review of TDEs in GR see also Stone et al. 2019) studied differences between the fallback rates from relativistic versus Newtonian tidal disruption simulations in detail, and found that for $r_{\rm p} > 10 r_{\rm g}$, the difference is $\lesssim 10\%$, and that the most significant corrections from

relativistic effects are at pericenter distances smaller than this.[30] They found that for $r_{\rm p} > 10r_{\rm g}$ the error in a non-relativistic tidal disruption simulation scales approximately as $v_{\rm p}^2 \sim r_{\rm g}/r_{\rm p}$ (though we emphasize that GR is a non-linear theory, and order unity effects are possible for the rare extreme encounters in which GR dominates the dynamics). For encounters in which relativistic effects are significant, the decay power law index remains approximately the same, and the most important differences are that the peak time is shifted to the right and the peak fallback rate is shifted down compared to the Newtonian case. The fraction of disruptions that require relativistic hydrodynamics in order to accurately model the mass fallback rate is $\sim \max(1, 10{\rm r_g/r_t})$ in the pinhole regime of loss cone repopulation, and a step function in the diffusive regime: $\sim$0 if $10r_{\rm g} < r_{\rm t}$, and $\sim$1 if $10r_{\rm g} > r_{\rm t}$. For a $1M_\odot$, $1R_\odot$ star, this is $\approx$5% for a $10^6 M_\odot$ BH and $\approx$20% for a $10^7 M_\odot$ BH. See Figure 6.20 in the Appendix for the range of applicability of Newtonian hydrodynamics simulations. Note that while relativistic effects may cause significant apsidal precession, the effect on the mass fallback rate to the BH is relatively small—and it is this quantity that tracks the luminosity evolution of TDEs so closely. While the library presented in this paper applies to the majority of TDEs, we plan to extend our setup to include relativistic encounters in future work.

Other extensions include studying orbits with different eccentricities, incorporating stellar spin (rather than performing new simulations with spinning stars, we could scale our dM/dt results with a parameterized stellar spin dependence based on the results of Golightly et al. 2019a), studying magnetic fields (we already have the framework for this, first studied in Guillochon & McCourt 2017), adding more stellar

[30] Though we note that Ryu et al. (2020d) argue for slightly larger effects due to the inclusion of GR.

masses and ages to the grid, sampling more finely in β (though this will not make a significant difference because of our dM/dt interpolation), and various extensions and upgraded functionality of the `STARS_library` tool (Law-Smith et al. 2020). Finally, we plan to use the interpolated fallback-rate library as the new backbone for the publicly available TDE fitting software `MOSFiT` (Guillochon et al. 2018; Mockler et al. 2019).

We do not perform an analysis of TDE rates as a function of stellar mass and stellar age, but below is a brief discussion. In terms of broad demographics, Kochanek (2016b) calculated that for $M_{\rm BH} \lesssim 10^7 M_\odot$, the typical TDE is due to a $0.3 M_\odot$ star, but that the mass function is relatively flat for $M_\star \lesssim M_\odot$. This study only considered effects due to the initial mass function (IMF) and did not include any dynamical interactions between stars, such as mass segregation in galactic centers, which segregates more massive stars closer to the BH and ejects less massive stars (e.g., Baumgardt et al. 2004; MacLeod et al. 2016c)—this would cause the stellar mass function for TDEs to peak at higher masses than suggested by a convolution of the IMF and the luminosity function of TDEs (De Colle et al. 2012; MacLeod et al. 2013). See also Figure 15 in MacLeod et al. (2012a) for the fraction of stars at different evolutionary stages contributing to TDE flares. For $M_{\rm BH} \lesssim 10^8 M_\odot$, MS stars make up >85%. In more detail, MacLeod et al. (2012a) find that the tidal disruption rate scales with the tidal radius of a given star as $\dot{n} \propto r_{\rm t}^{\alpha}$, where $\alpha \approx 0.2$–0.5. Ignoring other considerations, the physical cross-section increases with stellar age and leads to higher rates of tidal disruption for older MS stars. However, the ΔM lost at a given β decreases as the star becomes more centrally concentrated, leading to fainter flares.

The dynamical mechanisms operating in the relevant galactic center and the associated most likely age for a star to be disrupted are also important. The two-body relaxation time, which is ≈2 Gyr for a $10^6 M_\odot$ BH (Bar-Or et al. 2013) (the MS lifetime of a $1.5 M_\odot$ star), gives a characteristic limit for the approximate mass and age of a star upon disruption. However, there are many other mechanisms that disrupt stars earlier. Stars can interact with one another coherently inside the sphere of influence of the BH, in contrast to two-body relaxation, leading to rapid angular momentum evolution (Rauch & Tremaine 1996); for example, this occurs for eccentric nuclear disks (Madigan et al. 2018). The presence of a SMBH binary can also dramatically increase the TDE rate, driven by a combination of strong scatterings and KozaiLidov cycles between individual stars and the SMBH binary (e.g., Li et al. 2015). Other mechanisms that may disrupt stars over timescales $\ll 2$ Gyr include strong (non-diffusive) two-body scatterings, which make up a fraction of the TDE rate in any galaxy (Weissbein & Sari 2017), and radially anisotropic velocity fields or unusually dense star clusters, which may occur in post-starburst galaxies (Stone et al. 2018). Moreover, the fact that TDEs appear to be observed preferentially in rare post-starburst galaxies (Arcavi et al. 2014b; French et al. 2016b; Law-Smith et al. 2017c; Graur et al. 2018) means that many TDEs are sourced by unique stellar populations with particular dynamical histories.

6.4.3 Summary

We summarize the main points of this paper below.

1. We present a grid of tidal disruption simulations of stars with accurate stellar

structures and chemical abundances, using MESA models as initial conditions to FLASH simulations with a Helmholtz EOS.

2. We interpolated this grid in 3D (stellar mass, stellar age, and impact parameter) to provide the `STARS_library` tool (see Section 6.5), where one can request the dM/dt for any stellar mass, stellar age, and impact parameter.

3. The quantities $\beta_{\rm crit}, \Delta M, t_{\rm peak}, \dot{M}_{\rm peak}$, and n_∞ vary significantly with stellar mass and stellar age, but can be reduced to a single relationship that depends only on stellar structure, parameterized by $\rho_c/\bar{\rho}$, and impact parameter β (see Figures 6.5, 6.6, 6.11, and 6.13). We provide fitting formulae for these quantities applicable to any MS star (see Figure 6.16 in Appendix).

4. For the same ΔM, the shape of the dM/dt curve varies significantly with stellar mass, promising the potential determination of stellar properties from the TDE light curve alone (see Figure 6.10).

5. The critical impact parameter for full disruption increases with increasing central concentration, and scales approximately as $(\rho_c/\bar{\rho})^{1/3}$ for $\rho_c/\bar{\rho} \lesssim 500$ and $(\rho_c/\bar{\rho})^{1/2.3}$ for $\rho_c/\bar{\rho} \gtrsim 500$ (see Figure 6.6).

6. In general, more centrally concentrated stars have steeper dM/dt rise slopes and shallower decay slopes (see Figures 6.8 and 6.9).

7. We show that the shape of dM/dt depends only on the stellar density profile, and has little dependence on the internal EOS of the star (see Section 6.11 where we compare a $1M_\odot$ and $10M_\odot$ star with nearly identical density profiles), thus

extending the range of applicability of our interpolated library and fitting formulae to any MS star.

We hope the community makes use of the `STARS_library` tool (see Appendix), and we look forward to incorporating this library as the new backbone of the `MOSFiT` fitting software for TDEs, or any other TDE fitting framework, allowing for more accurate determinations of both the nature of the disrupted star and the BH.

6.5 Interpolated fallback-rate library

The STARS library of interpolated fallback rates, as well as up-to-date instructions for loading and using the library, is available on GitHub[31] and version 1.0.0 is archived on Zenodo (Law-Smith et al. 2020). One can create custom interpolated grids and one can also query for any stellar mass, stellar age, and impact parameter.

The basic interpolation between dM/dt's is the same as in the `MOSFiT` software (Guillochon et al. 2018; Mockler et al. 2019). We first interpolate in β for a given stellar mass and age. We then interpolate each of these β's in stellar mass, for a given fractional main-sequence stellar age (e.g., $0.3M_\odot$ ZAMS to $0.5M_\odot$ ZAMS). We then interpolate in stellar age for a given stellar mass. In the query/retrieval mode, in order to retrieve a dM/dt corresponding to a specific stellar mass, stellar age, and impact parameter that does not already exist in the interpolated library, we perform a quick series of interpolations on the nearest neighbor points in 3D space.

Figure 6.14 shows the STARS library interpolated dM/dt's for a small grid in

[31] `STARS_library`: github.com/jamielaw-smith/STARS_library.

stellar mass, stellar age, and impact parameter, for a single BH mass $M_{\rm BH} = 10^6 M_\odot$. This grid has 10 interpolated β points, 11 interpolated mass points, and 5 interpolated age points, with spacing in β and stellar mass logarithmic, and spacing in stellar age linear.

Figure 6.15 shows all of the STARS library interpolated dM/dt's in the same plot, for a single BH mass $M_{\rm BH} = 10^6 M_\odot$. The left panel is in absolute units, in order to emphasize the several orders of magnitude in $\dot{M}$ and time covered by this grid even for a single BH mass—roughly 6 orders of magnitude in fallback rate and 4 orders of magnitude in time (we extend the dM/dt's to later times than shown in this plot). The right panel is normalized to peak time and peak fallback rate, in order to emphasize the range of rise and decay slopes exhibited by the library. See Section 7.3 for more discussion of how these slopes depend on stellar structure. In general, more centrally concentrated stars have steeper rise slopes and shallower decay slopes. The more rounded behavior near peak is from post-critical-β disruptions; see e.g. the high-β behavior for a given star in Figure 6.7. We also overplot three dM/dt's in gray: a ZAMS $0.3 M_\odot$ star with $\beta = 0.6$, a ZAMS $1 M_\odot$ star with $\beta = 4.2$, and a ZAMS $3 M_\odot$ star with $\beta = 2.0$.

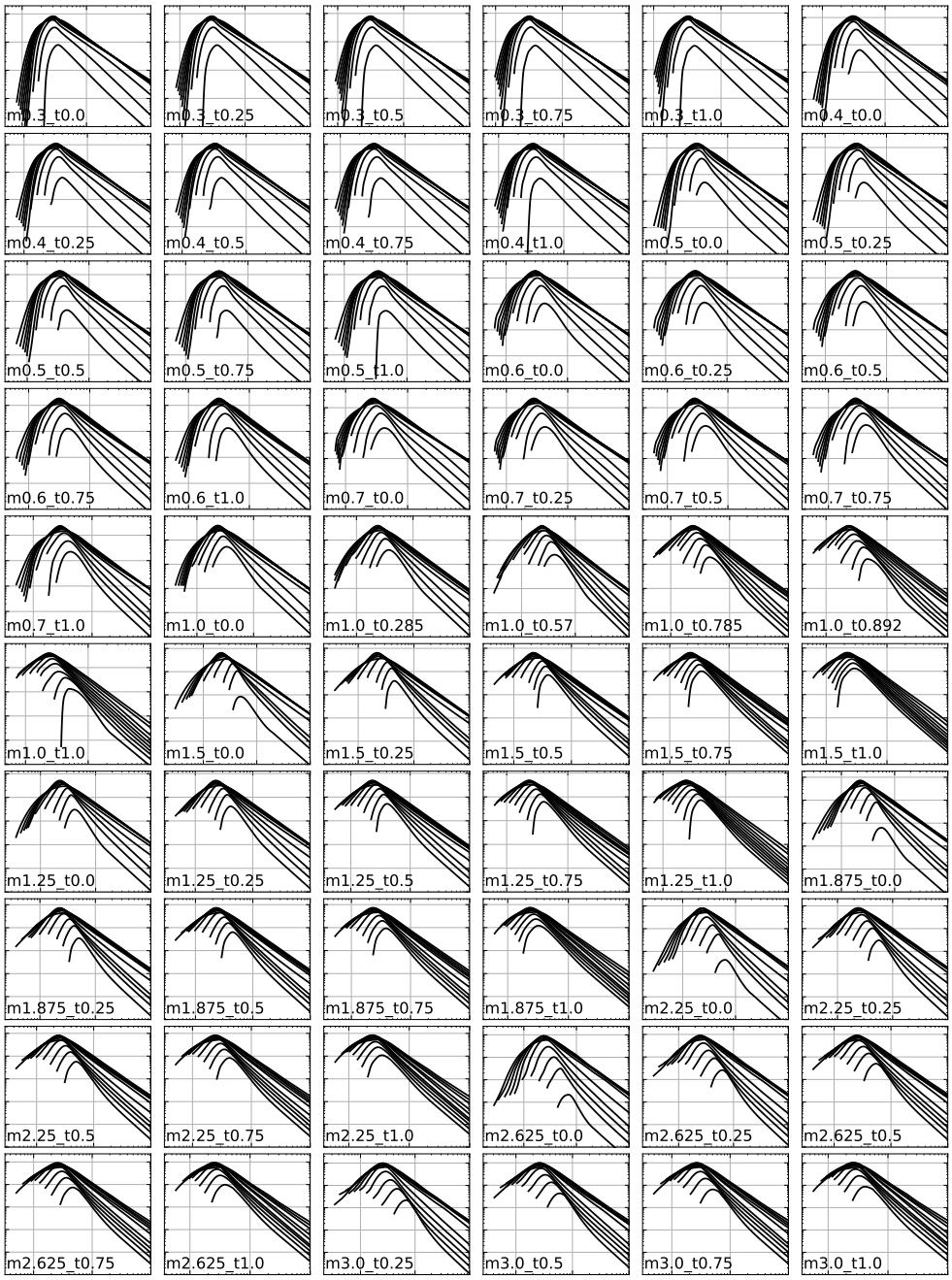

Figure 6.14: STARS library interpolated dM/dt's for a small grid of stellar mass, stellar age, and impact parameter, and at a single BH mass $M_{\rm BH} = 10^6 M_\odot$. Axes labels are removed for clarity, but are the same as in other figures in this paper (x-axis is time, from 0 to 1000 days, $y-$axis is $\dot{M}$, from 10^{-4} to 10 $M_\odot$/yr, both log-scaled). Note that we provide more finely spaced interpolated grids for download (see text). The directory name, in format mXX_tYY, where XX is the stellar mass in $M_\odot$ and YY is the fractional MS age, is in the lower left of each panel.

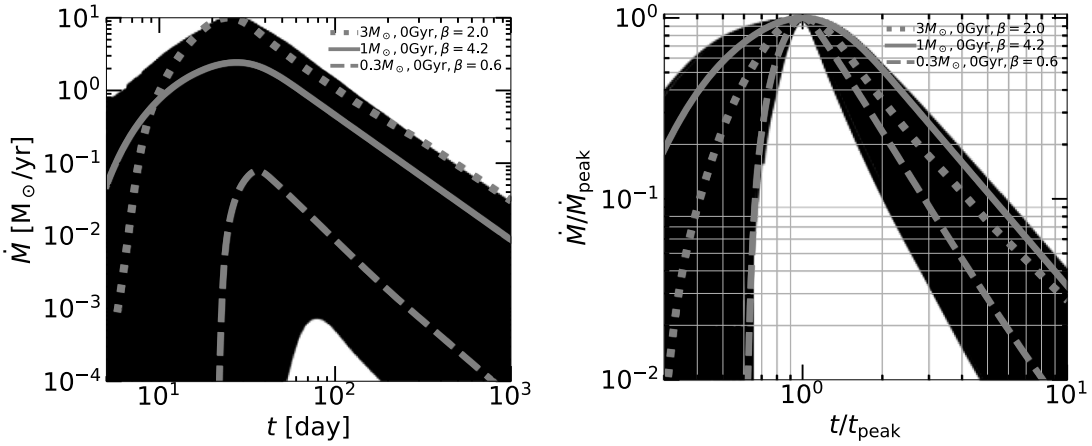

Figure 6.15: STARS library interpolated dM/dt's, all in one plot, for a single BH mass $M_{\rm BH} = 10^6 M_\odot$. Left: absolute units. right: normalized to peak time and peak fallback rate. We applied a fill between dM/dt's in order to emphasize the tune-able spacing of the 3D interpolation. Three dM/dt's are overplotted in gray: a ZAMS $0.3M_\odot$ star with $\beta = 0.6$ (dashed), a ZAMS $1M_\odot$ star with $\beta = 4.2$ (solid), and a ZAMS $3M_\odot$ star with $\beta = 2.0$ (dotted).

6.6 Fits to disruption quantities

Figure 6.16 shows fitted B-splines and analytic formulae for the mass lost from the star ($\Delta M/M_\star$), time of peak mass fallback rate ($t_{\rm peak}$), peak mass fallback rate ($\dot{M}_{\rm peak}$), and asymptotic decay power law index (n_∞). These fitting relations allow one to obtain the $\Delta M/M_\star$, $t_{\rm peak}$, $\dot{M}_{\rm peak}$, and n_∞ for any stellar mass, stellar age, and impact parameter. One must first obtain the $\rho_c/\bar{\rho}$ value for this star, e.g. from Table 6.1, a MESA model directly, or a pre-packaged grid of MESA models such as the MIST models (Choi et al. 2016).

The simple analytic fits are below. We were unable to fit the n_∞ data with a

simple formula, so the only option for this quantity is the B-spline.

$$\Delta M/M_\star = 1.055\tanh[(x+0.04)^{20}] - 0.025 \tag{6.9}$$

$$t_{\rm peak}\ [\rm day] = 2/x^{12} + 17x + 8 \tag{6.10}$$

$$\dot{M}_{\rm peak}/(M_\star/M_\odot)\ [\rm M_\odot/yr] = 0.9\sin(15x-1.5)/x^6 - 1.5x + 4.3 \tag{6.11}$$

$$n_\infty = \text{(unable to find simple analytic fit; see B spline below)} \tag{6.12}$$

$$x = \exp[(\beta/\beta_{\rm crit})^\alpha - 1], \quad \alpha = (\rho_c/\bar{\rho})^{-1/3} \tag{6.13}$$

$$\beta_{\rm crit} \approx \begin{cases} 0.5(\rho_c/\bar{\rho})^{1/3},\ \rho_c/\bar{\rho} \lesssim 500 \\ 0.39(\rho_c/\bar{\rho})^{1/2.3},\ \rho_c/\bar{\rho} \gtrsim 500 \end{cases} \tag{6.14}$$

The range for $\Delta M/M_\star$ is $x \in [0.8, 1.0]$ and for $t_{\rm peak}$ and $\dot{M}_{\rm peak}$ is $x \in [0.8, 1.7]$. We note that the equations for $\beta_{\rm crit}$ are only approximate.

Below we provide python code to read in and evaluate the B-spline fits to the disruption quantities $\Delta M/M_\star$, $t_{\rm peak}$, $\dot{M}_{\rm peak}$, and n_∞. This code will reproduce the blue lines in Figure 6.16. Note that the order of all of the splines is 3. The knots and coefficients have been rounded to 3 decimals, which gives precision indistinguishable from the original fitted splines.

```
import numpy as np

from scipy.interpolate import splev

# deltam/mstar
```

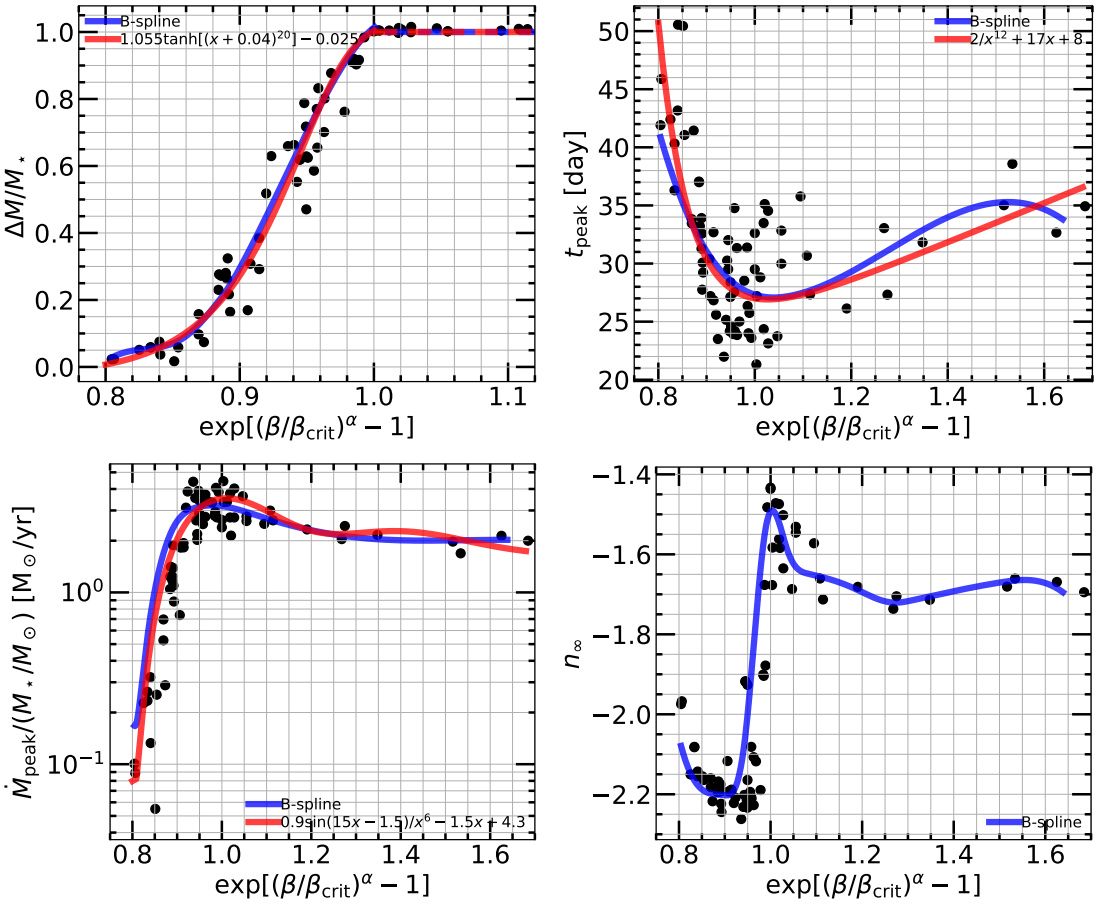

Figure 6.16: B-spline and analytic fits to disruption quantities $\Delta M/M_\star$, $t_{\rm peak}$, $\dot{M}_{\rm peak}$, and n_∞. Note for the top left panel, we extend $\Delta M/M_\star = 1$ after full disruption ($x \geq 1$).

```
knots = [0.804, 0.804, 0.804, 0.804, 0.859, 0.881, 0.892, 0.903, 0.957,
1.001, 1.001, 1.001, 1.001];
coeffs = [0.028, 0.068, 0.027, 0.159, 0.234, 0.416, 0.745, 0.97, 1.015,
0.0, 0.0, 0.0, 0.0]
# tpeak
knots = [0.804, 0.804, 0.804, 0.804, 1.082, 1.638, 1.638, 1.638, 1.638];
coeffs = [40.874, 27.579, 24.097, 39.004, 33.804, 0.0, 0.0, 0.0, 0.0]
# mdotpeak/mstar
knots = [0.804, 0.804, 0.804, 0.804, 0.897, 0.943, 1.082, 1.638, 1.638,
1.638, 1.638];
coeffs = [0.167, 0.127, 2.617, 3.477, 1.714, 2.034, 2.024, 0.0, 0.0,
0.0, 0.0]
# ninf
knots = [0.804, 0.804, 0.804, 0.804, 0.897, 0.943, 0.99, 1.036, 1.082,
1.175, 1.268, 1.314, 1.499, 1.638, 1.638, 1.638, 1.638];
coeffs = [-2.079, -2.212, -2.19, -2.218, -1.333, -1.637, -1.652, -1.675,
-1.73, -1.701, -1.671, -1.656, -1.695, 0.0, 0.0, 0.0, 0.0]


# evaluate B-splines
x = np.linspace(min(knots), max(knots), 100);
y = splev(x, [knots, coeffs, 3])
```

Note that in order to use the B-splines to retrieve values for a specific star, one needs to use the scaled x-axis, and thus input the $\rho_c/\bar{\rho}$ and $\beta_{\rm crit}$ values for the star. $\rho_c/\bar{\rho}$ can be obtained as above and $\beta_{\rm crit}$ can be obtained from either Table 6.2 or our simple formula (Eq. 6.14). Then one plugs these into

$$x = \exp[(\beta/\beta_{\rm crit})^{\alpha} - 1], \quad \alpha = (\rho_c/\bar{\rho})^{-1/3}. \tag{6.15}$$

This x is the value to plug into the B-spline in order to retrieve the desired y-axis value.

6.7 MESA profiles vs. polytropes

Figure 6.17 shows MESA density profiles vs. $\gamma = 5/3$ and $\gamma = 4/3$ polytropes, normalized to central density and stellar radius. One can see where a polytropic stellar model is sufficient and where we need to use a MESA stellar model as initial conditions for the FLASH simulations. For $M_\star = 0.1, 0.3 M_\odot$, the profiles are nearly identical to $\gamma = 5/3$ polytropic stellar structures. For $M_\star = 0.5, 0.7 M_\odot$ the profiles are in between $\gamma = 5/3$ $\gamma = 4/3$ polytropic stellar structures, and could in principle be simulated with a polytropic simulation using a γ that has been matched to this star. For $M_\star \gtrsim 1 M_\odot$, as the star evolves off the ZAMS, the profile becomes more centrally concentrated than $\gamma = 4/3$ and thus cannot be simulated self-consistently with a polytropic stellar structure, as these are unstable for $\gamma \lesssim 4/3$. One requires a Helmholtz EOS in order to provide hydrodynamic support for these non-ZAMS stars. Note that the ZAMS $M_\star \gtrsim 1 M_\odot$ stars are not uniformly well represented by $\gamma = 4/3$ polytropes—the only star that is quite well approximated by a $\gamma = 4/3$ polytrope is the $3 M_\odot$ ZAMS star. Though we

do not do FLASH simulations for intermediate ages between ZAMS and TAMS for the $1.5M_\odot$, $3M_\odot$, and $10M_\odot$ stars in this work (we interpolate instead; see Section 6.5), we show a MAMS profile at age $t \approx t_{\rm TAMS}/2$ for these higher mass stars (including for the $1M_\odot$ star, which we do simulate) for comparison. While the TAMS profiles are clearly much more centrally concentrated than a $\gamma = 4/3$ profile, the MAMS profiles are somewhat closer to the polytropic approximation, though still not a good fit.

One can also see that $\rho_c/\bar{\rho}$ does not map 1-1 exactly to the stellar density profile, though it is a very good approximation. Consider the 10Gyr $0.7M_\odot$ star ($\rho_c/\bar{\rho} = 36$) and the ZAMS $10M_\odot$ star ($\rho_c/\bar{\rho} = 38$). The $10M_\odot$ star has a slightly higher value of $\rho_c/\bar{\rho}$ but its density profile is slightly less centrally concentrated than that of the $0.7M_\odot$ star.

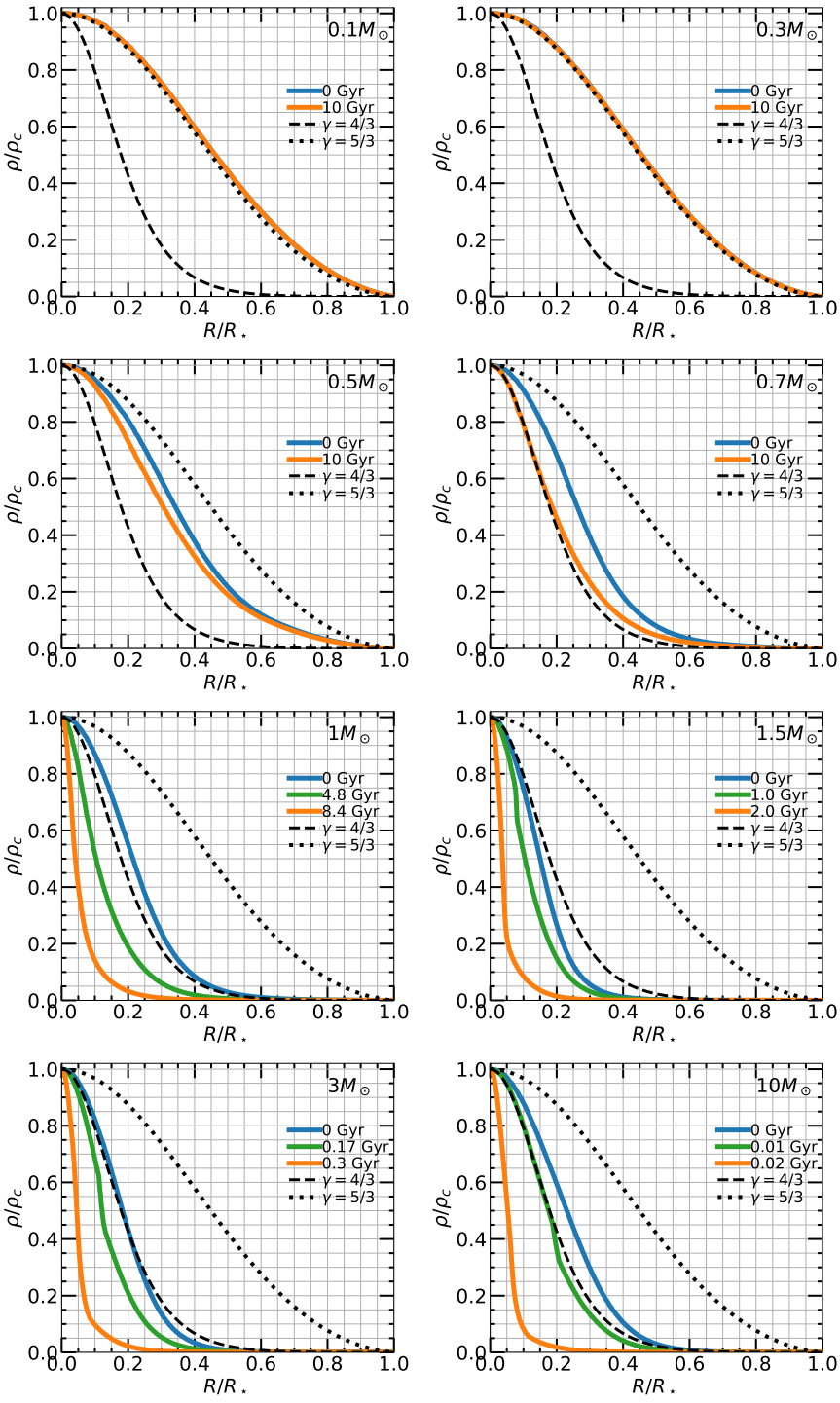

Figure 6.17: MESA density profiles vs. $\gamma = 5/3$ and $\gamma = 4/3$ polytropes, normalized to central density and stellar radius. Each panel is a different mass. Blue is ZAMS, green is MAMS (shown for $M_\star \geq 1M_\odot$), and orange is min(10 Gyr, TAMS).

6.8 Initial profiles after relaxation

Figure 6.18 shows the stellar density profiles after $5t_{\rm dyn}$ of relaxation onto the hydrodynamical grid in FLASH, compared to initial profiles from MESA. To be clear, these two profiles match exactly at the start ($t = 0$) of the FLASH simulation, but here they are shown after $5t_{\rm dyn}$. Our setup has been tested such that the density profile does not change significantly after $\approx 100t_{\rm dyn}$ of relaxation onto the hydrodynamical grid (without a BH present) in Guillochon et al. (2009).

As mentioned in Section 7.2, the most centrally concentrated stars, for which $\rho_c/\bar{\rho} \gtrsim 150$, have a higher initial resolution in FLASH of 512 cells across the diameter of the star. Stars with $\rho_c/\bar{\rho} \lesssim 150$ are initially resolved by 131 cells across their diameters.

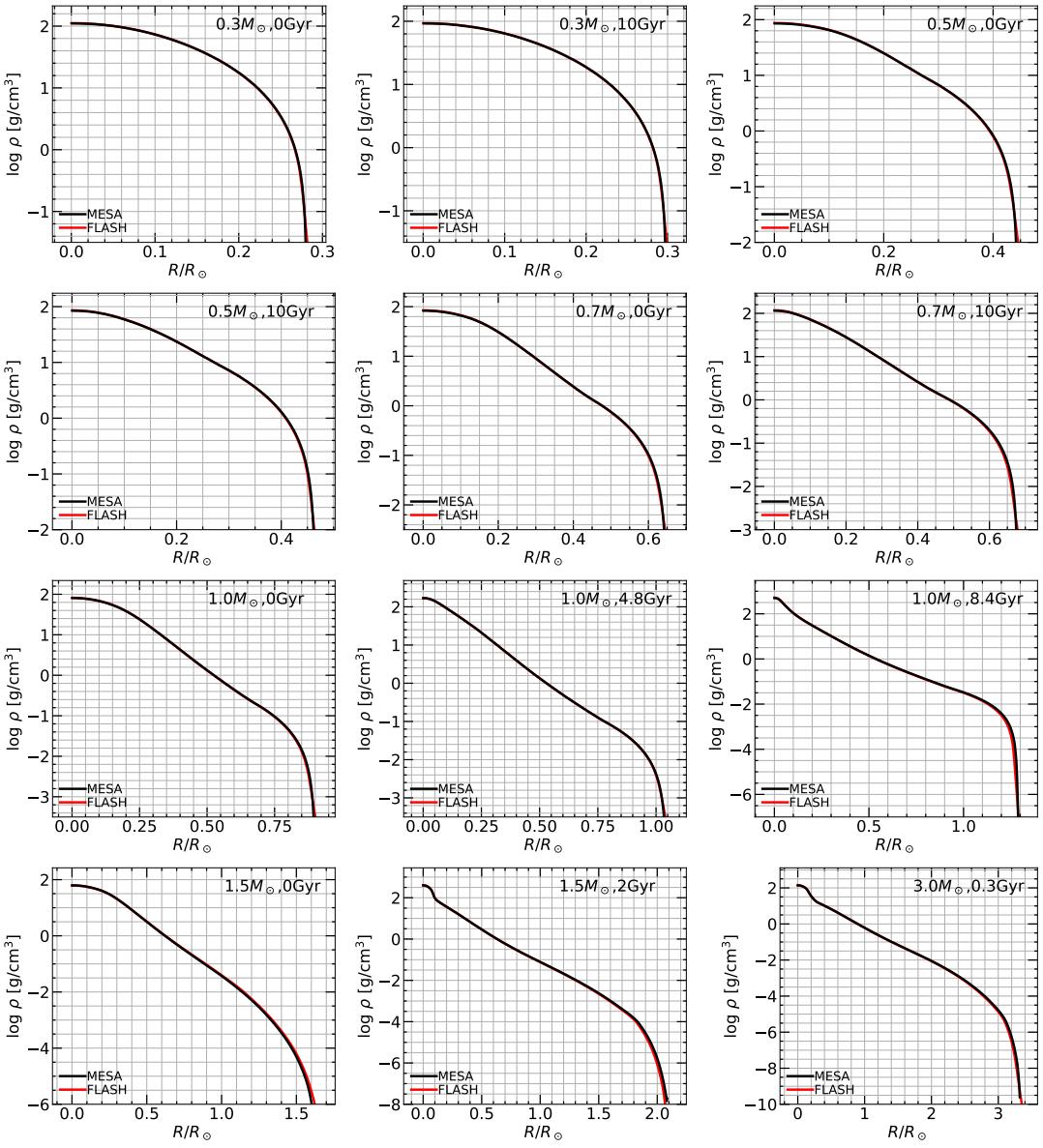

Figure 6.18: Stellar density profiles after $5t_{\rm dyn}$ of relaxation onto the hydrodynamical grid in FLASH (red), compared to initial profiles from MESA (black). These two profiles match exactly at the start of the simulation ($t = 0$).

6.9 Critical impact parameter and pericenter distance vs. stellar mass

Figure 6.19 shows critical β and critical pericenter distance over gravitational radius ($r_{\rm p}/r_{\rm g}$) as a function of stellar mass. See also Figure 6.6 for critical β as a function of $\rho_c/\bar{\rho}$, in which there is a simple power-law relationship. We find large ranges in critical β and critical $r_{\rm p}/r_{\rm g}$, especially with stellar age for $M_\star \gtrsim 0.8 M_\odot$. At a fixed stellar mass, $\beta_{\rm crit}$ can vary by a factor of $\approx$4. We also compare to the results from Ryu et al. (2020a,b,c,d). To avoid repetition, see Sections 7.2 and 7.5 for discussion of the differences between these works. We note that these authors studied only a single stellar age, so a direct comparison is often not possible. For physical pericenter distance, our average from 0.3 to $3 M_\odot$ is $r_{\rm p}/r_{\rm g} \approx 20.4$. Our results are consistent with those of Ryu et al. (2020a,b,c,d) for a $M_{\rm BH} = 10^5 M_\odot$, and for a $M_{\rm BH} = 10^6 M_\odot$ Ryu et al. (2020a,b,c,d) find $r_{\rm p}/r_{\rm g} \sim 26.9$, averaging from $0.15 M_\odot$ to $3 M_\odot$.

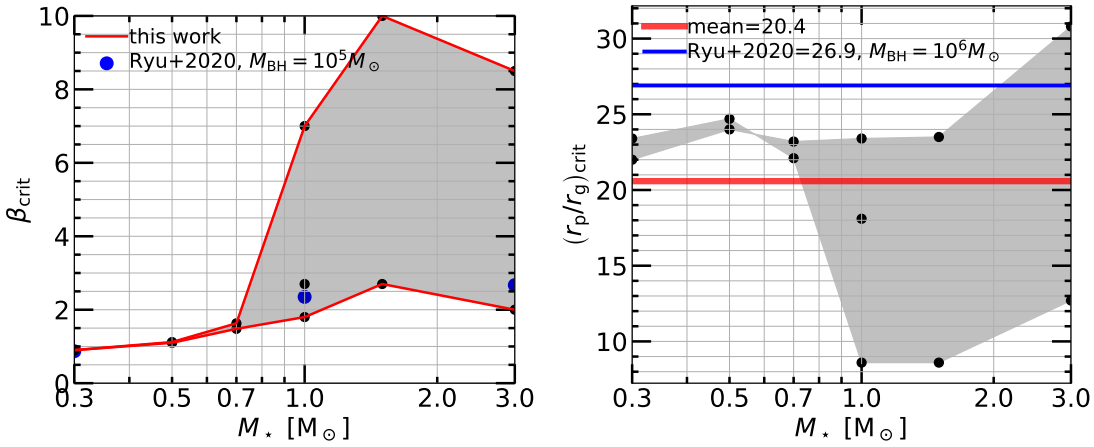

Figure 6.19: Left: critical β vs. stellar mass. See also Figure 6.6. Right: critical pericenter distance over gravitational radius ($r_{\rm p}/r_{\rm g}$) vs. stellar mass. Points at the same stellar mass have different stellar ages. Comparison to Ryu et al. (2020a,b,c,d) in blue.

6.10 Range of applicability of nonrelativistic TDE hydrodynamics simulations

Figure 6.20 shows regions where $r_{\rm p} > 10 r_{\rm g}$ for a few stars ($0.1 M_\odot$, $1 M_\odot$, $10 M_\odot$). This is where we expect nonrelativistic tidal disruption simulations to have $\lesssim$10% error. For more detailed discussion of relativistic effects, see Section 7.5. Note that the BH masses of the host galaxies of observed TDEs, found independently through new observations and the M–σ relationship (Wevers et al. 2017b, 2019), lie in the range $3 \times 10^5 M_\odot \leq M_{\rm BH} \leq 2 \times 10^7 M_\odot$ and peak at $10^6 M_\odot$. The stellar masses obtained through fitting TDEs (Mockler et al. 2019) are almost all $M_\star \lesssim 1 M_\odot$.

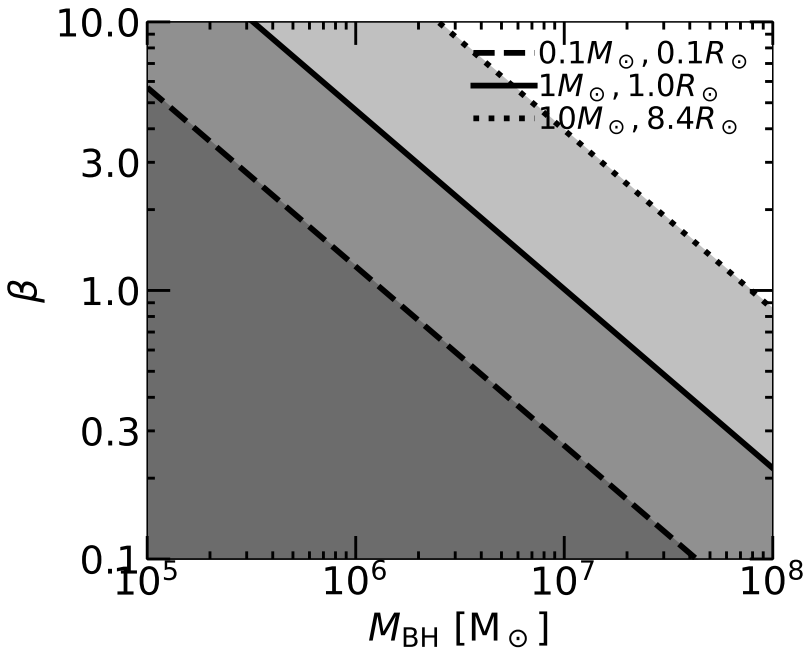

Figure 6.20: Range of applicability of nonrelativistic TDE fallback-rate simulations in β vs. BH mass. Lines are $r_{\rm p} = 10r_{\rm g}$. Shaded regions below lines are where $r_{\rm p} > 10r_{\rm g}$ and we expect nonrelativistic simulations to have $\lesssim$10% error.

6.11 Test of stellar structure vs. EOS

In this paper we claim that stellar structure is the sole determinant of several tidal disruption quantities. To make this claim more robust we must first disentangle the effects of the equation of state. As a test of the effects of stellar structure vs. the EOS, we run simulations of two stars that have very similar density profiles but different energy support (radiative vs. convective). We use a ZAMS $1M_{\odot}$ star (36 Myr) and a close-to-ZAMS $10M_{\odot}$ star (4 Myr). The $10M_{\odot}$ star is at central hydrogen fraction of $X = 0.65$, compared the ZAMS value of $X = 0.71$. The $1M_{\odot}$ and $10M_{\odot}$ star have very similar (but not identical) normalized density profiles, and $\rho_c/\bar{\rho} = 42$ for the $1M_{\odot}$ star and $\rho_c/\bar{\rho} = 45$ for the $10M_{\odot}$ star. We chose to have the profiles match nearly exactly, rather than have the $\rho_c/\bar{\rho}$ values match. We ran one simulation at $\beta = 1.5$ for each, a "solid" partial disruption.

Figure 6.21 shows a comparison of the density profiles for these two stars. They are very different in absolute scales, but normalized to ρ_c and $R_{\star}$, the profiles are nearly indistinguishable.

Figure 6.22 shows the dM/dt's, absolute and scaled with $M_{\star}$ and $R_{\star}$. The $1M_{\odot}$ star has $\Delta M/M = 0.581$ and the $10M_{\odot}$ star has $\Delta M/M = 0.583$. The dM/dt's are very similar, which supports the argument advanced in this paper that the shape of the dM/dt curve is determined by the stellar density profile, and allows us to provide the fitting formulae as a function of only $\rho_c/\bar{\rho}$ and β for disruption quantities for any stellar mass and age within our simulation grid range. In fact, if, from this initial study of stellar structure vs. EOS, we can conclude that these fitting formulae are robust for

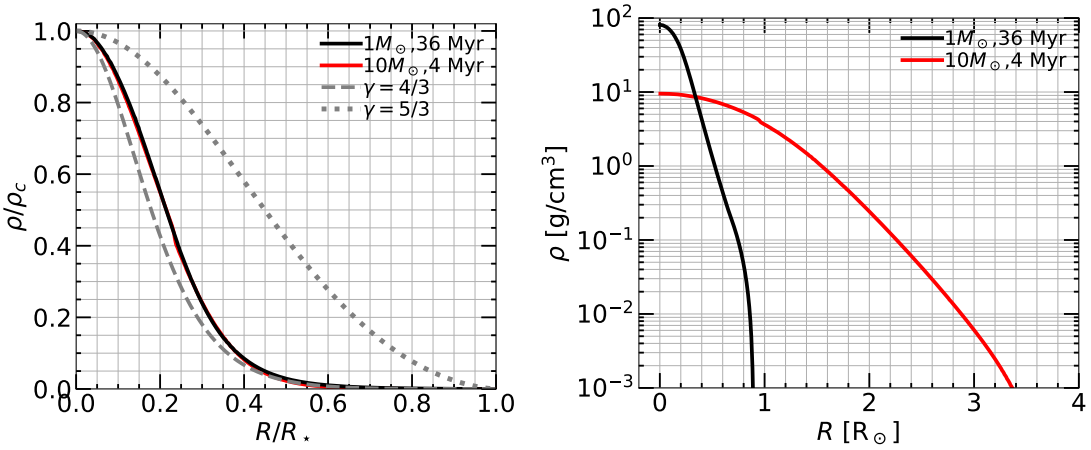

Figure 6.21: Density profiles for two stars in our "stellar structure vs. EOS" study. Left: absolute; right: normalized.

any star, then we can extend the scalings to stars with masses outside our grid range, as their different EOS's will have only a small effect on the resulting disruption quantities.

The differences in shape between these two dM/dt's could be due partially to the slightly different density profiles (note the small "notch" in the profile for the $10M_\odot$ star in Figure 6.21) and values of $\rho_c/\bar{\rho}$ of these two stars. However—and this is the motivation for this test—it could be due to differences in the EOS of the two stars. In particular, the change in slope at $t \approx 100$ days may be due to different transitions between $\gamma = 5/3$ and $\gamma = 4/3$ pressure support in the ρ–T plane for these two stars (e.g. see Figure 7 in Murguia-Berthier et al. 2017).

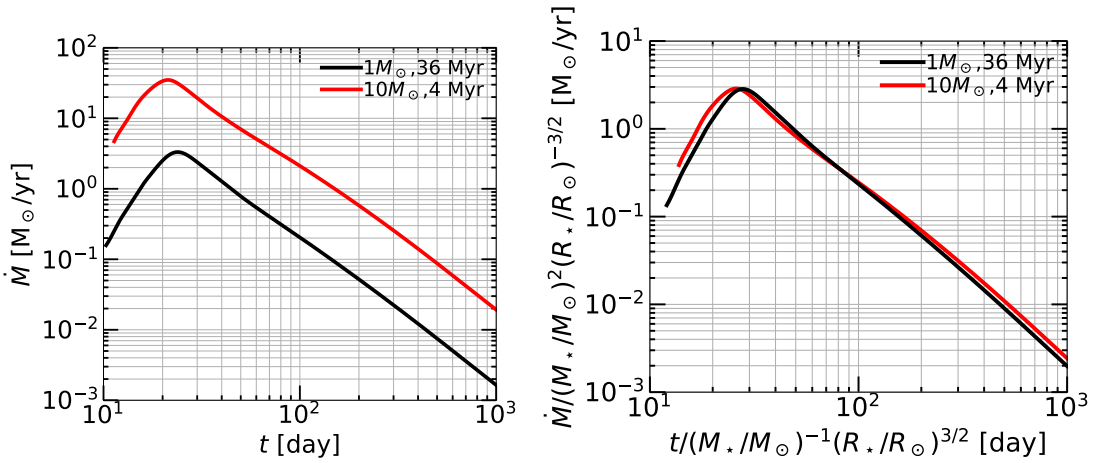

Figure 6.22: dM/dt's for two stars in our "stellar structure vs. EOS" study. Left: absolute; right: normalized using stellar mass and radius scalings (Eq. 6.4).

6.12 MESA and FLASH parameters

In Table 6.3 and Table 6.4 we list a few relevant parameters for the MESA and FLASH simulations. See Section 7.2 for explanations. MESA inlists are available upon request. We also turn on overshooting (not shown in the table) for $M_\star > 3M_\odot$ using the same parameter choices as in the MIST models (Choi et al. 2016).

Table 6.3: Relevant MESA parameters.

Parameter	Value
create_pre_main_sequence_model	.true.
new_net_name	'mesa_49.net'
new_rates_preference	2 ! jina
kappa_file_prefix	'a09'
initial_zfracs	6 ! AGSS09
kappa_lowT_prefix	'lowT_fa05_a09p'
kappa_CO_prefix	'a09_co'
initial_z	0.0142d0
initial_y	0.2703d0
Lnuc_div_L_zams_limit	0.999d0
mixing_length_alpha	2
delta_lg_XH_cntr_hard_limit	0.00432d0
do_element_diffusion	.true.
xa_central_lower_limit_species(1)	'h1'
xa_central_lower_limit(1)	0.001d0

Table 6.4: A few relevant FLASH parameters. `xmax` is in units of $R_\star$ and `tmax` is in units of the stellar dynamical timescale $t_{\rm dyn}$.

Parameter	Value
xmax	1.e3
tmax	1.e2
mpole_lmax	20
eos_tolerance	1.e-6
smalle	1.e7
smallt	1.e3
smlrho	1.e-12
smallp	1.e0
sim_rhoAmbient	1.e-11
sim_pAmbient	1.e1
sim_tAmbient	1.e3
order	3
slopeLimiter	''hybrid''
charLimiting	.true.
use_3dFullCTU	.true.
use_hybridOrder	.true.
RiemannSolver	''HYBRID''

Table 6.4 (cont'd): A few relevant FLASH parameters. `xmax` is in units of $R_\star$ and `tmax` is in units of the stellar dynamical timescale $t_{\rm dyn}$.

Parameter	Value
`shockDetect`	`.true.`

6.13 Numerical convergence

Figure 6.23 shows dM/dt's for different resolution simulations in FLASH, demonstrating numerical convergence for the resolutions we choose in this paper: 131 cells across the diameter of the star for less centrally concentrated stars ($\rho_c/\bar{\rho} \lesssim 150$) and 524 cells across the diameter of the star for highly centrally concentrated stars ($\rho_c/\bar{\rho} \gtrsim 150$). We show results for a ZAMS 0.3 $M_\odot$ star (less centrally concentrated, $\rho_c/\bar{\rho} = 6$), a MAMS $1M_\odot$ star (moderately centrally concentrated, $\rho_c/\bar{\rho} = 138$) and a TAMS $3M_\odot$ star (highly centrally concentrated, $\rho_c/\bar{\rho} = 1198$). We note that past simulations have had difficulty reaching convergence on the low-mass, "high-energy", tightly bound tail of debris that returns first to the BH. This tail is of observational interest, and we achieve convergence here.

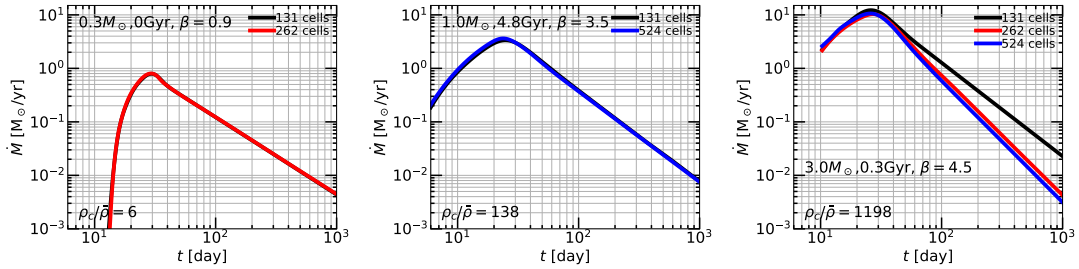

Figure 6.23: dM/dt's for different resolution simulations in FLASH for a few different examples. Lines are labeled by the number of cells across the diameter of the star. Central concentration (parameterized by $\rho_c/\bar{\rho}$) is shown in the bottom left. Left: $0.3M_\odot$, 0 Gyr (a less centrally concentrated star; we use 131 cells here). Middle: $1.0M_\odot$, 4.8 Gyr (a moderately centrally concentrated star; we use 131 cells here). Right: $3.0M_\odot$, 0.3 Gyr (a highly centrally concentrated star; we use 524 cells here).

Chapter 7

Successful Common Envelope Ejection and Binary Neutron Star Formation in 3D Hydrodynamics

Abstract

The coalescence of two neutron stars was recently observed in a multi-messenger detection of gravitational wave (GW) and electromagnetic (EM) radiation. Binary neutron stars that merge within a Hubble time, as well as many other compact binaries, are expected to form via common envelope evolution. Yet five decades of research on common envelope evolution have not yet resulted in a satisfactory understanding of the multi-spatial multi-timescale evolution for the systems that lead to compact binaries. In this paper, we report on the first successful simulations of common envelope

ejection leading to binary neutron star formation in 3D hydrodynamics. We simulate the dynamical inspiral phase of the interaction between a $12M_{\odot}$ red supergiant and a $1.4M_{\odot}$ neutron star for different initial separations and initial conditions. For all of our simulations, we find complete envelope ejection and a final orbital separation of ≈ 1.1–$2.8R_{\odot}$, leading to binary neutron stars that merge within a Hubble time. We find an $\alpha_{\rm CE}$-equivalent efficiency of ≈ 0.1–0.4 for the models we study, but this may be specific for these extended progenitors. We fully resolve the core of the star to $\lesssim 0.005R_{\odot}$ and our 3D hydrodynamics simulations are informed by an adjusted 1D analytic energy formalism and a 2D kinematics study in order to overcome the prohibitive computational cost of simulating these systems. The framework we develop in this paper can be used to simulate a wide variety of interactions between stars, from stellar mergers to common envelope episodes leading to GW sources.

7.1 Introduction

Until now, the majority of astrophysical sources detected by the advanced Laser Interferometer Gravitational-Wave Observatory (LIGO) and Virgo observatory have involved stellar mass binary black hole (BBH) mergers, with the two most notable exceptions being the (likely) binary neutron star (BNS) mergers GW170817 and GW190425 (Abbott et al. 2017a, 2020). While dynamical encounters may play a role in the origin of BBHs, they are not an effective pathway for the assembly of binary neutron star mergers (e.g., Ye et al. 2020), which are thought to form almost exclusively in interacting binaries (Tutukov & Yungelson 1973, 1993; Belczynski et al. 2016).

Massive stars are the progenitors of neutron stars and black holes, and the majority of massive (i.e., type B and O) stars are in close enough binaries such that interaction is inevitable as the stars evolve (Sana et al. 2012; Moe & Di Stefano 2017). A BNS is expected to form from the cores of well-evolved stars, and thus have much lower orbital energy and angular momentum than the original binary progenitor. For BNSs that merge in a Hubble time, after one of the progenitor stars evolves through the red giant phase and overflows its Roche lobe, the original binary is believed to significantly shrink during a phase of unstable mass transfer, which leads to a spiral-in of the binary and ejection of the envelope—this is collectively commonly referred to as common envelope (CE) evolution (e.g., Ritter 1975; Paczynski 1976; Iben & Livio 1993; Ivanova et al. 2013b). If this process leads to a deposition of orbital energy that is sufficient to eject the envelope of the giant, the predicted properties of the resulting compact binary could match the observed properties of the BNS population. Past attempts to model this process have failed because they cannot reproduce these observed properties. A more complete (and in particular, multidimensional) theoretical description is required in order to provide an accurate description of the evolution of a NS embedded in a common envelope. This work focuses on the decades-long pursuit of this elusive phenomenon.

A critical juncture in the life of a binary occurs just after mass transfer commences in the system. The system either coalesces or may survive to become an interacting binary. This is the case of the recently discovered M Supergiant High Mass X-Ray Binary (HMXB) 4U 1954+31 (Hinkle et al. 2020), which contains a late-type supergiant

of mass $9^{+6}_{-2} M_{\odot}$; it is the only known binary system of its type. It is difficult and rare to observe a system in this state, as the system evolves rapidly, yet this discovery may be the first observation of a system similar to the progenitor studied in this work. If mass transfer becomes unstable in this system it could lead to a CE episode. Two outcomes are then possible: (1) one star has a clear core/envelope separation and the other star is engulfed into its envelope, or (2) both stars have a core/envelope separation and the envelopes of the two stars overfill their Roche lobes (see e.g., Vigna-Gómez et al. 2020). Usually, the term CE is used to describe a situation in which the envelope is not co-rotating with the binary and is not necessarily in hydrostatic equilibrium. The state of the primary at onset of CE evolution is determined by the initial separation and the orbital evolution of the binary (see e.g., Klencki et al. 2021)—generally, it will begin when the radius of the primary overflows its Roche lobe. The outcome of the CE phase can be either a stellar merger or the formation of a close binary. If the binary remains bound and on a tight orbit after the second NS has been created, the system will merge due to the dissipation of gravitational waves (GWs). The merger timescale depends on the final orbital separation and energy of the binary; if these are small enough such that the binary merges within a Hubble time, the stellar remnants—either black holes, neutron stars, or white dwarfs—will merge and produce GW and possibly electromagnetic (EM) radiation.

In particular, BNS mergers expel metallic, radioactive debris (the light from which is referred to as a kilonova) that can be seen by telescopes (e.g., Kasen et al. 2017). In August 2017, for the first time, we detected both GWs and EM radiation

(e.g., Coulter et al. 2017; Abbott et al. 2017b; Goldstein et al. 2017) coming from the same astrophysical event. This landmark discovery, which has opened up new lines of research into several areas in astrophysics and physics, makes the study of interacting binaries and common envelope in particular, even more essential in our attempts to discern the assembly history of these probes of extreme physics. Yet, their formation process remains an open question.

In this work we present the first 3D hydrodynamics simulations of successful CE ejection leading to a BNS system. Simulations of this kind have not been performed so far due to the prohibitive computational cost—the relevant dynamic ranges of density and physical distance are $\gtrsim 10^6$ (e.g., the global problem must resolve a $R \approx 10^6$ cm neutron star within the envelope of a $R \approx 10^{13}$ cm giant star, whose density varies from $\rho \approx 10^6$ g/cm^3 to $\rho \approx 10^{-9}$ g/cm^3 within the relevant regions). Most 3D hydrodynamics simulations of CE evolution have been at relatively equal mass ratios and for relatively low stellar masses ($M_\star \lesssim 3 M_\odot$) (e.g., Zhang & Fryer 2001; Ricker & Taam 2008, 2012; Passy et al. 2012; Nandez & Ivanova 2016; Ohlmann et al. 2016; Iaconi et al. 2017, 2018; Prust & Chang 2019; Kramer et al. 2020; Sand et al. 2020; Chamandy et al. 2020), and there has been an early attempt and characterization of the difficulties faced by simulating a massive star binary by Ricker et al. (2019). Higher mass ratios involving NSs have been studied in 1D (e.g., MacLeod & Ramirez-Ruiz 2015a; Fragos et al. 2019).

In contrast to other contemporary studies, the initial conditions of our 3D hydrodynamics simulations are informed by an adjusted 1D analytic energy formalism and a 2D kinematics study. We start the 3D hydrodynamics simulation once the secondary

has reached a relatively small radius (after ejecting $< 0.1\%$ of the star's binding energy, at $r \approx 10 R_\odot$) compared to the full radius of the star. In contrast to other contemporary work in which the core is often replaced with a point mass, we fully resolve the core to $\lesssim 0.005 R_\odot$.

This paper is organized as follows. §7.2 describes our methods, including the 1D analysis, 2D kinematics, and 3D hydrodynamics, §7.3 describes our results, §7.4 compares to other work and discusses caveats and future work, and §7.5 concludes.

7.2 Methods

We simulate the CE evolution of an initially $12 M_\odot$ red supergiant primary (donor) and a $1.4 M_\odot$ point mass secondary (NS) in 3D hydrodynamics, for different initial separations and initial conditions. We build the primary with a 1D stellar evolution code (MESA). We use an adjusted 1D energy formalism to predict the likely CE ejection regime, and we use a 2D kinematics study to inform the initial conditions of the 3D hydrodynamics simulations. We import the stellar model to the 3D hydrodynamics simulation (FLASH), in which we excise the outermost layers of the star with negligible binding energy and start the secondary relatively close to the core of the primary where the CE ejection is predicted to take place.

7.2.1 MESA model

We use the 1D stellar evolution code MESA v8118 (Paxton et al. 2011, 2013, 2015) to construct the primary. We use an inlist from Götberg et al. (2018), which

is publicly available on Zenodo.[32] We construct a $12M_{\odot}$ solar-metallicity (X=0.7154, Y=0.270, Z=0.0142; Asplund et al. 2009) single-star primary as this is a typical mass to form a NS (Heger et al. 2003). In §7.3 we show the evolutionary history of this model and in §7.8 and §7.9 we show mass, density, composition, and binding energy profiles for the models we simulate in 3D hydrodynamics.

See Section 2.1 of Götberg et al. (2018) for details on the MESA setup. Additional uncertainties in the MESA modeling are discussed in Section 7.4. In brief, our setup is to use the `mesa_49.net` nuclear network of 49 isotopes, account for overshooting following Brott et al. (2011), and account for mass loss using the wind schemes of de Jager et al. (1988) and Vink et al. (2001).

7.2.2 Energy formalism

We perform CE energy formalism (α formalism; Livio & Soker 1988; van den Heuvel 1976; Webbink 1984; de Kool 1990; Iben & Livio 1993) calculations on the profiles to predict the radius ranges in which CE ejection is possible and to inform the initial conditions of the 3D hydrodynamics simulations. As in Wu et al. (2020a), we calculate the gravitational binding energy and orbital energy loss profiles (see §7.9) for the MESA model at all ages throughout its giant branch evolution. These profiles help determine the predicted ejection ranges (see §7.3). See Wu et al. (2020a) and Everson et al. (2020) for further details of these calculations.

Local 3D hydrodynamical simulations of CE have shown that during dynamical inspiral, the energy deposition from the secondary's plunge extends inward from

[32]MESA inlists, v8118: `https://zenodo.org/record/2595656`.

the secondary's location, heating and unbinding deeper envelope material (see, e.g., MacLeod et al. 2017a; De et al. 2020). To incorporate the effects of this energy deposition on the ejection radius range, we also apply an adjusted α formalism (Everson 2020) that requires the orbital energy loss to overcome the binding energy at radii deeper than that given by the orbital separation, corresponding to $r - R_a$ (where R_a is the Bondi accretion radius) or $r - R_{\rm Roche}$ (where $R_{\rm Roche}$ is the Roche radius); see below. The ejection ranges shown in Figure 7.1 were calculated using this adjusted α formalism as well as using work from Everson et al. (2020).

All α formalism calculations in, e.g., Figure 7.10, are based on, e.g., Ivanova et al. (2013b) and Kruckow et al. (2016). The change in orbital energy is defined as in Eqn. 2 of Kruckow et al. (2016):

$$\Delta E_{\rm orb} = -\frac{GM_{\rm core}M_{\rm secondary}}{2a_{\rm f}} + \frac{GM_{\rm donor}M_{\rm secondary}}{2a_{\rm i}}, \tag{7.1}$$

where $a_{\rm i}$ is the initial orbital separation and $a_{\rm f}$ is the final orbital separation, and the gravitational binding energy is defined as

$$E_{\rm bind} = -\int \frac{Gm}{r} dm. \tag{7.2}$$

For the $r - R_a$ adjusted formalism we use the accretion radius as defined in, e.g., Bondi & Hoyle (1944) and Hoyle & Lyttleton (1939):

$$R_a = \frac{2GM_{\rm secondary}}{v_\infty^2} \tag{7.3}$$

and for the $r - R_{\rm Roche}$ adjusted formalism we use the Roche radius (the radius equivalent to the volume of the Roche lobe) as in the approximation of Eggleton (1983).

We adapted a 2D integrator used to study the kinematics of CE inspiral with drag (MacLeod et al. 2017a) with the results from a 3D study of drag coefficients in CE evolution with density gradients (De et al. 2020) to determine an initial velocity vector for the radius at which we begin our 3D hydrodynamics simulations. We also compare to results using a circular initial velocity vector.

7.2.3 FLASH setup

The outline of our 3D hydrodynamics setup is the following: (1) excise the tenuous outer layers of the primary (donor) star, (2) initialize the primary on the grid, (3) relax the point particle secondary (neutron star) onto the grid, (4) initialize the point particle's velocity vector based on the 2D kinematics results, and (5) simulate the system in 3D hydrodynamics until the orbital separation stalls and "parks".

In this paper, we focus on evolutionary stages which we expect that will lead to a CE ejection *a priori* and then use 3D hydrodynamics to simulate the crucial dynamical inspiral phase of the CE evolution.

Numerical diffusion prohibits us from evolving the system for $\gtrsim 30$ orbits, since for many orbits, numerically-driven drag results in the companion inspiraling toward the core of the donor. See §7.4 for a detailed discussion of this. Thus, we consider only evolution in the 3D hydrodynamics on a timescale much shorter than the thermal timescale, to prevent including artificially merging or ejected cases.

We use a custom setup of the 3D adaptive-mesh refinement (AMR) hydrody-

namics code FLASH (Fryxell et al. 2000), version 4.3[33]. Our FLASH setup is based on that of Wu et al. (2020a), which was based on that of Law-Smith et al. (2019) and Law-Smith et al. (2020a), which was in turn based on that of Guillochon et al. (2009) and Guillochon & Ramirez-Ruiz (2013a). See these references for more details on the numerics. A brief summary including salient features and changes to the setup is below.

We use an Helmholtz equation of state with an extended Helmholtz table[34] spanning $10^{-12} \leq \rho$ [g cm^{-3}] $\leq 10^{15}$ and $10^3 \leq T$ [K] $\leq 10^{13}$. The Helmholtz equation of state assumes full ionization (Timmes & Swesty 2000) and thus does not include recombination energy in the internal energy. We track the same chemical abundances in the 3D hydrodynamics as in the MESA nuclear network for the star, for all elements above a mass fraction of 10^{-5} (this value is somewhat arbitrary but does not affect the results); this is 22 elements ranging from hydrogen (^{1}H) to iron (^{56}Fe). While including an arbitrary number of the elements tracked in MESA is possible, including all of the elements would unnecessarily increase the memory load of the 3D hydrodynamics.

We excise the outer envelope of the primary donor star, which constitutes $< 0.1\%$ of the total binding energy (see §7.2.2, §7.3, and §7.8 for further discussion) and is easily ejected, trimming the star to $R = 10R_\odot$. Our box size is $\Delta X_{\rm max} = 40R_\odot$ on a side. This technique was also employed in Wu et al. (2020a). We refine such that $\Delta X_{\rm min} \lesssim 0.005R_\odot$ within a factor of 100 of the maximum density, then derefine in the AMR with decreasing density, for $N \approx 272$ cells across the diameter of the star for the nominal simulations presented in this paper. We verified the hydrostatic equilibrium of

[33]The updates in later versions do not affect our setup.
[34]As of time of writing available at http://cococubed.asu.edu/code_pages/eos.shtml.

our initial conditions for several dynamical timescales of the star (and 100s of dynamical timescales of the core). Hydrostatic equilibrium following the relaxation scheme in our setup has also been tested in e.g., Law-Smith et al. (2020a). We initialize the secondary point mass (NS) at $r = 8R_{\odot}$, well within the envelope of the $10R_{\odot}$ trimmed star. After initializing the star on the grid, we gradually introduce the point mass secondary inside the envelope of the primary by gradually increasing its velocity to its initial velocity vector (see also §7.2.2). This technique is also used in MacLeod et al. (2017a) and Wu et al. (2020a).

We note that we performed an additional convergence simulation (in addition to the numerical convergence simulations discussed in §7.12) where the neutron star was initialized at $r = 16R_{\odot}$, twice that in our nominal study, and verified that it reaches the same radius at which we start our nominal simulations (i.e., it does not "stall" exterior to our initial conditions if we start our simulation further out). More realistic initial conditions would start at the point of Roche lobe overflow to take into account the transfer of energy and angular momentum from the orbit to the envelope, but this is computationally prohibitive for a $R_{\star} \approx 1000R_{\odot}$ primary with a density range of 15 orders of magnitude (from $\rho \approx 10^{6}$ to $\rho \approx 10^{-9}$ g/cm^{3}). However, we argue that the initial conditions used in this work are similar to the configuration if we had begun the simulation at this earlier stage and evolved it to the time we start our simulation. This is justified in §7.8 and using the methods of §7.2.2.

We use two initial velocity vectors: (1) circular and (2) informed by a 2D kinematics study using the stellar density profile. The 2D kinematics velocity vectors

are derived from orbits that are more eccentric than a circular orbit. However, we find that the initial velocity vector does not have a significant effect on the final outcome of the simulation, with both velocity vectors leading to qualitatively similar results. This weak dependence on the initial velocity vector is due to the fact that the point mass relatively quickly encounters drag and spirals inward dynamically, as was also found in Wu et al. (2020a).

We also perform a numerical convergence study (see §7.12 for details). For this, we run two simulations with the same initial conditions but one with 2.5 times higher linear resolution than the other, and find very similar results in the orbital evolution and energy of the envelope, verifying that our nominal resolution of $\Delta X_{\rm min} \lesssim 0.005 R_\odot$ is converged.

7.3 Results

7.3.1 1D modeling

The top panel of Figure 7.1 shows radius vs. time for the initially $12 M_\odot$ donor, evolved as a single star using the setup of Götberg et al. (2018). The red circles indicate the three different initial conditions we simulate in 3D hydrodynamics: near the first peak ($R_\star = 750 R_\odot$, $M_\star = 11.8 M_\odot$), on the second rise ($R_\star = 900 R_\odot$, $M_\star = 9.9 M_\odot$), and at the second peak ($R_\star = 1080 R_\odot$, $M_\star = 9.8 M_\odot$). The first peak corresponds to RLOF (Roche-lobe overflow) during late hydrogen-shell burning (case B; e.g., Kippenhahn & Weigert 1967) and the second peak to RLOF after core-helium burning (case C; e.g., Lauterborn 1970). In all three cases, the donor has a deep convective envelope and the

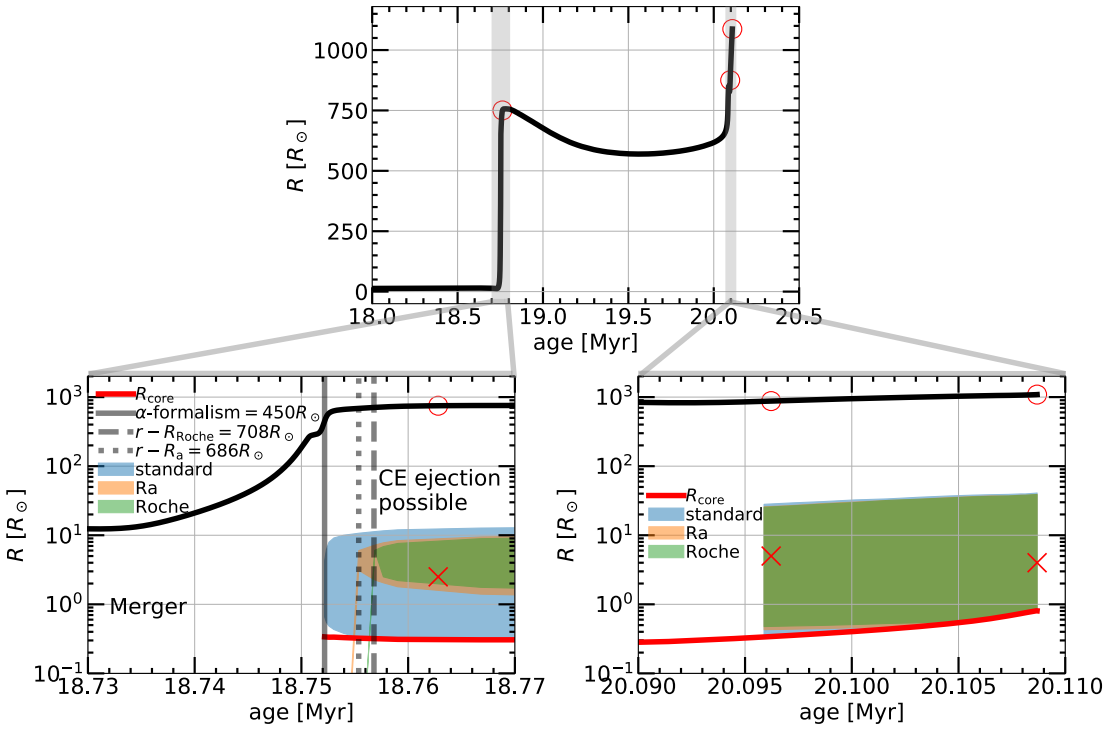

Figure 7.1: MESA evolutionary history for the $12M_{\odot}$ primary (donor) star. Top: radius vs. time. Red circles indicate the models we simulate in 3D hydrodynamics. Bottom left: focus on the first rise (expansion). Vertical lines indicate the earliest ages where CE ejection is possible and shaded regions indicate the radius ranges where CE ejection is possible according to our adjusted 1D energy formalism. Red line indicates the radius of the He core. Red 'X's indicate final orbital separation from our 3D hydrodynamics simulations. Bottom right: focus on the second rise. See §7.8 for further details on the MESA model.

mass transfer is dynamically unstable.

In the bottom panels, we zoom in on the first and second rises (expansions). The radius of the He core is shown in red (defined by the `he_core_mass` attribute in MESA, using `he_core_boundary_h1_fraction` $\geq$ `0.01` and `min_boundary_fraction` $\geq$ `0.1`). It is $R_{\rm core} = 0.31 R_\odot$ for the first peak, $R_{\rm core} = 0.36 R_\odot$ for the second rise, and $R_{\rm core} = 0.8 R_\odot$ for the second peak. For a given stellar age, the predicted radius ranges where CE ejection is possible as predicted by the three 1D energy formalisms (standard α formalism, $r - R_a$ adjusted formalism, and $r - R_{\rm Roche}$ adjusted formalism) are shown in shaded blue, orange, and green respectively (see §7.2.2). We start the FLASH simulations just within these ranges (see §7.2). Red 'X's indicate the time at which the envelope is ejected in our 3D hydrodynamics simulations (see Figure 7.4).

The bottom left panel focuses on the first rise. The earliest ages at which CE ejection is possible from the 1D energy formalisms are indicated by the vertical lines. The bottom right panel focuses on the second rise. Here the different energy formalisms predict a similar range of radii for possible CE ejection, and in the 3D hydrodynamics we eject the envelope within these ranges.

We calculate the minimum radius on the second rise in which Roche-lobe overflow is possible, accounting for orbital widening of the binary as a result of mass loss by fast stellar winds during its prior evolution (see §7.10 for discussion and details on this). We find that after the first peak (at $R_\star = 757 R_\odot$), for radii less than $R_\star = 900 R_\odot$ on the second rise, RLOF will not occur. Thus, we simulate three models in 3D hydrodynamics that are chosen to span the range of stellar structures in which dynamical

CE ejection is possible for a $12M_{\odot}$ primary: near the first peak ($R_{\star} = 750R_{\odot}$), on the second rise ($R_{\star} = 900R_{\odot}$), and at the second peak ($R_{\star} = 1080R_{\odot}$). We note that the $750R_{\odot}$ and $1080R_{\odot}$ models may appear fine-tuned in isolation, but they are chosen so that our suite of 3D hydrodynamics simulations in this paper span the parameter space of stellar structures that will lead to dynamical CE ejection.

7.3.2 3D hydrodynamics

Figure 7.2 shows 3D volume renderings of three fields (density, velocity, and energy) at three times: early in the evolution (11 hr), at an intermediate time (16 hr), and at a relatively late time (25 hr) when the envelope has just been ejected. We show renderings for the $900R_{\odot}, v_i = v_{\rm circ}$ (circular initial velocity) simulation. Results are qualitatively similar for all of the other simulations. The volume renderings are of the bottom half of the orbital plane ($z < 0$, with $J_{\rm orb} \parallel z$), with a color map and transfer function chosen to highlight the dynamic range and structure of the field being studied. See §7.6 for the detailed time evolution of these three fields and a zoom-in on the core.

The 1st row of Figure 7.2 shows the logarithm of gas density. In the first panel, one can see the density shells that are progressively disturbed as the secondary sweeps through the primary's envelope. At late times, the structure is quite disturbed and resembles a differentially rotating disk, though at even later times, the secondary stalls and "parks" at its final orbital separation (see Figure 7.3).

The 2nd row of Figure 7.2 shows the ratio of absolute magnitude of velocity to the local escape velocity for each cell, $|v|/v_{\rm esc,local}$. Pink corresponds to gas that is bound to the system (values < 1) and green corresponds to gas that is not bound

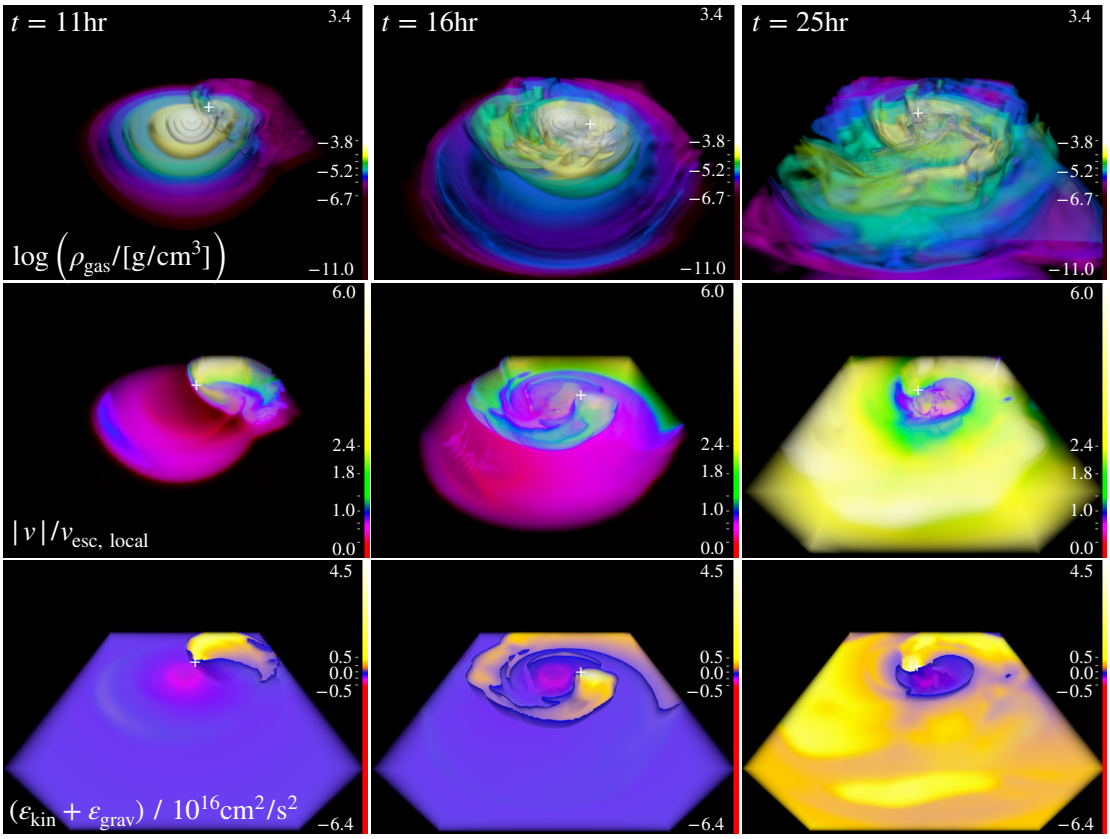

Figure 7.2: 3D renderings of three fields (density, velocity, and energy) at three times: early in the evolution (11 hr), at an intermediate time (16 hr), and at a moderately late time (25 hr) when the envelope has just been ejected. We show the $900 R_\odot, v_i = v_{\rm circ}$ simulation; results are qualitatively similar for all our other simulations. 1st row: logarithm of gas density. Shells corresponds to different density isosurfaces. 2nd row: ratio of velocity magnitude to local escape velocity, $|v|/v_{\rm esc,local}$. Blue isosurface is at $|v|/v_{\rm esc,local} = 1$, pink-red is < 1, green-yellow is > 1. 3rd row: sum of specific kinetic and potential energy. Blue isosurface at $\varepsilon = 0$, pink-purple corresponds to bound ($\varepsilon < 0$) and yellow corresponds to unbound ($\varepsilon > 0$). White '+' indicates position of secondary. Videos available at https://youtube.com/channel/UCShahcfGrj5dOZTTrOEqSOA.

to the system (values > 1). The blue isosurface is at $|v|/v_{\rm esc,local} = 1$. At late times (after a few orbits of the secondary), nearly all of the envelope is at $|v| > v_{\rm esc,local}$ and is gravitationally unbound from the star. Some of the envelope material is shocked to $|v| \gtrsim 6v_{\rm esc,local}$ on the leading edge of a spherically expanding shell. One can see the envelope being shocked and swept preferentially outwards as the secondary orbits the center of mass of the primary. As the secondary moves through the envelope of the primary, it acts as a local diffusive source term, giving surrounding material roughly outward velocities. We also analyzed the velocity vectors of each grid cell, and found that they are nearly all pointed outwards from the core as a result of the secondary's repeated passages, ejecting the envelope.

The 3rd row of Figure 7.2 shows specific energy (the sum of specific kinetic and potential energy, internal energy is not included). Pink-purple corresponds to bound ($\varepsilon < 0$) and yellow corresponds to unbound ($\varepsilon > 0$). There is a blue isosurface at $\varepsilon = 0$. At early times, the binding energy of most cells is negative. At late times, nearly all of the material in the box (except for the surviving core) has positive energy. The core and secondary have separate Roche lobes, and the equipotential surface of $\varepsilon = 0$ (blue isosurface) is confined to a small region around the core. The size of this region decreases with time and number of orbits until the secondary stalls at its final orbital separation. This qualitatively shows complete envelope ejection.

In the bottom left panel of Figure 7.2 one can see a crescent-shaped sliver of material on the left hand side of the panel that becomes unbound. This is due to the change in the mass distribution interior to the radius of this sliver (initially

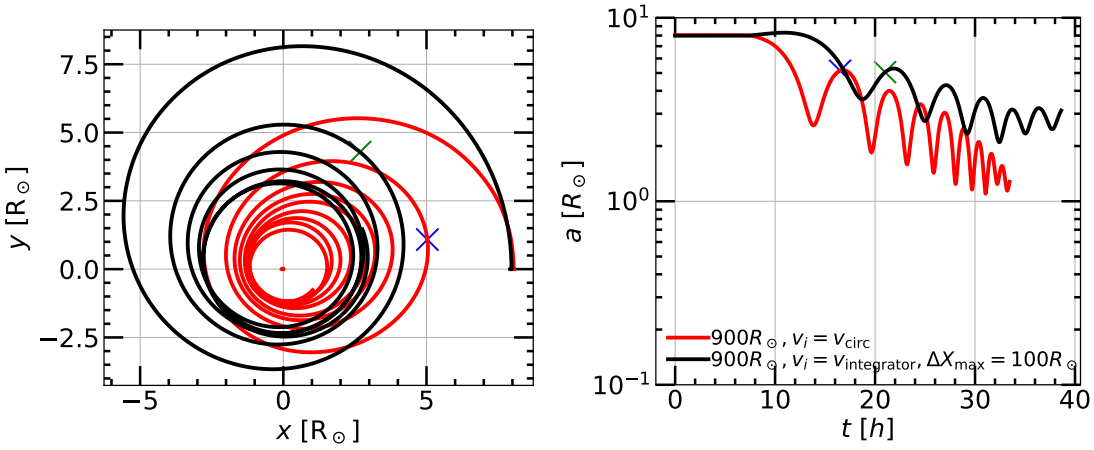

Figure 7.3: Trajectory and orbital separation for two $900R_\odot$ simulations with different initial velocities. Black is $900R_\odot, v_i = v_{\rm integrator}, \Delta X_{\rm max} = 100R_\odot$, red is $900R_\odot, v_i = v_{\rm circ}$. Blue and green 'X's mark the time at which the envelope is ejected for the $v_{\rm circ}$ and $v_{\rm integrator}$ runs respectively (see Figure 7.4). Left: trajectory. Black/red line is secondary (NS), red dot is center of mass of primary (donor star). Right: separation $a(t)$ between center of mass of primary and position of point mass secondary vs. time.

at $r \approx 10R_\odot$) caused by the secondary sweeping out mass on the right hand side. The gravitational potential due to the enclosed mass changes and this sliver of material becomes unbound due to gravitational effects (acting nearly instantaneously) as opposed to hydrodynamical effects (acting on the dynamical time).

We now discuss the orbital parameters of the two objects and in particular the secondary as it orbits the center of mass of the primary donor star. The left panel of Figure 7.3 shows the trajectory of the center of mass of the primary and the secondary as a function of time in two of our simulation box coordinates (x and y; because our simulation is symmetric along the z-axis, there is little evolution of the center of masses in z). We show the evolution for the two $900R_\odot$ simulations, with $v_i = v_{\rm circ}$ and $v_i = v_{\rm integrator}$, where $v_{\rm integrator}$ is the initial velocity vector informed by the 2D kinematics study. Blue and green 'X's mark the time at which the envelope is

ejected (see Figure 7.4).

The right panel of Figure 7.3 show the separation $a(t)$ between the center of mass of the primary and the position of the point mass secondary vs. time for the same two simulations. Results for our other simulations are qualitatively similar. The final orbital separations and the energies as a function of time for all simulations are shown in Figure 7.1 (and the next paragraph) and Figure 7.4 respectively. Several "bounces" are observed as the secondary orbits the core.

The initial velocity vector informed by the 2D kinematics (see Section 7.2) occurs near the pericenter of an eccentrically inspiraling orbit and it is thus higher energy (larger velocity) than the circular initial velocity. The run using this vector stalls and "parks" at an orbital separation of $a_{\rm f} \approx 2.8 R_\odot$. The circular initial velocity simulation parks at an orbital separation of $a_{\rm f} \approx 1.2 R_\odot$. For reference, the final orbital separation of the $750 R_\odot$ simulation is $a_{\rm f} \approx 1.1 R_\odot$ and the final orbital separation of the $1080 R_\odot$ simulation is $a_{\rm f} \approx 1.4 R_\odot$. After supernova kicks (calculated with 1000 randomly oriented kicks and a kick magnitude drawn from a Maxwellian distribution with 1D RMS $\sigma = 265$ km/s; Hobbs et al. 2005), we calculate that a significant fraction of these systems will form binary neutron stars that merge within a Hubble time. See §7.11 for details of this calculation.

We estimate the $\alpha_{\rm CE}$-equivalent efficiency, where $\alpha = E_{\rm bind,env}/\Delta E_{\rm orb} \approx 2 a_{\rm f} E_{\rm bind}/(G M_{\rm core} M_{\rm secondary})$. For the $R_\star = 900 R_\odot$ run, we take $a_f = 2.8 R_\odot$, $M_{\rm core} = 4.5 M_\odot$, $M_{\rm secondary} = 1.4 M_\odot$, and a binding energy at $2.8 R_\odot$ of $E_{\rm bind} \approx 5.5 \times 10^{47}$ erg (see Figure 7.11). This gives an $\alpha_{\rm CE}$-equivalent efficiency of $\alpha_{\rm CE} \approx 0.13$. Similarly, for

the $R_\star = 750 R_\odot$ run, taking $a_f = 1.1 R_\odot$, we find $\alpha_{\rm CE} \approx 0.38$. For the $R_\star = 1080 R_\odot$ run, taking $a_f = 1.4 R_\odot$, we find $\alpha_{\rm CE} \approx 0.08$. Thus, the $\alpha_{\rm CE}$ is small for the models we study, but we note that this may be specific for these extended progenitors.

In comparison, based on their final orbital separation, the 1D MESA study of Fragos et al. (2019) (who studied a different primary model; see Figure 7.10) find a high $\alpha_{\rm CE}$-equivalent efficiency of ≈ 5, though we note that this study finds envelope ejection in the self-regulated regime and $\alpha_{\rm CE}$ is calculated after a mass-transfer phase which occurs after the envelope is ejected. After envelope ejection, in our simulations, we expect a stable mass transfer phase to occur between the surviving core and the NS (as in Fragos et al. 2019), which will further alter the separation before the supernova takes place.

We now turn to a calculation of the energy of each cell in the simulation box as a function of time. Figure 7.4 shows specific energy ($\varepsilon = \varepsilon_{\rm kin} + \varepsilon_{\rm grav}$) vs. time, for material outside of the current orbit of the secondary (see Figure 7.3) for all of the models we simulate in 3D hydrodynamics. We note that the recombination energy, while not included in our simulations, is small compared to the binding energy of the envelope here; for hydrogen, $\varepsilon_{\rm recomb} \approx 13.6$ eV$/m_{\rm p} \approx 10^{19}$ erg/g, whereas the envelope energy is $\varepsilon \approx 10^{21}$ erg/g (Figure 7.4). The energy of this material increases with time, transitioning from negative (bound) to positive (unbound) at $t \approx 15$–20 h. Small-scale variations correspond to the "bounces" in orbital separation as a function of time with each successive orbit of the secondary (Figure 7.3).

We successfully eject the envelope for all of our simulated models, which span

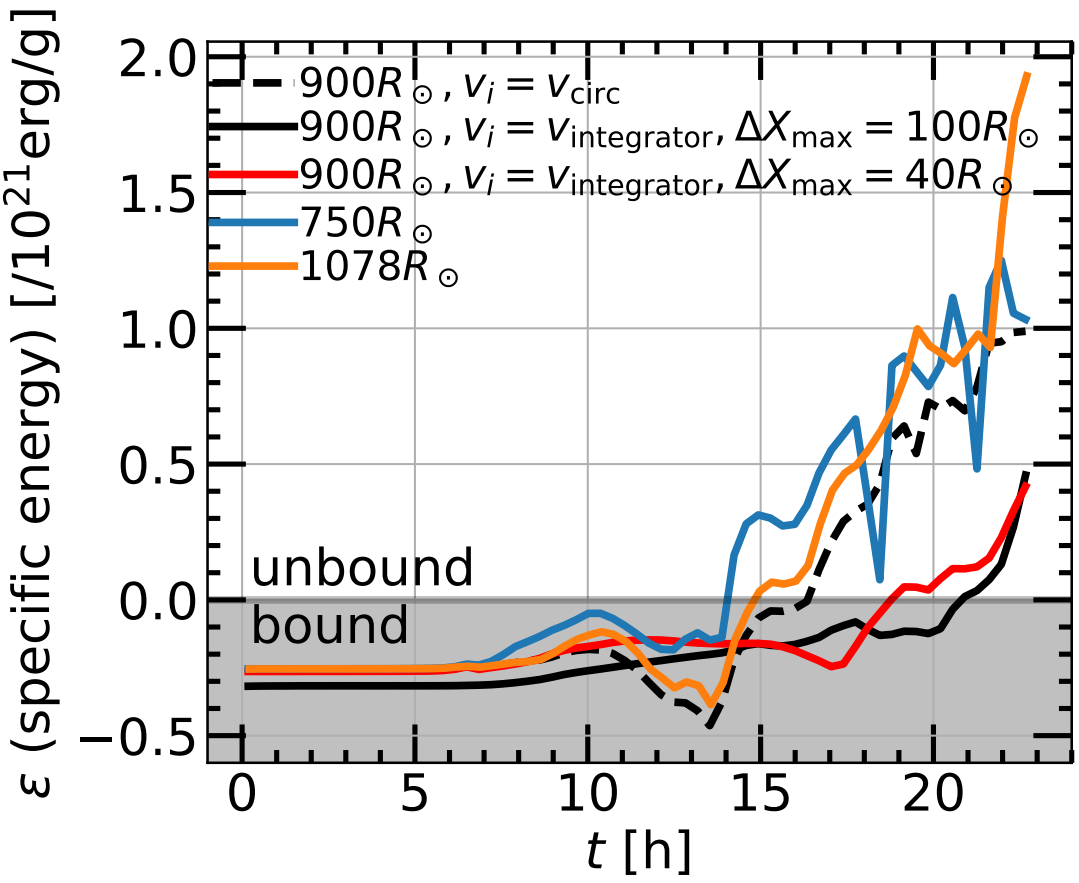

Figure 7.4: Sum of specific kinetic and potential energy ($\varepsilon = \varepsilon_{\rm kin} + \varepsilon_{\rm grav}$) vs. time for material outside of the current orbit of the secondary (see Figure 7.3) for all simulations. Envelope is bound for $\varepsilon < 0$ (grey region) and envelope is ejected for $\varepsilon > 0$.

the range of stellar age and radii in which dynamical CE ejection is predicted to be possible for an initially $12M_{\odot}$ primary. We note that we do not include internal or recombination energy in calculation of the envelope energy (which some contemporary studies do, and which is a positive quantity that helps with envelope ejection; however (see above), these energies are negligible for the models we study), only kinetic and gravitational potential energy.

As a second verification of envelope ejection, we also calculate the mass ejected (unbound) from the primary as a function of time. We find that the secondary ejects the entire mass of the envelope, including the mass interior to the neutron star's orbit and exterior to the Roche radius of the core (see Figure 7.14).

The mass enclosed inside the orbit of the secondary does not change appreciably over the course of the simulation; we verify that mass does not "leak" significantly from the inner regions of the star due to numerical effects (see §7.12). Thus, we estimate that the inspiral is not driven by the increased numerical drag due to the core mass leaking out towards the secondary (because none of this leaked mass reaches the secondary's orbit) but is instead driven by regular numerical drag due to the 3D hydrodynamical grid that is a resolution-dependent effect (see §7.12 for our numerical convergence study).

We now briefly discuss the chemical abundance of the ejecta. Figures 7.5 shows 3D renderings of the mass fraction of hydrogen, helium, and nitrogen, at three times for the $(900R_{\odot}, v_i = v_{\rm circ})$ run. Hydrogen, helium, and nitrogen mix with the outer debris; results for other runs are qualitatively similar. See §7.8 for 1D composition profiles of

these elements at the beginning of the simulation. All composition data is available upon request.

7.3.3 Recombination Transient

The most notable result is that the hydrogen envelope is completely ejected at late times; this implies no hydrogen will be visible in the spectrum of the surviving stripped star as the surface hydrogen mass fraction is essentially zero (it is comparable to the core's hydrogen abundance). The expanding hydrogen bubble is observable as a hydrogen recombination transient (or a luminous red nova) Ivanova et al. (2013a). We use Eqns. (A1), (A2), and (A3) of MacLeod et al. (2017b), based on Ivanova et al. (2013a)'s application of the analytic theory of recombination transients (e.g., Popov 1993; Kasen & Woosley 2009; Kasen & Ramirez-Ruiz 2010) to estimate the luminosity, timescale, and total energy of this recombination transient (see §7.7 for details of the calculation). Using $R_{\rm init} \approx 2R_{\odot}$ (approximate stalling orbital separation of the secondary across our models), $\Delta M \approx 5M_{\odot}$ (the entire mass of the envelope), $v_{\rm ej} \approx 18$ km/s (the velocity at $10R_{\odot}$ at the end of our simulation), $\kappa \approx 0.32$ cm^2 g, and $T_{\rm rec} \approx 4500$ K, we find $L_{\rm p} \approx 10^{37}$ erg s^{-1}, $t_{\rm p} \approx 274$ d, and $E_{\rm rad,p} \approx 2 \times 10^{44}$ erg. The mass of the stripped star is $M_{\star} \approx 4.5M_{\odot}$, radius $R_{\star} \approx 1R_{\odot}$. We note a stripped star and neutron star are also interesting as a "living" gravitational wave source potentially observable with LISA (Götberg et al. (2020); for lower mass systems see also Nelemans et al. (2004); Yungelson (2008); Wu et al. (2020b)). If the system is tight enough, the future evolution is determined by the radiation of GWs and no longer the evolution of the stripped star. See §7.4 for discussion on extensions to our framework to study the

remnant in more detail and for longer timescales.

Roughly 10% of the brightest luminous red novae (LRN) transients, which have been previously associated with stellar mergers and common-envelope ejections, are predicted to occur at some point in binary neutron star forming systems (Howitt et al. 2020; Vigna-Gómez et al. 2020). LRN have come to be associated with stellar mergers through detailed study of a few landmark events. M31 RV was one of the first LRN to be identified, in 1988, but the light curve of the transient is only captured during the decline (e.g., Mould et al. 1990). The galactic transient V1309 Sco proved essential in establishing the nature of these events as stellar mergers (Mason et al. 2010; Nicholls et al. 2013). Noteworthy transients arising from a relatively massive stars include M31LRN 2015 with a progenitor of $M_\star \approx 3$–$5.5 M_\odot$ (MacLeod et al. 2017b) and M101 OT2015-1 with a progenitor of $M_\star \approx 18 M_\odot$ (Blagorodnova et al. 2017a).

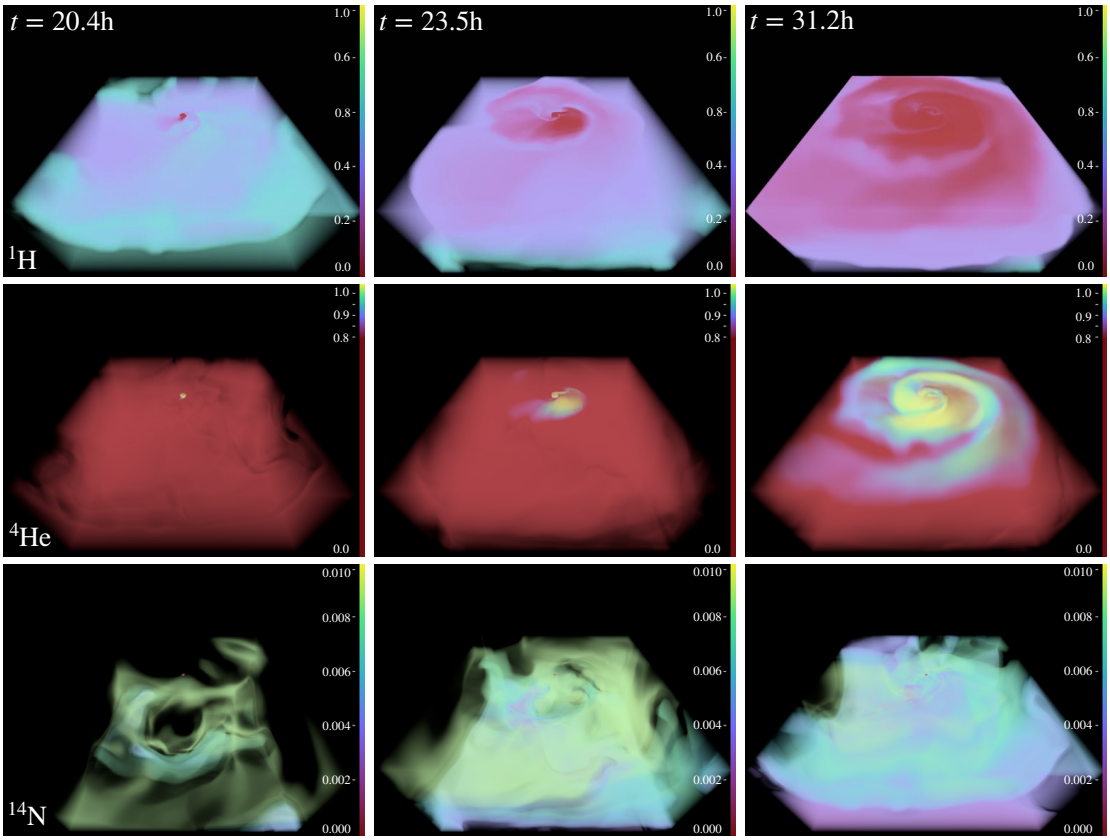

Figure 7.5: 3D renderings of mass fraction of hydrogen, helium, and nitrogen as a function of time, for the ($900R_{\odot}, v_i = v_{\rm circ}$) run. Results for other simulations are qualitatively similar. The colormap is the same for each element but note that the scale changes for each element in order to highlight the structure. For hydrogen and helium, mass fractions range from 0 (dark purple) to 1 (light yellow). For nitrogen, mass fractions range from 0 (dark purple) to 0.01 (light yellow).

7.4 Discussion

Here we briefly compare to other work, discuss uncertainties in the 1D stellar modeling, resolution-dependent effects in the 3D hydrodynamics, and comment on future work.

7.4.1 Comparison to other work

We briefly compare to other work below, though we note that no other 3D hydrodynamics simulations have been conducted to simulate CE ejection leading to a binary neutron star system, thus with our mass ratios (which are more extreme than the current literature) or stellar radii (which are also relatively larger than the current literature). The main difference with these works, besides the star studied, is that the initial conditions of our 3D hydrodynamics simulations are informed using an adjusted 1D energy formalism (see §7.2) and a 2D kinematics study.

There has been five decades of work on the CE phase (see e.g., Ivanova et al. 2013b), and there is an extensive literature on CE ejection (we review some below); however, the most relevant comparison for our work is to the 1D study of Fragos et al. (2019), who also study BNS formation through the CE phase. These authors study a different (though comparable) MESA model to ours (see Figure 7.10) and thus a direct comparison is not possible.

We note our 1D formalism predicts that the model studied by Fragos et al. (2019) is in a boundary region where the outcome of CE evolution is unclear. The authors find CE ejection in the self-regulated regime. We study CE ejection in the

dynamical regime, and find that for all of the models we simulate in 3D hydrodynamics, the envelope is ejected in the dynamical regime. Fragos et al. (2019) find a final orbital separation of $a_{\rm f} \approx 3.3$–$5.7 R_{\odot}$. We find final orbital separations of $a_{\rm f} \approx 1.1$–$2.8 R_{\odot}$. While it is valuable to model the CE evolution from start to finish, the 1D treatment that is necessary to facilitate this has inherent limitations. For example, Fragos et al. (2019) assume complete and instantaneous spherically symmetric sharing of orbital energy with the envelope. This is an nonphysical assumption that can only be addressed by 3D hydrodynamics.

Results from other studies of CE ejection for lower mass ratio systems are listed below. Generally, contemporary studies have been unable to eject the envelope in the course of the 3D simulation. The fact that we are able to successfully and robustly eject the envelope, without including internal or recombination energy (which is claimed to be essential to CE ejection in some contemporary work at lower masses; see below), is likely due to the fact that we study an evolved $12 M_{\odot}$ red supergiant primary; thus, the secondary encounters a very different density profile during its inspiral that the density profiles in the works listed below. Sandquist et al. (1998) find 23-31% envelope ejection in simulations with $3 M_{\odot}$ and $5 M_{\odot}$ AGB primaries. Staff et al. (2016) find 25% envelope ejection with a $3.05 M_{\odot}$ ($3.5 M_{\odot}$ ZAMS mass) AGB primary. Sand et al. (2020) find $<$20% envelope ejection when not accounting for recombination energy, and complete envelope ejection when including recombination energy, for a $1 M_{\odot}$, $174 R_{\odot}$ early-AGB star with companions of different masses. Chamandy et al. (2020) find an envelope unbinding rate of 0.1–$0.2 M_{\odot}$ yr^{-1}, implying envelope unbinding in $<$10 yr, for

a $1.8M_\odot$, $122R_\odot$ AGB primary with $1M_\odot$ secondary. Note that these studies calculate envelope energy outside of the Roche radius of the core, so we cannot compare results directly.

We note that many contemporary studies that attempt to simulate systems in which one star is highly centrally concentrated have replaced the core of that star with a point mass, and the core's density profile with a much less centrally-concentrated polytrope. It is possible that this creates artificial diffusion at the boundary, making it easier to eject the envelope. In this work we fully resolve the core of the star, allowing for a realistic treatment of the inspiral and material interior to the secondary's location as it stalls and "parks" at a final orbital separation.

7.4.2 Uncertainties due to prior evolution

There are four main disclaimers to our analysis, and indeed to our initial stellar models in general:

First, our model of the $12M_\odot$ donor was evolved as a single star. However, for the progenitor system of a BNS merger, the typical scenario includes a stable mass transfer phase before the formation of the NS (e.g., Tauris et al. 2017). Therefore, the donor star at the CE phase is the initially less massive star which has possibly accreted mass from the NS progenitor and survived the passage of the supernova shock. While the latter has only a moderate effect on the stellar structure (e.g., Hirai et al. 2018), the phase of stable mass transfer can lead to high rotation (e.g., Hut 1981; Cantiello et al. 2007; de Mink et al. 2013), chemical pollution with He (e.g., Blaauw 1993), and mixing of fresh hydrogen in the core. These effects can influence the stellar radius significantly

(e.g., rotation can increase the equatorial radius, He-richness can contribute to keep the star more compact), and most importantly change the density profile just outside the core (i.e., in the domain of our 3D simulation) with the rejuvenation-inducing mixing. A second order effect is the impact on the wind mass loss rate (and thus orbital evolution) of the system (e.g., Renzo et al. 2017). While these require further investigation, our models provide a proof-of-concept of our methods that could be applied to more realistic post-RLOF CE donors.

Second, we do not accurately know the distribution of separations that systems have at the time when star one is a neutron star and the other star is a red supergiant (e.g., Vinciguerra et al. 2020; Langer et al. 2020).

Third, in considering the orbital evolution prior to filling the Roche lobe, we use the Jeans approximation for widening as a result of stellar wind mass loss (see §7.10). The Jeans approximation may not actually hold for the donor star. The mass loss occurs in the late phases and the systems of interest in this work will be very close to Roche-lobe filling at this stage. We may have wind focusing (e.g., Mohamed & Podsiadlowski 2007). It is possible that the systems shrink instead of widening. In that case, the forbidden region (see §7.10) might no longer be forbidden.

Fourth, our results depend on how accurate our progenitor models are (e.g., Farmer et al. 2016). These are subject to all of the uncertainties that affect massive star evolution, most notably those related to mass loss (e.g., Renzo et al. 2017) and internal mixing (e.g., Davis et al. 2019). These affect the final structure and core mass at the moment of Roche-lobe filling.

7.4.3 Numerical resolution

Our resolution is sufficient to achieve common envelope ejection and stall/"park" at a final orbital separation of $a_{\rm f} \approx 1.1$–$2.8 R_{\odot}$ in our simulations. However, there is mass leakage and redistribution from the highly centrally concentrated core ($\rho_c \approx 10^3$–10^6 g/cm^3) at radii $R < 0.3 R_{\odot}$ (see Section 7.12). Because it occurs at radii significantly smaller than the position of the secondary, this redistribution of mass should not have an effect on the secondary's orbit (Gauss' theorem). The largest numerical effect on the secondary's orbit is the numerical diffusion introduced by the grid (as in any 3D hydrodynamics simulation). This effect decreases with increasing resolution. We discuss this further in Section 7.12.

Our FLASH setup uses a cartesian grid, which does not conserve angular momentum L (this happens any time there is rotational motion across a grid cell). This causes the point mass to inspiral more rapidly. This is in comparison to explicitly Galilean-invariant codes such as moving-mesh codes. For example, Ohlmann et al. (2016) quote that L was conserved during their run with an error below 1%. Technically, our FLASH setup violates Galilean invariance, as do other conventional grid-based hydrodynamics codes (when altering the background velocity at the same resolution), but as Robertson et al. (2010) showed, this is a resolution-dependent effect, and L in grid codes approaches perfect conservation at very high resolutions. The non-conservation of L becomes larger with each orbit (the longer the simulation is run). Thus, if we have successful CE ejection, which we do, this likely represents a "lower limit" of possible CE ejection, because with perfect conservation of L the point mass would orbit more

times and have longer to strip and eject the CE. While our detailed results are somewhat resolution-dependent to a certain extent (though not significantly; see §7.12), the main result of this work—successful CE ejection leading to binary neutron star formation for all of the models we study—is robust and will only become stronger at higher resolutions.

7.4.4 Future work

The framework developed in this work can be used to study various binary stellar phenomena. First, we can study the large parameter space of systems that can be accurately modeled as a star–point mass interaction, including different mass ratios, primary/donor stars, and metallicities. We plan to perform a parameter-space study of CE systems leading the binary neutron stars and black hole/neutron star binaries. We also plan to study the long-term evolution by exporting the FLASH simulation back to MESA (this capability was already explored in Wu et al. 2020a).

We plan to accurately calculate and include the effects of accretion onto the neutron star and the associated feedback and energy injection in the envelope. This has not been studied in sufficient detail yet. MacLeod & Ramirez-Ruiz (2015b) found that accretion onto the neutron star is suppressed by one to two orders of magnitude compared to the Hoyle-Littlelon prediction, and that during the CE phase neutron stars accrete only modest amounts of envelope material, $\lesssim 0.1 M_{\odot}$. Holgado et al. (2021) claim that the energy that accretion liberates via jets can be comparable to the orbital energy.

The astrophysical context provided by a detailed physical understanding of the CE phase allows one to use GW and EM observations of binary neutron star mergers

as tools to answer a broader set of questions than the raw GW data alone can answer, for example, on the lives and deaths of stars, the difficult-to-probe physics of the deep interiors of stars, and how nucleosynthesis operates in the Universe.

In another direction, we can adjust our framework to follow the ejected material in more detail to inform our understanding of supernovae that interact with material from CE ejections. This may also help to understand some stars in the Galaxy that have interacted with CE material.

In the longer term, we plan to extend our FLASH setup to initialize two separate MESA stars. This would (in theory) allow us to study the entire parameter space of star-star interactions, leading to both stellar mergers and CE ejections.

7.5 Conclusion

The main points of this paper are summarized below.

1. We study the dynamical common envelope evolution of an initially $12 M_{\odot}$ red supergiant star and a $1.4 M_{\odot}$ neutron star in 3D hydrodynamics.

2. Most earlier studies have focused on low mass stars. This is the first successful 3D hydrodynamics simulation of a high mass progenitor that will result in a binary neutron star that merges within a Hubble time.

3. We fully resolve the core of the star to $\lesssim 0.005 R_{\odot}$ and our 3D hydrodynamics simulations are informed by an adjusted 1D analytic energy formalism and a 2D kinematics study.

4. We study different initial separations where the donor fills its Roche lobe during the first ascent of the giant branch and after the completion of central helium burning.

5. We find complete envelope ejection (without requiring any other energy sources than kinetic and gravitational energy) during the dynamical inspiral for all of the models we study.

6. We find a final orbital separation of $a_{\rm f} \approx 1.1$–$2.8 R_\odot$ (before any supernova kick) for the models we study, which span the range of initial separations in which dynamical CE ejection is possible for a $12 M_\odot$ star. A significant fraction of these systems will form binary neutron stars that merge within a Hubble time. We find an $\alpha_{\rm CE}$-equivalent efficiency of ≈ 0.1–0.4 for the models we study, but this may be specific for these extended progenitors.

7. The framework developed in this work can be used successfully to study the diversity of common envelope progenitors in 3D hydrodynamics.

7.6 Detailed time evolution

Here we show the evolution during the neutron star's inspiral for the ($900 R_\odot$, $v_i = v_{\rm integrator}$) run. See Figure 7.3 for the trajectory and orbital separation as a function of time (black line). The animated video Figure 7.6 shows a 3D rendering of the material near the core of the primary, from initial inspiral through common envelope ejection

and stalling ("parking") of the neutron star at its final orbital separation. Different shells corresponds to different density isosurfaces. While the material inside the core of the primary remains relatively undisturbed (as the closest approach of the secondary is $r \approx 2R_\odot$ and the radius of the core is $R_{\rm core} \approx 0.35R_\odot$), the material outside the core (both interior to and exterior to the orbit of the neutron star) is swept away and cleared with each successive passage of the neutron star. Red '+' (or '$\rightarrow$' if it is outside the domain) indicates the position of the neutron star. It is apparent that the neutron star is able to effectively clear the material interior to its orbit but outside the core (in addition to ejecting the envelope), allowing it to "park" at a final orbital separation (for this simulation) of $a_{\rm f} \approx 2.8R_\odot$.

The animated video Figure 7.7 shows a 3D rendering of the material for the entire domain, as opposed to a zoom-in on the material near the core in Figure 7.6. While in Figure 7.6 we saw that the core remained relatively undisturbed and that there was not significantly more material in between the orbit of the neutron star and the core, here the focus is the severely disturbed material in the envelope. One can see the "spiral-wave" feature as the neutron star sweeps out envelope mass with each successive passage in its orbit. One can also see that some of the higher density material closer to the core is moved outward toward the periphery as the neutron star ejects this material.

The animated video Figure 7.8 shows a 3D rendering of the ratio of the velocity magnitude to the local escape velocity, $|v|/v_{\rm esc,local}$ as a function of time. As the neutron star orbits the center of mass of the red supergiant star, it strips off the envelope

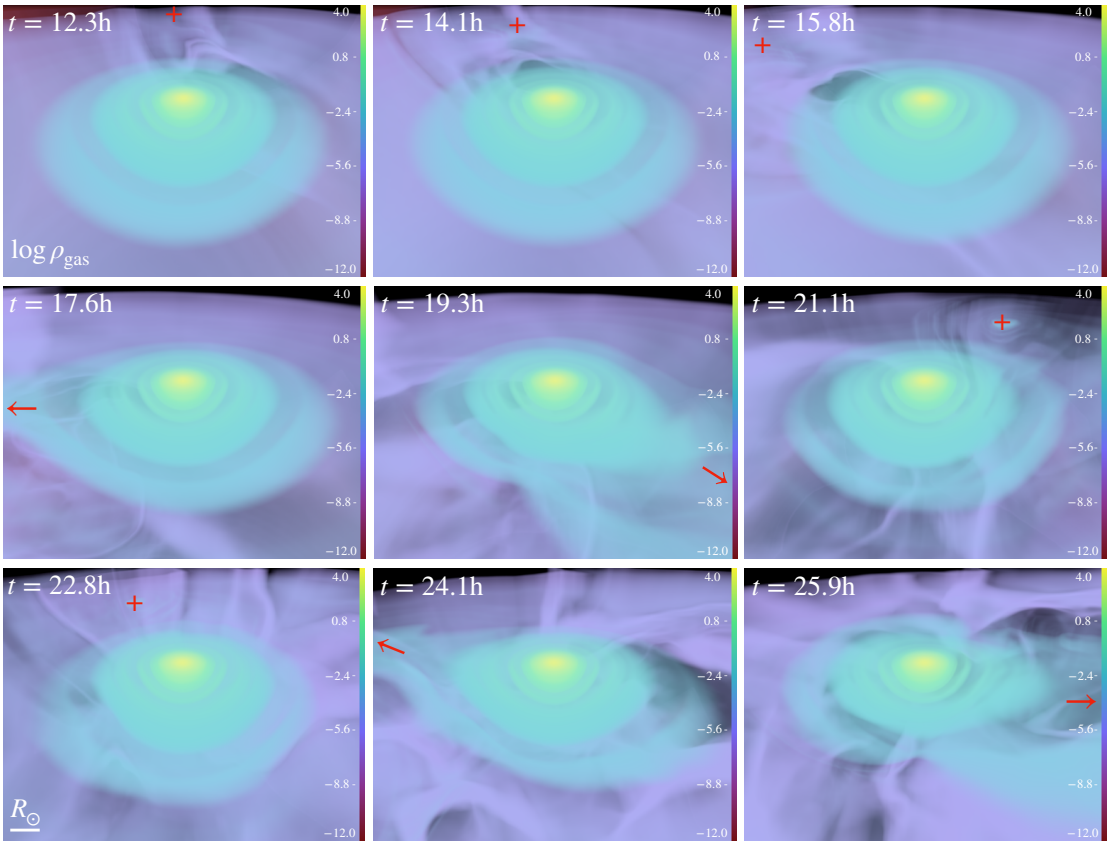

Figure 7.6: Video figure (viewable online). Video shows a 3D rendering of the logarithm of gas density ([g/cm^3]) for material near the core of the primary (the domain is of the video here is $x \approx 10R_\odot$ on a side) during the neutron star's inspiral for the ($900R_\odot$, $v_i = v_{\rm integrator}$) run. Shells correspond to different density isosurfaces; white is highest density, dark purple is lowest density. Video shows that the neutron star significantly disturbs the density structure of the envelope as it orbits and "stalls" at a final orbital separation, but that the core of the star remains largely undisturbed. Position of the neutron star is indicated by the red '+', or '→' if it is outside the domain. Videos also available at https://youtube.com/channel/UCShahcfGrj5dOZTTrOEqSOA.

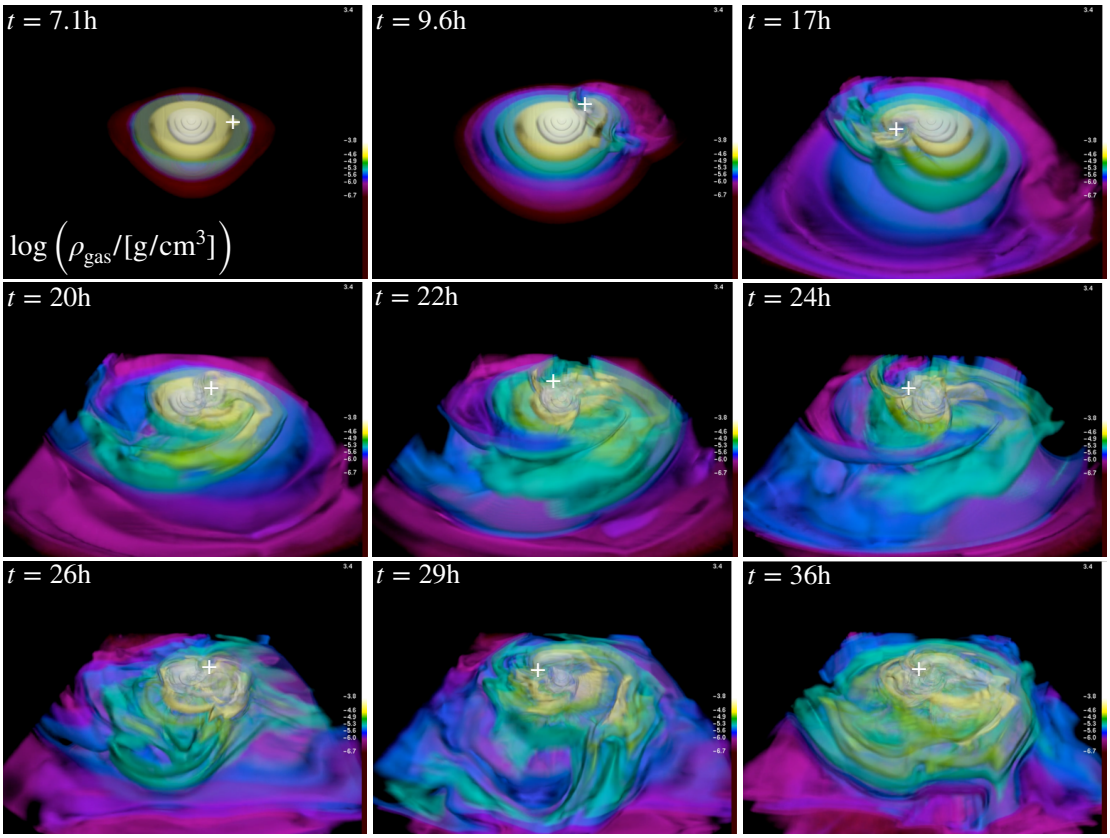

Figure 7.7: Video figure (viewable online). Video shows a 3D rendering of the logarithm of gas density for the full domain (compare to Figure 7.6) during the neutron star's inspiral for the ($900R_\odot$, $v_i = v_{\rm integrator}$) run. Shells correspond to different density isosurfaces; white is highest density, dark purple is lowest density. Video highlights the severely shocked and disturbed density structure of the outer envelope, which is ejected as the neutron star orbits the giant star. Position of the neutron star is indicated by the white '+'. Videos also available at https://youtube.com/channel/UCShahcfGrj5dOZTTrOEqSOA.

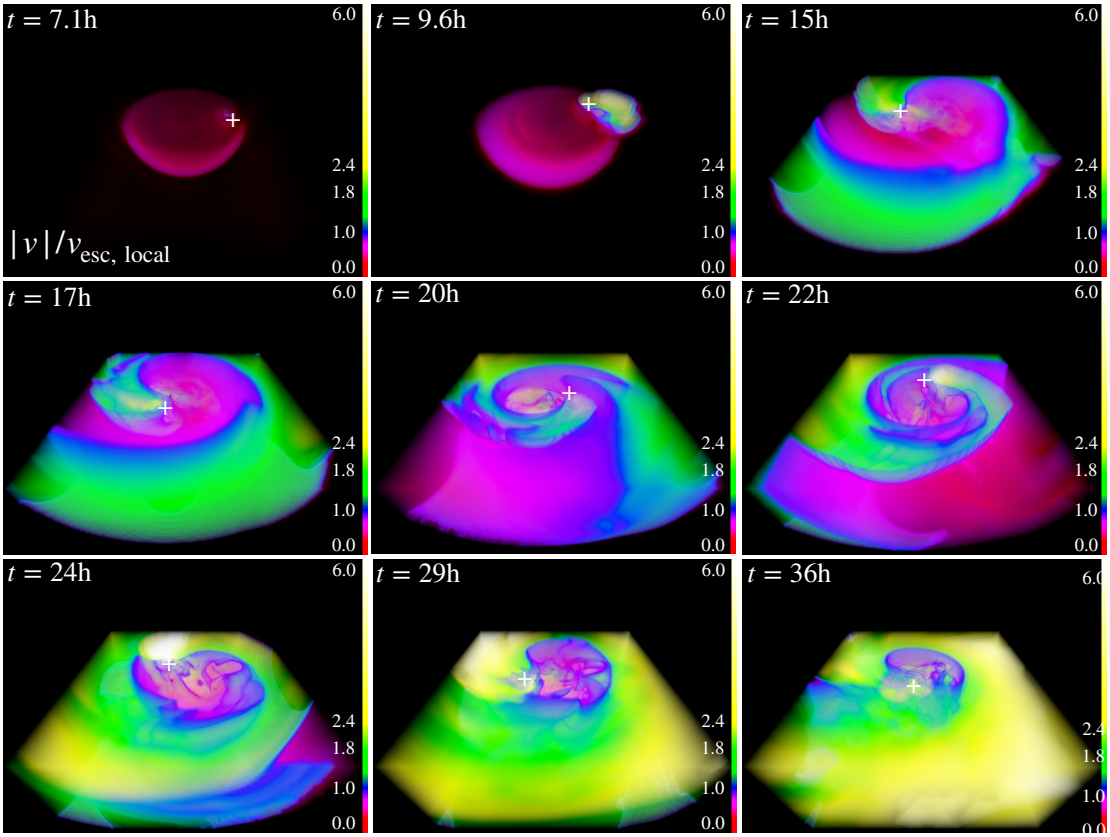

Figure 7.8: Video figure (viewable online). Video shows a 3D rendering of the ratio of velocity magnitude to local escape velocity for the full domain for the ($900R_\odot$, $v_i = v_{\rm integrator}$) run. Blue isosurface is at $|v|/v_{\rm esc,local} = 1$, pink-red is < 1, green-yellow is > 1. Position of the neutron star is indicated by the white '+'. Videos also available at https://youtube.com/channel/UCShahcfGrj5dOZTTrOEqSOA.

material outside its orbit, unbinding it and shocking this material to velocities in excess of $6v_{\rm esc,local}$. These large velocities are an indication of how efficiently the orbital energy of the neutron star is transferred to the energy of the envelope.

The animated video Figure 7.9 shows a 3D rendering of the sum of the specific kinetic and potential energy as a function of time. There is a blue isosurface at $\varepsilon = 0$, pink-purple corresponds to bound material ($\varepsilon < 0$), and yellow corresponds to unbound material ($\varepsilon > 0$). As in Figure 7.8, the envelope gains more energy with each orbital

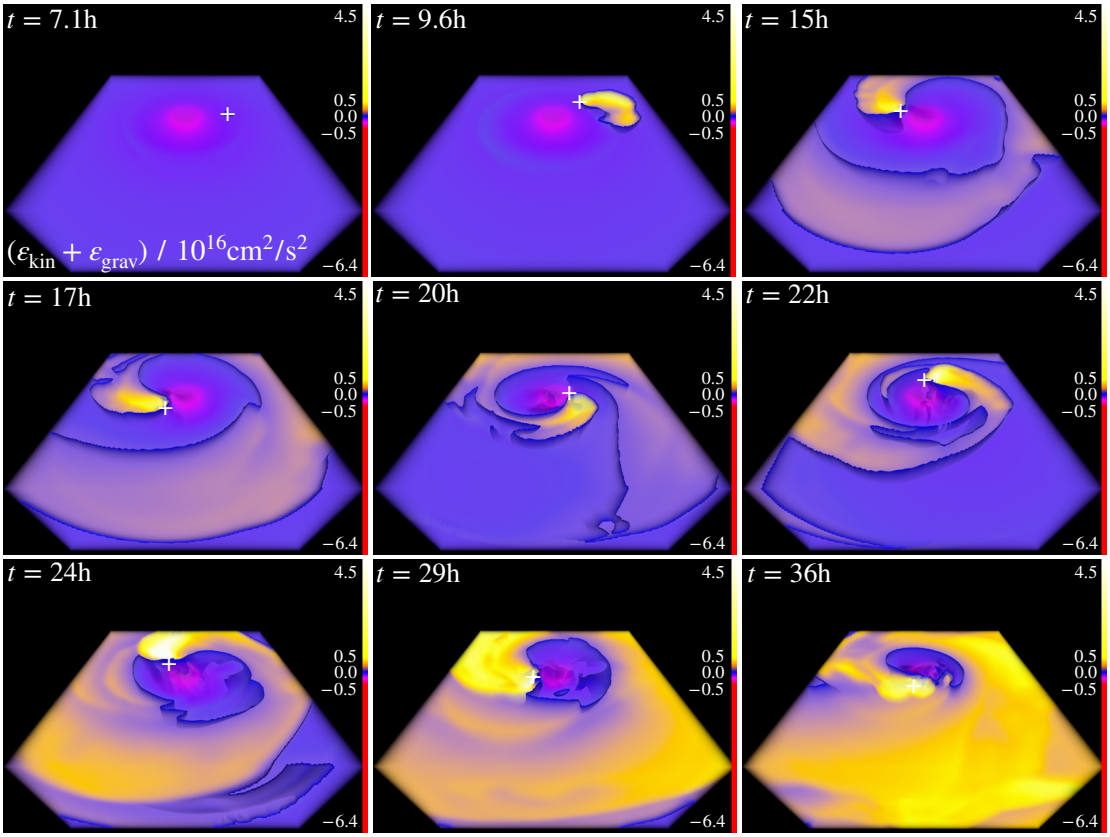

Figure 7.9: Video figure (viewable online). Video shows a 3D rendering of the sum of specific kinetic and potential energy for the full domain for the ($900R_\odot$, $v_i = v_{\rm integrator}$) run. Blue isosurface at $\varepsilon = 0$, pink-purple corresponds to bound ($\varepsilon < 0$) and yellow corresponds to unbound ($\varepsilon > 0$). Position of the neutron star is indicated by the white '+'. Videos also available at https://youtube.com/channel/UCShahcfGrj5dOZTTrOEqSOA.

passage of the neutron star and becomes progressively more unbound (the colors become a brighter yellow with time).

7.7 Hydrogen recombination transient

Here we outline the details of our estimate of the properties of the hydrogen recombination transient from the ejected hydrogen envelope (see §7.3). We use Eqns.

(A1), (A2), and (A3) of MacLeod et al. (2017b), based on Ivanova et al. (2013a)'s application of the analytic theory of recombination transients (e.g., Popov 1993; Kasen & Woosley 2009; Kasen & Ramirez-Ruiz 2010) to estimate the luminosity, timescale, and total energy of the hydrogen recombination transient predicted by our 3D hydrodynamics simulations:

$$L_{\rm p} \approx 4.2 \times 10^{37}\ {\rm erg\ s^{-1}} \left(\frac{R_{\rm init}}{10 R_\odot}\right)^{2/3} \left(\frac{\Delta M}{0.1 M_\odot}\right)^{1/3} \left(\frac{v_{\rm ej}}{100\ {\rm km\ s^{-1}}}\right)^{5/3} \times \left(\frac{\kappa}{0.32\ {\rm cm^2\ g^{-1}}}\right)^{-1/3} \left(\frac{T_{\rm rec}}{4500\ {\rm K}}\right)^{4/3}, \tag{7.4}$$

$$t_{\rm p} \approx 42\ {\rm d} \left(\frac{R_{\rm init}}{10 R_\odot}\right)^{1/6} \left(\frac{\Delta M}{0.1 M_\odot}\right)^{1/3} \left(\frac{v_{\rm ej}}{100\ {\rm km\ s^{-1}}}\right)^{-1/3} \times \left(\frac{\kappa}{0.32\ {\rm cm^2\ g^{-1}}}\right)^{1/6} \left(\frac{T_{\rm rec}}{4500\ {\rm K}}\right)^{-2/3}, \tag{7.5}$$

$$E_{\rm rad,p} \approx 1.5 \times 10^{44} {\rm erg} \left(\frac{\rm R_{init}}{10 R_\odot}\right)^{5/6} \left(\frac{\Delta \rm M}{0.1 M_\odot}\right)^{2/3} \left(\frac{\rm v_{ej}}{100\ {\rm km\ s^{-1}}}\right)^{4/3} \times \left(\frac{\kappa}{0.32\ {\rm cm^2\ g^{-1}}}\right)^{-1/6} \left(\frac{T_{\rm rec}}{4500\ {\rm K}}\right)^{2/3}. \tag{7.6}$$

Using $R_{\rm init} \approx 2 R_\odot$ (approximate stalling orbital separation of the secondary across our models), $\Delta M \approx 5 M_\odot$ (the entire mass of the envelope), $v_{\rm ej} \approx 18$ km/s (the velocity at $10 R_\odot$ at the end of our simulation), $\kappa \approx 0.32$ cm^2 g, and $T_{\rm rec} \approx 4500$ K, we find $L_{\rm p} \approx 10^{37}$ erg s^{-1}, $t_{\rm p} \approx 274$ d, and $E_{\rm rad,p} \approx 2 \times 10^{44}$ erg.

7.8 MESA profiles

Here we provide more detail on the 1D stellar models (the initial conditions for the 3D hydrodynamics) built in MESA. Our primary is constructed using the setup of Götberg et al. (2018), but for a single star. The top row of Figure 7.10 shows density profiles (vs. radius and mass coordinate) for the three models we simulate in 3D hydrodynamics. The bottom left panel shows the mass enclosed vs. radius. We also compare to the primary from the 1D MESA study of CE ejection of Fragos et al. (2019), which was $12M_{\odot}$ and $\approx 500R_{\odot}$. The density profiles are all very similar, being highly centrally concentrated with a core of $\approx 5M_{\odot}$ sequestered at $\lesssim 1R_{\odot}$. The greatest difference is in the inner $0.1R_{\odot}$, where the least centrally concentrated model ($750R_{\odot}$) has a central density of $\rho_c \approx 10^3$ g/cm^3 and the most centrally concentrated model ($1080R_{\odot}$) has a central density of $\rho_c \approx 10^6$ g/cm^3. The density drops from a central value of $\rho_c \approx 10^3$–10^6 g/cm^3 to $\rho \lesssim 10^{-5}$ g/cm ^{3} by $R = 10R_{\odot}$.

The bottom right panel of Figure 7.10 shows the 1D composition profiles for hydrogen, helium, carbon, and nitrogen at the beginning of the simulation (thus, they are identical to the MESA composition profiles) for the $900R_{\odot}$ star. See Figure 7.5 for 3D renderings of the chemical abundance of the system as a function of time. Note that the abrupt changes in composition are a result of the well-defined compositional layering from the MESA model (this is mapped exactly into FLASH, thus this is the same as the MESA composition profile).

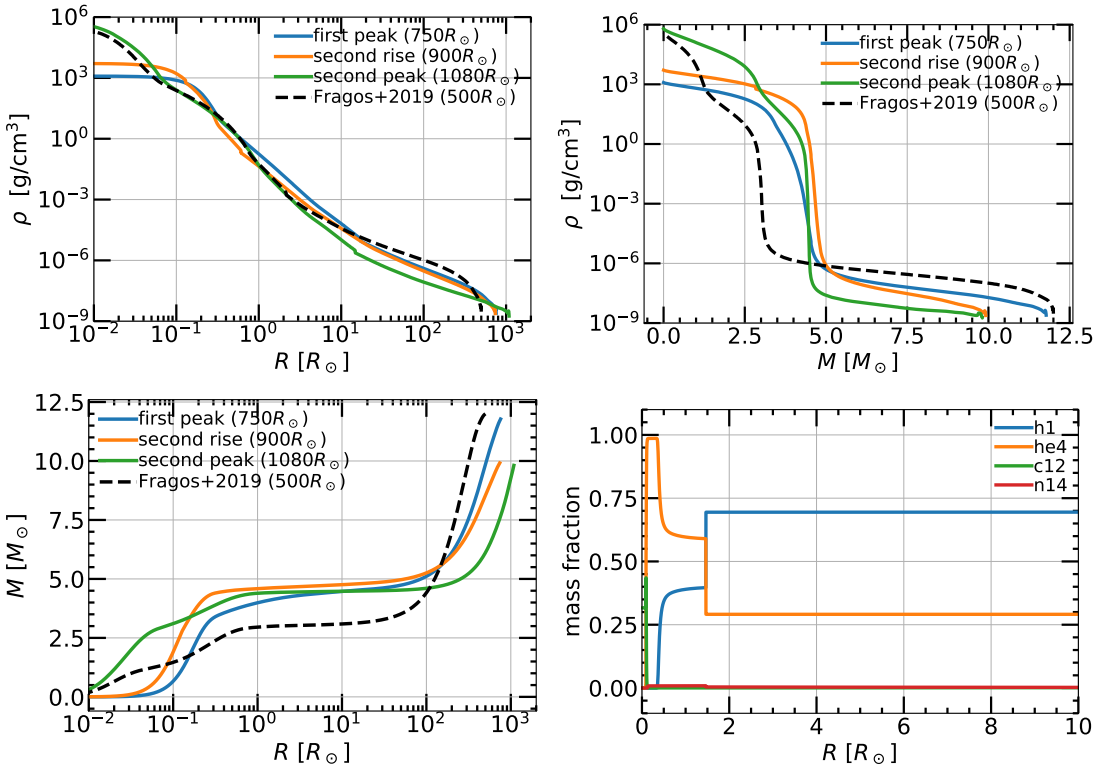

Figure 7.10: Top: MESA density profiles vs. radius and mass coordinate for the three models that we simulate in 3D hydrodynamics (see Figure 7.1) and for the primary from Fragos et al. (2019). Bottom left: enclosed mass vs. radius. Bottom right: initial 1D composition profiles of hydrogen, helium, carbon, and nitrogen for the $900R_\odot$ star.

7.9 Adjusted 1D energy formalism

Here we provide more detailed results of our 1D energy formalism (method discussed in §7.2.2). Figure 7.11 shows binding and orbital energies vs. radius and mass for the three models from that we simulate in 3D hydrodynamics (see Figures 7.1, 7.10). In the 1st row we compare gravitational binding energy $E_{\rm grav}$ between all three models. In other rows we show detailed results for each model including binding energy from the standard α formalism ($E_{\rm grav}$), the Bondi radius adjusted formalism ($E_{\rm grav,R_a}$), the Roche radius adjusted formalism ($E_{\rm grav,R_{Roche}}$), and the change in orbital energy ($\Delta E_{\rm orb}$). In general, we see that the binding energy profiles, similar to the density profiles (Figure 7.10), are also highly centrally concentrated and that $< 0.1\%$ of the binding energy is at radii larger than $10 R_\odot$. The different calculated energies (for the standard α formalism and for the $r - R_a$ and $r - R_{\rm Roche}$ adjusted formalism) are used to determine the predicted envelope ranges in the 1D energy formalism (see Section 7.2.2).

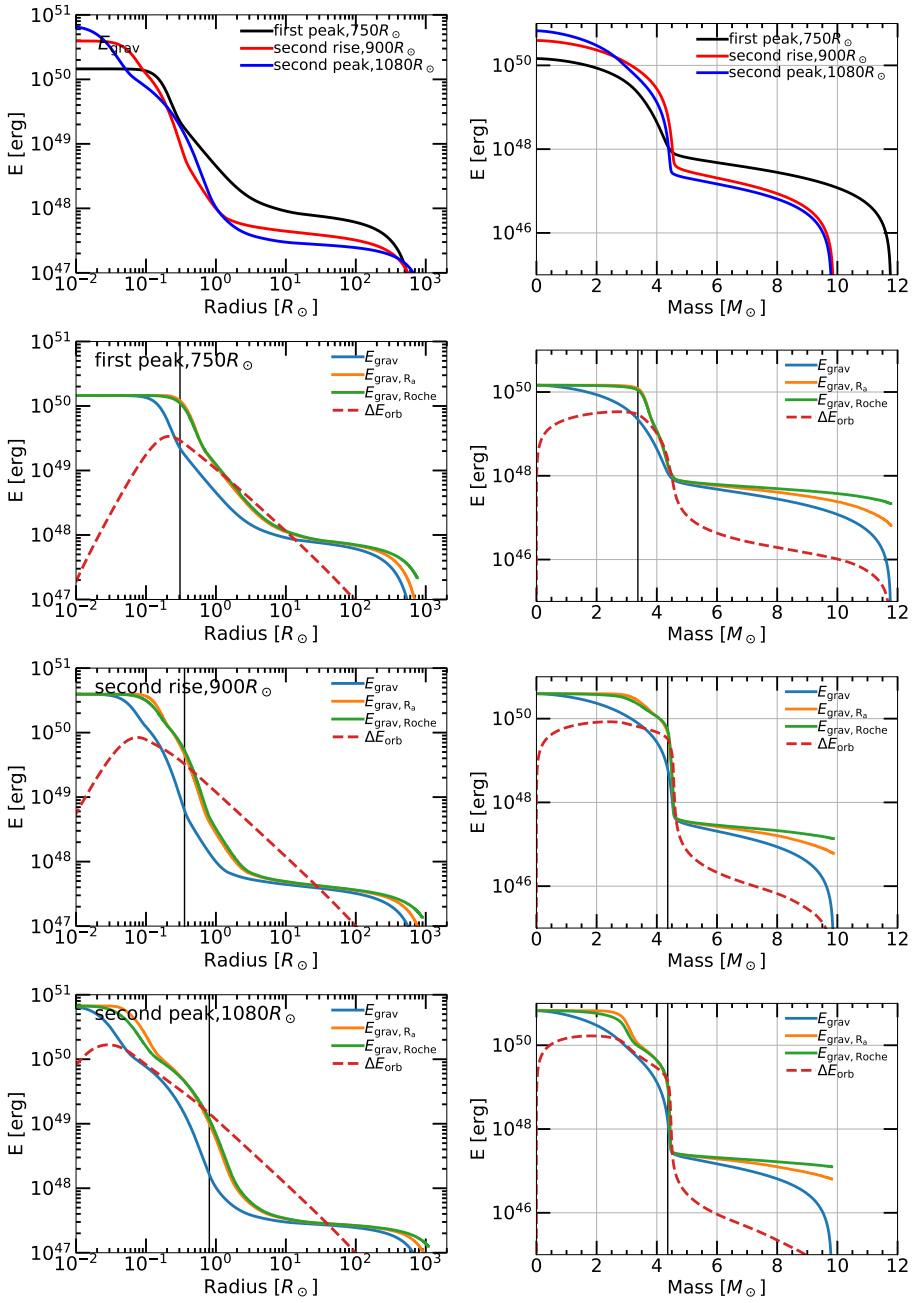

Figure 7.11: Absolute value of binding and orbital energies vs. radius and mass for the three models we simulate in 3D hydrodynamics (see Figure 7.1). Top: comparison of the binding energy $E_{\rm grav}$ between all three models. Other rows: detailed results for each model, including binding energies from the standard α formalism ($E_{\rm grav}$), the Bondi radius adjusted formalism ($E_{\rm grav,R_a}$), the Roche radius adjusted formalism ($E_{\rm grav,R_{Roche}}$), and the change in orbital energy ($\Delta E_{\rm orb}$). Vertical line indicates radius of the core (defined by `he_core_mass` attribute in MESA).

7.10 Forbidden donor radii

The star cannot fill its Roche lobe at an arbitrary moment in its evolution; it needs to have a size large enough such that it would not have filled its Roche lobe before. Simply including stellar ages where the stars radius exceeds any earlier radius it had is not sufficient, as the orbit is changing as well due to wind mass loss and possibly tidal interactions.

A standard assumption is to think about the orbital changes in the Jeans mode approximation, where the orbital change is a very simple function of the mass loss. It relies on the assumption that (i) mass loss is steady (i.e., in a smooth wind, not a sudden supernova explosion) and (ii) it is lost with a velocity that is high compared to the orbital velocities (such that, e.g., it cannot have any tidal interaction with the system) and (iii) it is lost from the vicinity of the mass-losing star in a spherically symmetric fashion in the reference frame of the mass-losing star.

This gives the following simple analytical result that $a \times (M_1 + M_2) = \text{constant}$. In this work, this means that any time t the separation $a(t)$ is the following function of the masses and initial parameters:

$$a(t) = a(t=0) \times \frac{M_d(t=0) + M_{NS}}{M_d(t) + M_{NS}} \tag{7.7}$$

We calculate the size of the Roche radius of a system with an initial separation of $a = 1301 R_\odot$—this is the initial separation of the widest system to fill its Roche lobe on the first ascent. The system widens with time due to the Jeans mode mass loss. A system with an initial separation slightly larger than $a = 1301 R_\odot$ would fill its Roche

lobe on the second ascent. But because of mass loss, the system will have widened in the meantime and the star needs to be $R_\star = 900R_\odot$ or larger. The star can thus not fill its Roche lobe for ages between $t(R = 757R_\odot)$ and $t(R = 900R_\odot)$, between the first peak and the second rise (see Figure 7.1).

In practice this means that the stellar models available to us in this work are: (a) stars that fill their Roche lobe on the first ascent, that is with radius smaller than $757R_\odot$, and (b) stars that fill their Roche lobe on the second ascent, provided their radius is larger than $900R_\odot$. In other words, we avoid using models with "forbidden radii" (radii between 757–$900R_\odot$).

7.11 Merger time distribution

In order to estimate the merger time distributions of these binary neutron star systems, we take a linear distribution in separations before the supernova (SN) from 1.1–$2.8R_\odot$. We then take each separation and run 1000 randomly oriented kicks. We sample kick magnitudes from a Maxwellian distribution with a 1D RMS $\sigma = 265$ km/s (following Hobbs et al. 2005)[35] and the final mass of the new neutron star after the SN is $1.4M_\odot$. To calculate the post-SN orbit we use Eqns. (7) and (8) of Andrews & Zezas (2019) and to calculate the merger times of these post-SN orbits we use Peters (1964). Figure 7.12 shows the merger time distribution of the two resulting neutron stars using this procedure.

The fraction of bound binaries after the SN is ≈38%. Of the binaries that

[35]This is likely an overestimate, as in a study of Galactic binary neutron stars, Beniamini & Piran (2019) find that a majority had a kick velocity much lower than those of standard pulsars (i.e., the distribution of Hobbs et al. 2005), with $v_{\rm kick} \lesssim 30$ km/s.

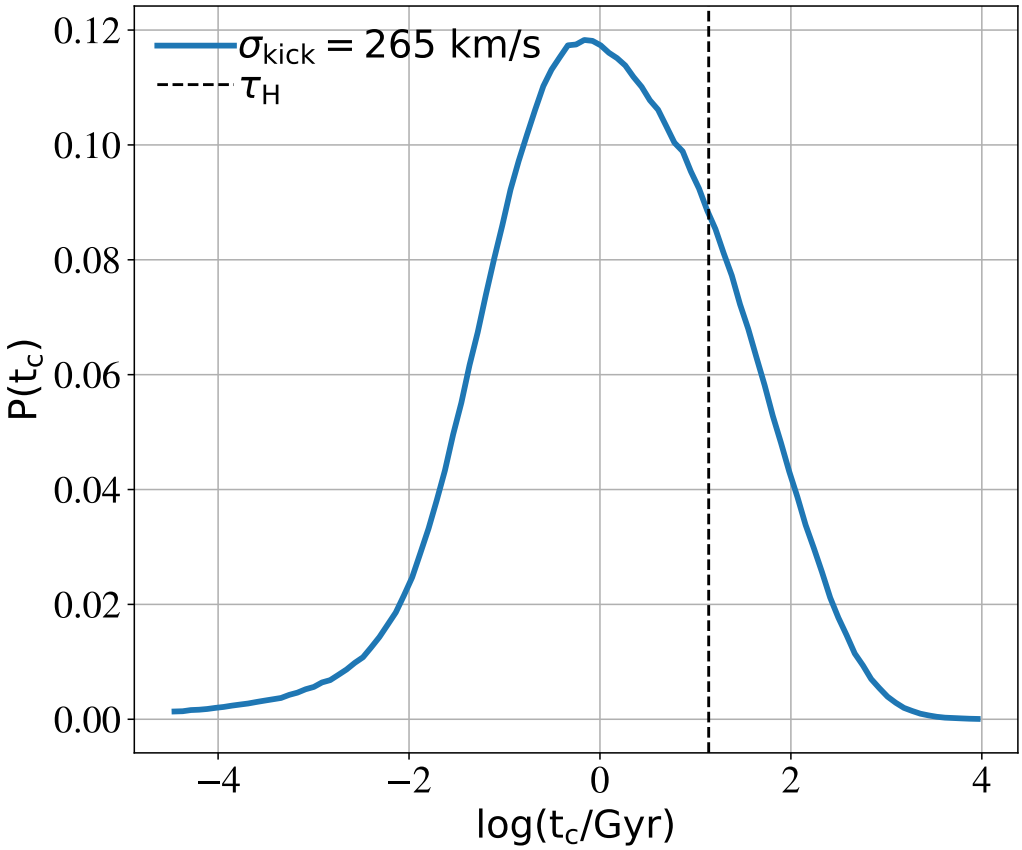

Figure 7.12: Merger time distribution of the two resulting neutron stars for supernova kick velocities drawn from a Maxwellian distribution with a 1D RMS $\sigma = 265$ km/s (following Hobbs et al. 2005). Dashed line indicates the age of the Universe.

remain bound after the SN, ≈79% will merge within a Hubble time.[36] We caution the reader that after envelope ejection we expect a stable mass transfer phase (case BB) to occur that will likely tighten the binary (see, e.g., Tauris et al. 2017; Dewi et al. 2002; Vigna-Gómez et al. 2020). As such, this calculation should be taken as a robust upper limit for the merger timescale.

[36]This is likely a conservative estimate, as in a delay time distribution study of Galactic binary neutron stars, Beniamini & Piran (2019) find that $\gtrsim 40\%$ of BNSs have merger times less than 1 Gyr.

7.12 Numerical convergence

Here we present a brief numerical convergence study of the effect of numerical diffusion on the simulation results. The 1st row of Figure 7.13 shows trajectories and orbital separation vs. time for two different resolution criteria for the $(900R_\odot, v_i = v_{\rm integrator})$ run. We use the same refinement criteria but two different box sizes: $\Delta X_{\rm max} = (100R_\odot, 40R_\odot)$, translating to a factor of 2.5X increase in linear resolution between the two simulations. The secondary does not inspiral as deeply for the higher resolution run. The higher resolution run stalls and attains a final orbital separation of $a_{\rm f} \approx 3.1R_\odot$, while the lower resolution run attains a final orbital separation of $a_{\rm f} \approx 2.8R_\odot$.

The 2nd row of Figure 7.13 shows the density profile along one direction in the orbital plane (other directions are similar) at a few different times throughout the simulation for the same two runs. For reference, the relaxation process is $t_{\rm relax} \approx 100t_{\rm dyn,core} \approx 6$ hr. After relaxation onto the grid, the central density decreases by a factor of ≈ 5. The lower resolution run ($\Delta X_{\rm max} = 100R_\odot$) shows lower core densities at radii of ($r < 1R_\odot$) and higher densities at radii of $r > 1R_\odot$, especially at later times, whereas the higher resolution run conserves its density profile to late times. This mass leakage from the core in the lower resolution run leads to a higher envelope density and thus a higher drag force (as $F_{\rm drag} \propto \rho$) for the lower resolution run. This likely explains its slightly deeper inspiral.

The 3rd row of Figure 7.13 shows mass enclosed vs. time at several radii for the same two runs. The $\Delta X_{\rm max} = 40R_\odot$ run conserves the inner mass shells much

better than the $\Delta X_{\rm max} = 100 R_\odot$ run. However, for both runs, while the innermost core expands and the mass spreads to somewhat larger radii, this has no effect on the secondary's orbit as the orbital separation is always at least $r \gtrsim 1 R_\odot$, whereas the mass is redistributed within $r \lesssim 0.5 R_\odot$.

Figure 7.14 shows the clearing of material interior to the neutron star's orbit and exterior to the Roche radius of the core, which is necessary to successfully "park" the neutron star to a final orbital separation. The left panel shows mass enclosed as a function of time in a (time-evolving) annulus from the Roche radius of the core ($R_{\rm Roche,core} \approx 1.3 R_\odot$) to the radius of the neutron star's orbit ($r_{\rm sec}$). The mass inside this annulus is initially $\approx 0.045 M_\odot$; this mass is successfully ejected. The initial rise and decline are due to mass leakage from the core and subsequent mass leakage from this annulus (see also Figure 7.13). The oscillatory "bumps" in the mass enclosed are a result of the shock produced by the neutron star's orbit, which successively ejects a mass $> 0.45 M_\odot$ from this region; compare to the "bumps" in the orbital separation as a function of time (Figure 7.3). The right panel shows mass enclosed inside three different radial locations: total mass inside the box, mass inside the radius of the neutron star's orbit, mass inside the Roche radius of the core. While there is mass leakage from the box at late times (see also Figure 7.13), mass is successfully ejected from the annulus interior to the neutron star's orbit and exterior to the Roche radius of the core.

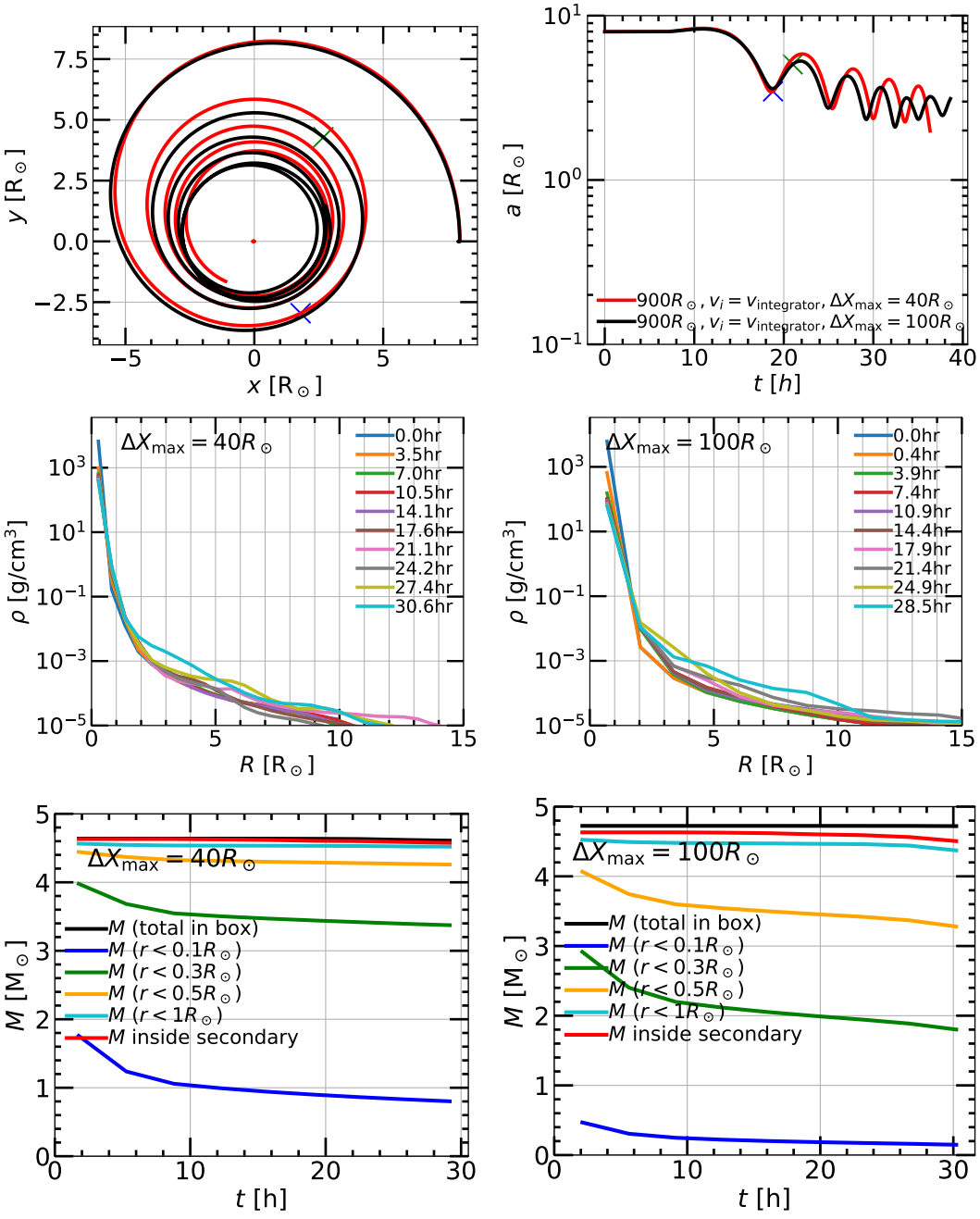

Figure 7.13: Numerical convergence study. 1st row: orbital separation vs. time for the $(900R_\odot, v_i = v_{\rm integrator})$ run, with box size $\Delta X_{\rm max} = 100R_\odot$ (black) and $\Delta X_{\rm max} = 40R_\odot$ (red, 2.5X linear resolution of other simulation) on a side. Green and blue 'X's mark the time at which the envelope is ejected for the black and red lines respectively (see Figure 7.4). 2nd row: density profile along one direction in FLASH as a function of time. Left panel is the $\Delta X_{\rm max} = 40R_\odot$ run and right panel is the $\Delta X_{\rm max} = 100R_\odot$ run. 3rd row: mass enclosed vs. time at several radii as a function of time.

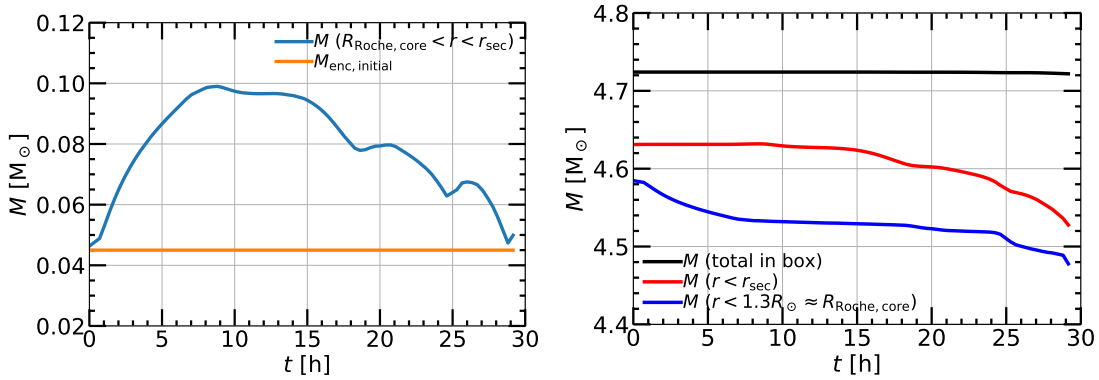

Figure 7.14: Ejection of material interior to the neutron star's orbit and exterior to the Roche radius of the core. Left: mass enclosed as a function of time in a (time-evolving) annulus from the Roche radius of the core ($R_{\rm Roche,core}$) to the radius of the neutron star's orbit ($r_{\rm sec}$). Right: mass enclosed inside three different radial locations: total mass inside the box, mass inside the radius of the neutron star's orbit, mass inside the Roche radius of the core. Note the y-axis is zoomed-in for clarity.

Chapter 8

Obstacles to Constructing de Sitter Space in String Theory

Abstract

There have been many attempts to construct de Sitter space-times in string theory. While arguably there have been some successes, this has proven challenging, leading to the de Sitter swampland conjecture: quantum theories of gravity do not admit stable or metastable de Sitter space. Here we explain that, within controlled approximations, one lacks the tools to construct de Sitter space in string theory. Such approximations would require the existence of a set of (arbitrarily) small parameters, subject to severe constraints. But beyond this one also needs an understanding of big-bang and big-crunch singularities that is not currently accessible to standard approximations in string theory. The existence or non-existence of metastable de Sitter

space in string theory remains a matter of conjecture.

8.1 Introduction: The de Sitter Swampland Conjecture

The observable universe appears to have emerged from a period of high curvature. Almost certainly, if we run the clock backwards, we encounter a period where classical general relativity does not apply. Remarkably, while string theory has provided tools to think about many questions in quantum gravity, cosmologies resembling our own remain inaccessible to controlled approximations in the theory. Conceivably the observed big bang is not described by a quantum theory of gravity or requires some still larger structure, but it would seem more likely that this simply represents a failure of our present collection of theoretical tools.

Strong evidence from supernovae (Perlmutter et al. 1999), CMB (Aghanim et al. 2018), and Large Scale Structure observations (Percival et al. 2010) suggest that our universe has entered a stage of exponential expansion, well-described as a de Sitter solution of Einstein's equations. At a time shortly after the big bang, there is good reason to think that the universe also went through a period of exponential expansion (Guth 1987; Starobinsky 1987; Linde 1982; Albrecht & Steinhardt 1987). So de Sitter space seems likely to play an important role in any understanding of our present and past universe. The inflationary period lasted only for a brief moment; our limited understanding of how de Sitter space might arise in string theory would suggest that even our present de Sitter universe is metastable.

The notion of a *cosmic landscape* introduces another role for spaces of positive

cosmological constant (c.c.). In particular, such a landscape might allow a realization of anthropic selection of the c.c. (Weinberg 1989), but would seem to require the existence of a vast set of metastable, positive c.c. vacua.

Given these considerations, the conjecture of Obied et al. (2018) that metastable de Sitter space lies in the swampland of quantum gravity theories is particularly interesting, with possible implications for inflation, the nature of the currently observed dark energy, and implementing the anthropic explanation of the c.c. We will not address the conjecture in its full generality, but we will examine the starting point. Obied et al. (2018) begin with the observation that it has proven difficult to construct de Sitter space in string theory. While there are constructions that appear to achieve a positive cosmological stationary point in a suitable effective action (Andriot 2019a,b), it is not clear that they are in any sense generic.

But one should first ask: what would it mean to construct de Sitter space in string theory? In most constructions, one starts with some classical solution of the equations of critical string theory. These solutions invariably have moduli or pseudo-moduli. Then one adds features, such as fluxes, branes, and orientifold planes which give rise to a potential for these moduli, and looks for a local minimum with positive four-dimensional c.c. These attempts to construct de Sitter space generally raise two questions. First, what is the approximation scheme that might justify any such construction? Second, any would-be de Sitter space found in this way is necessarily, at best, metastable: inevitably there is a lower energy density in asymptotic regions of the original moduli space. Quantum mechanically, the purported de Sitter state cannot

be eternal. It has a history; it will decay in the future and must have been created by some mechanism in the past. The quantum mechanics of this process is challenging to pin down. In this paper, we will see that already classically, the notion of an eternal de Sitter space in string theory is problematic; small perturbations near the de Sitter stationary point of the effective action evolve to singular cosmologies.

In more detail, there are at least two challenges to any search for metastable de Sitter space in string theory:

1. One requires a small parameter(s) allowing a controlled approximation to finding stationary points of an effective action. Here one runs into the problem described in Dine & Seiberg (1985). Without introducing additional, fixed parameters (i.e., introducing parameters not determined by moduli), would-be stationary points in the potential for the moduli lie at strong coupling. Typically, attacks on this problem (and the question of de Sitter space) exploit large fluxes[37]. If there is to be a systematic approximation, it is necessary that the string coupling be small and compactification radii large at any would-be stationary point found in this way. If the strategy is to obtain inverse couplings and radii scaled by some power of fluxes, it is also important that these fluxes (and possibly other discrete parameters) can be taken arbitrarily large, without spoiling the effective action treatment. Even allowing uncritically for this latter possibility, we will see that it is quite challenging to realize arbitrarily weak string coupling and large radius, with positive or *negative* c.c.[38]

[37]The KKLT (Kachru et al. 2003) constructions are, in some sense, an exception, which we will discuss later.

[38]This point has been noted earlier (Junghans 2019; Cribiori & Junghans 2019; Banlaki et al. 2019).

2. If one finds such a stationary point, one must ask about stability. More precisely, in string theory, we are used to searching for suitable background geometries and field configurations by requiring that the evolution of excitations about these configurations is described by a unitary S matrix. Classically, at least in a flat background, this is the statement that any initial perturbation of the system has a sensible evolution to some final perturbation. Again, we will see that this requirement is problematic for any would-be classical de Sitter stationary point in such a theory; even if all eigenvalues of the mass-squared matrix (small fluctuation operator) are positive, large classes of small perturbations evolve to singular geometries.

The problem of evolution of small perturbations is connected with the properties of the moduli of string compactifications, described above. We consider, in particular, disturbances of the moduli fields in a classical, eternal de Sitter space. We will see in this paper that some small fluctuations in the far past are amplified, rolling over the barrier to a contracting universe that culminates in a big crunch singularity. As a result, already classically, there is no notion of an S matrix (in the sense of describing the future of any small disturbance of the system), even restricted to very small perturbations localized near the metastable minimum of the potential. Within our current collection of calculational tools, we lack any framework in string theory to study such singularities. As a result, we will explain, the problem of constructing de Sitter space in string theory is not, at least at present, accessible to systematic analysis.

Overall, then, we will argue that we lack theoretical methods to address, in any

A broad critique, applicable to many non-perturbative scenarios, has been put forward in Sethi (2018).

systematic fashion, the problem of constructing de Sitter space in string theory, much as we lack the tools to understand big bang or big crunch singularities in any controlled approximation. The existence of metastable de Sitter states may be plausible or not, but it is a matter of speculation.[39] The failure to find such states in any controlled analysis appears, at least at present, inevitable.

8.2 The S Matrix and Classical Field Evolution

Much of our focus will be on the evolution of classical perturbations in metastable de Sitter space. We will argue that many of these perturbations evolve towards a big crunch singularity, and that this is outside of the scope of current methods in string theory/quantum gravity. In critical string theory, the object of interest is the S matrix. A *classical* solution of the string equations corresponds to a space-time for which one can define a sensible scattering matrix. The connection to classical scattering, in field theory and string theory, arises from considering the evolution of small disturbances. These correspond to initial *and final* isolated, localized states, with large occupation numbers. These can be considered as coherent states. For a single real scalar field, for example, one can develop a classical perturbation theory. Start, at lowest order, with a

[39] Grimm et al. (2020) gives non-perturbative arguments for the absence of de Sitter vacua in controlled approximations. Various scenarios for how de Sitter might arise, and how this might be understood, even lacking a systematic approximation, have been put forward. Among many examples, Garg & Krishnan (2019) and Garg et al. (2019) argue for a more refined version, based on explicit constructions; Heckman et al. (2019a,b) consider F-theory compactifications and associated prospects. Geng (2020) proposes another way in which de Sitter might arise. March-Russell & Petrossian-Byrne (2020) takes a phenomenological view of the problem. An alternative discussion of de Sitter space in flux vacua appears in Sethi (2018), who argues against flux stabilization on rather general grounds. Cicoli et al. (2019) takes an optimistic view of the prospects for such constructions and Cicoli et al. (2012, 2014, 2016) put forth several scenarios.

field configuration of the form

$$\phi(x) = \phi_{\vec{p}_1}(x) + \phi_{\vec{p}_2}(x) + \phi_{\vec{k}_1}(x) + \phi_{\vec{k}_2}(x) \tag{8.1}$$

where each term represents a localized wave packet with mean momentum $\vec{k}_i$. Momentum conservation requires $\vec{p}_1 + \vec{p}_2 = \vec{k}_1 + \vec{k}_2$ within the momentum uncertainty, and non-trivial scattering requires that the wave packets all overlap at a point in space-time. Quantum mechanically, the scattering problem we have outlined here corresponds to some large number of particles of each momentum in both the initial and final states. Making a decomposition into positive and negative frequency components:

$$\phi(x) = \phi^+(x) + \phi^-(x) \rightarrow \begin{cases} \phi^+(x)|\Phi\rangle = \Phi(x)|\Phi\rangle \\ \\ \langle\Phi|\phi^-(x) = \langle\Phi|\Phi^*(x) \end{cases} . \tag{8.2}$$

In momentum space, $\Phi^{\pm}(\vec{k})e^{i\vec{k}\cdot\vec{x}\mp i\omega t}$ corresponds to the positive and negative frequency components. Reality requires $\Phi^{\pm}(\vec{k}) = \Phi^{\pm *}(-\vec{k})$. Occupation numbers scale as $|\Phi^{\pm}(\vec{k})|$.

Order by order in the interaction, $\lambda\phi^4$, we can compute corrections to the classical scattering,

$$\delta\phi(x) = \delta\phi_{\vec{p}_1}(x) + \delta\phi_{\vec{p}_2}(x) + \delta\phi_{\vec{k}_1}(x) + \delta\phi_{\vec{k}_2}(x). \tag{8.3}$$

Evaluated at the interaction point, $\delta\phi$ defines an S matrix (more precisely a T matrix) on the space of coherent states. This can be decomposed as an S matrix on states of definite particle number; the classical approximation is valid when the occupation

numbers are large.

Phrased this way, the statement that one can construct an S matrix for large occupation numbers in initial and final states is the statement that one has sensible evolution from any initial classical configuration (described by $\vec{p}_1, \vec{p}_2$) to any final configuration $(\vec{k}_1, \vec{k}_2)$.

In the case of de Sitter space, the question of the existence of an S matrix is subtle (Marolf et al. 2013). We will focus, instead, on what we view as a minimal requirement that all classical perturbations in a would-be metastable de Sitter vacuum have a sensible evolution arbitrarily far into the future. We will see that some subset of possible perturbations evolve to singular geometries, over which we have no theoretical control. We argue that this means that one does not have a controlled construction of such spaces. The existence, or not, of such metastable de Sitter spaces then becomes a matter of conjecture.

8.3 Searching for Stationary Points of an Effective Action

We first explore some of the challenges to the construction of stationary points of the effective action with positive c.c. Typically, these efforts involve the introduction of branes, orientifold planes, and fluxes (Andriot 2019a). One searches for particular stationary points of the action with positive cosmological constant, and asks whether the string coupling is small and the compactification radii large at these points (Andriot et al. 2020a,b). This, by itself, does not address the question of whether there is a systematic approximation. The system with branes and fluxes is not a small perturbation

of the system without, and the range of validity of the expansion in one is not related to that of the other. If there is to be a systematic approximation of any sort, one requires a sequence of such stationary points as one increases the flux numbers; the would-be small parameters are the inverse of some large flux numbers. In our discussion we will assume that it makes sense to take such numbers arbitrarily large. Then the goal is to find stable, stationary points of the action where

1. The string coupling is small.

2. All compactification radii are large.

3. The cosmological constant is small and positive.

As reviewed in Andriot (2019b), satisfying this set of constraints is challenging. We review some of the issues in this section. Similar analyses, with similar conclusions, have appeared in Junghans (2019), Cribiori & Junghans (2019), and Banlaki et al. (2019). Our point of view is that this is not surprising. Searches at weak coupling were not likely to yield non-supersymmetric metastable vacua, dS or AdS, and provide little information about the existence or non-existence of such states. For the dS case, it is hard to see how such states could be understood without a much broader understanding of their cosmology, as we will discuss subsequently.

We follow Andriot (2019a) in studying type II theories in the presence of an O_p plane, and a background geometry with metric

$$ds^2 = g_{\mu\nu}dx^\mu dx^\nu + \rho\ g^0_{IJ}\ dy^I dy^J. \tag{8.4}$$

Here g^0_{IJ} represents a background reference metric for the compactified dimensions. $g_{\mu\nu}$ represents the metric of four dimensional space-time, which we hope to be de Sitter. Andriot (2019a) distinguishes directions parallel and perpendicular to the orientifold plane with an additional modulus σ; for simplicity, we assume $\sigma \sim 1$; this assumption can be relaxed without severe difficulty. We ignore other light moduli as well. We also include NS-NS 3-form and R-R q-form fluxes, $H^{(n)}_{IJK}$, $F^{(n)}_q$.

The fluxes will be understood as taking discrete, quantized values. The dependence of terms on the moduli ρ and $\tau = \rho^{3/2}\ e^{-\phi}$ is given in Andriot (2019a), and is readily understood from the following considerations:

1. In the NS-NS sector, there is a factor $1/g^2 = e^{-2\phi}$ in front of the action. The four-dimensional Einstein term has a coefficient $\tau^2 = \rho^3/g^2$. This can be brought to canonical form by the Weyl rescaling, $g_{\mu\nu} \to g_{\mu\nu}\tau^{-2}$. The moduli τ and ρ will be our focus.

2. Again in the NS-NS sector, terms involving the three-index tensor, before rescaling, contain a factor $\tau\rho^{-3}$; after the Weyl rescaling, they acquire an additional factor of τ^{-3} in front. Terms involving the six-dimensional curvature similarly scale as $\rho^{-1}\tau^{-3}$.

3. In the RR sector, the flux terms have, before rescaling, no factors of $1/g$. They have various factors of ρ depending on the rank of the tensor. The Weyl rescaling introduces a factor of τ^{-4}.

The resulting action is (Andriot 2019a):

$$V = -\tau^{-2}\left(\rho^{-1}R_6(\sigma) - \frac{1}{2}\rho^{-3}\sum_n \sigma^{6n-3(p-3)}\left|H^{(n)}\right|^2\right) - \tau^{-3}\rho^{\frac{p-6}{2}}\sigma^{\frac{(p-3)(p-9)}{2}}\frac{T_{10}}{p+1}$$
$$+\frac{1}{2}\left(\tau^{-4}\sum_{q=0}^{4}\rho^{3-q}\sum_n \sigma^{6n-q(p-3)}\left|F_q^{(n)}\right|^2 + \frac{1}{2}\tau^{-4}\rho^{-2}\sum_n \sigma^{6n-5(p-3)}\left|F_5^{(n)}\right|^2\right). \tag{8.5}$$

Again, we will ignore the index (n) in what follows and set $\sigma = 1$. To illustrate the issues, we will consider large F_2 and F_4. These fluxes satisfy, with $H_3 = 0$, Bianchi identities, with a source for F_4. These equations can be satisfied with large fluxes through two and four cycles.

For $3 \leq p \leq 7$ and choosing $T_{10} = 1$, $R_6 \sim 1$, we can drop the T_{10} term because the R_6 term will dominate. We can attempt to find large τ and ρ by turning on $F_2 = n_2$ and $F_4 = n_4$ (other combinations of fluxes give similar results). Then one has the relevant terms:

$$-\tau^{-2}\rho^{-1}R_6 + \frac{1}{2}\tau^{-4}\left(n_2^2\rho + n_4^2\rho^{-1}\right). \tag{8.6}$$

Differentiating with respect to ρ and τ, for $n_4 \gg n_2 \gg 1$, one has then

$$\rho^{-2}R_6 + \frac{1}{2}\tau^{-2}\left(n_2^2 - n_4^2\rho^{-2}\right) = 0 \tag{8.7}$$

and

$$\rho^{-1}R_6 - \tau^{-2}\left(n_2^2\rho + n_4^2\rho^{-1}\right) = 0. \tag{8.8}$$

We get a solution of the form:

$$\rho^2 = -\frac{1}{3}\left(\frac{n_4}{n_2}\right)^2 ;\ \tau^2 = \frac{2}{3}\frac{n_4^2}{R_6}. \tag{8.9}$$

Negative ρ^2 is not acceptable. But even if somehow ρ^2 had been positive, we would have had:

$$g^2 = \frac{\rho^3}{\tau^2} \propto R_6\left(\frac{n_4}{n_2^3}\right); \tag{8.10}$$

so the string coupling would not have been weak. The other terms we have neglected are suppressed at this point. For example, the term proportional to $T_{10}\rho^{-3/2}\tau^{-3}$ is suppressed by $(n_2/n_4)^2$.

For $p = 8$, which corresponds to the T_{10} term dominating, turning on, again, n_4 and n_2, one finds that $\rho^2 = -7n_4^2/n_2^2$, which is also negative. Parameterically, one now has $g^2 \propto n_4^3/n_2^7$, so again, even if one ignored signs, this regime would give large ρ and τ but also large g.

An interesting case is provided by $p = 8$ with n_0 and n_2 non-zero. In this case, one finds that

$$\rho^2 = \frac{1}{5}\frac{n_2^2}{n_0^2}\ ;\ \ \tau = \frac{8}{5}n_2^2 \tag{8.11}$$

so one requires $n_2 \gg n_0$. Both quantities are now positive, but the cosmological constant, consistent with expectations of Andriot (2019a), is negative, corresponding to AdS space. Setting this aside, one has that

$$g_s^2 \propto \frac{1}{n_2^2} \tag{8.12}$$

so the string coupling is small. But this is not good enough. If one considers higher derivative terms in the effective action at tree level (α' expansion) these are not suppressed. Writing the action in ten dimensions, the terms (written schematically)

$$\int d^4x d^6y \sqrt{g_4}\sqrt{g_6} \left(F_{IJ}F^{IJ} + \left(F_{IJ}F^{IJ}\right)^2 \right) \tag{8.13}$$

are both of the same order in the large flux, n_2^2, due to the two extra factors of ρ^{-2} coming from the two extra powers of inverse metric in the second term. For all values of p, if we just consider the H and F_q terms, $\partial V/\partial\tau = 0$ gives negative ρ^2.

In other cases, one finds these and other pathologies—AdS rather than dS stationary points and instabilities. Searches involving broader sets of moduli (Andriot et al. 2020a,b) seem to allow at best a few isolated regions of parameter space where such solutions might exist. Whether these might exhibit a sensible perturbation expansion is currently an open question, but our results above suggest that the combination is a tall order. So, even with the large freedom in flux choices we have granted ourselves, metastable de Sitter stationary points would appear far from generic in regimes where couplings are small and compactification radii are large.

8.4 Expectations for Evolution of Perturbations in de Sitter Space

String theory has had many dramatic successes in understanding issues in quantum gravity. But one severe limitation is its inability, to date, to describe cosmologies resembling our own, which *appear* to emerge from a big bang singularity or evolve to a big crunch singularity. This could reflect some fundamental limitation; more likely, it reflects the inadequacy of our present theoretical tools to deal with situations of high curvature and strong coupling. For example, consider a pseudomoduli space where the potential falls to zero for large fields in the positive direction. If one starts the system in the far past with expanding boundary conditions, then further in the past there is a big bang singularity; if one starts with contracting boundary conditions, there is a big crunch in the future (Banks & Dine 2001). These high curvature/strong coupling regions are inevitable, despite the system being seemingly weakly coupled through much of this history. It is possible that in any string cosmology, there need not be an actual curvature singularity, but the growth of the curvature means that the system enters a regime where any conventional sort of effective action or conventional weak coupling string description breaks down. It seems hard to avoid the conclusion that there is such a singularity (regime of high curvature) in the past or future of cosmological solutions on a moduli space. These problems might be avoided in some more complete treatment of the problem within the framework of a single cosmology, or perhaps something else, such as eternal inflation in a multiverse, is needed. In any case, the problem is beyond our present theoretical reach.

Our question, in this section, is: *are things better for metastable de Sitter space-times*? In particular, in efforts to construct de Sitter space-times in string theory, the strategy is to search some effective action for a positive c.c. stationary point, separated by a finite potential barrier from a region in field space where, asymptotically, the potential tends to zero. If we start the system at the local minimum of the potential, classically, it will stay there eternally. But how do small fluctuations evolve? Might there be small disturbances that drive the field to explore the region on the other side of the barrier, exhibiting the pathologies of the system on pseudomoduli spaces of Banks & Dine (2001)?

In one presentation of de Sitter space (which covers all of the space):

$$ds^2 = -d\tau^2 + \cosh^2(H\tau)\left[d\chi^2 + \sin^2\chi d\Omega_2^2\right]. \tag{8.14}$$

A homogeneous scalar field in this space, $\phi(\tau)$, obeys

$$\ddot{\phi} + 3H\frac{\sinh(H\tau)}{\cosh(H\tau)}\dot{\phi} + V'(\phi) = 0. \tag{8.15}$$

The equation is slightly more complicated if ϕ depends on r as well.

The metric of equation 8.14 respects an $SO(4,1)$ symmetry, as well as a Z_2 that reverses the sign of τ. Suppose, first, the potential for ϕ rises in all directions about a minimum (taken at $\phi = 0$ for simplicity). For large positive τ, any perturbation of ϕ about a local minimum damps; for large negative τ, the motion is amplified as τ increases (it damps out in the past). Correspondingly, in the far past and the far future,

the field approaches the local minimum (to permit a perturbative discussion, we must require that the maximum value of the disturbance at all times is small). Starting in the far past, we can think in terms of a localized disturbance in space (e.g., due to a source localized in space time) and study the Fourier transformed field. If the disturbance has some characteristic momentum k, this momentum will blueshift exponentially as $\tau \to 0$, and the amplitude will grow. For $\tau > 0$, the distribution will damp and redshift to longer wavelengths.

If the perturbation has scale smaller than H^{-1} (and in particular if the Hubble constant is small compared to the curvature of the potential), then the space-time near the disturbance is approximately flat, and, assuming rotational invariance, the disturbance breaks $SO(3,1) \times$ translations to $SO(3)$. In terms of the full symmetry of de Sitter space, the perturbation breaks $SO(4,1)$ to $SO(3)$. To summarize, any approximately homogeneous disturbance in eternal de Sitter corresponds to a solution that grows in the far past and decreases in the future. One can define *past* and *future* relative to the point where the scalar field is a maximum. The location of this point breaks much of the continuous symmetry of de Sitter space but leaves $SO(3) \times Z_2$, where the Z_2 represents time reversal about the point where the amplitude of the field oscillation is a maximum. The maximum of the field, indeed, provides a natural definition of the origin of time. At this point, the time derivative of the field vanishes.

Now for a potential that has a local minimum with positive energy density, and that falls to zero for large $|\phi|$, we might expect that if we create a small, localized perturbation at some (r_0, τ_0) this perturbation will damp out if $\tau_0 \gg 0$. But if $\tau_0 \ll 0$,

the perturbation will grow, possibly crossing over the barrier while $\tau \ll 0$. In this case, the emergent universe on the other side of the barrier is contracting, and we might expect the system to run off towards $\phi = \infty$, until the universe undergoes gravitational collapse. If this is the case, then the Z_2 symmetry might be said to be spontaneously broken; one has a pair of classical solutions, one with a singularity in the past, one in the future, related by the Z_2 symmetry.

Before establishing this fact, it is helpful to review some aspects of the Coleman-De Luccia (CDL) bounce from this perspective (Coleman & De Luccia 1980).

8.4.1 The Coleman-De Luccia bounce as a solution of the field equations with Minkowski signature

We are interested in disturbances which lead to motion over a barrier, rather than tunneling. We might expect, however, that once the system passes over the barrier, its subsequent evolution is not particularly sensitive to whether it passed over the barrier or tunneled through it. In the case of a thin-wall bubble, before including gravity, at large times, the bubble wall becomes relativistic, and the bubble radius is of order t, so one expects that the bubble energy is proportional to t^3, dwarfing any difference in the energy of order the barrier height at the time of bubble formation. The same is true for a thick-walled bounce connecting two local minima of some potential. In other words, at large time, at least for very small G_N, we might expect the solution to be a small perturbation of the bounce solution of Coleman (1977) and Coleman & De Luccia (1980), which we will review briefly.

8.4.2 Tunneling with $G_N = 0$

Consider, first, the bounce solution without gravity. We consider a potential, $V(\phi)$, with local minima at $\phi_{\rm true},\ \phi_{\rm false}$, where $V(\phi_{\rm false}) > V(\phi_{\rm true})$. Starting with the field equations,

$$\Box\Phi + V'(\phi) = 0, \tag{8.16}$$

for points that are space-like separated from the origin (the center of the bubble at the moment of its appearance), we introduce $\xi^2 = r^2 - t^2$, in terms of which

$$\frac{d^2\phi}{d\xi^2} + \frac{3}{\xi}\frac{d\phi}{d\xi} - V'(\phi) = 0. \tag{8.17}$$

This is the Euclidean equation for the bounce.

For points that are time-like separated, calling $\tau^2 = t^2 - r^2$,

$$\frac{d^2\phi}{d\tau^2} + \frac{3}{\tau}\frac{d\phi}{d\tau} + V'(\phi) = 0. \tag{8.18}$$

These equations are related by $\xi = i\tau$.

On the light cone, $\xi = \tau = 0$, we have $d\phi/d\tau = d\phi/d\xi = 0$, and we have to match $\phi(0) = \phi_0$. In the tunneling problem (Coleman 1977), ϕ_0 is determined by the requirement that $\phi \to \phi_{\rm false}$ as $\xi \to \infty$; this can be thought of as a requirement of finite energy relative to the configuration where $\phi = \phi_{\rm false}$ everywhere.

Independent of the quantum mechanical tunneling problem, the bounce is a

solution of the source-free field equations for all time (positive and negative) and everywhere in space. In the time-like region, the solution for negative time is identical to that for positive time. Translation invariance is broken, but $SO(3,1)$ invariance and the Z_2 invariance are preserved.

8.4.3 Classical perturbations of the false vacuum with $G_N = 0$

Without gravity, we might consider starting the system in the false vacuum and giving it a "kick" so that, in a localized region, the system passes over the barrier. On the other side, the system looks like a bubble, but not of the critical size. We might expect that the evolution of the bubble, on macroscopic timescales, is not sensitive to the detailed, microscopic initial conditions. For a thin-walled bubble, for example, we can think of configurations, as in Coleman (1977), where at time $t = 0$, one has a bubble of radius R_0, inside of which one has true vacuum, outside false vacuum, and a transition region described by the kink solution of the one dimensional field theory problem with nearly degenerate minima. Take the case of a single real field, ϕ, with potential:

$$V(\phi) = -\frac{1}{2}\mu^2\phi^2 + \frac{1}{4}\lambda\phi^4 + \epsilon\phi + V_0.$$

For small ϵ, the minima of the potential lie at

$$\phi_\pm \approx \pm\sqrt{\frac{\mu^2}{\lambda}}. \tag{8.19}$$

We can define our bubble configuration, with radius R large compared μ^{-1}, as the kink solution of the one dimensional problem,

$$\phi_B(r;R) = \frac{\phi_+ - \phi_-}{2}\tanh\left(\frac{\mu(r-R)}{\sqrt{2}}\right) + \frac{\phi_+ + \phi_-}{2}. \tag{8.20}$$

For our problem, we want to treat $R \to R(t)$ as a dynamical variable. If $R_0(t)$ is slowly varying in time (compared to μ^{-1}), then we can write an action for R,

$$S = \int dt \int r^2 dr d\Omega \left(\frac{1}{2}(\partial_t \phi_B(r;R(t)))^2 - (\vec{\nabla}\phi_B(r,R(t)))^2 - V(\phi_B(r,R(t)))\right) \tag{8.21}$$

$$\approx \int dt 4\pi R^2 \int_{R-\delta}^{R+\delta} dr \left(\frac{1}{2}(\partial_r \phi)^2\right)\left(\dot{R}^2 - 2\right),$$

where we have used the thinness of the wall to reduce the three-dimensional integral to a one-dimensional integral, and the fact that for the kink solution, the kinetic and potential terms are equal, to write the second term. We will restore the ϵ term in a moment.

The integral over the bounce solution is straightforward, yielding $\sqrt{2/3}$. So we have the effective action for R,

$$S = 4\pi \int dt \left(\sqrt{\frac{2}{3}}\mu^3(R^2\dot{R}^2 - 2R^2) + \frac{\epsilon}{3}R^3\right). \tag{8.22}$$

Correspondingly, the energy of the configuration is:

$$E(R,\dot{R}) = 4\pi\left(\sqrt{\frac{2}{3}}(R^2\dot{R}^2 + 2R^2 - \frac{1}{3}\epsilon R^3)\right) \equiv \frac{M(R)}{2}\dot{R}^2 + V(R). \tag{8.23}$$

We can extract several results from this expression. In particular we have:

1. The point where the potential vanishes, $R = R_1 = \frac{2\sqrt{2}\mu^3}{\epsilon}$.

2. The location and value of the potential at the maximum: $R = R_2 = \frac{4\sqrt{2}\mu^3}{3\epsilon}$.

3. We can determine $\dot{R}$ as a function of R and the initial value of R (for simplicity assuming $\dot{R}(0) = 0$).

We have checked, numerically, that starting with a field configuration corresponding to $\phi(x, t = 0) = \phi_B(r; R)$, $\dot{\phi}(x, t = 0) = 0$, to the left of the barrier, the bubble collapses. Starting slightly to the right, the wall quickly becomes relativistic and expands. This is consistent with an intuition that the energy of conversion of false vacuum to true is largely converted into the energy of the wall.

We can make this latter statement more precise. If we write:

$$\phi(r, t) = \phi_{\rm cr}(t, r) + \chi(t, r), \qquad |\chi| \ll \phi_{\rm cr}, \tag{8.24}$$

where $\phi_{\rm cr}$ is the critical bubble solution, then

$$(\partial^2 + m^2(r, t))\chi = 0. \tag{8.25}$$

Here m^2 is essentially a θ function, transitioning between the mass-squared of χ in the false and true vacua. Since the bubble wall moves at essentially the speed of light, and undergoes a length contraction by $t \sim \gamma$, we have that

$$m^2(t, r) \approx m^2(t^2 - r^2) \tag{8.26}$$

and the χ equation is solved by

$$\chi = \frac{1}{r}\chi(t^2 - r^2). \tag{8.27}$$

So the amplitude of χ decreases with time, and the energy stored is small compared to that in the bubble wall.

We expect the same to hold for a thick-walled bounce.

8.4.4 Behavior of the disturbance with small G_N

Consider the same system, now with a small G_N. Again, our disturbance, after a short period of time, approaches the critical ($G_N = 0$) bubble. At larger time, it will then agree with the Coleman-De Luccia solution, including the small effects of gravity.

As we will see in the next section, for the asymptotically falling potential, with expanding boundary conditions, the evolution of the configuration is non-singular. But with contracting boundary conditions, one encounters, as expected, a curvature singularity.

8.5 Behavior of the Bounce with Asymptotically Falling Potential

We have argued that, independent of the microscopic details of the initial conditions, in the case of a disturbance that connects two metastable minima of a scalar potential, the large time evolution of an initial disturbance that crosses the barrier is

that of the critical bubble, in the limit of small G_N. We expect that the same is true for a potential that falls asymptotically to zero. Once more, the underlying intuition is that at late times, the energy released from the change of false to true vacuum overwhelms any slight energy difference in the starting point. So we expect the solution to go over to $\phi(\tau)$. So in this section, we will focus principally on the behavior of the critical bubble, $\phi(\tau)$.

8.5.1 Field evolution with small G_N

For small but finite G_N, there is a long period where $G_N \times T_{00} \times \tau^2 \ll 1$, gravitation is negligible, and the picture of the previous section of the flat-space evolution of the bubble (or disturbance) is unaffected. For a vacuum bubble in de Sitter space, gravitational effects become important, for fixed $r \ll H^{-1}$, for example, only once $t \sim H^{-1}$. Provided the bubble has evolved to a configuration approximately that of the critical bubble, we can take over the critical bubble results (with gravity).

So we consider the bubble evolution in the region of Minkowski signature. Writing the metric in the form

$$ds^2 = -d\tau^2 + \rho(\tau)^2 \left(d\sigma^2 + \sinh^2(\sigma) d\Omega_2^2\right), \tag{8.28}$$

the equations for ρ and ϕ are:

$$\ddot{\phi} + 3\frac{\dot{\rho}}{\rho}\dot{\phi} + V'(\phi) = 0 \tag{8.29}$$

and

$$\dot{\rho}^2 = 1 + \frac{\kappa}{3}\left(\frac{1}{2}\dot{\phi}^2 + V(\phi)\right)\rho^2. \tag{8.30}$$

Note that if the bubble emerges in a region of large ρ ($\kappa\rho^2 V \gg 1$) then, for the asymptotically falling potential, the kinetic term quickly comes to dominate in the equation for ρ; the system becomes kinetic energy dominated. This is visible in the numerical results we describe subsequently.

We should pause here to consider the tunneling problem. We will see in the next section that if we take the positive root in equation 8.30, one obtains an expanding universe in the future, but there is a singularity in the far past (before the appearance of the bubble). Alternatively, if we take the negative root, the singularity appears in the far future. Which root one is to take brings us to questions of the long-time history of the universe, i.e., how the universe came to be in the metastable false vacuum. The point of our discussion in this paper is that this issue already arises classically.

8.5.2 Behavior of the equations for large τ

Before describing our numerical results, it is helpful to consider some crude approximations which give insight into the behavior of the system. In the region with $\xi = i\tau$, the equations become those of CDL in the time-like region:

$$\ddot{\phi} + 3\frac{\dot{\rho}}{\rho}\dot{\phi} + \frac{dV}{d\phi} = 0, \tag{8.31}$$

$$\dot{\rho} = \pm\sqrt{1 + \frac{\kappa}{3}\rho^2\left(\frac{1}{2}\dot{\phi}^2 + V(\phi)\right)}. \tag{8.32}$$

We argued at the end of the previous section that we might expect that the potential is not particularly relevant in the ϕ equation for large $\rho(0)$. Ignoring the potential, we can also ask, self consistently, whether the second term in the $\dot{\rho}$ equation dominates over the first. If it does, we have an FRW universe with $k = 0$ and

$$\rho \propto (\tau - \tau_0)^{1/3}, \quad \tau > \tau_0; \qquad \rho \propto (\tau_0 - \tau)^{1/3}, \quad \tau < \tau_0. \tag{8.33}$$

(These are the results for a universe with $p = w\rho;\ w = 1$.) We can see this directly from the equations. We have

$$\frac{\dot{\rho}}{\rho} = \pm\sqrt{\frac{\kappa}{6}}\dot{\phi}. \tag{8.34}$$

So

$$\frac{d^2\phi}{d\tau^2} \pm \sqrt{\frac{3\kappa}{2}}\dot{\phi}^2 = 0. \tag{8.35}$$

We look for a solution of the form

$$\dot{\phi} = \alpha(\tau - \tau_0)^{-1}, \tag{8.36}$$

$$\alpha = \sqrt{\frac{2}{3\kappa}}. \tag{8.37}$$

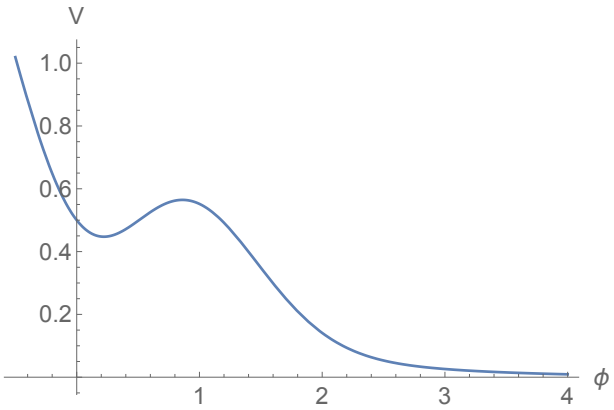

Figure 8.1: ϕ potential.

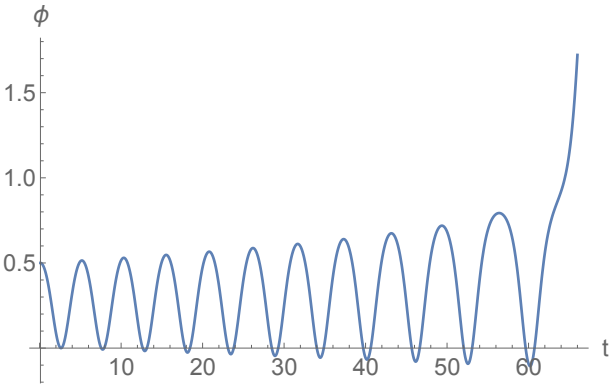

Figure 8.2: ϕ crosses the barrier.

Plugging this back into the $\dot{\rho}$ equation gives

$$\frac{\dot{\rho}}{\rho} = \pm\frac{1}{3}\frac{1}{\tau - \tau_0}, \tag{8.38}$$

which is consistent with the expected $(\tau - \tau_0)^{1/3}$ behavior. So we have a singularity in the past or the future.

For numerical studies, we designed a potential with a local de Sitter minimum

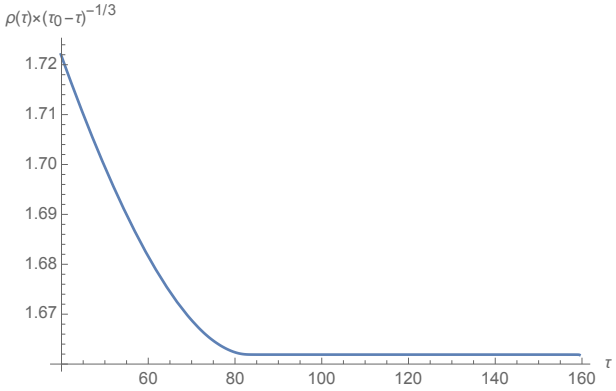

Figure 8.3: $\rho(\tau) \sim (\tau_0 - \tau)^{1/3};\ \tau_0 \approx 159.5.$

that tends to zero for large ϕ

$$V(\phi) = \frac{1}{2}e^{-\phi} + \phi^2 e^{-\phi^2}, \tag{8.39}$$

This is plotted in Figure 8.1; the local minimum lies near $\phi = 0.2$. The potential blows up for negative ϕ, but this will not concern us. We solve equations 8.31 and 8.32 with ϕ_0 taken to be not too far from the local minimum, with small $d\phi/d\tau$ and with the negative sign in the root of the ρ equation: $\phi(\tau = 0) = 1/2;\ \phi'(\tau = 0) = -10^{-6};\ \rho(\tau = 0) = 10$. One sees (Figure 8.2) the scalar field roll over the barrier after some number of oscillations. The ratio of potential to kinetic energy quickly tends to zero after the crossing. As we expect, we find a singularity at a finite time in the future, and indeed $\rho(\tau)$ behaves as $(\tau_0 - \tau)^{1/3}$ (Figure 8.3).

We have argued that for more general initial conditions, provided gravity is sufficiently weak, the system evolves quickly to the bounce configuration with $G_N \approx 0$. Its evolution will then be as above.

8.5.3 Implications of the singularity

Our main concern with the singularity is whether it is an obstruction to any sort of systematic analysis. If we have a weak coupling, small curvature description of the system, allowing a perturbative analysis, we expect to be able to write an effective Lagrangian including terms of successively higher dimension—higher numbers of derivatives—such as:

$$\mathcal{L} = \sqrt{g}\Big(\frac{1}{G_N}\mathcal{R} + \mathcal{R}^2 + \frac{1}{M^2}\mathcal{R}^4 + \dots \\ +(\partial_\mu\phi)^2 + \frac{1}{M^4}(\partial_\mu\phi)^4\Big). \tag{8.40}$$

If one tries to analyze the resulting classical equations perturbatively, in the presence of $\dot{\phi} \sim 1/(t-t_0)$ and $\mathcal{R} \sim 1/(t-t_0)^2$, at low orders, the terms in the expansion diverge and the expansion breaks down. This is similar to the phenomena at a big bang or big crunch singularity.

8.6 Conclusions

We have argued, from two points of view, that one cannot construct de Sitter space in any controlled approximation in string theory. First, we have seen that even allowing the possibility of arbitrarily large fluxes, it is very difficult to find stationary points for which both the string coupling is small and compactification radii are large, even before asking whether the corresponding cosmological constant is positive or negative. We have seen that typically when sensible stationary points exist, even if formally

radii are large and couplings small, higher order terms in the expansions are not small. Related observations have been made in Ooguri et al. (2019), based on conjectures about the behavior of quantum gravity systems.

But our second obstacle seems even more difficult to surmount: a set of small perturbations of any would-be metastable de Sitter state, classically, will evolve to uncontrollable singularities.

This is *not* an argument that metastable de Sitter states do not exist in quantum theories of gravity; only that they are not accessible to controlled approximations. The problem is similar to the existence of big bang and big crunch singularities; we have empirical evidence that the former exists in the quantum theory that describes our universe, but we do not currently have the tools to describe these in a quantum theory of gravity.

Kachru et al. (2019) have considered the question from the perspective of the KKLT (Kachru et al. 2003) constructions. These involve vacua with fluxes, but the small parameter is not provided by taking all fluxes particularly large; rather, it arises from an argument that there are so many possible choices of fluxes that in some cases, purely at random, there is a small superpotential. In other words, there is conjectured to be a vast set of (classically) metastable states of which only a small fraction permit derivation of an approximate four-dimensional, weak coupling effective action. Kachru et al. (2019) argue that such a treatment is self consistent. We are sympathetic to the view that such an analysis provides evidence that if in some cosmology one lands for some interval in such a state, the state can persist for a long period. But a complete

description of such a cosmology is beyond our grasp at present.

In considering the cosmic landscape, one of the present authors has argued that, even allowing for the existence of such states in some sort of semiclassical analysis, long-lived de Sitter vacua will be very rare, unless protected by some degree of approximate supersymmetry (Dine et al. 2009). The breaking of supersymmetry would almost certainly be non-perturbative in nature; searches for concrete realizations of such states (as opposed to statistical arguments for the *existence* of such states, along the lines of KKLT) would be challenging.

Ultimately, at a quantum level, reliably establishing the existence of metastable de Sitter space appears to be a very challenging problem. One needs a cosmic history, and it would be necessary that this history be under theoretical control, both in the past and in the future. As a result, the significance of failing to find stationary points of an effective action describing metastable de Sitter space is not clear. We have seen that even thought of as classical configurations, there are questions of stability and obstacles to understanding the system eternally, once small perturbations are considered. We view the question of the existence of metastable de Sitter space as an open one.

Bibliography

Abazajian, K. N., Adelman-McCarthy, J. K., Agüeros, M. A., et al. 2009, ApJS, 182, 543

Abbott, B. P., Abbott, R., Abbott, T. D., et al. 2017a, ApJ, 848, L13

—. 2017b, ApJ, 848, L12

—. 2020, ApJ, 892, L3

Abramowicz, M. A., & Fragile, P. C. 2013, Living Reviews in Relativity, 16, 1

Aghanim, N., et al. 2018, arXiv:1807.06209

Albrecht, A., & Steinhardt, P. J. 1987, Adv. Ser. Astrophys. Cosmol., 3, 158

Alexander, T. 2017, ArXiv e-prints, arXiv:1701.04762

Althaus, L. G., Miller Bertolami, M. M., & Córsico, A. H. 2013, A&A, 557, A19

Althaus, L. G., Serenelli, A. M., & Benvenuto, O. G. 2001, MNRAS, 323, 471

Andrews, J. J., & Zezas, A. 2019, MNRAS, 486, 3213

Andriot, D. 2019a, Fortsch. Phys., 67, 1800103

—. 2019b, Fortsch. Phys., 67, 1900026

Andriot, D., Marconnet, P., & Wrase, T. 2020a, arXiv:2006.01848

—. 2020b, arXiv:2005.12930

Antonini, F., Lombardi, Jr., J. C., & Merritt, D. 2011, ApJ, 731, 128

Antonini, F., & Merritt, D. 2013, ApJ, 763, L10

Arcavi, I., Gal-Yam, A., Sullivan, M., et al. 2014a, ApJ, 793, 38

—. 2014b, ApJ, 793, 38

Asplund, M., Grevesse, N., Sauval, A. J., & Scott, P. 2009, ARA&A, 47, 481

Auchettl, K., Guillochon, J., & Ramirez-Ruiz, E. 2017a, ApJ, 838, 149

—. 2017b, ApJ, 838, 149

Auchettl, K., Ramirez-Ruiz, E., & Guillochon, J. 2017c, ArXiv e-prints, arXiv:1703.06141

Ayal, S., Livio, M., & Piran, T. 2000, ApJ, 545, 772

Baldwin, J. A., Phillips, M. M., & Terlevich, R. 1981, PASP, 93, 5

Banks, T., & Dine, M. 2001, JHEP, 10, 012

Banlaki, A., Chowdhury, A., Roupec, C., & Wrase, T. 2019, JHEP, 03, 065

Bar-Or, B., Kupi, G., & Alexander, T. 2013, ApJ, 764, 52

Barth, A. J., Bentz, M. C., Greene, J. E., & Ho, L. C. 2008, ApJ, 683, L119

Baumgardt, H., Makino, J., & Ebisuzaki, T. 2004, ApJ, 613, 1143

Belczynski, K., Repetto, S., Holz, D. E., et al. 2016, ApJ, 819, 108

Beniamini, P., & Piran, T. 2019, MNRAS, 487, 4847

Blaauw, A. 1993, in Astronomical Society of the Pacific Conference Series, Vol. 35, Massive Stars: Their Lives in the Interstellar Medium, ed. J. P. Cassinelli & E. B. Churchwell, 207

Blagorodnova, N., Kotak, R., Polshaw, J., et al. 2017a, ApJ, 834, 107

Blagorodnova, N., Gezari, S., Hung, T., et al. 2017b, ApJ, 844, 46

Blagorodnova, N., Cenko, S. B., Kulkarni, S. R., et al. 2019, ApJ, 873, 92

Bloom, J. S., Giannios, D., Metzger, B. D., et al. 2011a, Science, 333, 203

—. 2011b, Science, 333, 203

Bondi, H., & Hoyle, F. 1944, MNRAS, 104, 273

Bongiorno, A., Merloni, A., Brusa, M., et al. 2012, MNRAS, 427, 3103

Bonnerot, C., & Lu, W. 2020, MNRAS, 495, 1374

Bonnerot, C., Rossi, E. M., Lodato, G., & Price, D. J. 2016a, MNRAS, 455, 2253

—. 2016b, MNRAS, 455, 2253

Bressan, A., Marigo, P., Girardi, L., Nanni, A., & Rubele, S. 2013, in European Physical Journal Web of Conferences, Vol. 43, European Physical Journal Web of Conferences, 03001

Bressan, A., Marigo, P., Girardi, L., et al. 2012, MNRAS, 427, 127

Brinchmann, J., Charlot, S., White, S. D. M., et al. 2004, MNRAS, 351, 1151

Brott, I., de Mink, S. E., Cantiello, M., et al. 2011, A&A, 530, A115

Brown, G. C., Levan, A. J., Stanway, E. R., et al. 2015, MNRAS, 452, 4297

Brown, J. S., Holoien, T. W.-S., Auchettl, K., et al. 2017, MNRAS, 466, 4904

Brown, J. S., Shappee, B. J., Holoien, T. W.-S., et al. 2016a, MNRAS, 462, 3993

Brown, J. S., Kochanek, C. S., Holoien, T. W.-S., et al. 2018, MNRAS, 473, 1130

Brown, W. R., Gianninas, A., Kilic, M., Kenyon, S. J., & Allende Prieto, C. 2016b, ApJ, 818, 155

Brown, W. R., Kilic, M., Kenyon, S. J., & Gianninas, A. 2016c, ApJ, 824, 46

Buchner, J., & Bauer, F. E. 2017, MNRAS, 465, 4348

Cantiello, M., Yoon, S. C., Langer, N., & Livio, M. 2007, A&A, 465, L29

Carter, B., & Luminet, J. P. 1982a, Nature, 296, 211

—. 1982b, Nature, 296, 211

—. 1983, A&A, 121, 97

Casey, C. M., Narayanan, D., & Cooray, A. 2014, Phys. Rep., 541, 45

Catalán, S., Isern, J., García-Berro, E., & Ribas, I. 2008, MNRAS, 387, 1693

Cenko, S. B., Bloom, J. S., Kulkarni, S. R., et al. 2012a, MNRAS, 420, 2684

Cenko, S. B., Krimm, H. A., Horesh, A., et al. 2012b, ApJ, 753, 77

Cenko, S. B., Cucchiara, A., Roth, N., et al. 2016, ApJ, 818, L32

Chabrier, G., Baraffe, I., Leconte, J., Gallardo, J., & Barman, T. 2009, in American Institute of Physics Conference Series, Vol. 1094, 15th Cambridge Workshop on Cool Stars, Stellar Systems, and the Sun, ed. E. Stempels, 102–111

Chamandy, L., Blackman, E. G., Frank, A., Carroll-Nellenback, J., & Tu, Y. 2020, MNRAS, 495, 4028

Chen, X., Madau, P., Sesana, A., & Liu, F. K. 2009, ApJ, 697, L149

Cheng, R. M., & Bogdanović, T. 2014a, Phys. Rev. D, 90, 064020

—. 2014b, Phys. Rev. D, 90, 064020

Choi, J., Dotter, A., Conroy, C., et al. 2016, ApJ, 823, 102

Chornock, R., Berger, E., Gezari, S., et al. 2014a, ApJ, 780, 44

—. 2014b, ApJ, 780, 44

Cicoli, M., De Alwis, S., Maharana, A., Muia, F., & Quevedo, F. 2019, Fortsch. Phys.,

67, 1800079

Cicoli, M., Klevers, D., Krippendorf, S., et al. 2014, JHEP, 05, 001

Cicoli, M., Maharana, A., Quevedo, F., & Burgess, C. 2012, JHEP, 06, 011

Cicoli, M., Quevedo, F., & Valandro, R. 2016, JHEP, 03, 141

Clausen, D., & Eracleous, M. 2011, ApJ, 726, 34

Colella, P., & Woodward, P. R. 1984, Journal of Computational Physics, 54, 174

Coleman, S. R. 1977, Phys. Rev., D15, 2929, [Erratum: Phys. Rev.D16,1248(1977)]

Coleman, S. R., & De Luccia, F. 1980, Phys. Rev., D21, 3305

Coughlin, E. R., & Nixon, C. J. 2019, ApJ, 883, L17

Coulter, D. A., Foley, R. J., Kilpatrick, C. D., et al. 2017, Science, 358, 1556

Cribiori, N., & Junghans, D. 2019, Phys. Lett. B, 793, 54

Cyburt, R. H., Amthor, A. M., Ferguson, R., et al. 2010, ApJS, 189, 240

Dai, L., Escala, A., & Coppi, P. 2013a, ApJ, 775, L9

—. 2013b, ApJ, 775, L9

Dai, L., McKinney, J. C., & Miller, M. C. 2015, ApJ, 812, L39

Davies, R. I., Müller Sánchez, F., Genzel, R., et al. 2007, ApJ, 671, 1388

Davis, A., Jones, S., & Herwig, F. 2019, MNRAS, 484, 3921

De, S., MacLeod, M., Everson, R. W., et al. 2020, ApJ, 897, 130

De Colle, F., Guillochon, J., Naiman, J., & Ramirez-Ruiz, E. 2012, ApJ, 760, 103

de Jager, C., Nieuwenhuijzen, H., & van der Hucht, K. A. 1988, A&AS, 72, 259

de Kool, M. 1990, ApJ, 358, 189

de Mink, S. E., Langer, N., Izzard, R. G., Sana, H., & de Koter, A. 2013, ApJ, 764, 166

Del Moro, A., Alexander, D. M., Mullaney, J. R., et al. 2013, A&A, 549, A59

Dewi, J. D. M., Pols, O. R., Savonije, G. J., & van den Heuvel, E. P. J. 2002, MNRAS, 331, 1027

Diener, P., Frolov, V. P., Khokhlov, A. M., Novikov, I. D., & Pethick, C. J. 1997, ApJ, 479, 164

Dine, M., Festuccia, G., & Morisse, A. 2009, JHEP, 09, 013

Dine, M., Law-Smith, J. A. P., Sun, S., Wood, D., & Yu, Y. 2021, Journal of High Energy Physics, 2021, 50

Dine, M., & Seiberg, N. 1985, Phys. Lett., 162B, 299

Dodd, S. A., Law-Smith, J. A. P., Auchettl, K., Ramirez-Ruiz, E., & Foley, R. J. 2021, ApJ, 907, L21

Driebe, T., Schoenberner, D., Bloecker, T., & Herwig, F. 1998, A&A, 339, 123

East, W. E. 2014, ApJ, 795, 135

Eggleton, P. P. 1983, ApJ, 268, 368

Ellison, S. L., Teimoorinia, H., Rosario, D. J., & Mendel, J. T. 2016, MNRAS, 458, L34

Esquej, P., Saxton, R. D., Freyberg, M. J., et al. 2007, A&A, 462, L49

Esquej, P., Saxton, R. D., Komossa, S., et al. 2008, A&A, 489, 543

Evans, C. R., & Kochanek, C. S. 1989a, ApJ, 346, L13

—. 1989b, ApJ, 346, L13

Everson, R. W. 2020, in prep.

Everson, R. W., MacLeod, M., De, S., Macias, P., & Ramirez-Ruiz, E. 2020, ApJ, 899, 77

Farmer, R., Fields, C. E., Petermann, I., et al. 2016, ApJS, 227, 22

Feldmeier-Krause, A., Kerzendorf, W., Neumayer, N., et al. 2017, MNRAS, 464, 194

Fragos, T., Andrews, J. J., Ramirez-Ruiz, E., et al. 2019, ApJ, 883, L45

Frank, J. 1978, MNRAS, 184, 87

Frank, J., & Rees, M. J. 1976a, MNRAS, 176, 633

—. 1976b, MNRAS, 176, 633

French, K. D., Arcavi, I., & Zabludoff, A. 2016a, ApJ, 818, L21

—. 2016b, ApJ, 818, L21

—. 2017a, ApJ, 835, 176

—. 2017b, ApJ, 835, 176

Fryxell, B., Olson, K., Ricker, P., et al. 2000, ApJS, 131, 273

Gafton, E., & Rosswog, S. 2019a, MNRAS, 1458

—. 2019b, MNRAS, 487, 4790

Gair, J. R., Tang, C., & Volonteri, M. 2010, Phys. Rev. D, 81, 104014

Gallegos-Garcia, M., Law-Smith, J., & Ramirez-Ruiz, E. 2018, ApJ, 857, 109

Garg, S. K., & Krishnan, C. 2019, JHEP, 11, 075

Garg, S. K., Krishnan, C., & Zaid Zaz, M. 2019, JHEP, 03, 029

Geng, H. 2020, Phys. Lett. B, 805, 135430

Georgiev, I. Y., & Böker, T. 2014, MNRAS, 441, 3570

Gezari, S., Chornock, R., Lawrence, A., et al. 2015, ApJ, 815, L5

Gezari, S., Heckman, T., Cenko, S. B., et al. 2009, ApJ, 698, 1367

Gezari, S., Chornock, R., Rest, A., et al. 2012a, Nature, 485, 217

—. 2012b, Nature, 485, 217

Goicovic, F. G., Springel, V., Ohlmann, S. T., & Pakmor, R. 2019, MNRAS, 487, 981

Goldstein, A., Veres, P., Burns, E., et al. 2017, ApJ, 848, L14

Golightly, E. C. A., Coughlin, E. R., & Nixon, C. J. 2019a, ApJ, 872, 163

Golightly, E. C. A., Nixon, C. J., & Coughlin, E. R. 2019b, ApJ, 882, L26

Götberg, Y., de Mink, S. E., Groh, J. H., et al. 2018, A&A, 615, A78

Götberg, Y., Korol, V., Lamberts, A., et al. 2020, ApJ, 904, 56

Goto, T. 2007, MNRAS, 381, 187

Graur, O., French, K. D., Zahid, H. J., et al. 2017a, ArXiv e-prints, arXiv:1707.02986

—. 2017b, ArXiv e-prints, arXiv:1707.02986

—. 2018, ApJ, 853, 39

Greene, J. E., & Ho, L. C. 2007a, ApJ, 667, 131

—. 2007b, ApJ, 667, 131

Grimm, T. W., Li, C., & Valenzuela, I. 2020, JHEP, 06, 009

Guillochon, J., Manukian, H., & Ramirez-Ruiz, E. 2014a, ApJ, 783, 23

—. 2014b, ApJ, 783, 23

Guillochon, J., & McCourt, M. 2017, ApJ, 834, L19

Guillochon, J., Nicholl, M., Villar, V. A., et al. 2018, ApJS, 236, 6

Guillochon, J., & Ramirez-Ruiz, E. 2013a, ApJ, 767, 25

—. 2013b, ApJ, 767, 25

—. 2015a, ApJ, 809, 166

—. 2015b, ApJ, 809, 166

—. 2015c, ApJ, 798, 64

Guillochon, J., Ramirez-Ruiz, E., & Lin, D. 2011, ApJ, 732, 74

Guillochon, J., Ramirez-Ruiz, E., Rosswog, S., & Kasen, D. 2009, ApJ, 705, 844

Gunn, J. E., Carr, M., Rockosi, C., et al. 1998, AJ, 116, 3040

Gunn, J. E., Siegmund, W. A., Mannery, E. J., et al. 2006, AJ, 131, 2332

Gurzadian, V. G., & Ozernoi, L. M. 1979, Nature, 280, 214

Guth, A. H. 1987, Adv. Ser. Astrophys. Cosmol., 3, 139

Haas, R., Shcherbakov, R. V., Bode, T., & Laguna, P. 2012, ApJ, 749, 117

Hansen, B. M. S., Kalogera, V., & Rasio, F. A. 2003, ApJ, 586, 1364

Hayasaki, K., Stone, N., & Loeb, A. 2012, in European Physical Journal Web of Conferences, Vol. 39, European Physical Journal Web of Conferences, 01004

Hayasaki, K., Stone, N., & Loeb, A. 2013a, MNRAS, 434, 909

—. 2013b, MNRAS, 434, 909

—. 2016, MNRAS, 461, 3760

Hayasaki, K., Zhong, S., Li, S., Berczik, P., & Spurzem, R. 2018, ApJ, 855, 129

Heckman, J. J., Lawrie, C., Lin, L., Sakstein, J., & Zoccarato, G. 2019a, Fortsch. Phys., 67, 1900071

Heckman, J. J., Lawrie, C., Lin, L., & Zoccarato, G. 2019b, Fortsch. Phys., 67, 1900057

Heger, A., Fryer, C. L., Woosley, S. E., Langer, N., & Hartmann, D. H. 2003, ApJ, 591, 288

Hills, J. G. 1975a, Nature, 254, 295

—. 1975b, Nature, 254, 295

Hinkle, K. H., Lebzelter, T., Fekel, F. C., et al. 2020, ApJ, 904, 143

Hinshaw, G., Larson, D., Komatsu, E., et al. 2013, ApJS, 208, 19

Hirai, R., Podsiadlowski, P., & Yamada, S. 2018, ApJ, 864, 119

Ho, L. C. 2009, ApJ, 699, 626

Hobbs, G., Lorimer, D. R., Lyne, A. G., & Kramer, M. 2005, MNRAS, 360, 974

Holgado, A. M., Silva, H. O., Ricker, P. M., & Yunes, N. 2021, arXiv e-prints, arXiv:2101.08267

Holoien, T. W. S., Brown, J. S., Auchettl, K., et al. 2018, MNRAS, 480, 5689

Holoien, T. W.-S., Prieto, J. L., Bersier, D., et al. 2014a, MNRAS, 445, 3263

—. 2014b, MNRAS, 445, 3263

Holoien, T. W.-S., Kochanek, C. S., Prieto, J. L., et al. 2016a, MNRAS, 463, 3813

—. 2016b, MNRAS, 455, 2918

—. 2016c, MNRAS, 455, 2918

Holoien, T. W. S., Vallely, P. J., Auchettl, K., et al. 2019a, ApJ, 883, 111

Holoien, T. W. S., Huber, M. E., Shappee, B. J., et al. 2019b, ApJ, 880, 120

Howitt, G., Stevenson, S., Vigna-Gómez, A., et al. 2020, MNRAS, 492, 3229

Hoyle, F., & Lyttleton, R. A. 1939, Proceedings of the Cambridge Philosophical Society, 35, 405

Hung, T., Gezari, S., Blagorodnova, N., et al. 2017a, ArXiv e-prints, arXiv:1703.01299

—. 2017b, ArXiv e-prints, arXiv:1703.01299

—. 2017c, ApJ, 842, 29

Hung, T., Foley, R. J., Ramirez-Ruiz, E., et al. 2020, arXiv e-prints, arXiv:2003.09427

Hurley, J. R., Pols, O. R., & Tout, C. A. 2000, MNRAS, 315, 543

Hut, P. 1981, A&A, 99, 126

Iaconi, R., De Marco, O., Passy, J.-C., & Staff, J. 2018, MNRAS, 477, 2349

Iaconi, R., Reichardt, T., Staff, J., et al. 2017, MNRAS, 464, 4028

Iben, Icko, J., & Livio, M. 1993, PASP, 105, 1373

Istrate, A. G., Marchant, P., Tauris, T. M., et al. 2016, A&A, 595, A35

Istrate, A. G., Tauris, T. M., Langer, N., & Antoniadis, J. 2014, A&A, 571, L3

Ivanov, P. B., Polnarev, A. G., & Saha, P. 2005, MNRAS, 358, 1361

Ivanova, N., Justham, S., Avendano Nandez, J. L., & Lombardi, J. C. 2013a, Science, 339, 433

Ivanova, N., Justham, S., Chen, X., et al. 2013b, A&A Rev., 21, 59

Ji, I., Peirani, S., & Yi, S. K. 2014, A&A, 566, A97

Jiang, Y.-F., Guillochon, J., & Loeb, A. 2016, ApJ, 830, 125

Jorgensen, I., Franx, M., & Kjaergaard, P. 1995, MNRAS, 276, 1341

Junghans, D. 2019, JHEP, 03, 150

Kachru, S., Kallosh, R., Linde, A. D., & Trivedi, S. P. 2003, Phys. Rev., D68, 046005

Kachru, S., Kim, M., McAllister, L., & Zimet, M. 2019, arXiv:1908.04788

Kaplan, D. L., Marsh, T. R., Walker, A. N., et al. 2014, ApJ, 780, 167

Kasen, D., Metzger, B., Barnes, J., Quataert, E., & Ramirez-Ruiz, E. 2017, Nature, 551, 80

Kasen, D., & Ramirez-Ruiz, E. 2010, ApJ, 714, 155

Kasen, D., & Woosley, S. E. 2009, ApJ, 703, 2205

Kauffmann, G., Heckman, T. M., White, S. D. M., et al. 2003a, MNRAS, 341, 33

—. 2003b, MNRAS, 341, 54

Kauffmann, G., Heckman, T. M., Tremonti, C., et al. 2003c, MNRAS, 346, 1055

Kesden, M. 2012a, Phys. Rev. D, 86, 064026

—. 2012b, Phys. Rev. D, 85, 024037

—. 2012c, Phys. Rev. D, 85, 024037

Khokhlov, A., Novikov, I. D., & Pethick, C. J. 1993a, ApJ, 418, 181

—. 1993b, ApJ, 418, 163

Kilic, M., Stanek, K. Z., & Pinsonneault, M. H. 2007, ApJ, 671, 761

Kippenhahn, R., & Weigert, A. 1967, ZAp, 65, 251

Kippenhahn, R., Weigert, A., & Weiss, A. 2012,

Klencki, J., Nelemans, G., Istrate, A. G., & Chruslinska, M. 2021, A&A, 645, A54

Kobayashi, S., Laguna, P., Phinney, E. S., & Mészáros, P. 2004, ApJ, 615, 855

Kochanek, C. S. 2016a, MNRAS, 458, 127

—. 2016b, MNRAS, 461, 371

—. 2016c, MNRAS, 461, 371

Komossa, S. 2015a, Journal of High Energy Astrophysics, 7, 148

—. 2015b, Journal of High Energy Astrophysics, 7, 148

Komossa, S., Halpern, J., Schartel, N., et al. 2004, ApJ, 603, L17

Komossa, S., Zhou, H., Wang, T., et al. 2008, ApJ, 678, L13

Kormendy, J., & Ho, L. C. 2013, ARA&A, 51, 511

Kramer, M., Schneider, F. R. N., Ohlmann, S. T., et al. 2020, A&A, 642, A97

Krolik, J. H., & Piran, T. 2011, ApJ, 743, 134

Kroupa, P. 2001, MNRAS, 322, 231

Kruckow, M. U., Tauris, T. M., Langer, N., et al. 2016, A&A, 596, A58

Laguna, P., Miller, W. A., Zurek, W. H., & Davies, M. B. 1993, ApJ, 410, L83

LaMassa, S. M., Heckman, T. M., Ptak, A., & Urry, C. M. 2013, ApJ, 765, L33

LaMassa, S. M., Yaqoob, T., Levenson, N. A., et al. 2017, ApJ, 835, 91

Langer, N., Schürmann, C., Stoll, K., et al. 2020, A&A, 638, A39

Lauterborn, D. 1970, A&A, 7, 150

Law-Smith, J., Guillochon, J., & Ramirez-Ruiz, E. 2019, ApJ, 882, L25

Law-Smith, J., MacLeod, M., Guillochon, J., Macias, P., & Ramirez-Ruiz, E. 2017a, ApJ, 841, 132

—. 2017b, ApJ, 841, 132

Law-Smith, J., Ramirez-Ruiz, E., Ellison, S. L., & Foley, R. J. 2017c, ApJ, 850, 22

Law-Smith, J. A., Coulter, D. A., & Mockler, B. 2020, jamielaw-smith/STARS_library v1.0.5

Law-Smith, J. A. P., Coulter, D. A., Guillochon, J., Mockler, B., & Ramirez-Ruiz, E. 2020a, ApJ, 905, 141

Law-Smith, J. A. P., Everson, R. W., Ramirez-Ruiz, E., et al. 2020b, arXiv e-prints, arXiv:2011.06630

Leloudas, G., Fraser, M., Stone, N. C., et al. 2016, Nature Astronomy, 1, 0034

Leloudas, G., Dai, L., Arcavi, I., et al. 2019a, arXiv e-prints, arXiv:1903.03120

—. 2019b, ApJ, 887, 218

Levan, A. J. 2015, Journal of High Energy Astrophysics, 7, 44

Levan, A. J., Tanvir, N. R., Starling, R. L. C., et al. 2014, ApJ, 781, 13

Li, G., Naoz, S., Kocsis, B., & Loeb, A. 2015, MNRAS, 451, 1341

Lidskii, V. V., & Ozernoi, L. M. 1979, Soviet Astronomy Letters, 5, 16

Lightman, A. P., & Shapiro, S. L. 1977, ApJ, 211, 244

Linde, A. 1982, Physics Letters B, 108, 389

Liu, S.-F., Guillochon, J., Lin, D. N. C., & Ramirez-Ruiz, E. 2013, ApJ, 762, 37

Livio, M., & Soker, N. 1988, ApJ, 329, 764

Lodato, G., King, A. R., & Pringle, J. E. 2009a, MNRAS, 392, 332

—. 2009b, MNRAS, 392, 332

Lodato, G., & Rossi, E. M. 2011, MNRAS, 410, 359

Lotz, J. M., Jonsson, P., Cox, T. J., & Primack, J. R. 2010, MNRAS, 404, 575

Lu, W., & Bonnerot, C. 2020, MNRAS, 492, 686

Luminet, J.-P., & Pichon, B. 1989, A&A, 209, 103

Macias, P. J., Windju, M., & Ramirez-Ruiz, E. 2015, ArXiv e-prints, arXiv:1504.00007

MacLeod, M., Antoni, A., Murguia-Berthier, A., Macias, P., & Ramirez-Ruiz, E. 2017a, ApJ, 838, 56

MacLeod, M., Goldstein, J., Ramirez-Ruiz, E., Guillochon, J., & Samsing, J. 2014, ApJ, 794, 9

MacLeod, M., Guillochon, J., & Ramirez-Ruiz, E. 2012a, ApJ, 757, 134

—. 2012b, ApJ, 757, 134

MacLeod, M., Guillochon, J., Ramirez-Ruiz, E., Kasen, D., & Rosswog, S. 2016a, ApJ,

819, 3

—. 2016b, ApJ, 819, 3

MacLeod, M., Macias, P., Ramirez-Ruiz, E., et al. 2017b, ApJ, 835, 282

MacLeod, M., & Ramirez-Ruiz, E. 2015a, ApJ, 803, 41

—. 2015b, ApJ, 798, L19

MacLeod, M., Ramirez-Ruiz, E., Grady, S., & Guillochon, J. 2013, ApJ, 777, 133

MacLeod, M., Trenti, M., & Ramirez-Ruiz, E. 2016c, ApJ, 819, 70

Madigan, A.-M., Halle, A., Moody, M., McCourt, M., & Nixon, C. 2017, ArXiv e-prints, arXiv:1705.03462

Madigan, A.-M., Halle, A., Moody, M., et al. 2018, ApJ, 853, 141

Madigan, A.-M., Hopman, C., & Levin, Y. 2011, ApJ, 738, 99

Madigan, A.-M., Levin, Y., & Hopman, C. 2009, ApJ, 697, L44

Magorrian, J., & Tremaine, S. 1999a, MNRAS, 309, 447

—. 1999b, MNRAS, 309, 447

Mainetti, D., Lupi, A., Campana, S., et al. 2017, A&A, 600, A124

Maksym, W. P., Lin, D., & Irwin, J. A. 2014, ApJ, 792, L29

Mandel, I., & Levin, Y. 2015, ApJ, 805, L4

Maoz, D., Badenes, C., & Bickerton, S. J. 2012, ApJ, 751, 143

March-Russell, J., & Petrossian-Byrne, R. 2020, arXiv:2006.01144

Marolf, D., Morrison, I. A., & Srednicki, M. 2013, Class. Quant. Grav., 30, 155023

Mason, E., Diaz, M., Williams, R. E., Preston, G., & Bensby, T. 2010, A&A, 516, A108

Maxted, P. F. L., Serenelli, A. M., Miglio, A., et al. 2013, Nature, 498, 463

McConnell, N. J., & Ma, C.-P. 2013, ApJ, 764, 184

McKinney, J. C., Dai, L., & Avara, M. J. 2015, MNRAS, 454, L6

Mendel, J. T., Simard, L., Palmer, M., Ellison, S. L., & Patton, D. R. 2014, ApJS, 210, 3

Merloni, A., Dwelly, T., Salvato, M., et al. 2015, MNRAS, 452, 69

Merritt, D. 2013,

Merritt, D., & Vasiliev, E. 2011, ApJ, 726, 61

Metzger, B. D., & Stone, N. C. 2016, MNRAS, 461, 948

Miller, J. M., Kaastra, J. S., Miller, M. C., et al. 2015, Nature, 526, 542

Mockler, B., Guillochon, J., & Ramirez-Ruiz, E. 2018, ArXiv e-prints, arXiv:1801.08221

—. 2019, ApJ, 872, 151

Mockler, B., & Ramirez-Ruiz, E. 2020, arXiv e-prints, arXiv:2007.12198

Moe, M., & Di Stefano, R. 2017, ApJS, 230, 15

Mohamed, S., & Podsiadlowski, P. 2007, in Astronomical Society of the Pacific Conference Series, Vol. 372, 15th European Workshop on White Dwarfs, ed. R. Napiwotzki & M. R. Burleigh, 397

Moore, K., & Garaud, P. 2016, ApJ, 817, 54

Mould, J., Cohen, J., Graham, J. R., et al. 1990, ApJ, 353, L35

Mullaney, J. R., Pannella, M., Daddi, E., et al. 2012a, MNRAS, 419, 95

Mullaney, J. R., Daddi, E., Béthermin, M., et al. 2012b, ApJ, 753, L30

Murguia-Berthier, A., MacLeod, M., Ramirez-Ruiz, E., Antoni, A., & Macias, P. 2017, ApJ, 845, 173

Nandez, J. L. A., & Ivanova, N. 2016, MNRAS, 460, 3992

Nandez, J. L. A., Ivanova, N., & Lombardi, J. C. 2015, MNRAS, 450, L39

Nelemans, G., Yungelson, L. R., & Portegies Zwart, S. F. 2004, MNRAS, 349, 181

Nelemans, G., Yungelson, L. R., Portegies Zwart, S. F., & Verbunt, F. 2001, A&A, 365, 491

Nelson, L. A., Dubeau, E., & MacCannell, K. A. 2004, ApJ, 616, 1124

Nicholls, C. P., Melis, C., Soszynski, I., et al. 2013, MNRAS, 431, L33

Nolthenius, R. A., & Katz, J. I. 1982, ApJ, 263, 377

Obied, G., Ooguri, H., Spodyneiko, L., & Vafa, C. 2018, arXiv:1806.08362

Ohlmann, S. T., Röpke, F. K., Pakmor, R., & Springel, V. 2016, ApJ, 816, L9

Ooguri, H., Palti, E., Shiu, G., & Vafa, C. 2019, Phys. Lett., B788, 180

Paczynski, B. 1976, in Structure and Evolution of Close Binary Systems, ed. P. Eggleton, S. Mitton, & J. Whelan, Vol. 73, 75

Pandya, V., Brennan, R., Somerville, R. S., et al. 2016, ArXiv e-prints, arXiv:1611.03869

Panei, J. A., Althaus, L. G., Chen, X., & Han, Z. 2007, MNRAS, 382, 779

Passy, J.-C., De Marco, O., Fryer, C. L., et al. 2012, ApJ, 744, 52

Patton, D. R., Qamar, F. D., Ellison, S. L., et al. 2016, MNRAS, 461, 2589

Paxton, B., Bildsten, L., Dotter, A., et al. 2011, ApJS, 192, 3

Paxton, B., Cantiello, M., Arras, P., et al. 2013, ApJS, 208, 4

Paxton, B., Marchant, P., Schwab, J., et al. 2015, ApJS, 220, 15

Peng, Y.-j., Lilly, S. J., Kovač, K., et al. 2010, ApJ, 721, 193

Percival, W. J., et al. 2010, Mon. Not. Roy. Astron. Soc., 401, 2148

Perlmutter, S., et al. 1999, Astrophys. J., 517, 565

Peters, P. C. 1964, Physical Review, 136, 1224

Pfuhl, O., Fritz, T. K., Zilka, M., et al. 2011, ApJ, 741, 108

Phinney, E. S. 1989, in IAU Symposium, Vol. 136, The Center of the Galaxy, ed. M. Morris (Dordrecht: Klewer Academic), 543

Piran, T., Sądowski, A., & Tchekhovskoy, A. 2015a, MNRAS, 453, 157

Piran, T., Svirski, G., Krolik, J., Cheng, R. M., & Shiokawa, H. 2015b, ApJ, 806, 164

Pooley, D., & Hut, P. 2006, ApJ, 646, L143

Pooley, D., Lewin, W. H. G., Anderson, S. F., et al. 2003, ApJ, 591, L131

Popov, D. V. 1993, ApJ, 414, 712

Pracy, M. B., Owers, M. S., Couch, W. J., et al. 2012, MNRAS, 420, 2232

Prieto, J. L., Krühler, T., Anderson, J. P., et al. 2016, ApJ, 830, L32

Prust, L. J., & Chang, P. 2019, MNRAS, 486, 5809

Ramirez-Ruiz, E., & Rosswog, S. 2009, ApJ, 697, L77

Rappaport, S., Verbunt, F., & Joss, P. C. 1983, ApJ, 275, 713

Rauch, K. P., & Ingalls, B. 1998, MNRAS, 299, 1231

Rauch, K. P., & Tremaine, S. 1996, New A, 1, 149

Rees, M. J. 1988a, Nature, 333, 523

—. 1988b, Nature, 333, 523

Reines, A. E., & Deller, A. T. 2012, ApJ, 750, L24

Renzo, M., Ott, C. D., Shore, S. N., & de Mink, S. E. 2017, A&A, 603, A118

Ricker, P. M., & Taam, R. E. 2008, ApJ, 672, L41

—. 2012, ApJ, 746, 74

Ricker, P. M., Timmes, F. X., Taam, R. E., & Webbink, R. F. 2019, IAU Symposium, 346, 449

Ritter, H. 1975, Mitteilungen der Astronomischen Gesellschaft Hamburg, 36, 93

Robertson, B. E., Kravtsov, A. V., Gnedin, N. Y., Abel, T., & Rudd, D. H. 2010, MNRAS, 401, 2463

Rosswog, S., Ramirez-Ruiz, E., & Hix, W. R. 2008a, ApJ, 679, 1385

—. 2009, ApJ, 695, 404

Rosswog, S., Ramirez-Ruiz, E., Hix, W. R., & Dan, M. 2008b, Computer Physics Communications, 179, 184

Roth, N., Kasen, D., Guillochon, J., & Ramirez-Ruiz, E. 2016, ApJ, 827, 3

Ryu, T., Krolik, J., Piran, T., & Noble, S. C. 2020a, arXiv e-prints, arXiv:2001.03501

—. 2020b, arXiv e-prints, arXiv:2001.03502

—. 2020c, arXiv e-prints, arXiv:2001.03503

—. 2020d, arXiv e-prints, arXiv:2001.03504

Sana, H., de Mink, S. E., de Koter, A., et al. 2012, Science, 337, 444

Sand, C., Ohlmann, S. T., Schneider, F. R. N., Pakmor, R., & Röpke, F. K. 2020, A&A, 644, A60

Sandquist, E. L., Taam, R. E., Chen, X., Bodenheimer, P., & Burkert, A. 1998, ApJ, 500, 909

Sarna, M. J., Ergma, E., & Gerškevitš-Antipova, J. 2000, MNRAS, 316, 84

Saxton, R. D., Read, A. M., Esquej, P., et al. 2012a, A&A, 541, A106

—. 2012b, A&A, 541, A106

Schödel, R., Eckart, A., Alexander, T., et al. 2007, A&A, 469, 125

Scudder, J. M., Ellison, S. L., & Mendel, J. T. 2012, MNRAS, 423, 2690

Serenelli, A. M., Althaus, L. G., Rohrmann, R. D., & Benvenuto, O. G. 2001, MNRAS, 325, 607

Seth, A. C., Cappellari, M., Neumayer, N., et al. 2010, ApJ, 714, 713

Sethi, S. 2018, JHEP, 10, 022

Shiokawa, H., Krolik, J. H., Cheng, R. M., Piran, T., & Noble, S. C. 2015, ApJ, 804, 85

Simard, L., Mendel, J. T., Patton, D. R., Ellison, S. L., & McConnachie, A. W. 2011, ApJS, 196, 11

Simard, L., Willmer, C. N. A., Vogt, N. P., et al. 2002, ApJS, 142, 1

Simard, L., Clowe, D., Desai, V., et al. 2009, A&A, 508, 1141

Soltan, A. 1982, MNRAS, 200, 115

Staff, J. E., De Marco, O., Macdonald, D., et al. 2016, MNRAS, 455, 3511

Starobinsky, A. A. 1987, Adv. Ser. Astrophys. Cosmol., 3, 130

Steinberg, E., Coughlin, E. R., Stone, N. C., & Metzger, B. D. 2019, MNRAS, 485, L146

Stone, N., Sari, R., & Loeb, A. 2013, MNRAS, 435, 1809

Stone, N. C., Generozov, A., Vasiliev, E., & Metzger, B. D. 2018, MNRAS, 480, 5060

Stone, N. C., Kesden, M., Cheng, R. M., & van Velzen, S. 2019, General Relativity and Gravitation, 51, 30

Stone, N. C., & Metzger, B. D. 2016a, MNRAS, 455, 859

—. 2016b, MNRAS, 455, 859

Stone, N. C., & van Velzen, S. 2016, ApJ, 825, L14

Strauss, M. A., Weinberg, D. H., Lupton, R. H., et al. 2002, AJ, 124, 1810

Strickler, R. R., Cool, A. M., Anderson, J., et al. 2009, ApJ, 699, 40

Strubbe, L. E., & Quataert, E. 2009a, MNRAS, 400, 2070

—. 2009b, MNRAS, 400, 2070

Sweigart, A. V., Greggio, L., & Renzini, A. 1990, ApJ, 364, 527

Tadhunter, C., Spence, R., Rose, M., Mullaney, J., & Crowther, P. 2017, Nature Astronomy, 1, 0061

Tauris, T. M., Kramer, M., Freire, P. C. C., et al. 2017, ApJ, 846, 170

Tejeda, E., Gafton, E., & Rosswog, S. 2017a, ArXiv e-prints, arXiv:1701.00303

Tejeda, E., Gafton, E., Rosswog, S., & Miller, J. C. 2017b, MNRAS, 469, 4483

Timmes, F. X., & Swesty, F. D. 2000, ApJS, 126, 501

Tout, C. A., Pols, O. R., Eggleton, P. P., & Han, Z. 1996, MNRAS, 281, 257

Trump, J. R., Sun, M., Zeimann, G. R., et al. 2015, ApJ, 811, 26

Tutukov, A., & Yungelson, L. 1973, Nauchnye Informatsii, 27, 70

Tutukov, A. V., & Yungelson, L. R. 1993, MNRAS, 260, 675

van den Heuvel, E. P. J. 1976, in Structure and Evolution of Close Binary Systems, ed. P. Eggleton, S. Mitton, & J. Whelan, Vol. 73, 35

van Velzen, S., & Farrar, G. R. 2014, ApJ, 792, 53

van Velzen, S., Stone, N. C., Metzger, B. D., et al. 2019, ApJ, 878, 82

van Velzen, S., Farrar, G. R., Gezari, S., et al. 2011, ApJ, 741, 73

van Velzen, S., Gezari, S., Hammerstein, E., et al. 2020, arXiv e-prints, arXiv:2001.01409

Vasiliev, E., & Merritt, D. 2013, ApJ, 774, 87

Vick, M., Lai, D., & Fuller, J. 2016, ArXiv e-prints, arXiv:1612.07316

Vigna-Gómez, A., MacLeod, M., Neijssel, C. J., et al. 2020, PASA, 37, e038

Vinciguerra, S., Neijssel, C. J., Vigna-Gómez, A., et al. 2020, MNRAS, 498, 4705

Vink, J. S., de Koter, A., & Lamers, H. J. G. L. M. 2001, A&A, 369, 574

Vinkó, J., Yuan, F., Quimby, R. M., et al. 2015, ApJ, 798, 12

Wang, J., & Merritt, D. 2004a, ApJ, 600, 149

—. 2004b, ApJ, 600, 149

Wang, T.-G., Zhou, H.-Y., Komossa, S., et al. 2012, ApJ, 749, 115

Webbink, R. F. 1984, ApJ, 277, 355

Wegg, C., & Nate Bode, J. 2011, ApJ, 738, L8

Weinberg, S. 1989, Rev. Mod. Phys., 61, 1

Weissbein, A., & Sari, R. 2017, MNRAS, 468, 1760

Wevers, T., van Velzen, S., Jonker, P. G., et al. 2017a, ArXiv e-prints, arXiv:1706.08965

—. 2017b, MNRAS, 471, 1694

Wevers, T., Stone, N. C., van Velzen, S., et al. 2019, MNRAS, 487, 4136

Wild, V., Heckman, T., & Charlot, S. 2010, MNRAS, 405, 933

Wu, S., Everson, R. W., Schneider, F. R. N., Podsiadlowski, P., & Ramirez-Ruiz, E. 2020a, ApJ, 901, 44

Wu, Y., Chen, X., Chen, H., Li, Z., & Han, Z. 2020b, A&A, 634, A126

Wyrzykowski, Ł., Zieliński, M., Kostrzewa-Rutkowska, Z., et al. 2017, MNRAS, 465,

L114

Ye, C. S., Fong, W.-f., Kremer, K., et al. 2020, ApJ, 888, L10

York, D. G., Adelman, J., Anderson, Jr., J. E., et al. 2000, AJ, 120, 1579

Yungelson, L. R. 2008, Astronomy Letters, 34, 620

Zalamea, I., Menou, K., & Beloborodov, A. M. 2010, MNRAS, 409, L25

Zhang, W., & Fryer, C. L. 2001, ApJ, 550, 357